From the holdings of the Department of Special Collections , Princeton University Library, Princeton, NJ

These documents are either in the public domain, or can only be used for educational and research purposes (Fair use) as per U.S. Copyright law (text below). By accessing this file, all users agree that their use falls in the public domain or within fair use as defined by the copyrightlaw. We do not charge any permission or usage fees for the publication of images of material inour collections, including those provided by Princeton University Library, via our website, catalog, or directly from staff.For more information regarding copyright, credit, and citation please review the information onthe Copyright, Credit and Citation Guidelines page of our website.
https://library.princeton.edu/special-collections/policies/copyright-credit-and-citation-guidelines. If you have any questions, including how to order higher-quality images from the collection, contact Special Collections Public Services via our Ask Us! Form. https://library.princeton.edu/special-collections/ask-us

---

Doctoral Dissertations, 2011-2026 Atmospheric and Oceanic Sciences

2016

Understanding geostrophic turbulence in a hierarchy of models

Chai, Junyi

Princeton, NJ : Princeton University

---

http://arks.princeton.edu/ark:/88435/dsp017h149s34f

U.S. Copyright law: The copyright law of the United States (Title 17, §108, United States Code) governs the making of photocopies or other reproductions of copyrighted material. Under certain conditions specified in the law, libraries and archives are authorized to furnish a photocopy or other reproduction. One of these specified conditions is that the photocopy or reproduction is not to be used for any purpose other than private study, scholarship, or research. If a user makes a request for, or later uses, a photocopy or reproduction for purposes in excess of fair use that user may be liable for copyright infringement. This institution reserves the right to refuse to accept a copying order if, in its judgment, fulfillment of the order would involve a violation of copyright law. https://www.copyright.gov/title17/title17.pdf

Understanding geostrophic turbulence in a hierarchy of models

Junyi Chai

A Dissertation
Presented to the Faculty
of Princeton University
in Candidacy for the Degree
of Doctor of Philosophy

Recommended for Acceptance
by the Program in
Atmospheric and Oceanic Sciences
Adviser: Isaac M. Held

September 2016

© Copyright by Junyi Chai, 2016.

All rights reserved.

Abstract

This thesis is concerned with turbulent motions on the very large scale (on the order of 100 to 1000 km) in the atmosphere and ocean. These large-scale motions are called geostrophic turbulence as they are fundamentally influenced by planetary rotation. However, the full Navier-Stokes equations, which include all aspects of turbulence, are often too complex to yield a meaningful understanding. We examine three idealized models with increasing levels of complexity.

We start with a forced-dissipated, two-dimensional fluid on a β-plane. The flow is approximated as a single layer and is stirred stochastically, while the spherical geometry is replaced with a tangible plane. Due to the β-effect, the eddies become anisotropic at a threshold scale called the turbulence-wave crossover scale. The traditional phenomenology assumes the forcing scale to be much smaller than the crossover scale so it has no influence. However, when the forcing scale is comparable to or even larger than the crossover scale, we find the forcing scale strongly influences jet formation. Numerical simulations reveal a new turbulent regime where the forcing scale is larger than the crossover scale, such that eddy/eddy interactions are negligible while eddy/mean-flow interactions dominate the nonlinear energy and enstrophy transfers. We update the current theoretical understanding by proposing a more general formulation of crossover scale and eddy diffusivity.

These results are applied to a simple climate model – the two-layer, quasi-geostrophic model. We obtain closure theories of eddy heat flux, which crucially depend on two nondimensional numbers: the criticality and the dimensionless friction. We further investigate the role of these two numbers in an idealized dry general circulation model (GCM) that closely resembles the real atmosphere. As the surface friction approaches zero, the dry GCM displays a novel way to equilibrate via an energy-recycling mechanism: eddy kinetic energy is converted back into potential energy by circulations on the largest scale and is then absorbed by radiative damping.

When the criticality varies around 1, we explain the change in the horizontal and vertical scales of the eddies with the linear instability theory; and the flow stays weakly nonlinear.

Acknowledgements

First I would like to thank my advisor Isaac Held and former advisor Geoffrey Vallis. They have always been encouraging my independent thinking and supporting my choices, while offering great guidance and thought-provoking comments along the way. Combined with seemingly unlimited computational power at GFDL, it is a unique experience to explore the frontiers of my research field with a free spirit, which helps me become an independent researcher.

My intellectual experience has also been greatly benefited from frequent conversations with my fellow students and postdocs. I am especially thankful for Thomas Flannaghan and Malte Jansen. From Malte I got many inspiration for new research projects. He has vast knowledge and genuine creativity at the same time, which I always turn to when modelling results seem to be puzzling. Tom is mild and always pleasant to help, who not only taught me all details of the dry GCM but always serves as my role model. In addition, Stephen Garner and Pablo Zurita-Gotor have also provided helpful criticism and suggestions on my research.

Finally, my five years at Princeton would not be so enjoyable without the vibrant AOS community, including students, postdocs, administrative staffs and faculties. It is my greatest fortune to know you as my friends. Most of all, I met Zhaoyi at Princeton, who is now my fiancée. Life is no longer a passive tracer in random walks when I am with you. As always, thanks to my parents who care and believe in me no matter what.

To my fiancée.

Life is no longer a passive tracer in random walks when I am with you.

Contents

Abstract iii

Acknowledgements v

1 Introduction **1**

1.1 The need for a hierarchy of models 5

1.2 Outline 13

2 Role of forcing scale on β-plane turbulence: jet formation **15**

2.1 Introduction 16

2.2 Theory 23

2.3 Model description and experiments 27

2.4 Results 30

2.5 Discussion and conclusion 40

3 Role of forcing scale on β-plane turbulence: eddy diffusion **54**

3.1 Introduction 55

3.2 Theory 59

3.3 Experiments 65

3.4 Results 66

3.5 Discussion and conclusion 73

4 Eddy heat fluxes in 2-layer quasi-geostrophic model **84**

4.1 The role of friction 86

5 Equilibration of a baroclinic planetary atmosphere toward the limit of vanishing bottom friction 93

5.1 Introduction 94

5.2 Idealized GCM and experiments 99

5.3 Results 103

5.4 Discussions and Conclusions 120

6 Horizontal and vertical scales of extratropical eddies in a dry GCM 137

6.1 Introduction 138

6.2 Notation and linear instability theory 143

6.3 Idealized GCM and experiments 152

6.4 Results 154

6.5 Conclusion and discussion 162

7 Conclusion 180

Bibliography 184

Chapter 1

Introduction

Turbulence is ubiquitous in the atmosphere and oceans, ranging from cumulus clouds often seen in a summer afternoon to the Great Red spot revolving between the magnificent jets on Jupiter. It is hard to give a precise definition on turbulence but we may summarize some of its general characteristics. A turbulent flow often features (a) eddies of a board range of spatial and temporal scales and (b) highly non-linear interactions between the scales which leads to (c) unpredictability and time irreversibly. It is probably safe to claim that all knowledge of turbulence is contained in the well-known Navier-Stokes (NS) equation, however, it is presumptuous or even foolish to say that the NS equation solves the turbulence problem (Frisch, 1995). In the least sense, the well-posedness of the NS equation is a Clay millennium problem that has yet to be proved. Despite much debate, it is often conjectured that the energy of an initially smooth flow could be dumped into an infinitesimal small point within finite time, resulting in a unphysical but mathematically possible finite-time blow-up in the NS equation (Tao, 2015). On the other hand, the NS equation contains vastly many different regimes that deserve studying in detail. Geostrophic turbulence is one of these regimes that is relevant for atmospheric and oceanic flows on the very large scale, examples of which are shown in Fig. 1.1. The planetary rotation introduces

an important effect called geostrophic balance to the large-scale flow, which means that the pressure gradient force is almost balanced by the Coriolis force. The result is that the flow is quasi- two-dimensional (2d) in nature. Thus geostrophic turbulence is much more similar to the beautiful flow on a soap bubble than the bumping turbulence one experiences on an airplane.

Rather than being a breed of three-dimensional (3d) turbulence, 2d turbulence is a totally different animal. The additional constraint introduced by being 2d is that a fluid parcel cannot stretch itself in the vertical direction, which would results in a change in vorticity (curl of the velocity, measuring how fast the parcel rotates) in a 3d flow. It is easy to envision that a 2d parcel will conserve its vorticity while interacting with its surrounding fluid as the pressure force is normal to every surface element of the parcel and thus cannot change how fast it rotates. The dynamical equation for a 2d flow can therefore be written as

$$\frac{\partial \zeta}{\partial t} + \mathbf{u} \cdot \nabla \zeta = \nu \nabla^2 \zeta, \tag{1.1}$$

where $\mathbf{u} = (u, v)$ is the 2d velocity vector, $\zeta = -\partial u/\partial y + \partial v/\partial x$ is the vorticity and ν is the viscosity. Integrals of any order of vorticity, including the enstrophy $\int \zeta^2 dxdy$, are invariants in addition to energy in the absence of dissipation. Due to these additional invariants, the well-posedness of (1.1) has long been proven, even in the case of zero viscosity (Ladyzhenskaya, 1969). The phenomenology, or mental picture, for 2d turbulence is also revised from it 3d counterpart. In 3d turbulence, larger eddies feed to smaller eddies and smaller eddies feed to even smaller ones until energy gets dissipated at the viscous scale. The energy dissipation rate, however, remains finite regardless of how small the viscosity. On the other hand, in 2d turbulence energy flows from small eddies to larger eddies, which is referred to as the inverse energy cascade opposing to the direct (forward) energy cascade in 3d turbulence. Therefore, viscosity plays a negligible role in dissipating energy. If there is no additional

large-scale dissipation, the total energy dissipation will be extremely weak and the flow could evolve towards an equilibrium state in the thermodynamics sense that is nontrivial compared to such a state in a 3d flow in which all energy has been quickly dissipated by viscosity. The flow evolving towards the thermodynamics equilibrium without forcing is often referred as the decaying turbulence. The final equilibrium state in many settings can be predicted using the statistical mechanics theory adapted to the 2d flow (Robert and Sommeria, 1991; Miller, 1990; see a review by Bouchet and Venaille, 2012). Generally speaking, the prediction is a stationary flow with the streamfunction being linearly proportional to the vorticity field. Such a stationary solution may be relevant for the long lived Great Red Spot in Jovian atmosphere, where the large scale frictional dissipation could be extremely small (Bouchet and Sommeria, 2002). However, most geophysical flows of interest for example, the terrestrial atmosphere and oceans, are strongly forced-dissipative systems and thus far from thermodynamic equilibrium. A statistical description of the flow is still essential for its chaotic nature, though the statistical mechanics theory for non-equilibrium system is far from rock-solid nor predictive. Therefore, there is currently no universal theory for most turbulence problems, but they are be attacked from different angles by keen observations of their uniquenesses. Here we briefly introduce two approaches that are fundamentally useful in many turbulence problems as well as in this thesis.

The first approach is the turbulence closure. The idea is to decompose a fluid field into a mean part and a fluctuating part as

$$s = \bar{s} + s',$$

and then predict the statistics of the fluctuating part – the eddies – from the mean flow. This decomposition can be also done by using a spatial mean and the deviation from it. For example, we can apply the decomposition to the velocity field and obtain the averaged NS equation in the x-direction as

$$\frac{\partial \bar{u}}{\partial t} + (\bar{\mathbf{u}} \cdot \nabla)\bar{u} = -\frac{\partial \bar{p}}{\partial x} - \nabla \cdot \overline{\mathbf{u}'u'},$$

for a constant density fluid. The term $\nabla \cdot \overline{\mathbf{u}'u'}$ is usually called the Reynolds stress. If we can write the eddy momentum flux $\overline{\mathbf{u}'u'}$ in terms of the mean flow $\bar{\mathbf{u}}$ (a closure), then we have an equation governing the mean flow itself. A usual closure for eddy flux is a diffusive closure, for example in the x-direction:

$$\overline{u's'} = -D\frac{\partial \bar{s}}{\partial x},$$

where D shall be referred as eddy diffusivity (or eddy viscosity if s is velocity field). The physical picture is that a fluid parcel is being advected much as a random walk due to the chaotic nature of turbulence. The physical property that the fluid parcel carries get mixed with the surroundings after traveling an average distance of the mixing length l_{mix}, which is analogous to the mean free path in thermodynamics. We can even come up with an estimate of diffusivity as $D \sim V l_{mix}$, where V is the velocity scale of the flow. This closure is much more appropriate for material conserved property such as tracer concentration, vorticity or potential vorticity that will be introduced later, than momentum, for which there exists the once puzzling phenomena of negative eddy viscosity (Starr, 1968).

The second approach is turbulent cascade phenomenology. Flow statistics is now examined in spectral space. The cascade phenomenology focuses on the transfer of invariants (energy, enstrophy, et. al.) in spectral space. For example, we can expand the velocity field in Fourier series as

$$\mathbf{u} = \sum_{\mathbf{k}} \{\mathbf{u}\}_{\mathbf{k}} e^{i\mathbf{k}\cdot\mathbf{x}},$$

where $\mathbf{k}$ is the wavevector and $\{\cdot\}_{\mathbf{k}}$ denotes the Fourier coefficient at wavevector $\mathbf{k}$. Kinetic energy spectrum can be defined as

$$\mathcal{E}(k) = \frac{1}{2}\Sigma_{|\mathbf{k}|=k} \{\mathbf{u}\}^*_{\mathbf{k}} \{\mathbf{u}\}_{\mathbf{k}},$$

where * denote complex conjugate. In isotropic turbulence, the inverse cascade phenomenology assumes a scale by scale energy transfer from the forcing scale where energy is injected into the flow to a much larger frictional dissipation scale where energy gets out of the flow. It further postulates an inertial range between the two scales within which all statistics are fully determined by the energy flux ε and wavenumber. As a result, a prediction of energy spectrum $\mathcal{E}(k)$ can be obtained by a dimensional analysis exercise as $\mathcal{E}(k) \sim \varepsilon^{2/3} k^{-5/3}$, which is directly testable (Kraichnan, 1967). Similar arguments can be applied to enstrophy and tracer variance in their cascade ranges.

1.1 The need for a hierarchy of models

The real geostrophic turbulence is obviously much more complicated than an ideal 2d flow. For example in the Earth's atmosphere, the air is not of constant density and is also compressible; the wind although predominately horizontal is varying in the vertical direction; there is fully developed 3d turbulence in the boundary layer near the surface, which has topography and land-sea contrast; the phase changes of water vapor releases latent heat, resulting in clouds and thus more complicated radiative transfer, as well as potential coupling of the dynamics between small-scale convection and large-scale flow. One path often pursued in climate studies is to build an Earth system model as complicated as possible, including atmosphere and ocean circulations together and even the biological cycles. We could study geostrophic turbulence in such climate models, which would be able to make a direct comparison with the observed flow. However, with all the dynamical and physical processes adding together, it would be extremely difficult to disentangle the mechanism behind a specific

phenomenon. As we have already seen in the beginning, the simple 2d flow illustrates many generally properties of the geostrophic turbulence and allows us to form a mental picture. Therefore, another path that may allow us to understand geostrophic turbulence is to start with simple models. Moreover, models with different levels of complexities can organize themselves into a hierarchy. In this hierarchy, each model contains the essential source of complexity of the phenomenon under scrutiny, but minimal extraneous details (Held, 2005, 2007). At the top of the hierarchy is the most complicated model with the NS equation and detailed physical processes. A simpler model can be formulated by making approximations to the NS equation. However, many times it is constructed from genuine physical intuitions and leaps of faith; for example, the surface quasi-geostrophic model that we will see later. Its relevance to real flows is exemplified by showing a qualitative or quantitative resemblance. To limit the number of models in this hierarchy so that each model can be studied intensively rather than just being examined by 2 or 3 people, each model must also be general enough to be interesting. This usually means that analytical solutions for these simpler models are still impossible but we need to resort to numerical solutions. In below we propose a list of models which may form such a hierarchy for the study of geostrophic turbulence. Notations are used such that ζ denotes relative vorticity, ψ for streamfunction, u, v and w for zonal, meridional and vertical winds respectively, $J(A, B)$ for the Jacobian of A and B. Streamfunction is related to the horizontal velocities as $u = -\partial\psi/\partial y$ and $v = \partial\psi/\partial x$.

a. 1-layer quasi-geostrophic (QG) model on β-plane

As we have mentioned, planetary rotation fundamentally determines flow, making it quasi-two dimensional in nature. An additional effect of planetary rotation is that on a sphere the planetary vorticity perpendicular to surface are different at each latitude, referring as the β-effect in which β is the rate of change of perpendicular

planetary vorticity relative to the latitudinal distance. Perhaps the simplest model that captures both effects of planetary rotation is the 1-layer QG model on β-plane, written as

$$\frac{\partial \zeta}{\partial t} + J(\psi, \zeta) + \beta v = F + D + (-1)^{n+1}\nu\nabla^{2n}\zeta, \tag{1.2}$$

in which F represents the forcing that provides an energy source, D represents a large scale dissipation and ν is (hyper-) viscosity. Although a small change from (1.1), Eq. (1.2) supports a new kind of motion – Rossby waves, which is of great importance to meteorology. To see the Rossby waves, linearize (1.2) with respect to a constant zonal flow U and we get

$$\frac{\partial \zeta'}{\partial t} + U\frac{\partial \zeta'}{\partial x} + \beta v' = 0, \tag{1.3}$$

where the prime A' denotes a disturbance to the mean flow. Plane wave

$$\psi' = e^{ik_x(x+ct)+ik_y y}$$

is a solution to the linearized Eq. (1.3) with phase speed

$$c = U - \frac{\beta}{k_x^2 + k_y^2}.$$

Due to the existence of Rossby wave, geostrophic turbulence on β-plane is different in many aspects compared to an isotropic 2d turbulence. Aspects such as spontaneous formation of jets, Rossby waves' influence on transport and mixing, Rossby wave propagating and breaking can be investigated in this model.

b. Shallow water model

Here we consider a 1-layer shallow water model on β-plane. As self-explained by its name, the model describes a layer of constant density fluid with a free surface, whose height is h and it should be small compared to the horizontal scales of the motion. The governing equations are

$$\frac{d\mathbf{u}}{dt} = -f\mathbf{k}\times\mathbf{u} - g'\nabla h, \tag{1.4}$$

$$\frac{dh}{dt} = -h\nabla\cdot\mathbf{u}, \tag{1.5}$$

where $\mathbf{k}$ is the unit vector in the vertical direction, g' is the effective gravitation acceleration that includes the density difference above and below the free surface, and $f = f_0 + \beta y$ is the Coriolis parameter in the β-plane approximation. The free surface h can be thought as an isentropic layer in the middle of the troposphere. The shallow water model may also serve as a crude approximation to the first baroclinic mode for the ocean or the Jupiter's upper atmosphere, where the stratification is greatly intensified in the top thin layer sitting above a neutrally stratified deep "abyssal" (Smith and Vallis, 2002; Ingersoll, 1990).

The shallow water model has features additional to the 1-layer model (1.2) in several aspects. The free surface allows it to have potential energy in addition to kinetic energy. It has additional divergent mode that is not in geostrophic balance, which allows for gravity waves and has some characteristics of 3d turbulence such as direct energy cascade (Yuan and Hamilton, 1994). After filtering out the ageostrophic motions, the QG shallow water model can be written as

$$\frac{\partial q}{\partial t} + J(\psi, q) = F + D + (-1)^{n+1}\nu\nabla^{2n}q, \tag{1.6}$$

where we add forcing as the flow cannot "force" itself, as well as dissipation to reach a steady state. The QG potential vorticity q is

$$q = f + \beta y + \zeta + \frac{\psi}{L_D^2}.$$

The only difference compared with the 1-layer model (1.2) is the the deformation radius L_D, given by

$$L_D = \frac{\sqrt{g'H}}{f},$$

where H is the mean height of the free surface h. The deformation radius introduces additional complexities to the flow. It influences the Rossby wave's dispersion relation and thus the jet formation (Smith, 2004). It can also halt inverse energy cascade Scott and Dritschel (2013). In additional, topography can be easily added to (1.6) and the induced stationary wave can be studied (Held, 1983). The QG shallow water equation contains some but not all features of the full model (1.4) and (1.5), for example the cyclone-anticyclone asymmetry (Polvani et al., 1994). These aspect due to the interactions between vortical and divergence modes may also be investigated in the full shallow water model.

c. Surface QG model

Unlike other models whose dynamics is governed by momentum equation, or Newton's second law of motion, in one form or another, the surface QG system is governed by the material advection of a surface temperature field $\theta(x, y, t)$ and the assumption that QG potential vorticity gradient is confined to the surface. As proposed by Held et al. (1995), the equations take the form

$$
\begin{aligned}
\frac{\partial \theta}{\partial t} + J(\psi, \theta) &= 0,\ \theta \equiv \partial_z \psi,\ z = 0 \\
(\partial_{xx} + \partial_{yy} + \partial_{zz})\psi &= 0,\ z > 0, \\
\psi \to 0 \quad &\text{as} \quad z \to \infty.
\end{aligned}
$$

The surface QG flow displays many features similar to a 3d rather than 2d turbulence. The energy cascades from larger scales to smaller scales. Singularity in inviscid flow can develop within finite time as seen from numerical simulations (Scott and Dritschel, 2014). This model belongs better to a hierarchy of its own kind rather than the one here, although its own hierarchy is currently in lack of enough intermediate models. This model is useful in capturing the vertical and horizontal structures of ocean eddies in the upper ocean (Lapeyre and Klein, 2006; Isern-Fontanet et al., 2008).

d. 2-layer QG model

The 2-layer QG model is perhaps the simplest model that can stir itself in a realistic way, and it is often regarded as the simplest turbulent "climate" model (Held, 2007). It can derived by truncating the vertical modes into barotropic and baroclinic modes (Flierl, 1978; Thompson and Young, 2007), or by partitioning the flow into two layers (Phillips, 1954). The two layers represents the flow in the upper (ψ_1) and lower (ψ_2) troposphere respectively. The QG potential vorticity q_k within each layer is

$$
q_k = \nabla^2 \psi_k + (-1)^k \lambda^{-2} (\psi_1 - \psi_2) + \beta y;\ k = 1, 2,
$$

where λ is the internal deformation radius. One way to force the model is to prescribe a mean thermal wind between the two layers, and the dynamical equations are

$$\begin{aligned}
&\frac{\partial q_1}{\partial t} + U\frac{\partial q_1}{\partial x} + \left(\beta + \frac{U}{\lambda^2}\right) v + J(\psi_1, q_1) = (-1)^{n+1}\nu\nabla^{2n} q_1, \\
&\frac{\partial q_2}{\partial t} - U\frac{\partial q_2}{\partial x} + \left(\beta - \frac{U}{\lambda^2}\right) v + J(\psi_2, q_2) = (-1)^{n+1}\nu\nabla^{2n} q_1 - r\zeta_2,
\end{aligned} \tag{1.7}$$

where a linear damping is added to the lower layer to represent Ekman friction. This model bridges the gap between 1-layer barotropic model and more realistic baroclinic models. A mental picture for baroclinic turbulence is that the barotropic mode $\psi = (\psi_1 + \psi_2)/2$ evolves in a similar way as the 1-layer 2d barotropic flow, exhibiting an inverse energy cascade; whereas the baroclinic mode $\tau = (\psi_1 - \psi_2)/2$, which represent the temperature field, is being advected by the barotropic flow similar to a passive tracer (Larichev and Held, 1995). Many aspects of baroclinic turbulence can be studied in this model, for example, self-maintenance of baroclinic jets (Robinson, 2006), closure for heat flux (Larichev and Held, 1995; Held and Larichev, 1996; Thompson and Young, 2007), linear and nonlinear instability (Lee and Held, 1991), baroclinic wave packet (Lee and Held, 1993), vertical structure of diffusivity (Jansen and Ferrari, 2013b).

e. Idealized primitive equation model

The primitive equation is the 3d NS equation with the only approximation that vertical momentum equation is replaced by the hydrostatic balance. The hydrostatic balance is well satisfied for the large-scale motion, therefore the primitive equation model is quite realistic. On a sphere and for an ideal gas atmosphere, the equations of motion are written as

$$\begin{aligned}
\frac{Du}{Dt} &= 2\Omega\sin\theta v + \frac{uv\tan\theta}{a} - \frac{1}{\rho a\cos\theta}\frac{\partial p}{\partial\lambda}, \\
\frac{Dv}{Dt} &= -2\Omega\sin\theta v - \frac{u^2\tan\theta}{a} - \frac{1}{\rho a}\frac{\partial p}{\partial\theta},
\end{aligned}$$

where Ω is the angular velocity of planetary rotation, θ is latitude, λ is longitude,p is pressure, ρ is density, a is planetary radius and

$$\frac{D}{Dt} = \frac{u}{a\cos\theta}\frac{\partial}{\partial\lambda} + \frac{v}{a}\frac{\partial}{\partial\theta} + w\frac{\partial}{\partial z}.$$

The equations can be solved combined with continuity equation, thermodynamic equation for gas and boundary conditions. The primitive equation model is used in many weather and climate prediction models in which complicated physical processes are included. For the simplest case, we can use Held and Suarez's (1994) highly idealized physics to build an idealized primitive equation model. The radiation is represented as a Newtonian relaxation of temperature to a prescribed radiative-convective equilibrium profile so that the thermodynamic equation becomes

$$\frac{\partial T}{\partial t} = \ldots - \gamma k_T (T - T_{eq}).$$

And the large-scale dissipation is represented by a linear damping of horizontal momentum near the surface. Even with such idealized physics, the resulted flow can still be quite realistic to some degree. The modeling results may be directly compared to the observed atmosphere so the idealized primitive equation model may serve as the bridge between the simpler models (such as the QG model) and the reality. An important complexity introduced by the primitive equation model is that the vertical stability is determined by the circulation rather than prescribed, as in the QG model. Therefore, what determines vertical stability is a research focus in the idealized primitive equation model (Schneider and Walker, 2006; Jansen and Ferrari, 2012, 2013a). The model has a somewhat realistic tropical circulation and stratosphere, and therefore can be used to study the interaction of these components with the geostrophic turbulence in the mid-latitude troposphere.

The models listed here are obviously not meant to be exhaustive but we can add more models into this hierarchy, for example, the continuous QG model and the idealized moist primitive equation model (Frierson et al., 2006). The logical structure of the hierarchy may be more complex than a pyramid but may be multi-branch tree. In this thesis, we study some of the models in the hierarchy in an attempt to understand geostrophic turbulence step by step.

1.2 Outline

We begin our study on geostrophic turbulence with the simplest model. In Chapter 2, we study the turbulence regimes in 1-layer QG model on β-plane, with particular emphasis on the jet formation. We discover a new turbulence regime and a scale associated with this regime. The eddy diffusion in this model is further investigated in Chapter 3, in which we come up with a new diffusivity scaling for the new turbulence regime. In Chapter 4, we move to 2-layer QG model and focus on the dependency of heat flux on external parameters. The knowledge we have learned from the 1-layer QG model can be directly applied to the barotropic mode of the 2-layer QG model. The behavior of baroclinic turbulence on two important non-dimensional parameters are examined: one parameter is the criticality and the other is related to surface friction. To connect our understandings from the highly idealized QG models to the real geophysical flow, we move up in the model hierarchy and study the idealized primitive equation model. How surface friction influences baroclinic turbulence in more realistic settings in the primitive equation model is explored in Chapter 5. We further propose a way for baroclinic turbulence to equilibrate toward the limit of vanishing friction by radiative damping, which may be relevant for Jovian atmosphere. In Chapter 6, we look at the other parameter, criticality. The dependency of horizontal and vertical scales of baroclinic eddies on criticality is studied, which shows additional

way to adjust compared to the 2-layer QG model. Finally, we briefly summarize this dissertation in Chapter 7.

The contents of Chapter 2 and 3 belong to two working papers (Chai et al., 2016b,a). Part of Chapter 4 was presented in the 2015 AGU Fall Meeting (Chai et al., 2015). The content of Chapter 5 appears in Chai et al. (2016c) and that of Chapter 6 appears in Chai and Vallis (2014).

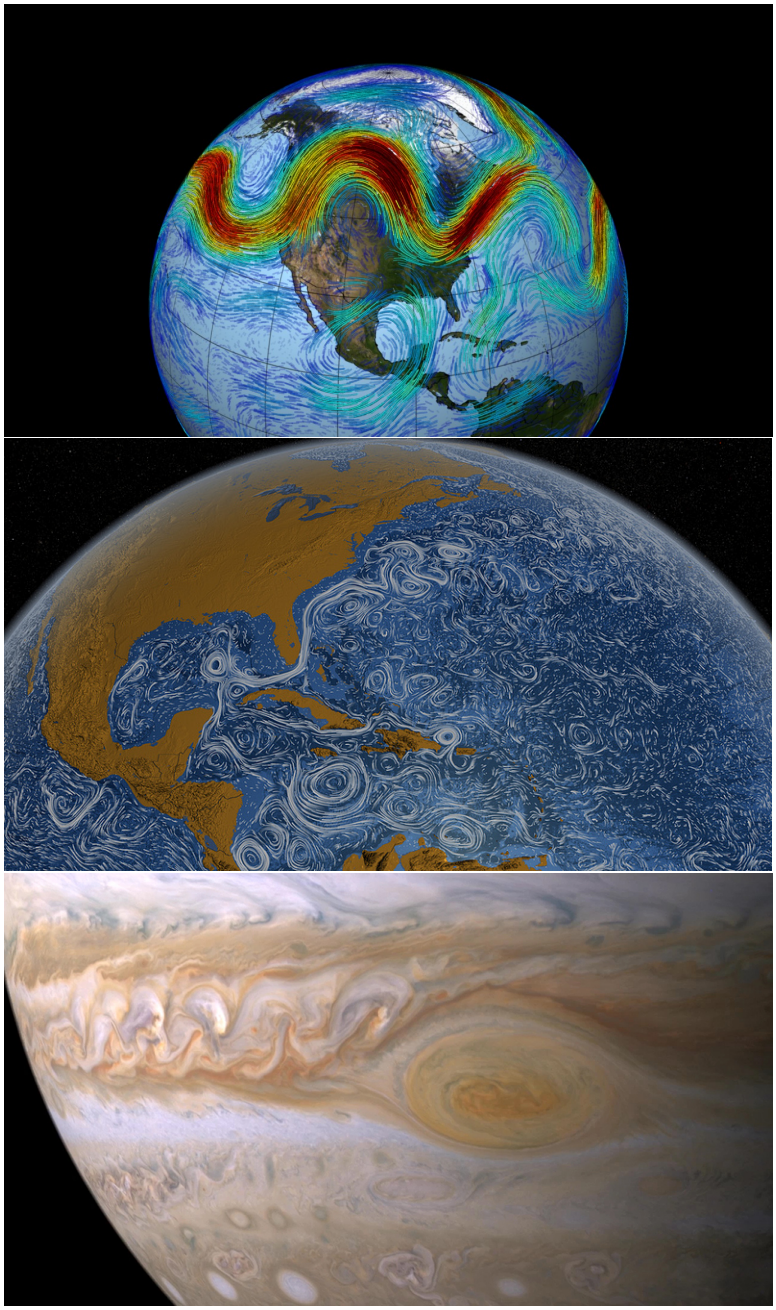


Figure 1.1: Examples of geostrophic turbulence: (top) polar jet stream in the Earth's upper atmosphere, (middle) Gulf stream and ocean rings, and (bottom) Great Red Spot and jets in Jovian cloud layer. Photo credit: NASA.

Chapter 2

Role of forcing scale on β-plane turbulence: jet formation

Turbulence regimes are examined in forced-dissipative, two-dimensional flow on β-plane with particular emphasis on jet formation. Two scales have been known to distinguish the flow from an isotropic turbulence: the Rhines wavenumber $k_{Rh} = \sqrt{\beta/2U_{rms}}$ and the turbulence-wave crossover wavenumber $k_\varepsilon = \mathcal{C}_\varepsilon \beta^{3/5}\varepsilon^{-1/5}$; here U is r.m.s. velocity, β is planetary potential vorticity gradient, $\mathcal{C}_\varepsilon$ is a constant of about 0.5$\sim$0.6, and ε is the upscale energy flux rate. The anisotropy of the flow is known to be largely determined by the zonostrophic index $Z = k_\varepsilon/k_{Rh}$. In this study, it is shown that the forcing scale k_f^{-1} also influences the anisotropy, especially when it is comparable to or even smaller than the crossover scale k_ε^{-1}. The role of forcing scale is conveniently characterized by the ratio $\Pi = k_f/k_\varepsilon$. When $\Pi < 1$, the crossover wavenumber is in the enstrophy cascade range and a new form is proposed as $k_\varepsilon \Pi^{-2/3}$, indicating a wider range of scales under β-effect than that would be predicted from Z alone. Turbulence regimes are explored in (Z, Π) space with numerical simulations. When $1.5 \lesssim Z \lesssim 2.5$, Z and Π both influence jet formation: jets are stronger and more coherent for larger Z or smaller Π. When $Z \gtrsim 2.5$, the flow are dominated by strong

jets. This regime has previously been characterized as the zonostrophic turbulence for $\Pi \gtrsim 4$. When Π decreases, the flow gradually transits into a new turbulence regime at $\Pi \lesssim 1$. This regime is "quasi-linear" in the sense that eddy-eddy interactions are negligible while eddy/mean-flow interactions dominate the nonlinear energy and enstrophy transfers. Energy injected at the forcing scale is directly transfered into the jets at the largest scale. The flow with zonal-mean potential vorticity similar to a staircase structure is approached in the corner of the quasi-linear regime when the zonostrophic index is very high ($Z \gtrsim 7$). The values of Π are estimated for Earth's atmosphere and oceans.

2.1 Introduction

Planetary rotation profoundly determines the macroturbulence in the atmosphere and ocean, distinguishing it from the flows at much smaller scales in two different ways. First, the large scale flow is in near geostrophic balance due to the rotation. Therefore macroturbulence is quasi- two-dimensional in nature, which fundamentally changes the picture for nonlinear energy transfer (Kraichnan, 1967; Charney, 1971), predictability (Leith, 1971; Leith and Kraichnan, 1972), and tracer transport/mixing (Batchelor, 1959; Shuckburgh and Haynes, 2003) from its three-dimensional counterpart. Second, the differential rotation on a sphere, or β-effect, introduces anisotropy to the flow. As a result, zonal jets spontaneously form, and the flow is rather an interplay of turbulence, Rossby waves and jets. Arguably, the simplest idealization to study the macroturbulence with both effects of planetary rotation is a forced-dissipated two-dimensional (2d) flow on a β-plane. This idealization contains the complexity of nonlinear interactions, yet it is fully determined by a handful of factors: forcing, dissipation (of both energy and enstrophy) and β-effect. In this idealized setting, it is promising to chart different turbulent regimes using a few nondimensional

parameters. These turbulent regimes have their correspondence in the real geophysical flows, as well as in models with increased complexity. Understanding these regimes will be a first step towards a general circulation theory.

An essential framework to discuss 2d turbulence is the dual cascade phenomenology. Consider an isotropic flow for the present, which is stirred by a spectrally localized forcing at wavenumber k_f. Energy and enstrophy injected at k_f will undergo two different branches of cascade: almost all the energy will inversely cascade to larger scales, whereas almost all the enstrophy will directly cascade to smaller scales. For the flow to reach equilibrium, frictional drag that is able to remove energy at large scales is needed, which halts the inverse energy cascade at wavenumber k_r. In this study, we limit ourselves to the regime in which the inverse energy cascade is halted before reaching the domain size, otherwise energy will condense into coherent structures of the domain scale and the classical inverse cascade picture is no longer relevant (Smith and Yakhot, 1993; Chertkov et al., 2007). For any finite viscosity, enstrophy will get dissipated at some small scale k_ν, which ends the enstrophy cascade. Statistics for eddies that undergo the energy cascade can be obtained from the following hypotheses. If the forcing scale is sufficiently separated from the frictional effects ($k_r \ll k_f$), there is assumed to be an energy *inertial range* $k_r \ll k \ll k_f$ in which neither forcing nor dissipation is important. The existence of the energy inertial range depends on the *locality hypothesis* that assumes the nonlinear energy transfer is local in scale. All the statistical properties within the energy inertial range are uniquely and universally determined by the wavenumber and the upscale energy flux rate ε (Kraichnan, 1967; Boffetta and Ecke, 2012; Vallis, 2006). Thus, the energy spectrum in the energy inertial range can be determined from a dimensional analysis exercise as

$$\mathcal{E}(k) = \mathcal{C}_\mathcal{K} \varepsilon^{2/3} k^{-5/3}, \tag{2.1}$$

where $\mathcal{C}_\mathcal{K}$ is the universal Kolmogorov constant. Using a similar argument, the energy spectrum within the inertial range of the enstrophy cascade is uniquely determined by the enstrophy flux η as

$$\mathcal{E}(k) = \mathcal{C}_{\mathcal{K}'}\eta^{2/3}k^{-3}. \tag{2.2}$$

These energy and enstrophy cascade spectra with spectral slope -5/3 and -3 respectively have been robustly observed both numerically and experimentally when the flow is free of coherent vortices; the Kolmogorov constants $\mathcal{C}_\mathcal{K}$ and $\mathcal{C}_{\mathcal{K}'}$ are found to be about $6 \sim 7$ and $1.3 \sim 1.6$ respectively (Maltrud and Vallis, 1991; Smith and Yakhot, 1993; Paret and Tabeling, 1997; Chen et al., 2006; Borue, 1993; Gotoh, 1998).

On a β-plane, two additional scales have been proposed to characterize the β-effect: the Rhines wavenumber as

$$k_{Rh} = (\beta/2U_{rms})^{1/2}, \tag{2.3}$$

where U_{rms} is the rms velocity of the whole flow (Rhines, 1975); and the turbulence-wave crossover wavenumber as

$$k_\varepsilon = \mathcal{C}_\varepsilon\beta^{3/5}\varepsilon^{-1/5}, \tag{2.4}$$

where $\mathcal{C}_\varepsilon$ is a constant of about $0.5 \sim 0.6$ (Vallis and Maltrud, 1993; Galperin et al., 2010; Smith and Vallis, 2002). It is assumed that k_ε marks the boundary between isotropic eddies and Rossby waves, as at this scale an isotropic eddy has the same turnover time as the Rossby wave period. The isotropic turbulence phenomenology is modified as follows: (a) eddies smaller than the crossover scale ($k > k_\varepsilon$) are only weakly influenced by the β-effect, thus behaving as isotropic turbulence with an inertial range; (b) if friction is weak enough so that inverse cascade proceeds beyonds the crossover scale ($k_r < k_\varepsilon$), the eddies that are larger than the crossover scale k_ε^{-1} are

strongly influenced by the β-effect and therefore behave as Rossby waves. The unique dispersion relation of Rossby waves strongly modifies their energy transfer in a way that most of the energy is directed into the zonal modes so that jets spontaneously form and the flow becomes anisotropic (a simple explanation is given by Vallis and Maltrud [1993]; another explanation exploring a new invariant unique for Rossby waves is given by Balk [1991, 2005], Nazarenko and Quinn [2009]).

On the other hand, the form and meaning of Rhines scale have been under debate since it has been proposed. In some studies, rms velocity of the eddies or the meridional wind has been used instead of U_{rms} in (2.3), while the Rhines scale itself has been used as an estimate for either eddy scale, jet scale, or the scale where energy gets channeled into jets (Williams, 1978; Jansen and Ferrari, 2012; Chai and Vallis, 2014; Liu and Schneider, 2015; Chemke and Kaspi, 2015). The proposed *zonostrophic turbulence* regime lands the Rhines scale on a quantitative ground (Sukoriansky et al., 2002; Galperin et al., 2010). In this regime, the inverse energy cascade extends well beyond the crossover scale k_ε^{-1} and the flow is strongly anisotropic. As illustrated in Fig. 2.1, energy in the zonal modes (jets) is thought to follow a universal spectrum determined by β and wavenumber as

$$\mathcal{E}_{\mathcal{Z}}(k) = \mathcal{C}_{\mathcal{Z}}\beta^2 k^{-5},\ k_x = 0, \tag{2.5}$$

where k_x is the zonal wavenumber, and the constant $\mathcal{C}_{\mathcal{Z}}$ is found to be about 0.5 (Sukoriansky et al., 2002; Smith and Vallis, 2002; Galperin et al., 2010). The residual modes (eddies) still follow the isotropic inverse cascade spectrum (2.1). Zonal and eddy kinetic spectra intersect at the crossover wavenumber k_ε. As the zonal energy spectrum is much steeper than the eddy kinetic energy spectrum, at scales larger than the crossover scale the zonal modes contain much more energy than the eddies. The role of β-effect is not to halt the energy cascade, but to direct the cascade into jets, and to support such a zonal energy spectrum much steeper than that of an isotropic

energy cascade. Eventually, friction halts the energy cascade at jet scale k_r^{-1}. If the jet scale is sufficiently larger than the crossover scale, most energy is in the zonal modes. The total energy of the flow $U_{rms}^2/2$ can then be estimated by an integration of (2.5) from k_r to ∞, which yields $k_r \simeq 1.2k_{Rh}$. In this regime, the Rhines scale has a clear meaning as the energy halting scale or jet scale. The central piece of the zonostrophic turbulence – the universal spectrum of the zonal modes (2.5) together with an isotropic energy cascade spectrum (2.5) in eddies – has been observed in many numerical simulations (Chekhlov et al., 1996; Smith and Vallis, 2002; Huang et al., 2001; Sukoriansky et al., 2002, 2007), more or less in the Jovian atmosphere (Sukoriansky et al., 2002; Choi and Showman, 2011; Galperin et al., 2014) and even in high-resolution ocean simulations (Galperin et al., 2004).

The ratio between Rhines scale and crossover scale

$$Z = k_\varepsilon/k_{Rh} \tag{2.6}$$

clearly determines how anisotropic the flow is in the zonostrophic regime: the larger Z is, the more the energy is in jets rather than eddies. In addition, it determines whether or not the flow has reached the zonostrophic regime in the first place. Specifically, Galperin et al. (2010) divide β-plane turbulence into two regimes – zonostrophic regime and *friction-dominated* regime – and the transition between them based on Z. Therefore, Z is coined as the *zonostrophic index*. Zonostrophic turbulence with the universal spectrum (2.5) is only reached when Z is large enough: $Z \gtrsim 2.5$. When $Z \lesssim 1.5$, the regime is called friction-dominated as the inverse energy cascade is halted by friction before reaching the crossover scale. The flow is close to isotropic turbulence. The spectrum (2.5) is no longer universal but the zonal spectrum is no more special than any of the other modes.

Under the above picture, whether jets form or not, strong or weak, seems to only be determined by the zonostrophic index Z. However, additional conditions to reach the zonostrophic turbulence regime are noted by Sukoriansky et al. (2007): (a) the forcing scale is small enough compared with the crossover scale, specifically the ratio $k_f/k_\varepsilon \gtrsim 4$; (b) energy cascade is halted before reaching the domain scale to avoid domain-scale energy condensation. The condition (a) can be understood from the locality hypothesis. Between the forcing scale and crossover scale the inverse energy cascade is close to that in isotropic turbulence with an inertial range (beyond the crossover scale, eddies transfer energy directly into jets on the largest scale so that energy transfer is highly non-local [Manz et al. 2009]). At end of the inertial range (at k_ε), the forcing scale may have no influence but only the energy flux rate ε matters. The extent of the inverse cascade needed for the forcing scale to lose its influence depends on how local the energy transfer is under inverse cascade. Chen et al. (2006) pointed out that the inverse cascade is only weakly local in scale: energy flux across scale l involves the thinning of subscale eddies 4 to 8 times smaller than l by the strain at l. Therefore, an isotropic inverse cascade must at least extend to 4 times the forcing scale in order for the forcing scale to lose its influence. Condition (a) $k_f/k_\varepsilon \gtrsim 4$ is likely to be the minimum bound for the forcing scale to have no influence in the zonostrophic turbulence regime.

Assuming an extended isotropic inverse cascade range so that forcing scale and other details of the forcing are irrelevant (and also assuming the viscosity to be irrelevant), and condition (b) so that domain size is irrelevant, the zonostrophic index Z is in fact the only nondimensional number that fully determines the flow. However, such an extended inverse cascade hardly exists in many real geophysical flows. In Earth's atmosphere, the forcing scale is the baroclinic instability scale, and it is very close to the largest eddy scale and the jet scale (Schneider and Walker, 2006; Merlis and Schneider, 2009). A clear isotropic inverse cascade with the theoretical spectrum

(2.1) is not seen. In the ocean, which displays some hints of an inverse cascade, the scale separation between forcing and energy halting scales is within 2 to 3 times (Tulloch et al., 2011). Therefore, the role of forcing scale is not likely to be negligible.

Moreover, literature on potential vorticity (PV) staircase hints that the flow may reach a new turbulence regime when $k_f/k_\varepsilon < 1$ and Z is large enough. PV staircase has long been hypothesized as a model for jet formation, which is the limiting case that PV is perfectly mixed between jets while having distinct jumps at the center of jets (Marcus, 1993; Marcus and Lee, 1998; Dunkerton and Scott, 2008; Dritschel and McIntyre, 2008). As a mathematical fact of a perfect PV staircase, the zonal kinetic energy spectrum is approximately $\mathcal{E}_\mathcal{Z}(k) \sim k^{-4}$ at large scales (Saffman, 1971; Danilov and Gryanik, 2004). The flow with a near-perfect PV staircase structure has been recently realized in simulations by Scott and Dritschel (2012). Energy spectra of the flow deviate from those in the zonostrophic regime. The slope of zonal kinetic energy spectrum appears to be closer to -4 than -5, and the slope of eddy kinetic energy spectrum is clearly much steeper than -5/3. Therefore, the PV staircase flow probably does not belong to the zonostrophic turbulence regime although Scott and Dritschel (2012) suggest the very high zonostrophic index as the key to obtain the PV staircase. Examining conditions (a) and (b), it is likely that condition (b) is satisfied whereas condition (a) is strongly violated. Using their experiment setup, our calculation suggests that in Scott and Dritschel's (2012) simulations $k_f/k_\varepsilon < 1$, which may be the criterion for the formation of PV staircase in addition to the high zonostrophic index.[1]

In this study, we aim to answer how the forcing scale influences the flow. From the above discussion, the ratio

[1]In a later study, Scott and Tissier (2012) suggest that PV staircase can easily form when the forcing scale is as large as the jet scale and $k_f/k_\varepsilon \lesssim 1/6$, which is more extreme than the condition we suggest here. This extreme regime is reached by a rather unusual topographic forcing without large scale friction, which makes it not straightforward to compare with the forced-dissipative turbulence in this study.

$$\Pi = k_f/k_\varepsilon \tag{2.7}$$

suggests itself as an important nondimensional number to characterize the role of the forcing scale. When $\Pi < 1$, the scale k_ε^{-1} is now within the direct enstrophy cascade range and therefore loses it meaning as the turbulence-wave crossover scale. This paper is organized as followings. In section 2, we derive a new crossover scale in the enstrophy cascade branch for $\Pi < 1$. In section 3, a set of experiments varying both Π and Z are carried out. Experiment results are analyzed in section 4, which are understood using turbulent phenomenology and our new crossover scale. In section 5, we conclude with an updated chart for turbulence regimes in the (Z, Π) space and discuss its relevance with the observed geophysical flows.

2.2 Theory

Consider the first case where β-effect does not affect the flow at the forcing scale so that the classical dual cascades extend from the forcing wavenumber k_f. Energy inversely cascades to larger scales and enstrophy directly cascades to smaller scales. The inverse of eddy turnover time defines a strain rate, or "turbulence frequency" ω_t, consisting of two branches: an inverse energy cascade branch for $k < k_f$ and a direct enstrophy cascade branch for $k > k_f$. From dimensional analysis, the turbulence frequency in the inverse energy cascade branch is

$$\omega_t = \mathcal{C}_{\omega,\varepsilon}\varepsilon^{1/3}k^{2/3}, \tag{2.8}$$

and in the direct enstrophy cascade branch is

$$\omega_t = \mathcal{C}_{\omega,\eta}\eta^{1/3}, \tag{2.9}$$

where $\mathcal{C}_{\omega,\varepsilon}$ and $\mathcal{C}_{\omega,\eta}$ are universal constants. If the forcing scale is well localized, enstrophy flux is related to energy flux by

$$\eta = k_f^2 \varepsilon. \tag{2.10}$$

As ω_e must be continuous across k_f, we have

$$\mathcal{C}_{\omega,\varepsilon} \varepsilon^{1/3} k_f^{2/3} = \mathcal{C}_{\omega,\eta} \eta^{1/3}.$$

Using the relation (2.10), we relate the two constants as $\mathcal{C}_{\omega,\varepsilon} = \mathcal{C}_{\omega,\eta}$. Therefore, a general form for ω_t can be written as

$$\omega_t = \mathcal{C}_{\omega,\varepsilon} \varepsilon^{1/3} \begin{cases} k^{2/3}, & k < k_f \\ k_f^{2/3}, & k > k_f \end{cases}, \tag{2.11}$$

which is a monotonic function increasing with k.

The well-known Rossby wave frequency is

$$\omega_\beta = -\frac{\beta k_x}{k^2}. \tag{2.12}$$

As the crossover scale is at the isotropic turbulence boundary, we take $k_x \sim k$ and the magnitude of Rossby wave frequency is

$$|\omega_\beta| \simeq \frac{\beta}{k}. \tag{2.13}$$

As illustrated in Fig. 2.2, the classical crossover wavenumber k_ε is assumed to be the intersection of the energy cascade branch of ω_t and $|\omega_\beta|$, written as

$$k_\varepsilon = \mathcal{C}_{\omega,\varepsilon}^{-3/5} \beta^{3/5} \varepsilon^{-1/5}. \tag{2.14}$$

However, it is also possible that the enstrophy cascade branch of ω_t intersects $|\omega_\beta|$ at

$$k_\eta = \mathcal{C}_\mathcal{K}^{-1/2} \beta \varepsilon^{-1/3} k_f^{-2/3}. \tag{2.15}$$

The relationship between k_ε and k_η can be seen clearly using the non-dimensional number Π we proposed in the introduction as

$$k_\eta = \Pi^{-2/3} k_\varepsilon. \tag{2.16}$$

As $|\omega_\beta|$ monotonically decreases with k and ω_t monotonically increases with k, ω_t and $|\omega_\beta|$ will intersect at a unique wavenumber. We regard this wavenumber as the generalized crossover wavenumber, denoted by k_β. As seen from Fig. 2.2, which branch of ω_t intersects with $|\omega_\beta|$ and therefore which one of k_ε and k_η gives the generalized crossover wavenumber k_β can be conveniently determined by Π. If $\Pi > 1$, the crossover scale is within the energy cascade range, in which the formally evaluated k_η obeys

$$k_\eta < k_\varepsilon = k_\beta < k_f,$$

and the classical crossover wavenumber keeps its meaning. If $\Pi < 1$, the crossover scale in now within the enstrophy cascade regime, and we have

$$k_f < k_\varepsilon < k_\eta = k_\beta.$$

Now the classical crossover wavenumber loses its meaning. At $\Pi = 1$, all the three wavenumbers k_f, k_ε and k_η are identical. For both energy and enstrophy cascade ranges, the generalized crossover wavenumber can be conveniently summarized as

$$k_\beta = \max(k_\varepsilon, k_\eta) = k_\varepsilon \max(1, \Pi^{-2/3}), \tag{2.17}$$

where $\max(x, y)$ returns the larger one out of x and y.

The range of of scales influenced by the β-effect determines how anisotropic the flow is. When $\Pi < 1$, the classical scaling k_ε underestimates the generalized crossover wavenumber. In this case, the zonostrophic index Z underestimates the range of scales under β-effect and thus underestimates the anisotropy of the flow. Using the generalized crossover wavenumber k_β, we may define a "jet index" to properly measure the width of the range of scales under β-effect as

$$Z_J = \frac{k_\beta}{k_{Rh}} = \max(1, \Pi^{-2/3}) Z. \tag{2.18}$$

Here we assume that the Rhines scale still roughly gives the energy halting scale, though the energy halting scale will inevitably have a dependency on Π as the universal spectrum (2.5) does not hold in the $\Pi < 1$ regime. Using the jet index, we would expect the jets to be even stronger if Π is reduced to below 1 for the same zonostrophic index. As an analogy of the transition between friction-dominated and zonostrophic regimes based on Z, a more general condition for jet formation may be that Z_J be larger than a critical value Z_c:

$$Z_J \gtrsim Z_c,$$

which gives

$$Z \gtrsim Z_c \min(1, \Pi^{2/3}).$$

This means that jet formation may be easier when Π is reduced below 1 for the same zonostrophic index Z. The boundary of jet formation is now determined by both Z and Π.

A caveat in the above derivation is that the turbulence frequency (2.9) is in the form of an isotropic turbulence. However, when $\Pi < 1$ we have $k_f < k_\beta$ so we cannot expect eddies at the forcing scale to be isotropic. The derivation is rescued by assuming a non-local enstrophy cascade. The dominate straining for $k > k_f$ comes

from the shear of the largest scale jets. The eddies are sheared apart by the jets and thus transfer enstrophy directly to the viscosity scale. The turbulence frequency should now be interpreted as the eddy decorrelation rate, which scales with the shear of the jets and therefore is independent of k. So the form of ω_t in (2.9) is retained and so is the rest of the derivation. The non-local enstrophy cascade dominated by eddy/mean-flow interactions is seen in previous studies (Manz et al., 2009) and also in our simulations (Section 4). Even in pure isotropic 2d turbulence, some studies suggest that the enstrophy cascade may be highly non-local, and the process is close to the cascade of a passive tracer (Borue, 1993; Falkovich and Lebedev, 1994).

2.3 Model description and experiments

Forced-dissipated 2d flow on a β-plane described as

$$\frac{\partial \zeta}{\partial t} + J(\psi, \zeta) + \beta v = \vartheta - \nu \nabla^8 \zeta - r\zeta \tag{2.19}$$

is solved on a doubly-periodic $2\pi \times 2\pi$ square domain. On the left hand side, ψ is the stream function, $v = \partial\psi/\partial x$ is the meridional velocity, ζ is the relative vorticity $\zeta = \nabla^2\psi$, and β is the planetary vorticity gradient. On the right hand side, ϑ represents forcing, while the dissipation consists of a linear friction $-r\zeta$ and an 8th order hyperviscosity dissipation $-\nu\nabla^8\zeta$. The hyperviscosity ν is adjusted adaptively in the numerical model using an optimal estimate based on the simulated flow (Maltrud and Vallis, 1991; Smith and Vallis, 2002). The forcing ϑ is defined in spectral space via its Fourier transform $\{\vartheta\}_k$, which has a uniform distribution within a narrow band $[k_f - \delta k_f, k_f + \delta k_f]$. The half width of the spectrum band is $\delta k_f = 2$ in all our simulations. In time, $\{\vartheta\}_k$ is random Markovian with a very short decorrelation time (correlation falls under 5% after 5 time steps) and normalized at each time step so

that the energy injection rate

$$\varepsilon_0 = -\langle \psi \vartheta \rangle \tag{2.20}$$

is fixed at a prescribed level, which is very close to the upscale energy flux ε when forcing scale is far away from grid scale. The angle bracket $\langle * \rangle$ denotes domain averaging. Numerical integration is performed using a de-aliased pseudo-spectral method for space differentiating with a maximum resolved wavenumber of 511 (1024^2 equivalent horizontal gridpoints), and a leap-frog method with a weak Robert filter for time stepping (Patterson and Orszag, 1971). More details on the model is described in Smith and Vallis (2002).

Ignoring the dependency on the exact form of the random forcing, Eq. (2.19) is fully characterized by 4 non-dimensional numbers constructed from $\{\varepsilon,\beta,r,k_f,L,\nu\}$, where L is the size of the domain. Suppose that the energy has not reached domain size so that L does not matter, and that the enstrophy is dissipated at a small enough scale so that hyperviscosity ν, which determines the exact scale of enstrophy dissipation, does not matter. Under these assumptions, the system is fully characterized by 2 non-dimensional numbers constructed from $\{\varepsilon,\beta,r,k_f\}$. As mentioned in the introduction, the two non-dimensional numbers are chosen as the zonostrophic index

$$Z = k_\varepsilon / k_{Rh}, \tag{2.21}$$

and

$$\Pi = k_f / k_\varepsilon.$$

Multiplying (2.19) with $-\psi$ yields an equation governing the time evolution of total energy E as

$$\frac{dE}{dt} = \varepsilon - 2rE. \tag{2.22}$$

In equilibrium, the domain averaged total kinetic energy E and thus rms velocity U_{rms} can be related to upscale energy flux and frictional rate r as

$$2rE = \varepsilon,$$

where

$$E = \frac{1}{2}\langle u^2 + v^2 \rangle = \frac{1}{2}U_{rms}^2.$$

The Rhines wavenumber in (2.3) can be rewritten as

$$k_{Rh} = 2^{-1/2}\beta^{1/2}r^{1/4}\varepsilon^{-1/4}. \tag{2.23}$$

Now we can express Z and Π using $\{\varepsilon,\beta,r,k_f\}$ as

$$Z = 0.85\beta^{1/10}\varepsilon^{1/20}r^{-1/4}, \tag{2.24}$$

and

$$\Pi = 1.67\beta^{-3/5}\varepsilon^{1/5}k_f, \tag{2.25}$$

where we use $\mathcal{C}_\varepsilon = 0.6$ in (2.4).

As Z and Π have the highest power law dependency on r and k_f respectively, it is easiest to vary r and k_f to explore the (Z, Π) space. In order to make sure that the energy halting scale is always smaller than the domain scale when we vary r, we impose the ratio $\varepsilon_0/r=(\pi/4)^2$ and $\beta = 16\pi$ so that $k_{Rh} \simeq 5.7$, as the way used by Scott and Dritschel (2012). In the actual simulations, the number of jets varies from 3 to 5, which largely agrees with the Rhines wavenumber. The linear friction rate r is varied among $10^{-4}\times$(4096, 1024, 256, 64, 8, 1) so that the zonostrophic index Z varies from 1.4 to 7.3. A consideration on the choice of forcing scale is that the forcing scale

should be smaller than the energy halting scale. Otherwise the flow is uninteresting as energy is directly dissipated by friction at the forcing scale without much nonlinear interactions. For each frictional rate r, forcing wavenumber k_f is varied among 16, 32, 64 and 128 (for the lowest friction $r = 10^{-4}$, one experiment $k_f = 128$ is not carried out due to the high computational cost to simulate such a low-friction flow). The largest forcing scale at wavenumber $k_f = 16$ is still sufficiently smaller than the jet scale so that we ensure there is enough range of nonlinear interactions. In (Z, Π) space, we can draw a crude boundary that Π and Z should at least satisfy for the flow to be interesting:

$$\Pi Z = k_f / k_{Rh} > 1. \tag{2.26}$$

The (Z, Π) space that is explored is shown in Fig. 2.3, where each simulation is indicated by either dot or triangle. The regime $\Pi < 1$ is reached in some simulations with relatively large zonostrophic index $Z \gtrsim 3$.

Theoretically, we can sample the corner of (Z, Π) space that has both high Z and Π by simply increasing the forcing wavenumber. In reality, however, this would require a prohibitive computational power. The high Z regime needs a long time to equilibrate, which can be roughly estimated as $1/r$. In practice, the flow with the highest $Z = 7.3$ requires computational time 4 to 5 orders of magnitudes higher than the flow with $Z = 1.4$. Further increasing Π by increasing forcing wavenumber for the $Z = 7.3$ run requires increasing horizontal resolution as well, which becomes computationally prohibitive with our current resources.

2.4 Results

In the zonostrophic turbulence picture, the anisotropy of the flow is determined by the zonostrophic index Z, and the flow regime is divided into friction-dominated

($Z \lesssim 1.5$), transitional ($1.5 \lesssim Z \lesssim 2.5$) and zonostrophic ($Z \gtrsim 2.5$). In this section, we look at the influence of Π on the flow when the zonostrophic index Z is relatively small ($Z \lesssim 2.5$) or large ($Z \gtrsim 2.5$). Finally, the formation of PV staircase when Z is very large ($Z \gtrsim 7.3$) is examined.

a. Jet formation boundary ($Z \lesssim 2.5$)

To have an overview on what the anisotropy (or jet strength) looks in the (Z, Π) space, we define an anisotropy index χ as

$$\chi = \langle \frac{u^2}{u^2 + v^2} \rangle,$$

which measures the percentage of energy in the zonal wind. For isotropic turbulence, the anisotropy index χ should be 0.5 as there is no difference between u and v. In the (Z, Π) space, the anisotropy index is shown in Fig. 2.3. Black dots indicate that jets have formed in the corresponding run, whereas gray triangles indicate there is no visually identifiable jet in that run. Across the whole parameter space here, Z is the dominant factor that shapes the overall behavior of the anisotropic index: χ increases monotonically from about 0.5 to near 1 when Z increases from about 1.4 to 7.3. For the lowest $Z = 1.4$, $\chi \approx 0.5$ confirms the flow to be in the friction-dominated regime as that would be predicted by the criterion $Z \lesssim 1.5$. Indeed, no jet or even slight hint of jet is seen in $Z = 1.4$ runs. Flow in the friction-dominated regime seems not to be strongly dependent on Π as seen from χ here, as well as from the eddy diffusivity as will be discussed in Part II of this study (Chai et al., 2016b).

Jets start to form when $Z \gtrsim 1.8$. For the two series of runs $Z = 1.8$ and 2.4 within the transitional regime $1.5 \lesssim Z \lesssim 2.5$, Π clearly influences the anisotropy of the flow as χ increases when Π decreases. The influence of Π on the formation and strength of the jet is seen more clearly from the vorticity and zonal velocity fields

shown in Fig. 2.4 (for $Z = 1.8$) and 2.5 (for $Z = 2.4$). Arguably, among $Z = 1.8$ runs, visually identifiable jets are only seen in the run with the smallest $\Pi = 1.5$. Though whether jets have formed or not in this run is objective, it is clear that the flow with $\Pi = 1.5$ is much more anisotropic than the one with $\Pi = 11.9$ (comparing Fig. 2.4 top with bottom). For the larger $Z = 2.4$, jets form in all runs (up to some debates for the run with $\Pi = 9.0$), but are stronger and more coherent when Π is smaller. Therefore, we conclude that not only the zonostrophic index Z but also Π determines the boundary for jet formation, as well as the coherence and strength of the jets. This dependency on Π qualitatively agrees with our theory, which predicts that the jet index Z_J – as an indicator of jet strength – increases when Π decreases. Quantitatively however, our theory predicts that such a dependency only exists when $\Pi < 1$. In the simulations, the influence of Π extends to a much greater extent than $\Pi < 1$. Nevertheless, it is clear that the influence is especially strong when Π is closer to 1, and Π gradually loses importance when it becomes larger than 4 (as seen in inset of Fig. 2.3 and by visually examining the flows and the advected tracer fields). The observed larger extent of influence than $\Pi < 1$ is hardly a surprise. As we mentioned in the introduction, the inverse energy cascade must at least extend to 4 times of the forcing scale in order for the forcing scale to lose its influence (Chen et al., 2006). Therefore, we expect Π to influence jet formation as far as $\Pi \lesssim 4$ but to gradually lose importance when Π increases above 4.

b. From zonostrophic to "quasi-linear" turbulence ($Z \gtrsim 2.5$)

The condition for zonostrophic turbulence is $Z \gtrsim 2.5$ and $\Pi \gtrsim 4$ (Sukoriansky et al., 2007; Galperin et al., 2010). In our simulations with $Z = 4.8$, Π varies from about 0.6 to 4.5. As seen from vorticity and zonal wind fields in Fig. 2.6, the jets are coherent and strong for all values of Π. Still, for smaller $\Pi < 1$, the jets are even sharper than those in the zonostrophic turbulence regime with $\Pi = 4.5$, consistent

with prediction from the jet index Z_J. More importantly, when $\Pi \lesssim 1$ the generalized crossover scale k_β^{-1} is smaller than the forcing scale so we expect $\Pi < 1$ to be a new turbulence regime with a different picture for energy cascade than the zonostrophic regime. In the following, we focus on characterizing and understanding this regime in the spectral space.

The kinetic energy spectrum can be evaluated as

$$\mathcal{E}(k) = \frac{1}{2}\sum_{|\mathbf{k}|=k} k^2 |\{\psi\}_{\mathbf{k}}|^2 = -\frac{1}{2}\sum_{|\mathbf{k}|=k} \{\zeta\}_{\mathbf{k}} \{\psi\}^*_{\mathbf{k}}, \tag{2.27}$$

where the bracket $\{A\}_{\mathbf{k}}$ denotes the Fourier component of A at wave vector $\mathbf{k} = (k_x, k_y)$, the star A^* denotes complex conjugate of A. The spectrum $\mathcal{E}(k)$ can be decomposed into a sum of the eddy kinetic energy (EKE) spectrum

$$\mathcal{E}_{eddy}(k) = \frac{1}{2}\sum_{|\mathbf{k}|=k, k_x\neq 0} k^2 |\{\psi\}_{\mathbf{k}}|^2, \tag{2.28}$$

and the zonal kinetic energy (ZKE) spectrum

$$\mathcal{E}_{\mathcal{Z}}(k) = \frac{1}{2}\sum_{|\mathbf{k}|=k, k_x=0} k^2 |\{\psi\}_{\mathbf{k}}|^2. \tag{2.29}$$

The energy spectra of the total flow $\mathcal{E}(k)$, of the eddies $\mathcal{E}_{eddy}(k)$ and of the zonal flow $\mathcal{E}_{\mathcal{Z}}(k)$ are shown in Fig. 2.7. The theoretical spectrum for inverse energy cascade range (2.1), enstrophy cascade range (2.2), and zonal modes in the zonostrophic turbulence (2.5) are shown for a comparison. The universal constants are chosen as $\mathcal{C}_{\mathcal{K}} = 6$, $\mathcal{C}_{\mathcal{K}'} = 1.6$ and $\mathcal{C}_{\mathcal{Z}} = 0.5$ as those reported in the literature (Boffetta and Ecke, 2012; Galperin et al., 2010).

For the runs with $\Pi = 4.5$ and 2.3, the energy spectra roughly agree with the picture of the zonostrophic regime illustrated in Fig. 2.1. The total energy spectrum $\mathcal{E}(k)$ is very close to the EKE spectrum $\mathcal{E}_{eddy}(k)$ from the forcing wavenumber k_f

to the crossover wavenumber k_ε, from where $\mathcal{E}(k)$ steepens above $\mathcal{E}_{eddy}(k)$ at scales larger than the crossover scale k_ε^{-1} due to the zonal modes. Between k_ε and the energy halting wavenumber k_r (about 3$\sim$4), the zonal energy spectrum $\mathcal{E}_{\mathcal{Z}}(k)$ roughly follows a -5 slope, although the theoretical universal spectrum (2.5) overestimates the energy level. The EKE spectrum $\mathcal{E}_{eddy}(k)$ roughly follows the theoretical isotropic inverse cascade spectrum (2.1) with the -5/3 slope from the forcing scale all the way to slightly less than the energy halting scale. In the enstrophy cascade range ($k > k_f$), the spectral slope is steeper than -3, which is probably due to a lack of resolution to resolve an extended enstrophy cascade range.

When Π decreases below 1 to $\Pi = 0.6$, energy injected at k_f is still transfered to jets and eddies much larger than the forcing scale. For $k < k_f$, the slope of the EKE spectrum $\mathcal{E}_{eddy}(k)$ is much steeper than -5/3 and is close to -3. The lack of an inverse cascade spectrum with $-5/3$ slope clearly differentiates the flow from zonostrophic turbulence. In the enstrophy cascade range ($k > k_f$), the $\mathcal{E}_{eddy}(k)$ is close to but slightly steeper than -3 slope, which may suggest the need of a log-correction (Kraichnan, 1971). In the $\Pi < 1$ regime, the generalized crossover wavenumber k_β is given by k_η in the enstrophy cascade range. The total spectrum $\mathcal{E}(k)$ is close to $\mathcal{E}_{eddy}(k)$ for $k \gtrsim k_\eta$, but steepens above $\mathcal{E}_{eddy}(k)$ for $k \lesssim k_\eta$ due to energy in the zonal modes, which indicates the flow does become anisotropic near the generalized crossover scale. Theoretically, we expect the spectrum (2.5) with -5 slope may become no longer universal when $\Pi \lesssim 1$. In practice, however, it is difficult to measure the slope of the zonal energy spectrum accurately as it is distributed as a series of peaks rather than a smooth curve.

For $\Pi < 1$, the flow lacks a near-isotropic inverse cascade range. Instead, eddies at the forcing scale are already influenced by the β-effect. What difference does this have on energy cascade? To answer this question, we resort to the spectral energy budget, which is obtained by multiplying $-\widetilde{\psi}^*_{\mathbf{k}}$ to the Fourier transform of the

vorticity equation (2.19) and then using the form of the energy spectrum in (2.27). The spectral energy budget is

$$\frac{\partial \mathcal{E}(k)}{\partial t} = T(k) - \sum_{|\mathbf{k}|=k} \{\psi\}^*_{\mathbf{k}} \{\vartheta\}_{\mathbf{k}} - 2r\mathcal{E}(k), \tag{2.30}$$

where we neglect energy dissipation by hyperviscosity. The term $T(k)$ is the nonlinear energy transfer into wavenumber k:

$$T(k) = \sum_{|\mathbf{k}|=k} \{\psi\}^*_{\mathbf{k}} \{J(\psi, \zeta)\}_{\mathbf{k}}\,. \tag{2.31}$$

And the terms $-\Sigma_{|\mathbf{k}|=k} \{\psi\}^*_{\mathbf{k}} \{\vartheta\}_{\mathbf{k}}$ and $-2r\mathcal{E}(k)$ are forcing and dissipation respectively. We can decompose the flow into a sum of the eddy and zonal-mean as

$$\psi = \overline{\psi} + \psi',$$

where the $\overline{A}$ denotes the zonal mean of A, and the A' denotes the deviation from the zonal mean. The spectral EKE budget can be formulated as

$$\frac{\partial \mathcal{E}_{eddy}(k)}{\partial t} = T_{EE}(k) - T^e_{EM}(k) - \sum_{|\mathbf{k}|=k} \{\psi'\}^*_{\mathbf{k}} \{\vartheta'\}_{\mathbf{k}} - 2r\mathcal{E}_{eddy}(k), \tag{2.32}$$

where the eddy-eddy interaction is

$$T_{EE}(k) = \sum_{|\mathbf{k}|=k} \{\psi'\}^*_{\mathbf{k}} \{J(\psi', \zeta')\}_{\mathbf{k}}\,, \tag{2.33}$$

and the eddy/mean-flow interaction is

$$T^e_{EM}(k) = -\sum_{|\mathbf{k}|=k} \{\psi'\}^*_{\mathbf{k}} \left\{ \overline{u} \frac{\partial \zeta'}{\partial x} + v' \frac{\partial \overline{\zeta}}{\partial y} \right\}_{\mathbf{k}}. \tag{2.34}$$

The spectral ZKE budget is

$$\frac{\partial \mathcal{E}_{\mathcal{Z}}(k)}{\partial t} = T^m_{EM}(k) - 2r\mathcal{E}_{\mathcal{Z}}(k), \tag{2.35}$$

where the eddy/mean-flow interaction is

$$T^m_{EM}(k) = \sum_{|\mathbf{k}|=k} \left\{\overline{\psi}\right\}^*_{\mathbf{k}} \left\{\overline{J(\psi', \zeta')}\right\}_{\mathbf{k}}. \tag{2.36}$$

The eddy/mean-flow interaction terms take different forms in the EKE and ZKE spectral budgets: $T^e_{EM}(k)$ means the rate of energy transfer out of eddies of wavenumber k, and $T^m_{EM}(k)$ is energy transfer rate into the zonal flow of wavenumber k. Integrated over all wavenumbers, $\int T^e_{EM}(k)dk$ equals $\int T^m_{EM}(k)dk$. However, $T^e_{EM}(k)$ can have a broad distribution over a range of scales while $T^m_{EM}(k)$ may narrowly peak at the Rhines wavenumber. Physically, this means that eddy-mean transfer is non-local.

Energy flux across a wavenumber k for the total flow can be defined as

$$F(k) = \int_k^\infty T(k')dk'. \tag{2.37}$$

Similarly, we can define energy flux due to eddy-eddy interactions and that due to eddy/mean-flow interactions as

$$F_{EE}(k) = \int_k^\infty T_{EE}(k')dk', \tag{2.38}$$

$$F_{EM}(k) = \int_k^\infty \left[-T^e_{EM}(k') + T^m_{EM}(k')\right] dk'. \tag{2.39}$$

A positive (negative) F means there is a net downscale (upscale) energy transfer across k. Energy fluxes $F(k)$, $F_{EE}(k)$ and $F_{EM}(k)$ normalized by ε are shown in Fig. 2.8 for various Π. The energy flux of the total flow $F(k)$ looks similar for different Π: a robust upscale energy transfer from the forcing wavenumber k_f to the energy halting wavenumber with nearly a constant rate, which means that frictional

dissipation is negligible at scales smaller than the energy halting scale. However, the partition of energy transfer between eddy-eddy and eddy/mean-flow interactions changes drastically when Π reduces from 4.5 to 0.6. For the largest $\Pi = 4.5$, eddy-eddy flux $F_{EE}(k)$ dominates over eddy/mean-flow flux $F_{EM}(k)$ before the inverse cascade reaches the crossover scale k_ε^{-1}, beyond which eddy/mean-flow flux dominates. This is consistent with the zonostrophic turbulence picture in which a near-isotropic inverse cascade is assumed between k_f and k_ε. Though here the $F_{EM}(k)$ within k_ε and k_f is far from negligible, indicating that a perfect zonostrophic picture may only be reached for even larger Π. When Π decreases, eddy/mean-flow transfer $F_{EM}(k)$ gradually becomes more and more dominating. For $\Pi = 0.6$, the eddy-eddy flux $F_{EE}(k)$ becomes negligible. Therefore, the upscale energy flux is overwhelmingly dominated by eddy/mean-flow interactions.

To see the scales where the energy gets channeled into the jets, the detailed spectral EKE and ZKE budgets are shown in Fig. 2.9. For $\Pi = 4.5$, in the EKE budget the energy cascades to larger scales via eddy-eddy interactions. Within a wide range of scales $5 \lesssim k \lesssim 70$, EKE is channeled into jets. The fact that eddies much smaller than the crossover scale k_ε^{-1} still transfer their energy into jets may indicate that k_ε should be the boundary where the β-effect has become significant rather where it starts to take effect. It is likely that within $k_\varepsilon \lesssim k \lesssim 70$, the eddies behave as a duality of isotropic eddies and Rossby waves. In the ZKE budget, energy transfer into jets T_{EM}^M sharply peaks at wavenumber 4, which coincides with the number of jets. The EKE and ZKE spectra together shows a nonlocal transfer of energy from eddies of a wide range of scales directly into the largest scale jets. For $\Pi = 0.6$, the EKE budget looks widely different. Energy is directly transfered from eddies into the mean flow at the forcing scale. Although eddies larger than the forcing scale have a higher energy level (Fig. 2.7), their energy transfer into the jets is negligible compared with that by eddies at the forcing scale. Therefore, the injected energy is directly transfered into

the zonal jets, and it is then dissipated by friction as seen from the ZKE budget in Fig. 2.9 (bottom).

For the runs with $Z = 3.2$, the above discussions are largely the same. The spectral enstrophy budget is also calculated. It shows a similar picture to the spectral energy budget, that eddy/mean-flow interactions dominate downscale enstrophy transfer in the regime $\Pi < 1$. To get an impression of how the non-local transfer happens, we carry out an initial-value run with similar parameters to $Z = 4.8$ but without forcing and friction. The initial condition is the time and zonal mean flow from the $Z = 4.8$ and $\Pi = 0.6$ run with a small-amplitude eddy perturbation. The instantaneous eddy vorticity fields ζ' at time $t = 0$, 0.78 and 1.56 are shown in Fig. 2.10. At $t = 0$, the eddy vorticity field shows the perturbation to the mean zonal flow. The perturbation is uniformly distributed within wavenumber ring $14 \leq k \leq 18$, which resembles a "pulse" of forcing. At $t = 0.78$, eddies are tilted and elongated by the shear of the jets, which clearly transfers enstrophy to smaller scales in the y-direction. As the circulation of an eddy is conserved while it is being elongated, the velocity of the eddy must reduce, and therefore eddy kinetic energy is transfered into the jet (Kraichnan, 1976). At $t = 1.56$, the whole eddy seems to smear into the jet and eventually gets destroyed by hyperviscosity, though almost no energy is dissipated by hyperviscosity. This picture closely resembles the vortex thinning mechanism discussed by Manz et al. (2009). In this physical space picture, the role of the β-effect is only implicit as jets with strong shear cannot spontaneously form without β-effect. The role of the β-effect together with the shear of the jets is seen more explicitly in the spectrum space. Gürcan (2012) shows that the shear further weakens the already weak resonance interactions between Rossby waves, thus making energy transfer into jets even more favored.

We conclude that for relatively large zonostrophic index $Z \gtrsim 2.5$, a new regime exists for $\Pi \lesssim 1$, which is different from the zonostrophic turbulence ($\Pi \gtrsim 4$). In this

regime, eddy/mean-flow interactions dominate in energy and enstrophy transfers, whereas eddy-eddy interactions are negligible. Therefore, we expect the statistical properties of the flow in this regime to be well captured in the "quasi-linear" model, in which with eddy-eddy interactions are removed but the eddy/mean-flow interactions are retained (O'Gorman and Schneider, 2007; Tobias and Marston, 2013). We carry out a series of quasi-linear simulations with $Z = 3.2$ and Π varying from about 0.5 to 8. Indeed, when $\Pi = 0.5$ the jets in the quasi-linear model have similar scale as in the full nonlinear model. When Π increases, the jet scale changes little in the full nonlinear model but keeps decreasing in the quasi-linear model. At sufficiently large $\Pi = 8$, no clear jet is seen in the quasi-linear model. Therefore, we shall refer the regime $\Pi \lesssim 1$ and $Z \gtrsim 2.5$ as the "quasi-linear" turbulence.

c. Potential vorticity staircase ($Z \gtrsim 7.3$)

As mentioned in the introduction, we predict that the potential vorticity (PV) staircase should only be reached when $\Pi \lesssim 4$. Otherwise, the spectrum in the zonal modes should follow the universal k^{-5} spectrum rather than the k^{-4} spectrum of a perfect PV staircase. For the simulations with $Z = 7.3$, Π varies from 0.4 to 1.5. Time and zonal mean potential vorticity fields $q = \zeta + \beta y$ from these simulations are shown in Fig. 2.11. The smallest $\Pi = 0.4$ run resembles the PV staircase: PV is nearly perfectly mixed at some latitudinal bands separated by sharp jumps. Though this run has almost the same parameters as Scott and Dritschel (2012), our staircase structure is less perfect compared to theirs, which may require additional time to reach due to the extremely low mixing. Such a staircase structure is much less clear in the $\Pi = 1.5$ run. Although at some latitudes there is a PV jump, there is not a wide region with near perfectly mixed PV. Instead, in most regions away from the jet center where the PV jump is, the PV gradient is similar to the planetary vorticity gradient β. Therefore, we narrow the boundary for PV staircase formation to $\Pi \lesssim 1$.

At such a high zonostrophic index, jets are very strong in all three runs. Still, jets are even sharper in the smallest $\Pi = 0.4$ run.

2.5 Discussion and conclusion

An updated chart for regimes in β-plane turbulence is shown in Fig. 2.12, guided by our theory and simulations. Now the boundary that determines whether jets form or not is not a straight vertical line $Z = Z_c$, but rather a curve determined by both Z and Π. For relatively small Z within about 1.8 and 2.5, jets are much easier to form and are more coherent for smaller Π, especially if Π is close to or smaller than 1. The influence of Π on jet formation may be understood from the crossover scale in the enstrophy cascade range that we proposed. For $\Pi < 1$, the crossover scale k_η^{-1} is smaller than the forcing scale, and k_η^{-1} becomes even smaller if Π further reduces, which indicates that a wider range of scales are influenced by the β-effect. For $Z \gtrsim 2.5$, the zonostrophic turbulence regime is at $\Pi \gtrsim 4$. In this regime, the inverse energy cascade first proceeds from the forcing scale to larger scales by eddy-eddy interactions as isotropic turbulence with a characteristic $k^{-5/3}$ energy spectrum. After reaching the crossover scale k_ε^{-1}, the energy is channeled into the zonal jets, whose energy spectrum follows a universal form with k^{-5} slope and dominates over the eddy kinetic energy spectrum. When Π decreases to below 1, the flow transits into the new "quasi-linear" regime. In this regime, eddy-eddy interactions are negligible while eddy/mean-flow interactions dominate the nonlinear energy and enstrophy transfers. The energy injected at the forcing scale is directly transferred into the jets at the largest scale, whereas eddy-eddy interactions are negligible in the energy cascade. The isotropic energy cascade spectrum $k^{-5/3}$ is not seen but is replace by a roughly k^{-3} spectrum even at scales larger than the forcing scale. For the same Z, the jets are even sharper when Π reduces to below 1. The PV staircase structure can form

in the corner of the "quasi-linear" regime when the zonostrophic index is very high ($Z \gtrsim 7$).

It is tempting to put the observed geophysical flows into our updated chart of turbulence regimes. Galperin et al. (2004) argue that the oceanic turbulence is close to the zonostrophic regime with estimated zonostrophic index $Z_{ocean} \sim 2$. On the other hand, the atmospheric flow is in the friction-dominated regime with $Z_{atmos} \sim 1$ (Galperin et al., 2010). We can estimate Π in order to put these flows into the (Z, Π) space. In Earth's atmosphere, the EKE generation rate is about 2 W m^{-2}, which translates into $\varepsilon \sim 2 \times 10^{-4}$ m^2 s^{-2}. Using the value of β at midlatitudes, the crossover scale of the energy cascade branch is about $k_\varepsilon^{-1} \sim 700$ km. The typical deformation radius is about 1000 km. As eddy kinetic energy is generated at a scale similar to or even larger than the deformation radius (Chai and Vallis, 2014), Earth's atmosphere is likely to be within the $\Pi \lesssim 1$ regime. Another evidence is that many features of the general circulation are recovered in the quasi-linearized model so that the atmosphere may lie close to the "quasi-linear" regime (O'Gorman and Schneider, 2007). For the ocean, it is hard to estimate ε and thus k_ε. However, the kinetic energy spectrum from high-resolution ocean simulation shows that the energy spectrum seems to follow the -5/3 slope before the inverse cascade reaches the crossover scale, from where the spectrum steepens to -5 slope (see Fig. 2 from Galperin et al. [2004]). This spectrum agrees with the zonostrophic turbulence picture so that Π must be a larger than 1. Otherwise for $\Pi < 1$, the EKE spectrum should instead follow a -3 slope as seen in Fig. 2.7. Based on the forcing scale relative to the turbulence-wave crossover scale, we may understand the ocean dynamics to be more nonlinear than those of the atmosphere.

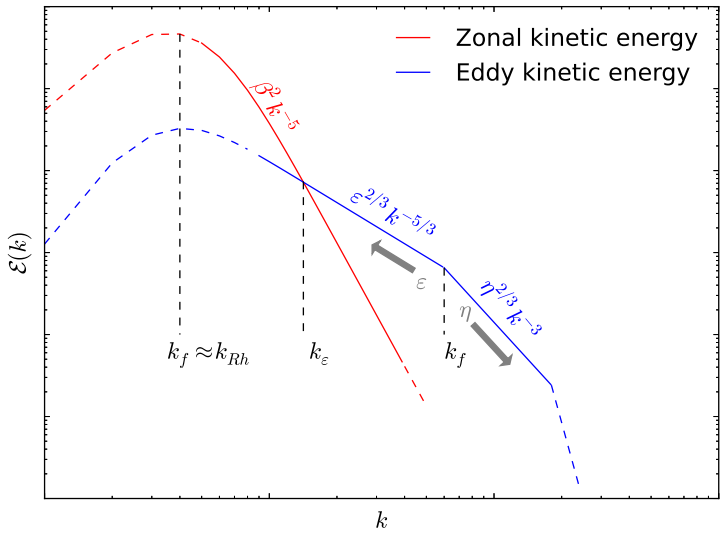


Figure 2.1: Schematic illustration of kinetic energy spectrum in zonal modes (red line) and eddies (blue) for the zonostrophic turbulence regime. Zonal and eddy kinetic energy spectra intersect at the crossover wavenumber k_ε, which is thought to be the boundary between near-isotropic turbulence and Rossby waves. Inverse cascade is halted by friction at k_r, which is close to the Rhines wavenumber k_{Rh}. The forcing is narrowly centered at k_f.

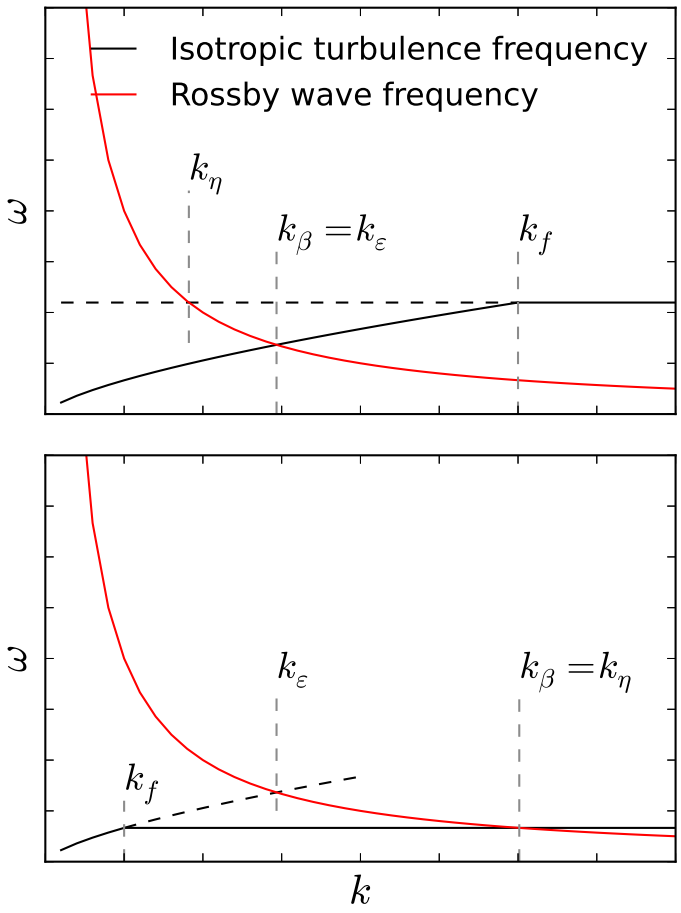


Figure 2.2: Schematic illustration of isotropic turbulence frequency ω_t (black line) and Rossby wave frequency $|\omega_\beta|$ (red line). ω_t and $|\omega_\beta|$ intersect (top) within the inverse energy cascade range or (bottom) within the direct enstrophy cascade range. The generalized turbulence-wave crossover wavenumber k_β is given by either k_ε or k_η depending on within which range ω_e and $|\omega_\beta|$ intersect.

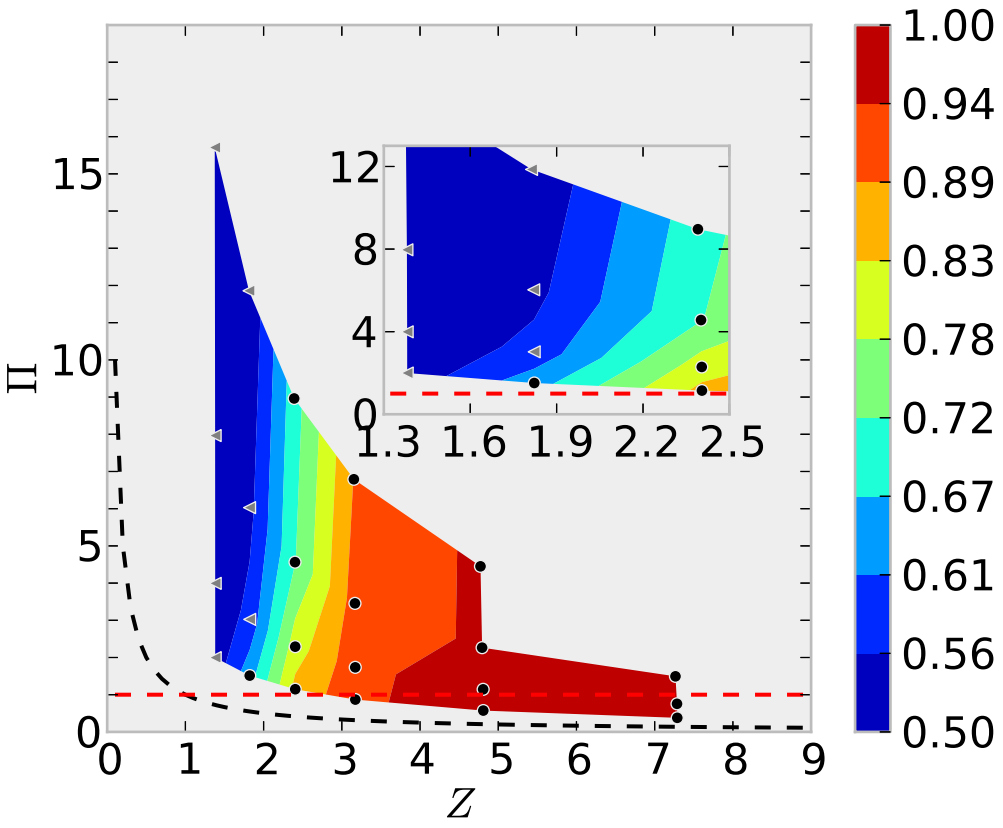


Figure 2.3: Anisotropy index defined as $\chi = \langle u^2/(u^2+v^2)\rangle$ in the (Z, Π) space. The black dots indicate the runs in which jets have formed, whereas the gray triangles donate runs that have no clear visually identifiable jets. The inset is a zoom-in of the region $Z \lesssim 2.5$.

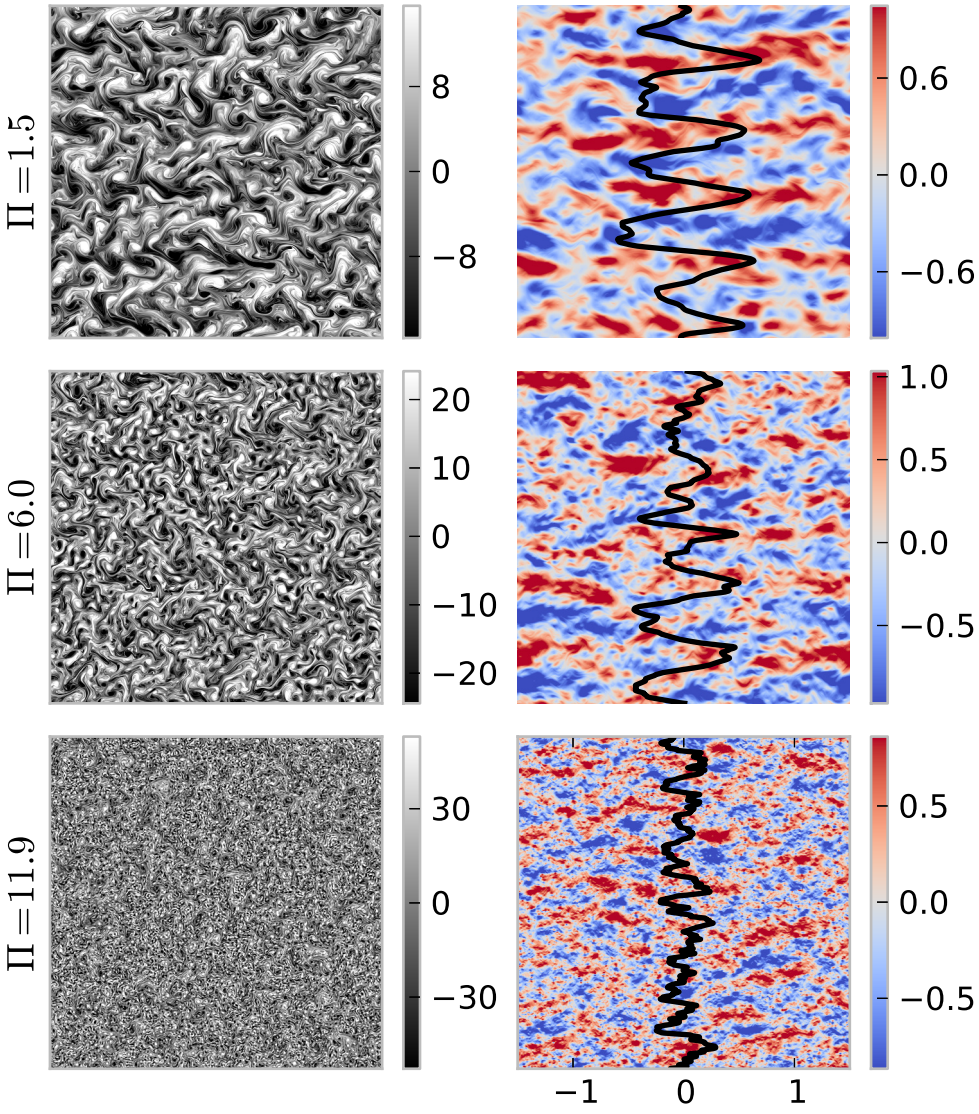


Figure 2.4: Snapshots of relative vorticity (left) and zonal velocity (right) from $Z = 1.8$ runs with $\Pi =$ (top) 1.5, (middle) 6.0, and (bottom) 11.9. The black line in the right panels denote zonal and time mean zonal wind, with its axis in the bottom right subplot.

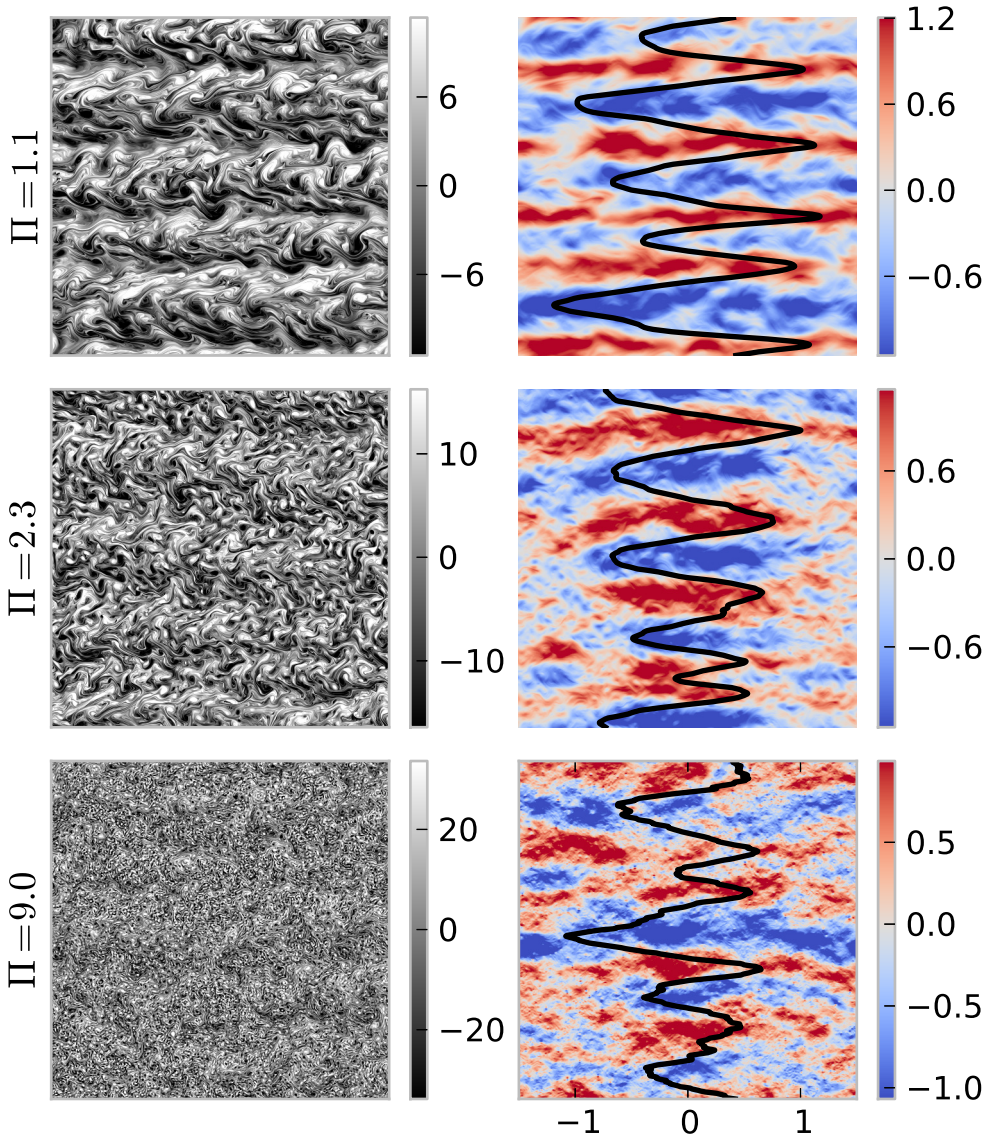


Figure 2.5: Snapshots of relative vorticity (left) and zonal velocity (right) from $Z = 2.4$ runs with $\Pi =$ (top) 1.1, (middle) 2.3, and (bottom) 9.0. The black line in the right panels denote zonal and time mean zonal wind, with its axis in the bottom right subplot.

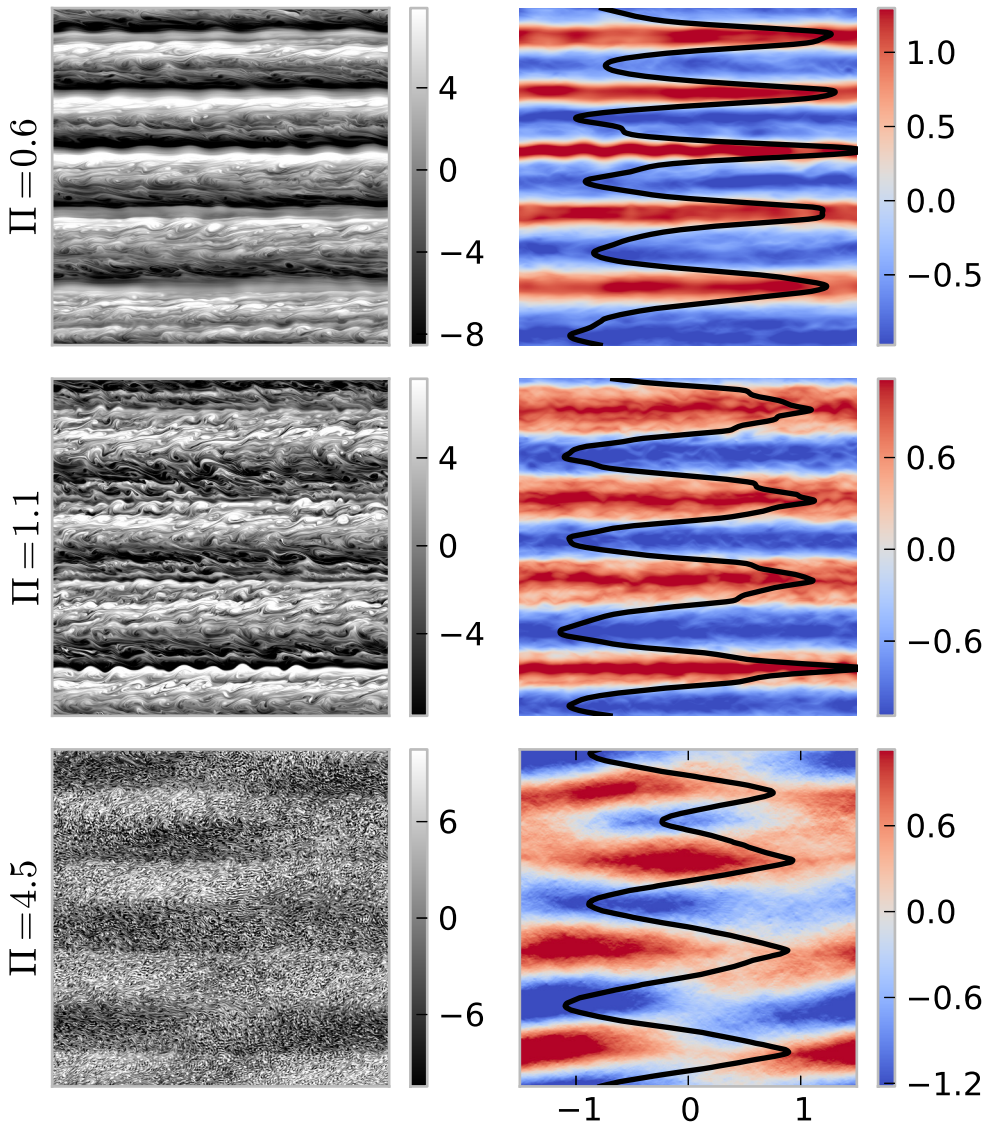


Figure 2.6: Snapshots of relative vorticity (left) and zonal velocity (right) from $Z = 4.8$ runs with $\Pi =$ (top) 0.6, (middle) 1.1, and (bottom) 4.5. The black line in the right panels denote zonal and time mean zonal wind, with its axis in the bottom right subplot.

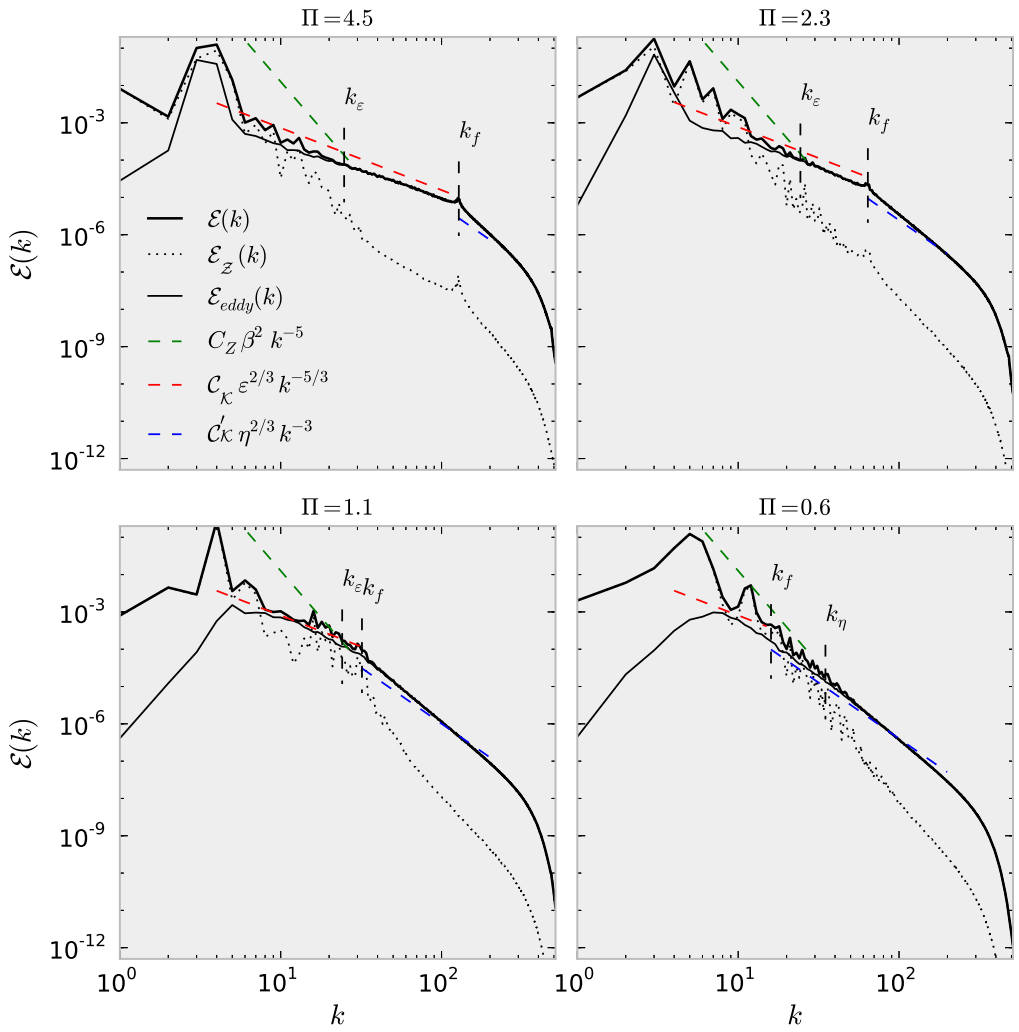


Figure 2.7: The energy spectra of the total flow $\mathcal{E}(k)$ (thick solid black line), eddies $\mathcal{E}_{eddy}(k)$ (thin solid black line) and the zonal flow $\mathcal{E}_\mathcal{Z}(k)$ (dotted black line) from simulations with $Z = 4.8$ and various values of Π varying from 0.6 to 4.5 as indicated above the plots. The theoretical spectra in energy and enstrophy cascade ranges are shown in red and blue dashed lines respectively. The universal energy spectrum of the zonal modes with -5 slope for zonostrophic turbulence regime is shown in green dashed line.

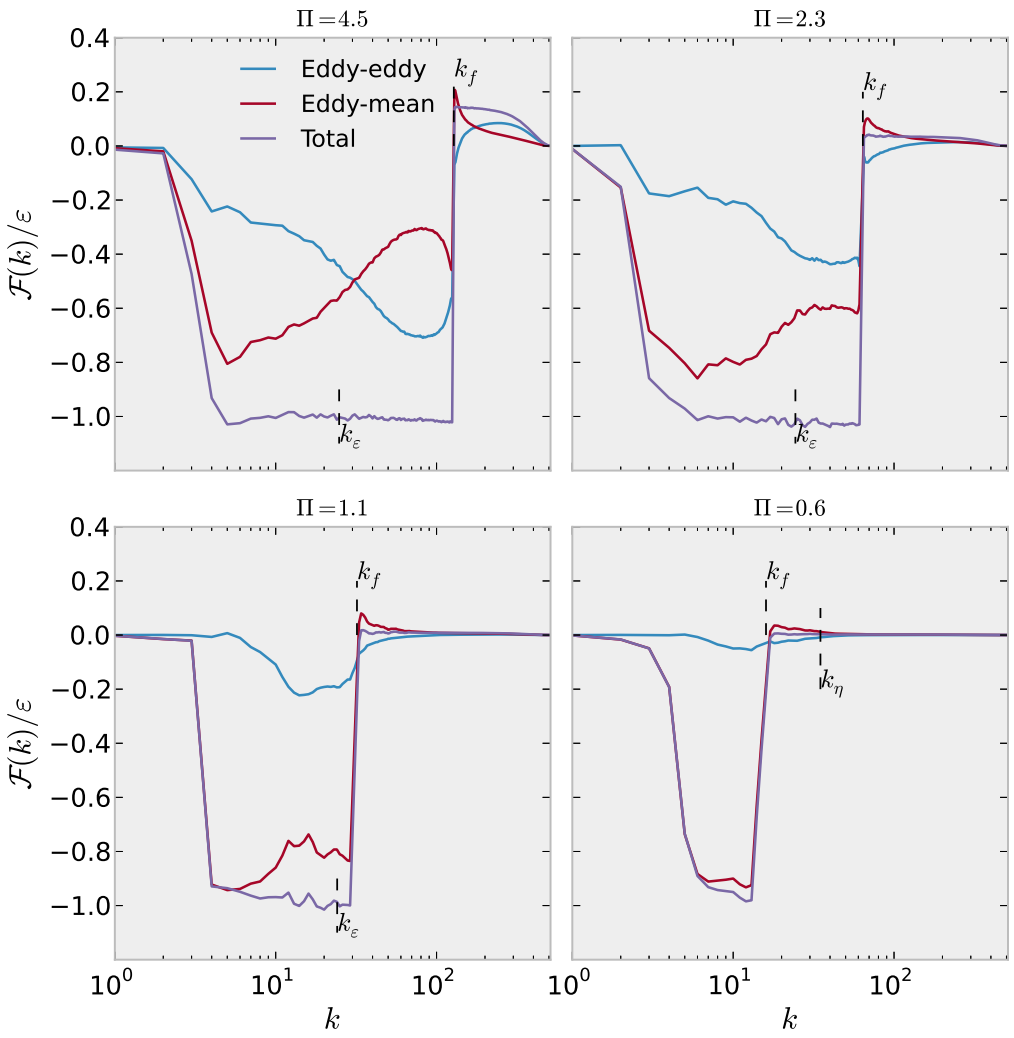


Figure 2.8: Energy flux across wavenumber k for simulations with $Z = 4.8$ and various values of Π. Energy flux of the total flow $F(k)$ is the purple line, that of the eddy-eddy interactions $F_{EE}(k)$ is the blue line, and that of the eddy/mean-flow interactions is the red line.

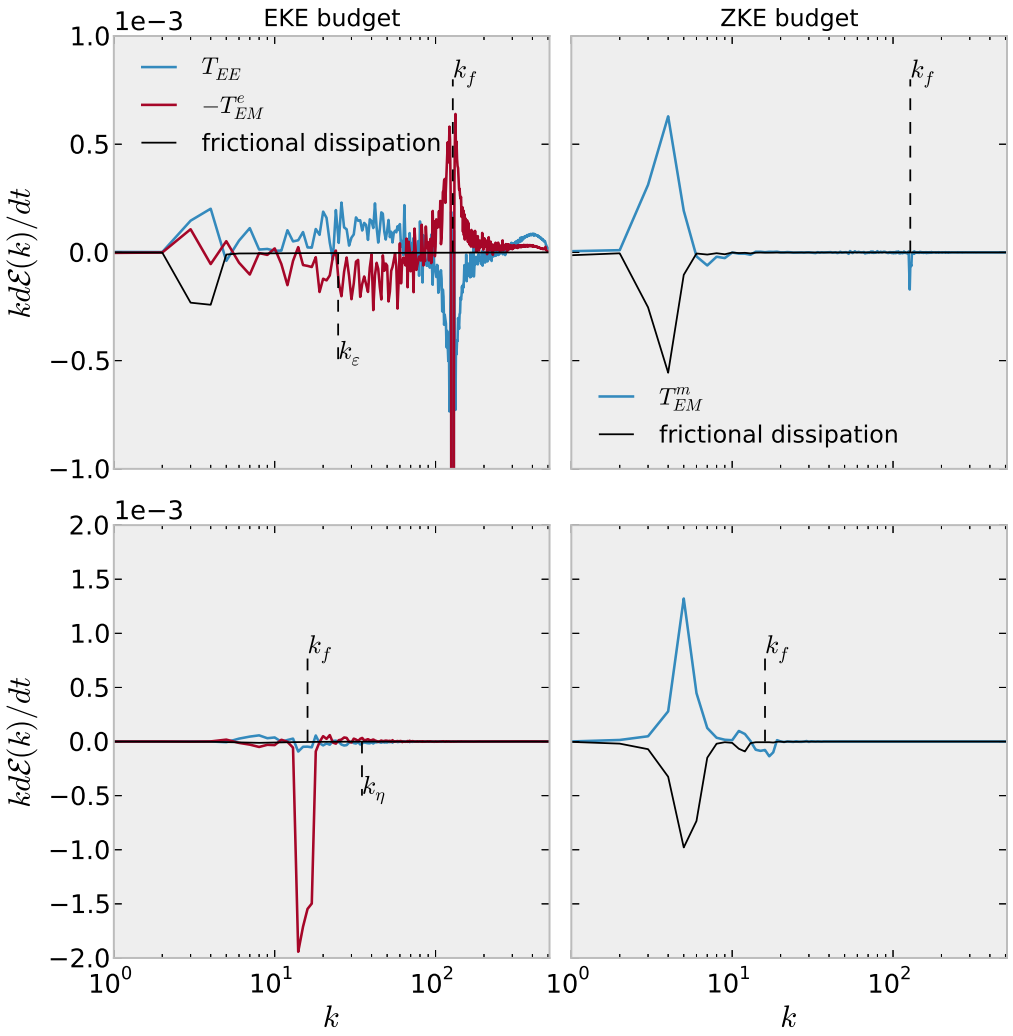


Figure 2.9: Spectral EKE and ZKE budgets for simulations with $Z = 4.8$ and Π =(top) 4.5 and (bottom) 0.6. The formulation for these budgets are given in (2.28) and (2.35).

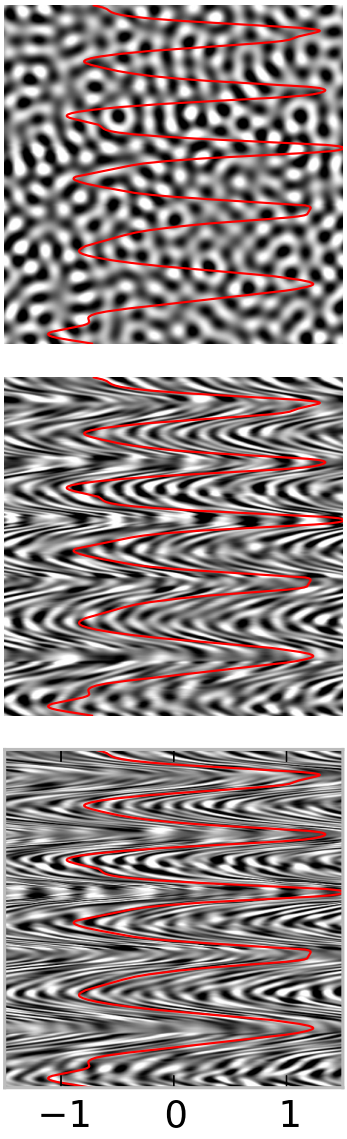


Figure 2.10: Snapshots of eddy relative vorticity at time $t = 0$ (top), 0.78 (middle) and 1.56 (bottom) from an initial-value run. The red lines denote the zonal mean zonal wind, with its axis in the bottom subplot. The parameters for this simulation is the same as $Z = 4.8$ but without forcing and friction. The initial condition is the time and zonal mean flow from the simulation with $Z = 4.8$ and $\Pi = 0.6$ run with a small-amplitude eddy perturbation, which is shown as eddy vorticity field at $t = 0$.

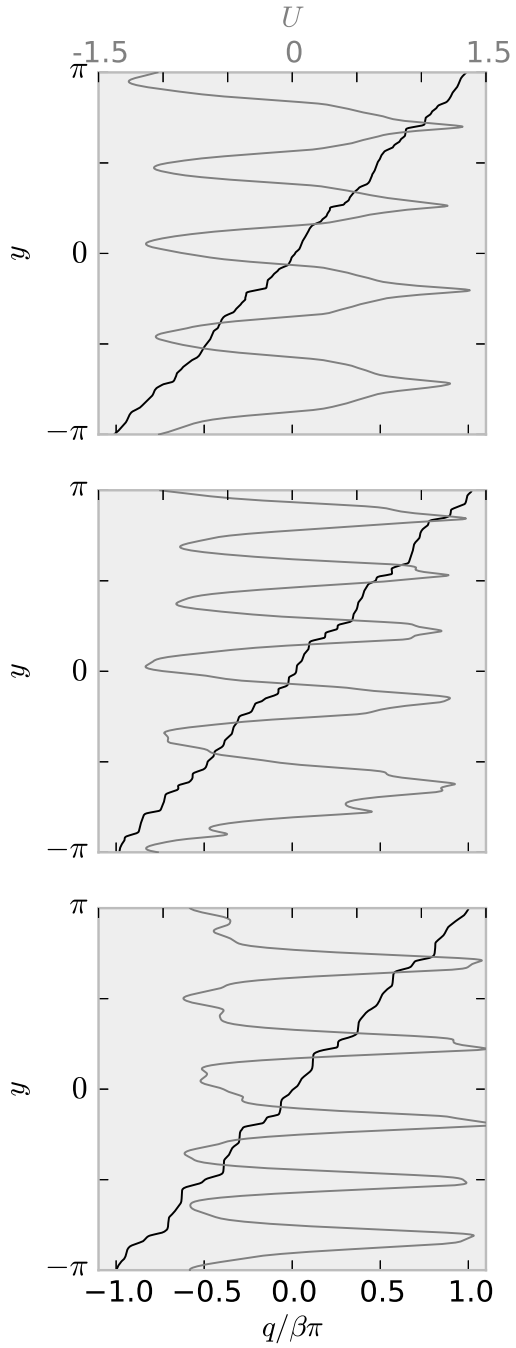


Figure 2.11: Zonal and time mean potential vorticity $\overline{q}$ (black line) and zonal velocity $\overline{u}$ (gray line) from simulations with $Z = 7.3$ and Π =(top) 1.5, (middle) 0.76, and (bottom) 0.4. The potential vorticity profile at equivalent latitude is almost indistinguishable from $\overline{q}$, so it is not shown.

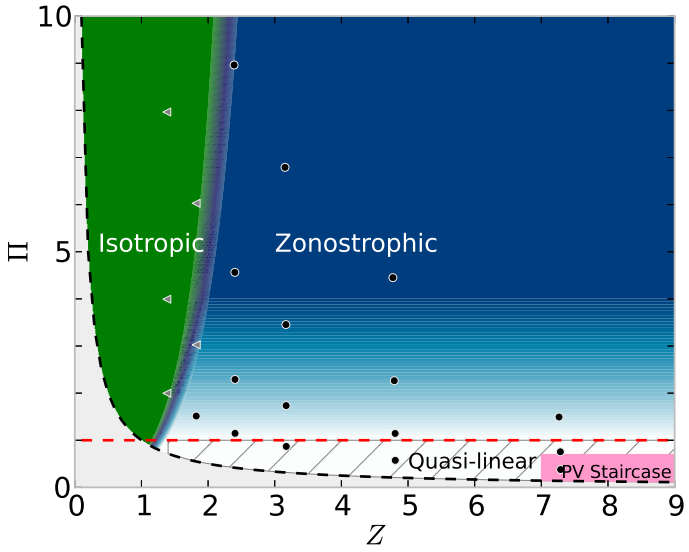


Figure 2.12: Chart of turbulence regimes in (Z, Π) space.

Chapter 3

Role of forcing scale on β-plane turbulence: eddy diffusion

Scaling theories of meridional eddy diffusivity are derived in a forced-dissipative, two-dimensional flow on β-plane following two pathways. The first pathway assumes the eddy diffusion to be dominated by eddies at the turbulence-wave crossover scale, which is the threshold for turbulence anisotropization. Eddies larger than the crossover scale are thought to be wave-like and do not contribute to mixing. The second pathway is based on an analytical formula of the diffusivity caused by a single wavenumber wave, which captures the essence of how diffusivity of waves is suppressed compared with isotropic eddies with similar velocity and length scales due to the relative propagation of the waves to the mean flow. In both pathways, the form of diffusivity scaling depends on the forcing scale relative to the crossover scale. When the forcing scale is smaller than the crossover scale, the diffusivity scaling is $D_\varepsilon \sim \varepsilon^{3/5}\beta^{-4/5}$ and has appeared in past studies, where ε is the upscale energy flux rate. When the forcing scale is larger than the crossover scale, the diffusivity follows a new scaling determined by the enstrophy flux rate η as $D_\eta \sim \beta^{-2}\eta$. These two scalings agree well with numerical simulations in their corresponding regimes. A semi-empirical formula

that smoothly bridges two scalings is proposed, whose usefulness is demonstrated in deriving a closure for heat flux in a two-layer quasi-geostrophic model. Although the two pathways give the same diffusivity scalings, they have different predictions on the dominant scale in eddy diffusion. When the crossover scale is smaller than the forcing scale, the assumption of the first pathway that eddy diffusion is dominated by eddies at the crossover scale does not agree with simulations, which actually show that wave-like eddies much larger than the crossover scale dominate eddy diffusion and agrees better with predictions from the second pathway. The suppression of diffusivity due to the relative wave/mean-flow propagation should be a more fundamental principle than assuming waves do not contribute to mixing.

3.1 Introduction

Eddies pervade in atmosphere and oceans, transporting great amounts of heat and tracers. Eddy diffusion is an important concept in understanding transport properties of the complicated eddying flow (Held, 1999). Due to the analogy between a passive tracer and the potential vorticity, and to a lesser extent the temperature, a scaling for eddy diffusivity is crucial in formulating a closure theory for circulations in the midlatitude atmosphere as well as in the Southern Ocean (Held and Larichev, 1996; Barry et al., 2002; Jansen and Ferrari, 2013a; Nikurashin and Vallis, 2011, 2012). The standard mixing length argument states that eddy diffusivity is a product of eddy velocity V and mixing length l_{mix}. Mixing length is similar to the concept of mean free path in thermodynamics: a fluid parcel can travel an average distance of l_{mix} while conserving its properties before getting mixed with the the surroundings. In isotropic turbulence, l_{mix} is usually assumed to be the length L of the largest eddies, so a scaling of eddy diffusivity is

$$D = Vl_{mix} \sim VL. \tag{3.1}$$

Due to the planetary differential rotation, or the β-effect, the macro- or mesoscale eddies in near-geostrophic balance are not isotropic. As a result, the eddies are rather an interplay of turbulence and Rossby waves, and zonal jets can spontaneously form. Due to the emergence of zonal jets, zonal and meridional transport and mixing are different in nature (Smith, 2005). In this study, we focus on meridional eddy diffusivity (hereinafter referred as diffusivity for short).

How to incorporate the β-effect into the diffusivity scaling? One approach is based on the turbulence phenomenology. The turbulent flow consists of eddies with a range of length and velocity scales. The so-called turbulence-wave crossover scale sets the threshold of turbulence anisotropization. It is assumed that turbulent diffusion is only carried out by eddies smaller than the crossover scale so that they are sufficiently close to isotropic turbulence; beyond the crossover scale, the eddies are wave-like and do not contribute to turbulent diffusion (Sukoriansky et al., 2009; Smith and Vallis, 2002). For clarity, we will refer to this assumption as the no-wave-mixing assumption. A diffusivity scaling then suggests itself to be the same as (3.1) but with V and L replaced by those of eddies at the crossover scale.

The no-wave-mixing assumption is obviously an extreme idealization for the fact that mixing by waves is greatly reduced compared to turbulent eddies of the same length and velocity scales, which is exemplified as the transport barrier at the jet center despite the co-located eddy velocity maximum there as seen in many diagnostic studies (Haynes et al. 2007 and references therein). Recently, Ferrari and Nikurashin (2010) reveal the essential mechanism that reduces waves' ability in mixing. Consider eddies in a background zonal flow. Under β-effect, eddies behave as Rossby waves, so they are not purely advected by mean flow but propagating westwards relative to the mean flow. It is this relative propagation against the mean flow that suppresses

the meridional (cross-stream) diffusivity, which may be qualitatively understood from the mixing of a Lagrangian tracer parcel shown in Fig. 3.1 (Klocker et al., 2012). At $t = 0$ a particle is at position A, and the eddy flow is shown as the black streamline. If the eddy does not propagate relative to the mean flow, in the reference frame moving with mean flow the particle will be advected to position B after a quarter of an eddy turnover time. Assuming that the particle gets mixed by this time, the mixing length is then given by the meridional displacement between A and B. However, if the eddy propagates westwards relative to the mean flow as shown by the dashed blue streamline, the parcel ends up at C so that the mixing length is greatly reduced.

For eddies containing a single wavenumber, analytical formulas exist to represent the suppression of cross-stream diffusivity by the relative propagation of eddies to the mean flow (Ferrari and Nikurashin, 2010; Klocker et al., 2012; Srinivasan and Young, 2014; Green, 1971; Killworth, 1997). Despite small difference in details, the suppressed diffusivity can be generally expressed by Ferrari and Nikurashin's (2010) formula (hereinafter referred as the FN formula)

$$D_k = \frac{D_0}{1 + \tau^2 k_x^2 (c_w - U)^2}, \tag{3.2}$$

where k_x and c_w are the eddy wavenumber and phase speed respectively along the mean flow direction; τ is the eddy decorrelation time; U is the velocity of the mean flow which we assume to be zonal. D_0 is the "unsuppressed" diffusivity if eddies were not propagating with respect to the zonal flow, which is well predicted by the isotropic mixing-length scaling (3.1) as

$$D_0 = V_k l_{mix} \sim V_k k^{-1}, \tag{3.3}$$

where V_k is the velocity scale for an eddy with wavenumber k and we use the eddy length scale as the mixing length l_{mix} (Klocker and Abernathey, 2014).

The FN formula applies not only to Rossby waves but generally to any kind of waves that propagate relative to the mean flow, for example surface edge waves (Ferrari and Nikurashin, 2010; Klocker et al., 2012). The suppression by the relative propagation is a purely kinematic effect except that some dynamical mechanism is needed for the waves to have a finite decorrelation time τ. The Lorentzian shaped dependency of diffusivity on the mean flow speed U in (3.2) is accurately reproduced by advecting a tracer using the same eddy velocity field but manipulating the zonal flow (Klocker and Abernathey, 2014). In general, the FN formula well captures the global pattern of eddy diffusivity in the ocean if properties of the eddies (velocity and length scales, decorrelation time) are diagnosed from observations (Klocker and Abernathey, 2014; Ferrari and Nikurashin, 2010; Klocker et al., 2012).

Both physical interpretation and observational evidence suggest the FN formula to be richer and more fundamental than the no-wave-mixing assumption. However, the apparently oversimplified no-wave-mixing assumption yields a diffusivity scaling that works quite well in a range of flows (Sukoriansky et al., 2009; Smith and Vallis, 2002). In this study, we seek to derive a diffusivity scaling for β-plane turbulence using the FN formula as the foundation, and to reveal the relationship between the FN formula and the no-wave-mixing assumption. The role of forcing scale enters the diffusivity scaling as the crossover scale takes a new form when it is smaller than the forcing scale as discovered in Part I of this study (Chai et al., 2016a). Using this new form of crossover scale and the corresponding velocity scale in (3.1), we immediately have a new diffusivity scaling for this regime. This paper is organized as followings. In Section 2, we derive diffusivity scalings from both no-wave-mixing assumption and the FN formula for two turbulence regimes depending on whether or not the crossover scale is smaller than the forcing scale. Predictions for diffusivity and the dominate scale in eddy diffusion are made. A series of experiments is carried out and is described in Section 3. The theoretical predictions are tested in Section 4,

which proves the new diffusivity scaling and also favors the FN formula to be a more general principle. The application of the new diffusivity scaling is demonstrated in deriving a closure theory for heat flux in a two-layer quasi-geostrophic model. Section 5 summarizes the results and concludes the study.

3.2 Theory

Arguably the simplest model to study eddy diffusion with enough relevance to geostrophic turbulence is a homogeneous forced-dissipated two-dimensional (2d) flow on a β-plane. The forcing is spectrally localized at wavenumber k_f with a prescribed energy injection rate, which almost equals the upscale energy flux rate ε. A linear friction removes energy from large scales for the flow to reach statistical equilibrium; and a (hyper-)viscosity dissipation removes enstrophy at the smallest scales. Even in such a simple model there exists multiple turbulent regimes, which demand different diffusivity scalings.

a. Turbulence phenomenology

The diffusivity scaling based on the no-wave-mixing assumption centers on the turbulence-wave crossover scale. If the β-effect is not felt at the forcing scale, the crossover wavenumber is where the isotropic eddies under an inverse energy cascade are first sufficiently influenced by the β-effect and thus "become" Rossby waves. The crossover wavenumber can be written as (to within a dimensionless factor; Vallis and Maltrud 1993)

$$k_\varepsilon \sim \beta^{3/5}\varepsilon^{-1/5}. \tag{3.4}$$

As eddies are assumed to be isotropic turbulence before reaching the crossover scale k_ε^{-1}, an inertial range exists between k_f and k_ε. By dimensional analysis, the velocity

scale at k_ε is $\sim \varepsilon^{1/3} k_\varepsilon^{-1/3}$. Under the no-wave-mixing assumption, eddy diffusion is dominated by eddies at the crossover scale, and therefore diffusivity is

$$D_\varepsilon \sim \varepsilon^{1/3} k_\varepsilon^{-4/3} \sim \varepsilon^{3/5} \beta^{-4/5}. \tag{3.5}$$

This scaling has been shown to correctly predict diffusivity in a range of flows (Sukoriansky et al., 2009; Smith and Vallis, 2002) and is used as the building block in many closure theories of baroclinic turbulence (Held and Larichev, 1996; Jansen and Ferrari, 2013a). The no-wave-mixing assumption also seems to be valid as the tracer flux spectrum peaks near the crossover scale, despite the larger eddies being much more energetic (Smith and Vallis, 2002).

For k_ε to have the assumed physical meaning, the forcing scale must be smaller than the crossover scale, equivalently the ratio

$$\Pi = k_f / k_\varepsilon \tag{3.6}$$

needs to be larger than 1; otherwise the forcing scale is already being influenced by the β-effect. As discussed in Part I, Π plays an important role in determining turbulent regimes, and thus we continue to use Π to characterize the role of the forcing scale in eddy diffusion. In the case $\Pi < 1$, we discovered a new form of crossover scale in Part I, which immediately leads to a new form of diffusivity scaling as seen below. The crossover wavenumber is now in the enstrophy cascade branch determined by the enstrophy flux rate η as

$$k_\eta \sim \beta \eta^{-1/3}, \tag{3.7}$$

and the velocity scale at k_η is $\sim \eta^{1/3} k_\eta^{-1}$.[1] This suggests a new form of diffusivity scaling as

$$D_\eta \sim \eta^{1/3} k_\eta^{-2} \sim \beta^{-2} \eta. \tag{3.8}$$

b. Suppressed diffusivity

Now we seek to derive the diffusivity scaling from the FN formula of suppressed diffusivity. The relative propagation speed is given by the intrinsic Rossby wave speed as

$$c_w - U = -\frac{\beta}{k^2}, \tag{3.9}$$

which assumes either that the mean flow $U(y)$ varies at a much larger scale than the eddy length scale, or that eddies are dissipated at the same latitude that they are generated. Further assuming eddies to have similar zonal and meridional scales due to nonlinear advection so that $k_x \sim k$, we can rewrite the suppressed diffusivity (3.2) as

$$D_k \sim \frac{D_0}{1 + \tau^2 \beta^2 k^{-2}}. \tag{3.10}$$

To get an expression for the diffusivity in β-plane turbulence with a spectrum of eddies across a range of scales, we make two assumptions:

- (a): The decorrelation time τ and unsuppressed diffusivity D_0 at wavenumber k are similar to those of isotropic turbulent eddies.
- (b): The eddy diffusion is dominated by eddies at a wavenumber that maximizes D_k, and as a result the diffusivity $D \sim \max(D_k)$.

[1] As discussed in Part I, an inertial range does not need to exist but a non-local enstrophy cascade gives the same scaling for velocity scale.

For a pure plane wave, the decorrelation time is infinite. However, actual wave-like eddies have a finite decorrelation time due to nonlinear interactions with eddies of other scales. It makes sense to assume that it is the turbulent aspect of the eddies that determines their decorrelation time, which may be similar to that of the isotropic eddies within an inertial range.[2] Alternatively, the decorrelation time is often estimated to be the eddy turnover time as

$$\tau \sim \left(k^2 \mathrm{EKE}_k\right)^{-1/2}, \tag{3.11}$$

where EKE_k is the eddy kinetic energy (EKE) at wavenumber k (Ferarri and Nikurashin 2010; Klocker and Abernathey 2014). As seen in Part I, even in flow with sufficient anisotropy, the EKE spectra often still take the theoretical forms from the inertial range argument for the isotropic turbulence. Both scalings of decorrelation time (3.11) and unsuppressed diffusivity (3.3) are fully determined by the EKE spectrum, so they should be similar as those in isotropic turbulence. The only deviation from the theoretical spectrum happens in the inverse cascade range when $\Pi < 1$, but we postpone the discussion on how our predictions are modified to Section 4. Under the assumption (a), an eddy is hypothesized to be a duality of turbulence and Rossby wave: it decorrelates in a similar way to turbulence, while it exhibits the dispersion relation of Rossby waves.

Assumption (b) is consistent with the usual assumption in isotropic turbulence that the largest eddies dominate the eddy mixing and thus determines the diffusivity, whose rationale is illustrated schematically in Fig. 3.2. A mean tracer gradient is assumed on the domain scale in the meridional direction. Consider eddies at a larger and smaller scales as indicated by outer and inner dashed blue lines. In isotropic

[2]Frictional drag can damp the eddies and thus makes them decorrelate. However, the locality hypothesis suggests that for a wide range scales smaller than the energy halting scale frictional dissipation is negligible. Moreover, for sufficiently anisotropic flow the energy is mostly dissipated in the zonal mean flow, so frictional dissipation on eddies of all scales is negligible as we have seen from Part I.

turbulence, D_k is larger for the larger eddies. The tracer contours, which initially align in the zonal direction, are stirred by the larger eddies and becomes strongly deformed as shown by the solid black line. As a result, the smaller eddies do not feel the mean meridional tracer gradient but instead the local gradient created by larger eddies. The tracer variance created by the smaller eddies, shown by the dashed gray line, do not necessarily contribute to the meridional tracer flux. In spectral space, a consistent picture is that tracer variance is created from mean tracer gradient by the largest eddies and then cascades to smaller and smaller scales by smaller and smaller eddies until it eventually gets dissipated by microscopic diffusion. In β-plane turbulence, D_k may actually be very small at the largest eddy scale. Therefore, the tracer contour may be only slightly deformed from being zonal by the largest eddies. So smaller eddies still feel the mean meridional tracer gradient. Assume that D_k peaks at a single wavenumber and decreases monotonically away from this wavenumber. At this wavenumber, the eddies deform the tracer contours large enough from being zonal so that eddies smaller than it no longer feel the mean meridional gradient. It is reasonable to believe that eddy diffusion is dominated by eddy at this wavenumber, where D_k determines the overall diffusivity.

First, consider eddies within the inverse cascade range $k < k_f$ with an upscale energy flux ε. From assumption (a), even though eddies are under β-effect, the unsuppressed diffusivity can still be obtained from a dimensional analysis as

$$D_0 \sim \varepsilon^{1/3} k^{-4/3}, \tag{3.12}$$

and the decorrelation time

$$\tau \sim \varepsilon^{-1/3} k^{-2/3}. \tag{3.13}$$

Using these expressions, the suppressed diffusivity (3.10) can be fully determined as

$$D_k \sim \frac{(k_\varepsilon/k)^{4/3}}{1+(k_\varepsilon/k)^{10/3}}\varepsilon^{1/3}k_\varepsilon^{-4/3}, \tag{3.14}$$

in which the role of k_ε in (3.4) is highlighted. Immediately we see that the suppressed diffusivity equals D_ε in (3.5) multiplied by the suppression factor $f(x) = x^{4/3}/(1+x^{10/3})$, where $x = k_\varepsilon/k$. As illustrated in Fig. 3.3 (top), D_k peaks near the crossover wavenumber k_ε and decreases rapidly away from it.

For eddies within the direct enstrophy cascade range with an enstrophy flux rate η, similarly the unsuppressed diffusivity is

$$D_0 \sim \eta^{1/3}k^{-2}, \tag{3.15}$$

and the decorrelation time is

$$\tau \sim \eta^{-1/3}. \tag{3.16}$$

The suppressed diffusivity can be expressed using k_η in (3.7) as

$$D_k \sim \frac{1}{1+(k/k_\eta)^2}\beta^{-2}\eta. \tag{3.17}$$

The suppressed diffusivity monotonically decreases with k as shown in Fig. 3.3 (bottom). The maximum D_k is obtained at k_f in the enstrophy cascade branch.

From assumption (b), the overall diffusivity is given by the maximum D_k. Depending on Π, the maximum D_k is reached in either energy or enstrophy cascade range. When $\Pi \gg 1$ the crossover wavenumber $k_\varepsilon \ll k_f$, D_k in the energy and enstrophy branches are illustrated in Fig. 3.3 (top) by solid and dashed lines respectively. The maximum D_k is reached in the energy cascade range near k_ε, given that the inverse energy cascade is not halted before reaching k_ε. This follows the no-wave-mixing assumption that the eddies larger than the crossover scale k_ε^{-1} do not contribute much

to mixing. The overall diffusivity scales with $\varepsilon^{1/3}k_\varepsilon^{-4/3}$, which is also the diffusivity scaling D_ε in (3.5) derived under the classical assumption.

In the other limit $\Pi \ll 1$, the relationship between k_f and the two forms of crossover wavenumbers is $k_f \ll k_\varepsilon \ll k_\eta$. As shown in Fig. 3.3 (bottom), D_k increases with k in the energy cascade branch $k < k_f$ (solid black line) and then decreases in the enstrophy cascade branch $k > k_f$ (dashed black line). The maximum D_k scales with $\beta^{-2}\eta$, which gives a diffusivity scaling the same as D_η in (3.8). However, D_k peaks at the forcing scale instead of the crossover scale k_η^{-1}. Therefore, unlike the no-wave-mixing assumption, our derivation based on the FN formula suggests that eddy diffusion is dominated by wave-like eddies at the forcing scale when $\Pi \ll 1$.

Interestingly, our new diffusivity scaling $D \sim \beta^{-2}\eta$ for $\Pi \ll 1$ can be derived in a different way under Nakamura's effective diffusivity framework. This derivation highlights the similarity between potential vorticity and passive tracer and is included in Appendix A.

3.3 Experiments

Forced-dissipated 2d flow on a β-plane is simulated for a wide range of turbulent regimes in a doubly-periodic square domain as documented in Part I. At the same time, a passive tracer χ is advected by the simulated 2d flow, and the governing equation is

$$\frac{\partial \chi}{\partial t} + J(\psi, \chi) + v = -\kappa \nabla^8 \chi, \tag{3.18}$$

where ψ is the stream function of the 2d turbulent flow, v is the meridional velocity, κ is the hyperdiffusivity. The hyperdiffusivity κ takes the same value as the hyperviscosity that applies on the relative vorticity field, and it is adjusted adaptively in the numerical model using an optimal estimate based on the simulated flow (Smith et. al.

2002). The tracer variance is generated from a fixed large-scale meridional gradient (which is set to be 1 for simplicity) and is absorbed by small-scale dissipation. The meridional eddy diffusivity D is diagnosed as the domain averaged tracer flux over the fixed tracer gradient as

$$D = -\langle v\chi \rangle,$$

where $\langle \cdot \rangle$ denotes a domain average.

3.4 Results

In Part I, turbulent regimes are characterized using Π and another non-dimensional number called the zonostrophic index Z, which is defined as

$$Z = k_\varepsilon / k_{Rh},$$

where k_{Rh} is the Rhines wavenumber, $k_{Rh} = \sqrt{\beta/2U}$, and U is the r.m.s velocity of the flow. For relatively large zonostrophic index $Z \gtrsim 2.5$, strong zonal jets dominate the flow. The flow is further divided into two turbulent regimes based on Π: zonostrophic turbulence for $\Pi \gtrsim 4$ and quasi-linear turbulence for $\Pi \lesssim 1$. From our derivations in Section 2, we see that the diffusivity scaling has different forms depending on Π. In order to characterize the diffusivity in the non-dimensional (Z, Π) space, we need to also non-dimensionalize the diffusivity. As the two diffusivity scalings are formally related by

$$D_\eta = D_\varepsilon \Pi^2, \tag{3.19}$$

we can conveniently non-dimensionalize diffusivity using D_ε. The dimensionless diffusivity $\tilde{D}$ is then

$$\tilde{D} = \varepsilon^{-3/5}\beta^{4/5}D. \tag{3.20}$$

The two scaling limits for $\tilde{D}$ can be combined as

$$\tilde{D} = \min(1, \Pi^2). \tag{3.21}$$

In the (Z, Π) space, we expect the dimensionless diffusivity $\tilde{D}$ to have no dependency on Z but a strong dependency on Π. When Π reduces below 1, we predict $\tilde{D}$ to have a power law dependency on Π as Π^2; when Π increases above 1, the dependency on Π saturates and $\tilde{D}$ should approach a constant.

In analyzing the results, the crossover wavenumber of the energy cascade branch k_ε is calculated with the dimensionless constant included in (3.4) as $k_\varepsilon = \mathcal{C}_\varepsilon \beta^{3/5}\varepsilon^{-1/5}$, where C_ε is taken to be 0.6 in accordance with Part I and previous works (Galperin et al., 2010; Smith and Vallis, 2002). The other crossover wavenumber k_η is calculated from k_ε via the relationship $k_\eta = \Pi^{-2/3}k_\varepsilon$, which can be obtained from (3.4), (3.7) and $\eta = k_f^2\varepsilon$ (refer to Part I for details).

a. Eddy diffusivity scaling

As shown in Fig. 3.4, $\tilde{D}$ varies over 2 orders of magnitudes across the (Z, Π) space that we explored. It has a strong and monotonic dependency on Π but quite a weak dependency on Z. More clearly in Fig. 3.5 (left), for all different values of Z the scattering of $\tilde{D}$ vs. Π nearly collapses onto a single smooth functional form of Π, except for the smallest $Z = 1.38$. The series of runs with $Z = 1.38$ is known to be within the "friction-dominated" regime from Part I, which means that the inverse energy cascade is halted before even reaching the crossover scale. The flow is close to isotropic turbulence and we confirm its dimensional diffusivity to be well predicted by the scaling for isotropic turbulence (3.1). In the limit of the small Π, the power law

$\tilde{D} \propto \Pi^2$ is clearly seen. This power law dependency extends to at least $\Pi \lesssim 2$. When Π increases above 2, $\tilde{D}$ increases with Π slower and slower. A complete saturation seems only to be reached when $\Pi \sim 10$, which can be regarded as a complete loss of dependency on the forcing scale. Our scalings are only meant for two limits $\Pi \ll 1$ and $\Pi \gg 1$. It is reasonable to use a semi-empirical function to smoothly bridge these two limits. For example, we can use the harmonic mean of the two limits Π^2 and the constant 1 as

$$g(\Pi) = \frac{C_1}{1 + (\Pi/\Pi_0)^{-2}}, \tag{3.22}$$

where the constant C_1 is related to the implicit constant in (3.5) and the other constant Π_0 determines the transitional boundary. Minimizing the difference between $\log g(\Pi)$ and $\log \tilde{D}$ gives a best fit at $C_1 = 2.5$ and $\Pi_0 = 3.5$. Neglecting the $Z = 1.4$ runs, the semi-empirical function $g(\Pi)$ nicely captures the relationship between $\tilde{D}$ and Π, with the relative error $\tilde{D}/g(\Pi)$ within about [0.8, 1.8] (Fig. 3.5 right). Interestingly, the transitional value Π_0 is close to 4, which coincides with the boundary at which the forcing scale starts to lose its influence over the jets (see Part I).

b. Dominant scale in tracer flux spectrum

The rate of tracer variance generation from the mean meridional tracer gradient by eddies at wavenumber k is given by the spectral tracer flux as

$$F_S(k) = -\sum_{|\mathbf{k}|=k} \{S\}^*_{\mathbf{k}} \{v\}_{\mathbf{k}}\,, \tag{3.23}$$

where the bracket $\{A\}_{\mathbf{k}}$ denotes the Fourier component of A at wave vector $\mathbf{k} = (k_x, k_y)$. The dominant eddies in turbulent diffusion should show up as a peak in the spectral tracer flux as they are most efficient in creating eddy tracer variance from the mean gradient. The tracer variance then cascades to smaller and smaller scales

by smaller eddies until gets absorbed by hyper-diffusion. In the both cases $\Pi \gg 1$ and $\Pi \ll 1$, our diffusivity scalings based on the FN formula are the same as those based on the no-wave-mixing assumption. However, when $\Pi \ll 1$ the no-wave-mixing assumption and the FN formula have different predictions for the dominant scale in eddy diffusion, which provides a test to answer which picture is more fundamental.

The series of runs with $Z = 4.8$ provide a good testing case as Π varies widely enough – from about 4.5 to 0.6. Tracer flux spectra for different values of Π, along with the crossover wavenumber k_ε or k_η, forcing wavenumber k_f and energy containing eddy wavenumber k_E, are shown in Fig. 3.6. At the some of the largest scales (mostly k at about 1 to 4), the tracer flux spectrum is negative and therefore not shown. The energy containing eddy wavenumber is defined as the centroid of the EKE spectrum as

$$k_E = \frac{\int k\mathrm{EKE}(k)dk}{\int \mathrm{EKE}(k)dk},$$

and it provides a representation of the largest eddy scale.

In the zonostrophic regime ($\Pi = 4.5$), the tracer flux spectrum peaks near the crossover wavenumber k_ε. The energy containing scale k_E^{-1} is much larger than the crossover scale k_ε^{-1}. It is clear that eddy diffusion is strongly suppressed at scales larger than the crossover scale k_ε^{-1} and contributes little to the overall eddy diffusion. This agrees with the no-wave-mixing assumption. When Π decreases from 4.5 to 1.1, the crossover wavenumber k_ε does not change, whereas the peak of the tracer flux spectrum shifts to larger and larger scales. At $\Pi = 1.1$, the tracer flux spectrum peaks at a scale larger than the crossover scale k_ε^{-1}, though there may be uncertainty in the exact crossover scale depending on the choice of the dimensionless constant C_ε. When Π further reduces to 0.6, the crossover wavenumber moves into the enstrophy cascade range and is now k_η. The large separation between the peak of the tracer flux spectrum and k_η clearly proves that eddy diffusion is dominated by the large

wave-like eddies rather than the small eddies at the crossover scale k_η^{-1}. Therefore, we conclude that the FN formula is favored over the no-wave-mixing assumption as the latter is no longer valid in the $\Pi < 1$ regime, although it incidentally gives the correct diffusivity scaling D_η.

One deviation from the FN formula is that the tracer flux spectrum of the run $\Pi = 0.6$ peaks closer to the energy containing eddy wavenumber k_E than the forcing wavenumber k_f as we predicted. This deviation may be caused by the fact that the EKE spectrum in the range $k < k_f$ does not follow the spectrum $\mathrm{EKE}_k \sim k^{-5/3}$ of an energy cascade inertial range. As seen in Part I (Fig. 7), the EKE spectrum instead closely resembles the spectrum $\mathrm{EKE}_k \sim k^{-3}$ of an enstrophy cascade inertial range even within $k < k_f$, which may be a general property of the regime $\Pi < 1$. Therefore, the suppressed diffusivity D_k should take the form of the enstrophy cascade range (3.17) within $k < k_f$, which is shown as the dashed gray line in Fig. 3.3 (bottom). Across all eddy scales D_k decreases monotonically, so we should expect the tracer flux spectrum to peak near the largest eddy scale, or the energy containing eddy scale.

c. Application to two-layer quasi-geostrophic model

Except for the friction-dominated regime in which the flow is close to an isotropic turbulence, our semi-empirical formula (3.22) can serve as a good diffusivity estimate for a wide range of flows. We can use it in a closure theory for baroclinic turbulence. Here we demonstrate its usefulness in the two-layer quasi-geostrophic (QG) model on a β-plane, which has a baroclinic mode τ in addition to the barotropic mode ψ (Vallis, 2006). The baroclinic mode τ represents the temperature field of more realistic models. The mean meridional gradient of τ , or equivalently the mean thermal wind, is prescribed to be U. The phenomenology of the two-layer QG model can be summarized as a direct cascade of baroclinic energy and an inverse cascade of barotropic energy as follows (Salmon, 1978, 1980; Larichev and Held, 1995). It

is thought that the baroclinic mode is stirred by the barotropic flow as if a passive tracer. Eddy available potential energy, which is proportional to the variance of the baroclinic mode, cascades to smaller and smaller scales until it arrives at the deformation radius λ, where it is converted into barotropic EKE. In the barotropic mode, EKE then inversely cascades to larger scales much like in 2d turbulence. The evolution of the barotropic mode ψ is similar to that of 2d turbulence forced at a scale close to the deformation radius λ. Based on this picture, we can use a diffusive closure for the heat flux as

$$\langle v'_\psi \tau' \rangle \approx U D_\psi, \tag{3.24}$$

where A' denote the deviation of A from its zonal mean, v_ψ is the meridional eddy velocity of the barotropic flow, and D_ψ is the eddy diffusivity of the barotropic flow. In this homogeneous two-layer model, the rate of eddy energy production per unit mass is directly coupled to the heat flux as (see Held and Larichev 1996 or Thompson and Young 2007 for details)

$$\varepsilon = \frac{U}{\lambda^2} \langle v'_\psi \tau' \rangle. \tag{3.25}$$

As almost all the produced eddy energy gets dissipated by bottom drag at the largest scales, ε can be taken as the energy flux rate in the barotropic mode if the barotropic mode contains much more energy than the baroclinic mode. Once an estimate for eddy diffusivity of the barotropic mode D_ψ can be constructed from ε and external parameters as that for 2d turbulence, we immediately have a closure theory for the heat flux.

Held and Larichev (1996) used $D_\varepsilon \sim \varepsilon^{3/5} \beta^{-4/5}$ in (3.5) as D_ψ and arrived at the celebrated closure:

$$\langle v'_\psi \tau' \rangle / \left(U^2 \lambda \right) \sim \xi^2, \tag{3.26}$$

where ξ is

$$\xi = \frac{U}{\beta \lambda^2}. \tag{3.27}$$

The non-dimensional parameter ξ is usually referred as (super-)criticality and crucially determines various aspect of baroclinic turbulence in models with different levels of complexity (Chai and Vallis, 2014).

As seen from Subsection (a) above, the scaling $D_\varepsilon \sim \varepsilon^{3/5} \beta^{-4/5}$ only works well for regimes when the forcing scale is much smaller than the crossover scale. We can update the estimate of D_ψ by our semi-empirical formula (3.22) to incorporate the role of the forcing scale, which enters implicitly through Π. In dimensional form, our formula (3.22) becomes

$$D_\psi = \frac{C_1 \varepsilon^{3/5} \beta^{-4/5}}{1 + (\Pi / \Pi_0)^{-2}}. \tag{3.28}$$

Baroclinic energy is converted into barotropic energy near the deformation radius, therefore we can use the deformation radius as the forcing scale so that

$$\Pi \sim \lambda^{-1} k_\varepsilon^{-1}.$$

Combining these with (3.24) and (3.25), we get an estimate for the heat flux as

$$\langle v'_\psi \tau' \rangle / \left(U^2 \lambda \right) \sim \xi^2 (1 - \xi^{-2})^{5/2}, \tag{3.29}$$

where we neglect the constants C_1 and Π_0 in (3.28). This is similar to Lapeyre and Held's (2003) scaling

$$\langle v'_\psi \tau' \rangle / \left(U^2 \lambda \right) \sim \xi^2 (1 - \xi^{-1})^{3/2}, \tag{3.30}$$

which is found to fit better with simulations than the original Held and Larichev's (1996) scaling (3.26). Lapeyre and Held's (2003) scaling is derived by applying the diffusivity estimate $D_\varepsilon \sim \varepsilon^{3/5} \beta^{-4/5}$ not to the barotropic mode but to the lower layer, whose rationale is that the diffusive picture works better in the lower layer than the upper layer. This rationale can actually be understood from the FN formula (3.2): the speed of relative propagation $|c_w - U|$ is smaller in the lower layer than in the upper layer so that eddy diffusion in the lower layer is more similar to that of isotropic turbulence. Though additional inconsistency exists in applying the diffusivity estimate $D_\varepsilon \sim \varepsilon^{3/5} \beta^{-4/5}$ to the lower layer, as its potential vorticity gradient is $\beta(1 - \xi)$ rather than β. In this sense, the scaling we derived in (3.29) seems to be more consistent.

3.5 Discussion and conclusion

In this paper, we have studied eddy diffusion in forced-dissipated β-plane turbulence using both theoretical arguments and numerical simulations. Two pathways are explored in deriving a scaling for meridional eddy diffusivity. The first pathway assumes that the meridional transport and mixing are dominated by turbulent eddies at the turbulence-wave crossover scale, and contribution of the larger wave-like eddies is negligible. The usual crossover wavenumber is determined by the energy flux rate ε and β as $k_\varepsilon \sim \beta^{3/5} \varepsilon^{-1/5}$, which yields a diffusivity scaling as $D_\varepsilon \sim \varepsilon^{3/5} \beta^{-4/5}$. However, we point out that this crossover scale and the corresponding diffusivity scaling D_ε are only relevant when the forcing scale k_f^{-1} is smaller than the crossover scale, or equivalently $\Pi > 1$ with $\Pi = k_f / k_\varepsilon$. For $\Pi < 1$, we obtain a new relation for the eddy diffusivity that depends on the enstrophy flux rate η as $D_\eta \sim \beta^{-2} \eta$, using the newly discovered crossover scale in the enstrophy cascade range from Part I of this

study. The second pathway is based on Ferrari and Nikurashin's (2010) formula for diffusivity of eddies at a single wavenumber, along with two additional assumptions we proposed. It predicts the same diffusivity scalings D_ε and D_η for the two limits $\Pi \gg 1$ and $\Pi \ll 1$ respectively. It also supports the assumption that wave-like eddies do not contribute much to eddy diffusion in the limit $\Pi \gg 1$. However, in the limit $\Pi \ll 1$, it predicts that eddy diffusion is dominated by wave-like eddies at the forcing scale rather than the turbulent eddies at the crossover scale.

Numerical simulations are carried out to test these predictions. Our new diffusivity scaling D_η agrees well with simulations up to $\Pi \lesssim 2$. In this regime, the diffusivity strongly depends on the forcing scale if ε and β are kept the same. When Π increases above 2, the dependency on forcing scale gradually disappears and the diffusivity approaches the other scaling limit, D_ε. The two scaling limits can be combined using a semi-empirical formula, which well predicts diffusivity for a wide range of flows. We further demonstrate its usefulness in deriving a closure for heat flux in a two-layer quasi-geostrophic model. To test the predictions for the dominant scale in eddy diffusion, tracer flux spectra are evaluated for flows in the two regimes $\Pi \gg 1$ and $\Pi \ll 1$. When $\Pi \gg 1$, the tracer flux spectrum peaks close to the crossover scale, which confirms that the mixing by the wave-like eddies is strongly suppressed and therefore can be neglected. However when $\Pi \ll 1$, the tracer flux is dominated by wave-like eddies much larger than the crossover scale, which contradicts the no-wave-mixing assumption but generally agrees with our prediction based on Ferrari and Nikurashin's (2010) formula especially if our prediction is further revised to include the observed eddy kinetic energy spectrum. We conclude that Ferrari and Nikurashin's (2010) formula is more fundamental than the no-wave-mixing assumption in capturing the influence of the β-effect on eddy diffusion.

Appendix A: Alternative derivation of eddy diffusivity

The barotropic potential vorticity (PV) $q = \beta y + \zeta$ for a 2d flow on β-plane satisfies

$$\frac{\partial q}{\partial t} + J(\psi, q) = \nu \nabla^2 q - r\zeta + \vartheta, \tag{3.31}$$

where ζ is the relative vorticity, $\nu\nabla^2 q = \nu\nabla^2\zeta$ is the viscosity, $-r\zeta$ is the linear friction, and ϑ is the random forcing at wavenumber k_f. Normal viscosity is used here instead of hyperviscosity in order to have an effective diffusivity definition that is rigorously positive-definite. Though effective diffusivity can also be defined for hyperviscosity, and it is shown to share similar properties as that of the normal viscosity.

Despite the similarity between PV and a passive tracer (Green 1970), PV flux in the 2d flow is actually not directly related to the tracer flux. This can be easily seen at the center of the westerly jet, where the PV flux $\overline{v'q'} = -\partial\overline{u'v'}/\partial y$ needs to be up-gradient in order to accelerate the jet, whereas tracer flux is everywhere downgradient. In Nakamura's framework, PV flux through a PV contour is defined and is shown to be diffusive in nature (see Nakamura and Zhu 2010a and references therein). This diffusive PV flux is directly related to the tracer flux and then we may constrain tracer diffusivity from the dynamical equation (3.31). Here we briefly introduces Nakamura's framework, which leads to an alternative derivation of the eddy diffusivity scaling D_η in (3.8).

In a domain that is re-entrant in x-direction with length L_x, applying the finite amplitude wave activity operator Δ_Σ to a 2d field $X(x, y)$ as

$$\Delta_\Sigma X = L_x^{-1} \left(\int_0^{L_x} dx \int_{q \geq Q(Y), y \leq Y_0} dy - \int_0^{L_x} dx \int_{Y \leq y \leq Y_0} dy \right) X,$$

the result is positive definite and its spatial structure is described in a new coordinate called equivalent latitude $Y(q)$, which is defined by equating the area occupied by PV greater than a threshold value q to that bounded by the latitude line $y > Y(q)$. The inverse function $Q(Y)$ is also well defined as $Y(q)$ is a monotonic function of q by construction. Y_0 is a reference latitude that is northward enough so that it does not intersect the PV contour with value Q. In the case that PV is dominated by the planetary vorticity βy, a crude impression is that the structure of PV with respect to equivalent latitude $Q(Y)$ is similar to the zonally averaged PV $\overline{q(y)}$ when ignoring the difference between Y and y.

Applying the finite amplitude wave activity operator to each term in Eq. (3.31), we get

$$\frac{\partial A}{\partial t} + \overline{v'q'} = -K^q_{eff}\frac{\partial Q}{\partial Y} + \Delta_\Sigma \vartheta - r\Delta_\Sigma \zeta, \tag{3.32}$$

where $A = \Delta\Sigma q$ represents the finite amplitude wave activity, and $\overline{v'q'}$ is zonal mean PV flux at latitude $y = Y$. On the right hand side (RHS), the effective diffusivity at Y is

$$K^q_{eff} = \langle \nu |\nabla q|^2 \rangle_Q \left(\frac{\partial Q}{\partial Y}\right)^{-2},$$

where $\langle\cdot\rangle_Q$ denotes the area-weighted average around the Q contour. The effective diffusivity K^q_{eff} measures microscopic diffusion $\nu\nabla^2 q$ magnified by stirring. The term $-K^q_{eff}\partial Q/\partial Y$ is the downgradient diffusive flux across equivalent latitude Y, which is similar in nature to the tracer flux. Both theoretical arguments and experiment results suggest K^q_{eff} to be determined by large scale flow and largely independent of microscopic diffusivity ν if there is sufficient stirring (Shuckburgh and Haynes 2003). Therefore, we would expect the tracer field to experience the same effective diffusivity

as the PV field although they may have different microscopic diffusivity. The eddy diffusivity for tracer can thus be estimated as

$$D \sim \langle K^q_{eff} \rangle. \tag{3.33}$$

To have an estimate of the effective diffusivity, we need to examine the rest of the terms on the RHS of (3.32). The forcing term $\Delta_\Sigma \vartheta$ is shown to be everywhere positive and is the reason to cause PV flux to be different from tracer flux as discussed in Nakamura and Zhu (2010a, b). The additional term $-r\Delta_\Sigma \zeta$ is found to be much smaller than the other two terms on the RHS in our simulations. In a time and domain average, terms on the left hand side of (3.32) vanish, so we have

$$\langle K^q_{eff} \frac{\partial Q}{\partial Y} \rangle \approx \langle \Delta_\Sigma \vartheta \rangle. \tag{3.34}$$

Now the question becomes what determines the forcing term $\Delta_\Sigma \vartheta$. Conveniently, Nakamura and Zhu (2010b) provided a parameterization for it as

$$\Delta_\Sigma \vartheta \sim \frac{\overline{\vartheta' q'}}{\partial \overline{q}/\partial y}, \tag{3.35}$$

and immediately we see that

$$\langle \Delta_\Sigma \vartheta \rangle \sim \frac{\langle \vartheta' \zeta' \rangle}{\beta} = \frac{\eta}{\beta}, \tag{3.36}$$

where we assume $\partial Q/\partial Y \sim \beta$ and enstrophy generation rate $\langle \vartheta' \zeta' \rangle$ equals the down-scale enstrophy flux rate η. Combining (3.33) (3.34) and (3.36), finally we get

$$D \sim \beta^{-2} \eta. \tag{3.37}$$

This is the same diffusivity scaling as D_η in (3.8) for flow with $\Pi < 1$.

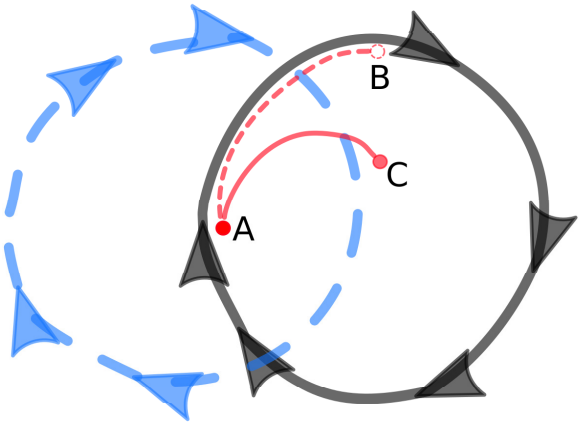


Figure 3.1: Suppression of mixing length by the relative propagation of eddies to the mean flow.

A detailed examination reveals that the parameterization (3.35) breaks down when $\Pi \gg 1$. Nakamura and Zhu (2010a) showed in the small amplitude limit, the finite wave amplitude A is approximate to the pseudo-momentum as

$$A \approx \frac{1}{2} \frac{\overline{q'^2}}{\partial \overline{q}/\partial y}, \tag{3.38}$$

which is the small-amplitude wave activity derived from a linearized eddy PV equation. By analogy, in the small amplitude limit the forcing term should also be approximate to its form (3.35) in linearized eddy PV equation. As illustrated by the representative PV contours in Fig. 3.7, the small amplitude limit is obviously more relevant for $\Pi < 1$ flow than $\Pi \gg 1$ flow. In the $\Pi < 1$ flow, a PV contour is mostly slightly displaced from a latitude with a wave-like form. Whereas in the $\Pi \gg 1$ flow, PV is dominated by small scale fluctuations and a PV contour spreads out much wider in latitudes.

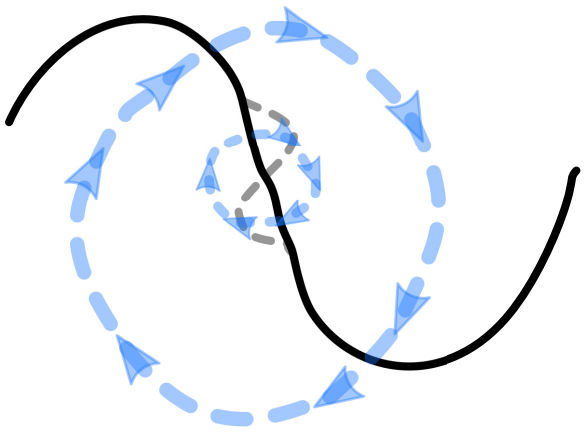


Figure 3.2: A material line (or an isopleth of tracer concentration) is shown as the solid black line. The two blue dashed lines represents eddy flows of larger and smaller scales. In a later time, the material line is further stirred by the smaller eddy into the dashed gray line.

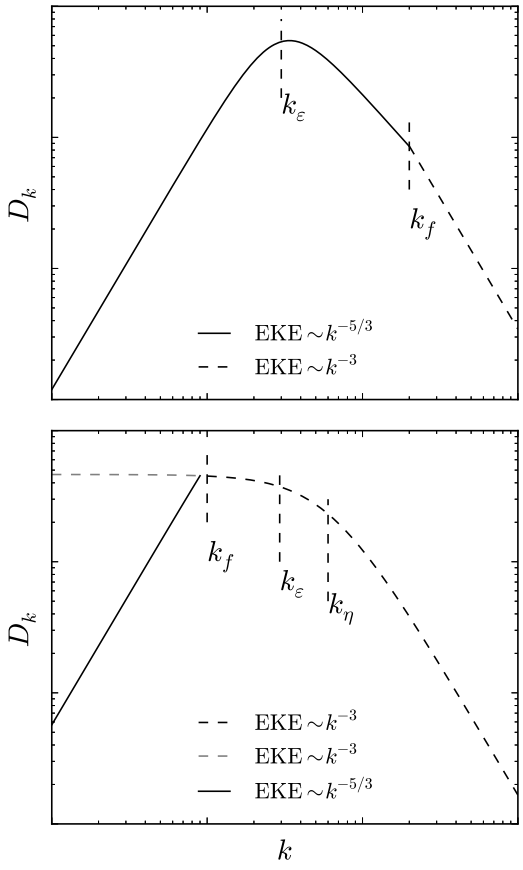


Figure 3.3: Suppressed eddy diffusivity $D(k)$ at each wavenumber k in (upper) energy cascade range and (lower) enstrophy cascade range. The legend shows the assumed eddy kinetic energy spectrum corresponding to $D(k)$.

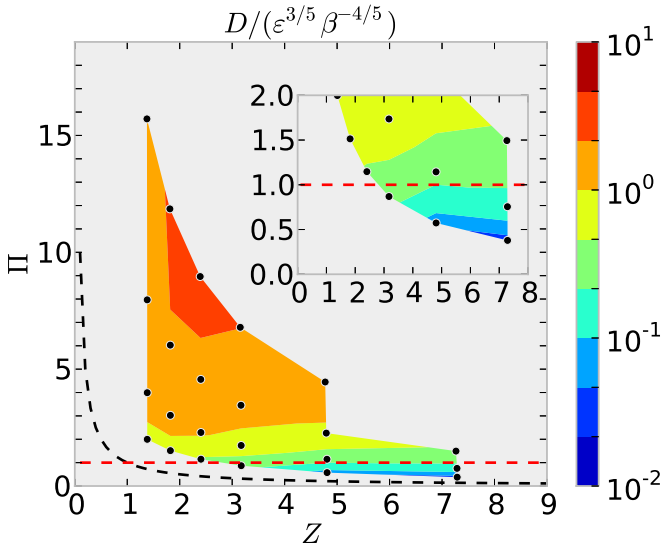


Figure 3.4: Meridional eddy diffusivity D non-dimensionalized by $\varepsilon^{3/5}\beta^{-4/5}$ in the (Z, Π) space. Black dots correspond to simulations that are carried out in this study. Black dashed line is $Z\Pi = 1$, which is the estimated boundary for forcing scale to be smaller than energy halted scale. Red dashed line is $\Pi = 1$. The inset figure is a zoom in of the region with $\Pi < 2$.

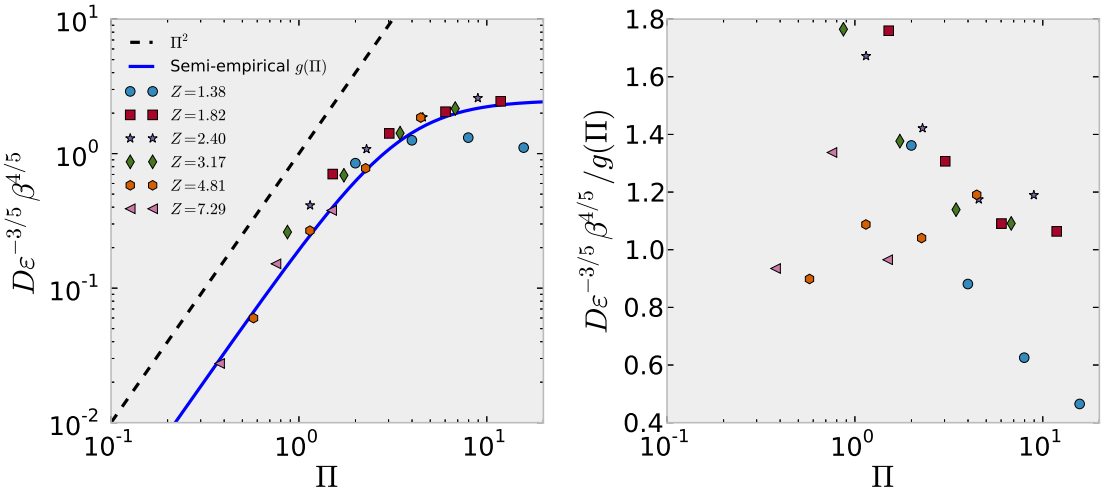


Figure 3.5: (Left) dimensionless diffusivity $D\varepsilon^{-3/5}\beta^{4/5}$ vs. Π for all simulations with different Z. Dashed black line corresponds to power law Π^2. Blue solid line is semi-empirical fit to the dimensionless diffusivity as $g(\Pi) = 2.5(1 + (\Pi/3.5)^{-2})^{-1}$. (Right) Relative error of the semi-empirical fit as $D\varepsilon^{-3/5}\beta^{4/5}/g(\Pi)$.

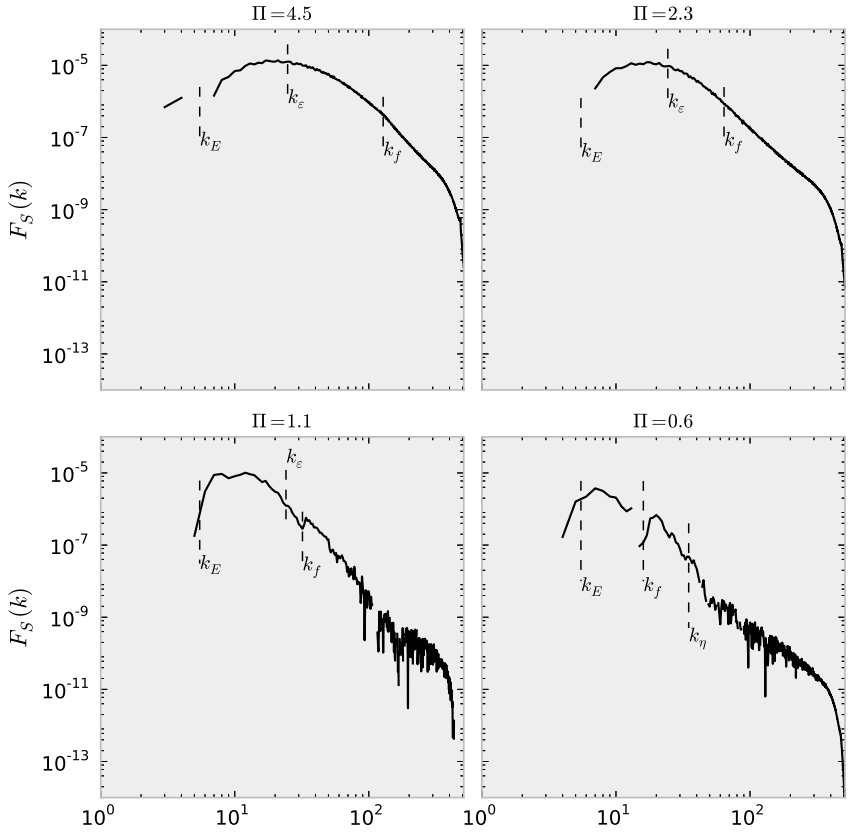


Figure 3.6: Tracer flux spectrum $F_S(k)$ for simulations with $Z = 4.8$ and various values of Π. The vertical dashed lines denote forcing wavenumber k_f, energy containing wavenumber k_E, crossover wavenumber in energy cascade range k_ε, and crossover wavenumber in enstrophy cascade range k_η.

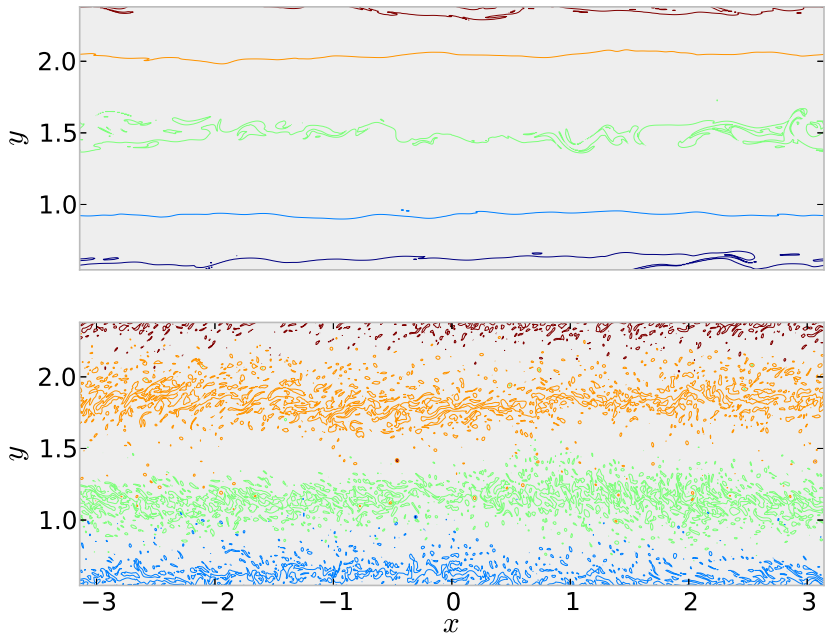


Figure 3.7: Representative potential vorticity contours in part of the domain from simulations with $Z = 4.8$ and different values of Π: (top) $\Pi = 0.6$ and (bottom) $\Pi = 4.5$.

Chapter 4

Eddy heat fluxes in 2-layer quasi-geostrophic model

At the end of the last chapter, we briefly discussed the closure theory of heat flux in 2-layer QG model. In this chapter, we look at the 2-layer QG model in more details, which serves as a bridge between the 1-layer model and more realistic baroclinic turbulence. The governing equation (1.7) can be written into modular form using the barotropic and baroclinic modes ψ and τ respectively. The barotropic mode is governed by

$$\nabla^2\psi_t + J(\psi, \nabla^2\psi) + \beta\psi_x = F_\psi - r\nabla^2(\psi - \tau) + (-1)^{n+1}\nu\nabla^{2n+2}\psi, \qquad (4.1)$$

where the forcing on the barotropic mode is

$$F_\psi = -J(\tau, \nabla^2\tau) - U\nabla^2\tau_x.$$

The baroclinic mode is governed by

$$\tau_t + J(\psi, \tau) + U\psi_x = R_\tau - \lambda^2 r\nabla^2(\psi - \tau) + (-1)^{n+1}\nu\nabla^{2n+2}\tau, \qquad (4.2)$$

where

$$R_\tau = \lambda^2 \left(\nabla^2 \tau_t + J(\psi, \nabla^2 \tau) + J(\tau, \nabla^2 \psi) + U \nabla^2 \psi_x + \beta \tau_x \right).$$

The phenomenology of the 2-layer QG model, summarized as a direct cascade of baroclinic mode and an inverse cascade of barotropic mode, can be seen from the above two equations (4.1) and (4.2). The barotropic mode ψ evolves as if a 1-layer fluid forced by F_ψ. The baroclinic mode evolves as a chemical tracer: it is advected by the barotropic flow while its concentration is being created or removed via the reaction term R_τ. By scaling analysis, we shall see that the reaction term R_τ only influences τ near the deformation radius λ. It is therefore thought that the variance of baroclinic mode, or available potential energy, cascades to smaller scales until it arrives at the deformation radius, where it gets converted into the barotropic mode. On the other hand, the forcing on the barotropic mode F_ψ does not have the same form as R_τ. Though if the spectrum slope of τ is flattener than k^{-3} between the largest scale and the deformation radius, we could see again that F_ψ peaks near the deformation radius. In numerical simulations, the variance of τ is clearly removed near the deformation radius, however, the barotropic mode is forced at a scale much larger than the deformation radius (Larichev and Held, 1995).

The closure of the 2-layer model centers on the eddy diffusivity of temperature D_τ defined as (hereinafter referred as diffusivity for short)

$$D_\tau \equiv U^{-1} \langle \psi_x \tau \rangle. \tag{4.3}$$

The eddy energy generation, or the energy dissipation by friction, is related to the diffusivity as

$$\varepsilon = \frac{U^2}{\lambda^2} D_\tau. \tag{4.4}$$

From Buckingham π theorem, we know that the diffusivity can be written as

$$D_\tau = U\lambda \tilde{D}_\tau \left(\xi, \tilde{r}, \frac{L}{\lambda}, \frac{\nu}{UL^{2n+1}} \right),$$

where $\tilde{D}_\tau$ is a dimensionless function, L is the domain size. If the domain size is much larger than the jet scale so that L does not matter, and there is an extended enstrophy cascade range so that ν does not matter, the system is fully determined by two non-dimensional numbers, criticality

$$\xi = \frac{U}{\beta\lambda^2}$$

and dimensionless friction

$$\tilde{r} = \frac{r}{U/\lambda}.$$

The dimensionless diffusivity is then

$$\tilde{D}_\tau \left(\xi, \tilde{r}, \frac{L}{\lambda}, \frac{\nu}{UL^{2n+1}} \right) \simeq \tilde{D}_\tau(\xi, \tilde{r}).$$

4.1 The role of friction

The dependency of the dimensionless diffusivity $\tilde{D}_\tau$ on friction has been studied by Thompson and Young (2007), who vary $\tilde{r}$ from 0.64 to 0.02. In this study, we explore a much wider regime by varying $\tilde{r}$ across 5 orders of magnitudes. Three series of simulations with criticality ξ=1.4, 1.6 and 1.8 are carried out for each combination of $\tilde{r}$ and ξ. The deformation radius λ is kept at $\lambda = 2\pi/500$ and the domain is a $2\pi \times 2\pi$ doubly-periodic square. Fig. 4.1 shows that the dimensionless diffusivity $\tilde{D}_\tau$ decreases with $\tilde{r}$ when friction is small enough regardless of the criticality. The

dependency is especially strong for the smallest criticality $\xi = 1.4$ with a nearly linear $\tilde{D} \sim r$ dependency, and it is weaker for the largest criticality $\xi = 1.8$.

The turbulence regime of the barotropic mode can be characterized using the two non-dimensional parameters Z and Π introduced before. The forcing scale in the barotropic mode is calculated from the forcing spectrum as

$$k_f^2 = \frac{\int \{\psi\}_k^* \{F_\tau\}_k k^2 dk}{\int \{\psi\}_k^* \{F_\tau\}_k dk},$$

where $\{A\}_k$ denotes the Fourier component of A at wavenumber k, and * denotes complex conjugate. In this definition, the enstrophy and energy fluxes are still related by forcing scale as $\eta = k_f^2 \varepsilon$. Fig. 4.2 shows Z and Π vs. dimensionless friction. When the dimensionless friction $\tilde{r}$ decreases from 0.5 to 5×10^{-5}, the zonostrophic index Z increases from $\sim$1 to about 7$\sim$8. In consistent, the flow becomes highly anisotropic with very strong jets in the low friction end. At the same time, the other parameter Π decreases from above 1 to below 1. For $\xi = 1.4$, the forcing F_τ actually removes enstrophy ($\int \{\psi\}_k^* \{F_\tau\}_k k^2 dk < 0$) in the lowest two friction runs so that k_f cannot be defined. Π is generally larger when criticality is larger or friction is larger. However, for all the runs here Π is always smaller than 2, which means that the flow is not in the zonostrophic regime. The decrease of Π with friction is mostly due to the increase of the crossover wavenumber $k_\varepsilon \sim \beta^{3/5} \varepsilon^{-1/5}$ as ε decreases with friction. The forcing wavenumber k_f decreases very slightly when friction decreases.

As Π is always smaller than 2, we expect the diffusivity to be dependent on Π based on the discussion in the last part. Therefore, our updated diffusivity scaling $D \sim \varepsilon^{3/5} \beta^{-4/5} g(\Pi)$ that incorporates the dependency on Π should work better than the scaling in the zonostrophic regime $D_\varepsilon \sim \varepsilon^{3/5} \beta^{-4/5}$ as we have already seen. However, the resulted closure for $\tilde{D}_\tau$ is a function of criticality ξ only and has no dependency on $\tilde{r}$. Here we examine two assumptions our deviation is based on to see why our diffusivity scaling fail to capture the dependency on $\tilde{r}$.

The first assumption is that the eddy diffusivity of temperature D_τ is similar to the eddy diffusivity of a passive tracer advected by the barotropic flow. Under this assumption, we use the diffusivity scaling derived in the 1-layer model as D_τ. To test this assumption, a passive tracer with a fixed meridional gradient is advected by the barotropic flow for the series of run with criticality $\xi = 1.6$. Eddy diffusivity of the tracer D_t is calculated from the tracer flux. The comparison between tracer diffusivity D_t and heat diffusivity D_τ is shown in Fig. 4.3. When friction reduces, the two diffusivities follows a quite accurate linear relationship except for the largest friction run. When friction is large enough, the wind at lower layer is very small so that barotropic and baroclinic modes have comparable energy. In this case, the picture that baroclinic mode is being advected as a passive tracer by the barotropic mode may no longer be valid. Except for this largest friction case, the assumption $D_\tau \simeq D_t$ holds to a high degree of accuracy.

The second assumption is the scaling of eddy diffusivity D_t in the barotropic mode. Although the diffusivity scaling may work well in the 1-layer model, due to the coupling between ε and D_τ in the 2-layer model as seen in (4.4), the same scaling may not be accurate enough in the 2-layer model. As seen from Fig. 3.4, the dimensionless diffusivity $D\varepsilon^{-3/5}\beta^{4/5}$ slightly decreases with increasing zonostrophic index Z. In the 2-layer model, Z increases when $\tilde{r}$ decreases as seen in Fig. 4.2. Although we may safely neglect this weak dependency on friction in the 1-layer model, the dependency is amplified by the coupling (4.4). To see this, we include a dependency of diffusivity on friction as

$$D \sim \varepsilon^{3/5}\beta^{-4/5} g(\Pi)\tilde{r}^{\alpha},$$

which is a modification to our semi-empirical diffusivity scaling. Combined with (4.4), we get

$$D \sim U\lambda\xi^2 g(\Pi)^{5/2}\tilde{r}^{(5/2)\alpha},$$

in which we immediately see that the power law dependency on friction is amplified by a factor of 5/2. Moreover, as Π decreases when friction decreases due to the change of ε and thus k_ε, the dependency on $\tilde{r}$ is further amplified.

Due to the amplification effect, any slight dependency of diffusivity on friction in the 1-layer barotropic model will translate into a much stronger dependency in the 2-layer baroclinic model. Still, we propose a possible physical mechanism and scaling here to understand the role of friction. The framework is still Ferrari and Nikurashin's (2010) suppressed diffusivity formula (3.2), and we write it down again for the ease of reading

$$D_k = \frac{D_0}{1 + \tau^2 k_x^2 (c_w - U)^2}. \tag{4.5}$$

In the last part, we used intrinsic Rossby wave phase speed as c_w so that $c_w - U = -\beta/k^2$. However, when friction is very weak, the jets are so strong that their curvature should enters the potential vorticity (PV) gradient so that β should be modified to an effective $\beta_{eff} = \beta - U_{yy}$. In the extreme case that PV staircase forms, the waves become edge wave instead of Rossby wave in the center of the jet. This is especially important for the 2-layer model as eddies are not spatially uniform but they are generated at the center of the jet where the baroclinicity is the strongest. Fig. 4.4 shows such an example. The PV staircase structure is clear and the eddies are mostly trapped at the center of the jet. Space-time spectrum in Fig. 4.5 shows that the largest eddies indeed behave as edge waves. Therefore, we may use the edge wave phase speed in (4.5) as $c_w - U = \Delta q/(2k_x)$. Using the approximation $k_x \sim k$ and $D_0 \sim V_k k^{-1}$ as we did before, (4.5) becomes

$$D_k \sim \frac{V_k^3 k}{\Delta q^2}.$$

The numerator $V_k^3 k$ can be estimated from a dimensional analysis as

$$V_k^3 k \sim \varepsilon.$$

The PV jump at the center of the jet may be estimated as

$$\Delta q \sim \beta l_J,$$

where l_J is the jet scale which may be estimated from the Rhines scale as

$$l_J \sim \mathrm{KE}^{1/4} \beta^{-1/2},$$

and the total kinetic energy KE can be quite accurately estimated by

$$\mathrm{KE} \simeq 0.5\varepsilon/r.$$

Combining these together with the coupling (4.4), we get

$$D \sim \lambda^2 r \xi^2.$$

In the dimensionless form

$$\tilde{D} \sim \tilde{r} \xi^2.$$

Finally, we have a linear dependency of diffusivity on friction.

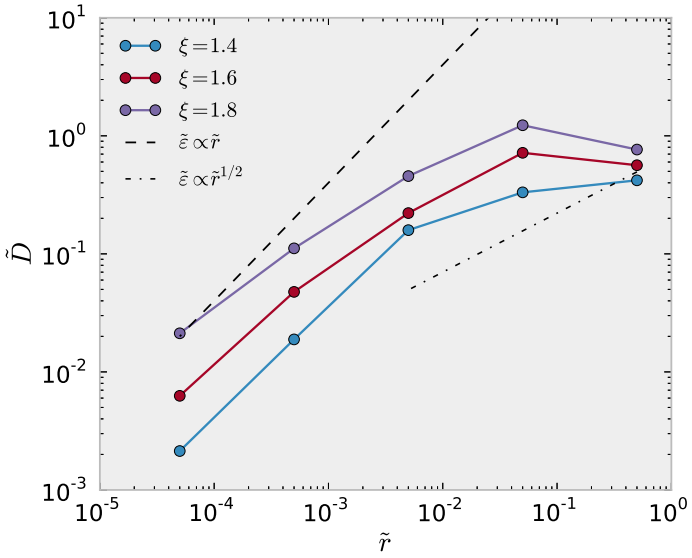


Figure 4.1: Dimensionless diffusivity $\tilde{D} = D_\tau/(U\lambda)$ vs. dimensionless friction for three series of simulations with different criticality.

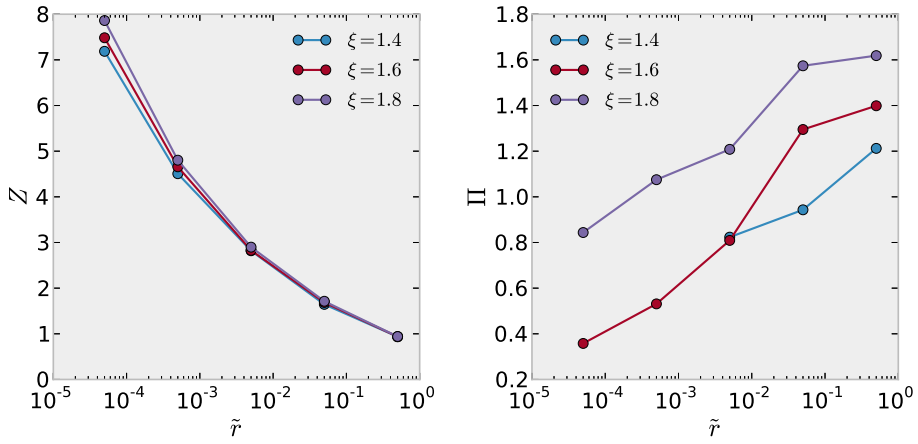


Figure 4.2: (Left) zonostrophic index Z and (right) Π vs. dimensionless friction for three series of simulations with different criticality.

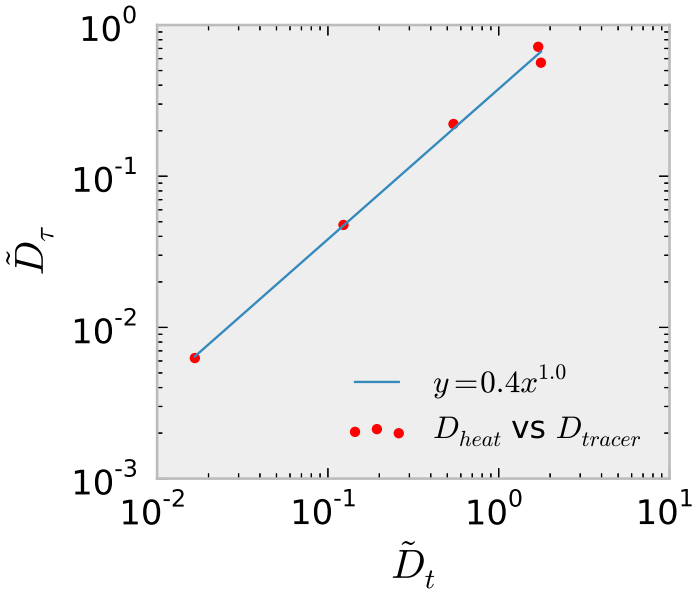


Figure 4.3: Eddy diffusivity of a passive tracer $\tilde{D}_t$ vs that of the temperature $\tilde{D}_\tau$ for the series of runs with $\xi = 1.6$. Both diffusivities are non-dimensionalized by $U\lambda$.

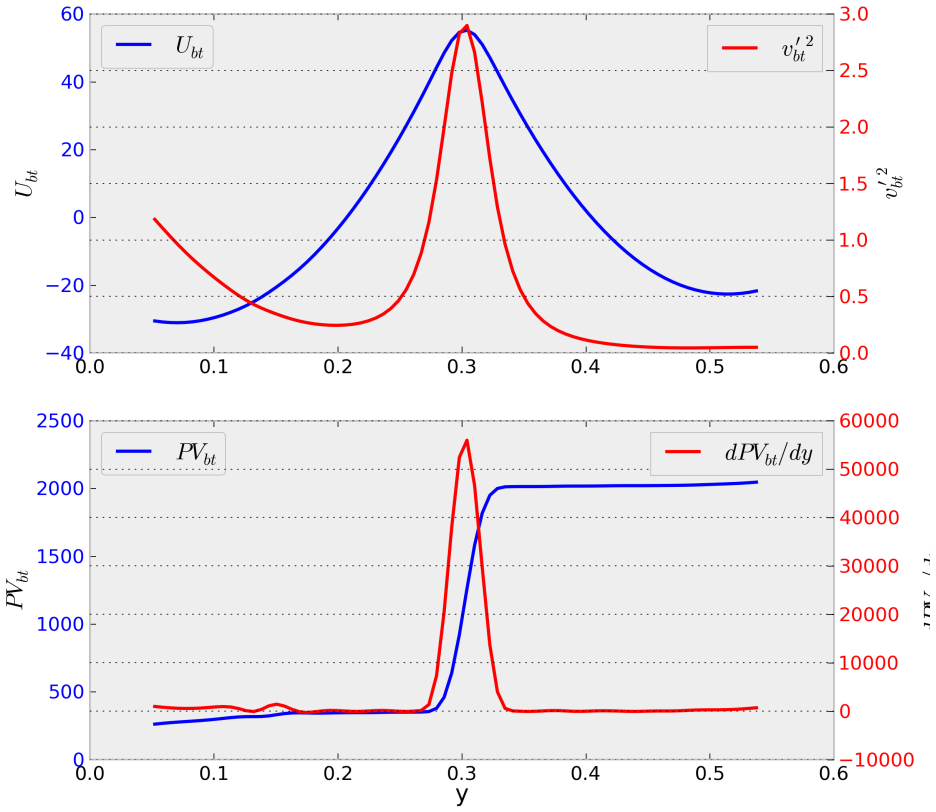


Figure 4.4: An example of a jet in a low friction run. (Top) Zonal mean zonal wind (blue line) and eddy velocity square (red line). (Bottom) zonal mean potential vorticity (blue line) and its meridional gradient (red line). These quantities are of the barotropic mode and are time averaged.

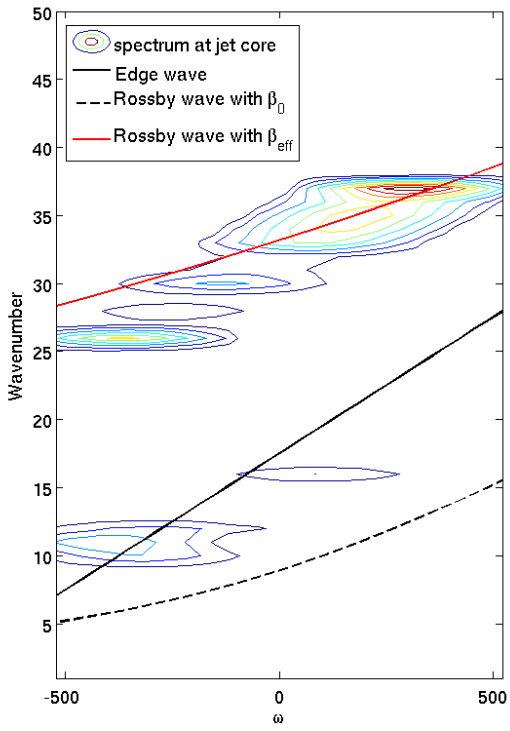


Figure 4.5: Space-time spectrum of eddies at the center of the jet in Fig. 4.4. The red line denotes Rossby wave dispersion relation $\omega = Uk_x - \beta_{eff}/k_x$. The solid black line denotes edge wave dispersion relation $\omega = Uk_x - \Delta q/(2k_x)$, where Δq is the potential vorticity jump across the jet.

Chapter 5

Equilibration of a baroclinic planetary atmosphere toward the limit of vanishing bottom friction

This paper discusses whether and how a baroclinic atmosphere can equilibrate with very small bottom friction in a dry, primitive equation, general circulation model. The model is forced by a Newtonian relaxation of temperature to a prescribed temperature profile, and it is damped by a linear friction near the lower boundary. When friction is decreased by four orders of magnitude, kinetic energy dissipation by friction gradually becomes negligible, while "energy recycling" becomes dominant. In this limit kinetic energy is converted back into potential energy at the largest scales, thus closing the energy cycle without significant frictional dissipation. The momentum fluxes are of opposite sign in the upper and lower atmosphere: in the upper atmosphere, eddies converge momentum into the westerly jets, however, in the lower atmosphere, the eddies diverge momentum out of the westerly jets. The secondary circulation driven by the meridional eddy momentum fluxes thus acts to increase the baroclinicity of

the westerly jet. This regime may be relevant for the Jovian atmosphere, where the frictional time scale may be much larger than the radiative damping time scale.

5.1 Introduction

Bottom friction (also referred to as surface drag) that acts at large scales plays a crucial role in the equilibration of baroclinic turbulence for Earth's atmosphere. The importance of bottom friction can be illustrated by considering the momentum and energy budgets. The zonal-mean angular momentum budget at midlatitudes is characterized by a transfer of angular momentum from the eddies into the westerly jets. In a statistically steady state this momentum-flux convergence must be balanced by frictional drag in the bottom boundary layer (Green 1971; Held 1975; Edmon et al. 1980). The energy budget is constrained by the quasi-two-dimensional character of the large-scale dynamics. Little kinetic energy generated by baroclinic instability can cascade to smaller scales (see a review on two-dimensional turbulence by Boffetta and Ecke 2012); instead, most kinetic energy cascades to larger scales or gets channeled into the zonal jets (Vallis and Maltrud, 1993). The bottom drag is needed to ultimately remove the kinetic energy, thus closing the energy cycle and bounding the kinetic energy. By considering the atmosphere to work as a heat engine, the entropy budget provides an additional perspective (Held, 2007). The large scale radiative damping decreases the entropy of the flow, as the warmer equatorial region gets heated and polar region gets cooled. In a statistical steady state, the decrease in entropy is balanced by the creation of entropy due to bottom friction for the dry dynamics.

Such budgets are less clear for Jupiter's atmosphere or the atmospheres of other Jovian planets as the strength of bottom friction is highly uncertain. In one line of studies, a model for Jupiter's atmospheric circulation considers a thin shell upper

atmosphere ($\sim$ 1 bar) sitting on top of a deep fluid interior. The upper atmosphere is often referred as the weather layer for it is hypothesized to be Earth-like: the flow is governed by similar geophysical fluid dynamics as Earth, and the strong jets and turbulent eddies are energized by baroclinic instability or by convection coupled to large scale dynamics, with the deep interior rather crudely treated as a lower boundary condition (Williams and Halloway 1982; Williams 1985; see a review by Vasavada and Showman 2005). In modeling the circulation of the weather layer, a major uncertainty lies in the strength of bottom friction, which parameterizes the coupling between the thin weather layer and the deep interior. As a gas giant planet, Jupiter's atmosphere transits smoothly into its deep fluid interior, while the flow is only visible at the cloud top ($0.5 \sim 1$ bar). To find a rigid bottom boundary on Jupiter that may be analogous to Earth's surface, one needs to reach far down below the weather layer, perhaps up to about 0.8 Jupiter's radius, where the pressure reaches more than 10^6 bar so that the molecular hydrogen transits into metallic hydrogen and can be viewed as in near solid-body rotation (Guillot, 2005). On the one hand, bottom friction acting on the weather layer thus must be very small or even vanishing as the weather layer does not have a rigid bottom boundary or topography (Dowling, 1995). On the other hand, some coupling between the metallic hydrogen interior and the weather layer is expected, otherwise there is nothing unique about the reference frame rotating with the metallic hydrogen core (the existence of latitudinal jets on Uranus suggests that the jets are controlled by internal rotation [Ingersoll 1990]).

Most researchers have in fact included a bottom friction with a somewhat arbitrary strength when modeling the weather layer (e.g., Williams, 1985), although the source of the drag remains unclear. One possibility (Showman et al., 2006; Lian and Showman, 2008; Schneider and Liu, 2009) is that a mean meridional circulation, akin to the Ferrel cell in Earth's atmosphere, extends from the deep interior to the weather layer. If this were to couple the magnetohydrodynamic (MHD) drag in the interior

to the weather layer it could act as a kind of drag and allow the weather layer to equilibrate (Liu and Schneider, 2010, 2011), and/or explain how shallow forcing at the cloud level could drive deep jets in the interior (Lian and Showman, 2008). Still, there is evidently much uncertainty in the mechanism of bottom friction, and hence the effective drag could be extremely small.

Intuitively it might seem hard for an atmosphere to equilibrate in the limit of vanishing bottom friction. It is well-known that for two-dimensional turbulence driven by random stirring, energy will keep accumulating at the largest scale with time in the absence of large scale friction (Kraichnan, 1967; Smith and Yakhot, 1993; Chertkov et al., 2007). In a primitive equation model simulating Jupiter's upper atmosphere, Liu and Schneider (2015) varied the frictional drag time scale by 3 orders of magnitude and found that the energy dissipation rate, which scales with U^2/τ_f, stays nearly constant (U is a scale for zonal wind speed and τ_f is the frictional damping time scale). In their simulation, the fixed surface heating induces convective stirring at the grid scale, which generates most of the kinetic energy and is similar to the random stirring in two-dimensional turbulence studies. However, for a flow self-stirred by baroclinic instability, the behavior is expected to be different as the stirring itself is influenced by the large scale flow. Interestingly, Lian and Showman (2008) simulated multiple jets driven by baroclinic instability in a primitive equation model with *zero* bottom friction. Although not explicitly studied, it appears that the flow approaches equilibrium after thousands of days of integration (see their Fig. 5).

It is not known whether a high or low value of friction produces more realistic Jovian atmospheric simulations. More fundamentally, the question of whether a baroclinic atmosphere can equilibrate as surface friction tends to zero remains open. In this study we therefore focus on the effects of bottom friction, and in particular the behaviour of a baroclinic atmosphere in both Earth-like and Jovian regimes, as friction becomes very small. Understanding the pathways between the production and

dissipation of energy are central to our understanding of baroclinic turbulence in this limit, and three hypotheses concerning the kinetic energy production rate ϵ suggest themselves.

1. The energy production rate ϵ stays finite, while the total kinetic energy increases without bound to maintain the necessary frictional dissipation, as in two-dimensional turbulence. This limit is implied by Held and Larichev's (1996) scaling that in a two layer quasi-geostrophic model, the kinetic energy production rate scales as $\epsilon \sim U^5/(\beta^2 L_R^5)$, where U is the mean thermal wind, β is the planetary vorticity gradient, and L_R is the Rossby deformation radius. In the pure form of this scaling, ϵ does not depend on bottom friction, which agrees with Liu and Schneider's (2015) simulation. To be a physically realizable system, some mechanism must eventually bound the energy level when the friction becomes small enough. For example, at some point the Rossby number may become sufficiently large so that the flow is no longer quasi two-dimensional and thus allows a forward cascade, in which case ϵ can be balanced by dissipation at small scales.

2. The energy production rate ϵ approaches zero as the flow becomes stabilized by the barotropic flow, and the flow ends up in a zonally symmetric state. James and Gray (1986) found that when bottom friction is reduced, the baroclinic instability of the time mean flow is greatly suppressed. This is explained by the increase of the barotropic shear when friction is reduced, which reduces the growth rate of the most unstable mode. It is coined as the "barotropic governor" mechanism (James and Gray, 1986; James, 1987). It is conceivable that toward the zero friction limit, the "barotropic governor" may become so strong that it completely suppresses the baroclinic instability. This could happen either with the barotropic flow equilibrating at a finite value or there could be a singular limit, in which the kinetic energy diverges but the divergence is such that the

energy dissipation rate still goes to zero. The thermal mean state in this case would have to be such that the radiative forcing no longer represents an entropy sink (since there is no obvious source of entropy).

3. The total energy generation and dissipation rate goes to zero, but the flow remains turbulent with a significant energy cycle. This could happen in the following way. At the Rossby deformation radius, eddies convert available potential energy (APE) into eddy kinetic energy (EKE). The EKE then cascades to larger scales, but instead of being accumulated at the largest scale, the inverse cascade is halted at some scale where kinetic energy is converted back into APE, and APE is ultimately dissipated by long wave radiation. For the whole flow, the net ϵ is negligible: radiative forcing would not generate or dissipate APE. In terms of entropy, radiative forcing would again not be a significant sink of entropy. This mechanism is essentially conjectured by Showman (2007) for Jupiter's atmosphere to equilibrate with little friction. In a shallow water system, it is well-known that the flow can equilibrate without friction, but solely damping of the height perturbation, which represents radiative damping (Showman and Ingersoll, 1998; Showman, 2007; Scott and Dritschel, 2013). However, it is not clear whether this mechanism can work in a continuously stratified flow which possesses a barotropic mode.

To see which is a physically realizable limit, we use an idealized, dry, primitive equation model to simulate a baroclinic atmosphere with varying bottom friction. The model setup and experiments are discussed in Section 2. The simulation results and analysis are discussed in Section 3, The results suggest that a mixture between the second and third hypothesis above is most applicable. The implications of our results and their relevance for Jupiter's atmosphere are discussed in Section 4.

5.2 Idealized GCM and experiments

We investigate whether and how a baroclinic atmosphere can equilibrate close to the limit of vanishing bottom friction in an idealized GCM, which is set to either Earth-like or Jupiter-like parameters. The general model description is given in subsection a, and the settings that are specific for Earth or Jupiter are described in subsection b and c respectively.

a. Model description

The GCM consists of the Geophysical Fluid Dynamical Laboratory (GFDL) spectral atmospheric dynamical core with the Held and Suarez (1994) forcing, which is a thermal relaxation back to a specified temperature. The model solves the primitive equations for a dry ideal gas atmosphere on a sphere in $\sigma-$coordinate with the spectral transform method in the horizontal, and centered difference scheme in the vertical. There is no bottom topography at the lower boundary. The bottom friction is represented by a Rayleigh damping of horizontal velocities near the lower boundary,

$$\frac{\partial \mathbf{v}}{\partial t} = ... - k(\sigma)\mathbf{v}, \tag{5.1}$$

where the drag coefficient $k(\sigma)$ decreases linearly from its maximum value k_f at the bottom boundary ($\sigma = 1$) to zero at $\sigma_b = 0.7$,

$$k(\sigma) = k_f \max(0, \frac{\sigma - \sigma_b}{1 - \sigma_b}). \tag{5.2}$$

Radiative effects are represented by a Newtonian relaxation of temperature to a prescribed "radiative-convective equilibrium" profile,

$$\frac{\partial T}{\partial t} = ... - \alpha_T(T - T_{eq}), \tag{5.3}$$

where the forcing rate α_T adopts the same value everywhere ($\alpha_T = 1/40$ day^{-1}, Earth day is used thereinafter). The prescribed profile T_{eq} is zonally symmetric, and it is chosen to be suitable for either Earth or Jupiter (see subsections below). Apart from the Rayleigh friction and Newtonian heating, the only other dissipative process is an 8th order hyper-diffusion ∇^8 imposed on vorticity, divergence and temperature fields, with a damping time scale of 0.1 day for the smallest waves.

The initial condition is an isothermal state (200 K) at rest in the rotating reference frame, with some small temperature perturbation to break the zonal symmetry. If the bottom friction is identically zero, the climatology will inevitably depend on the initial condition, as the total angular momentum must be conserved if there is no friction. We will thus restrict our simulations to the limit of very small but finite friction, and return to a discussion of the zero friction limit at the end.

b. Earth-like simulations

In this subsection we discuss simulations using Earth parameters, i.e., Earth's radius, rotation rate, and the gas constant of air. The "equilibrium" temperature profile T_{eq} is adapted from Held and Suarez (1994) as

$$T_{eq} = \max\left\{T_{st}, \left[T_0 - \Delta_y T \sin^2\phi - \Delta_z\theta \ln\left(\frac{p}{p_0}\right)\right]\left(\frac{p}{p_0}\right)^{\kappa}\right\}, \tag{5.4}$$

where $T_{st} = 200\,\mathrm{K}$ is the stratospheric equilibrium temperature, $T_0 = 315\,\mathrm{K}$ is the equatorial equilibrium temperature at the surface, $\Delta_y T = 60\,\mathrm{K}$ sets the meridional temperature gradient, and $\Delta_z\theta$ sets the vertical static stability. The reference pressure $p_0 = 1000$ mb and $\kappa = 2/7$. The only difference with the original Held and Suarez's (1994) profile is that we relax to a stable static stability profile everywhere in the troposphere, while Held and Suarez (1994) only apply it within the tropics. This prescribed vertical stability may be interpreted as a crude parameterization

of unresolved moist convective processes. From a modeling perspective, our main concern is to limit gravitational instability and the associated grid-scale convection (Frierson et al., 2007), which are not properly simulated by our hydrostatic GCM and are resolution dependent. We aim to only simulate the large scale motions related to baroclinic instability, i.e., baroclinic turbulence. The vertical stability parameter is chosen as $\Delta_z\theta = 20\,\mathrm{K}$. As the criticality $\xi \sim \Delta_y T/\Delta_z\theta$ for the equilibrium temperature profile is larger than 1, the eddies will tend to increase vertical stability so as to reduce criticality to $\sim$1 (Schneider and Walker, 2006; Chai and Vallis, 2014; Jansen and Ferrari, 2013a). Therefore, the lower limit for the Rossby radius can be estimated from the equilibrium temperature profile as $L_R \sim \sqrt{R\Delta_z\theta}/f$.[1] Choosing the midlatitude value for the Coriolis parameter as $f \sim 10^{-4}\ \mathrm{s}^{-1}$, the lower limit for the Rossby radius is about $L_R \sim 760$ km or spherical wavenumber $\sim$26.

Bottom friction is reduced towards the zero limit by varying the frictional damping time scale $\tau_f = 1/k_f$ across 4 orders of magnitude: $\tau_f = 1$ (control), 10, 10^2, 10^3, and 10^4 days. The largest frictional value $\tau_f = 1$ day is used by Held and Suarez (1994) to produce an Earth-like climate. We use T42 resolution in the horizontal and 30 evenly spaced σ levels in the vertical. This choice sacrifices resolution in the stratosphere but allows for better resolution of the baroclinic eddies in the troposphere as in the previous studies (Held and Larichev, 1996; Zurita-Gotor, 2008; Chen and Plumb, 2014; Lorenz, 2015). All simulations are integrated for 30,000 days, except that the lowest friction simulation ($\tau_f = 10^4$ day) is integrated for 60,000 days to reach a statistically steady state. At T42 resolution, the Rossby radius should be adequately resolved. In order to study the dynamical convergence of the flow field with horizontal

[1]The Rossby radius is usually estimated as $L_R = N_p(p_s - p_t)/f$, where $N_p^2 = -(\rho^s\theta^s)^{-1}\partial_p\theta^s$ is a vertical stability measure; p_s and p_t are the surface pressure and tropopause pressures respectively; θ is potential temperature and the superscript s denotes that the value is taken near the surface (Merlis and Schneider, 2009; Chai and Vallis, 2014). Approximations are made such that $p_s - p_t \sim p_s$, $(p_s - p_t)\partial_p\theta^s \sim \Delta_z\theta$, $\rho^s\theta^s = \rho^s T^s (p_0/p_s)^\kappa \sim \rho^s T^s = p_s/R$, therefore we obtain $L_R \sim \sqrt{R\Delta_z\theta}/f$.

resolution, we repeat the simulations using T127 resolution. For the simulation with $\tau_f = 10^3$ days, one additional run using T213 resolution is further carried out.

c. Jupiter-like simulations

Similar to the Earth-like simulations, the Jupiter model simulates a thin shell atmosphere extending from the top of the atmosphere to an artificial rigid lower surface. The mean surface pressure is 3 bar, which is used in a series of studies by Schneider and Liu (Schneider and Liu, 2009; Liu and Schneider, 2010, 2011, 2015). The planetary parameters are set to those of Jupiter: planetary radius $a = 6.986 \times 10^4$ km, planetary angular velocity $\Omega = 1.7587 \times 10^{-4}$ s^{-1}, and specific gas constant $R = 3605.38$ J kg^{-1}K^{-1}(Liu and Schneider, 2010). The equilibrium temperature profile roughly represents Jupiter, and is similar to that used by Lian and Showman (2008):

$$T_{eq} = T_{ref}(p) + \delta T(\phi). \tag{5.5}$$

In the vertical direction, the reference temperature profile T_{ref} corresponds to an isothermal stratosphere at 110 K above 0.15 bar level, a troposphere with some vertical stability specified by $\Delta_z\theta$, and a smooth transition between them. Analytically, it is

$$T_{ref}(p) = G(p)T_{st} + [1 - G(p)]\,[T_0 - \Delta_z\theta \ln(p/p_0)]\,(p/p_0)^\kappa, \tag{5.6}$$

where the stratosphere temperature $T_{st} = 110$ K, the reference pressure $p_0 = 1000$ mb, the temperature at reference pressure $T_0 = 170$ K, and $\kappa = 2/7$. $G(p) = [1 - (p/p_{trop})^2]^{-1}$ marks the transition from the stratosphere to the troposphere at $p_{trop} = 150$ mb. The vertical stability is $\Delta_z\theta = 5$ K. Therefore, the lower limit for the Rossby radius is about 1000 km at midlatitudes, or a spherical wavenumber of about 200. In the meridional direction, a temperature gradient is imposed to drive

baroclinic turbulence

$$\delta T(\phi) = \Delta_y T \left[1/3 - \sin^2(\phi)\right], \tag{5.7}$$

where the equator-pole temperature difference is set to $\Delta_y T = 15$ K. This value is significantly larger than the latitudinal temperature difference observed in Jupiter's upper atmosphere (0∼0.5 bar), which is typically around 5 K (Simon-Miller et al., 2006), although it is comparable to Schneider and Liu's (Schneider and Liu, 2009; Liu and Schneider, 2010, 2011, 2015) series of Jupiter simulations, where the equator-pole temperature difference in equilibrium is about 12 K. From a modeling perspective, using a smaller $\Delta_y T$ (we have tested 10 K) results in weaker baroclinic eddy activity as the criticality $\xi \sim \Delta_y T/\Delta_z \theta$ becomes small, although strong jets can form with quite weak baroclinicity (Kaspi and Flierl, 2007). Reducing vertical stability $\Delta_z \theta$ can maintain the same criticality and thus keep strong eddy activity even for smaller $\Delta_y T$. However, smaller vertical stability leads to smaller Rossby radius and therefore requires higher resolution.

We consider five different values of bottom friction: $\tau_f = 5$, 50, 500, and 5000 days. The simulations are integrated for 20,000 days at T213 resolution. There are 30 unevenly spaced σ levels, chosen such that there are equal number of levels in the stratosphere and troposphere. All simulations are initialized from an isothermal motionless atmosphere with small thermal perturbations, except for the $\tau_f = 5000$ day run, which is initialized from the end of the $\tau_f = 50$ day run and yields better hemispheric symmetry (the low friction simulations are dependent on initial condition due to jet merging during model spin-up).

5.3 Results

Although our motivation arises, at least in part, from Jupiter's atmosphere, most of our conclusions are universal for a dry baroclinic atmosphere and apply in both

Jovian and Earth-like regimes. The Earth-like simulations are more efficient to run and diagnose, and we will thus mostly show results from the Earth-like simulations, and resort to Jupiter-like simulations when they provide additional insights. If not specified, the simulations refer to the Earth-like simulations.

a. Basic climatology

To see whether the atmosphere has equilibrated, we calculate the time evolution of the global averaged kinetic energy (KE) and eddy kinetic energy (EKE) per unit mass (with unit m^2s^{-2}), as shown in Fig. 5.1. For simulations with $\tau_f = 1$ to 10^3 days, the flow equilibrates after a few hundred to a few thousand days. For the $\tau_f = 10^4$ days run, the flow is initially close to a zonally symmetric state as the EKE is negligible. Until at about 23,000 days, the flow abruptly transits into an eddying state and then equilibrates with large fluctuations. For $\tau_f = 10^3$ and 10^4 days runs, there is long term variability on the time scale of hundreds to thousands of days, but on an even longer time scale, the flow appears to be equilibrated. The long term variability for low friction runs is also seen in James and Gray's (1986) simulations. In their lowest friction simulation, the flow is nearly zonally symmetric similar to our run with $\tau_f = 10^4$ days in the first 10,000 days. However, they did not observe the regime transition into a strongly eddying state possibly because their simulations are limited to 500 days. When the bottom friction is reduced from $\tau_f = 1$ to 10^4 days, the average KE increases monotonically. However, the average EKE is not monotonic with friction. Instead, the average EKE decreases when friction is reduced from $\tau_f = 1$ to 10^2 days and then increases when friction is further reduced.

Fig. 5.2 shows the climatology for the series of runs with different surface friction. The control run with $\tau_f = 1$ day is comparable to Earth's climate. When friction is reduced, the jets become stronger and sharper, and become dominated by their barotropic components. Near the surface, the eddy potential temperature (PT) flux

moves equatorward from the midlatitudes. Comparison to the Jupiter-like simulations shown in Fig. 5.3 suggests that more generally the eddy PT flux moves from the westerly jet regions into the easterly jet regions when surface friction is reduced. This may be understood from the fact that a sharp westerly jet is known to suppress mixing across it (Dritschel and McIntyre, 2008). In Earth's atmosphere, the jet-stream near the tropopause forms a north-south mixing barrier (Mahlman, 1997). In our simulations when surface friction is low enough, the jet-stream extends all the way to the surface, thus suppressing mixing even near the surface. Therefore, the baroclinic eddy activity moves into the easterly jets in the presence of sharp barotropic westerly jets. Notice that when friction is small, there is significant latitudinal surface pressure variation, which is required to support strong barotropic jets. This causes some missing contours near 1000 mb in Fig. 5.2 and near 3000 mb in Fig. 5.3, as there is no flow field at the given pressure level and latitude. In Fig. 5.3, the lack of super-rotation at the equator in our Jupiter-like simulations compared with Schneider and Liu (2009) might be due to the lack of internal heating and therefore a lack of strong convective instability at the equator. We specifically want to suppress this energy source in order to focus on baroclinic turbulence only.

To get an impression on the characteristics of the flow, snapshots of instantaneous fields are shown in Figs. 5.4 and 5.5. Ertel's potential vorticity (PV) on isentropic surface $\theta = 330$ K, calculated as

$$PV = -g(\zeta + f)\frac{\partial \theta}{\partial p}, \tag{5.8}$$

is shown in Fig. 5.4 for Earth-like simulations with high (τ_f =1 day) and low ($\tau_f = 10^3$ and 10^4 days) surface friction (Haynes and McIntyre, 1987). For all simulations, Ertel's PV has a sharp gradient across the jet stream. In the simulation with τ_f= 1 day, the jet meanders strongly and filaments indicate wave-breaking and mixing

of PV. In $\tau = 10^3$ and 10^4 days simulations, the jet stream is more regular and is visually similar to the stratospheric vortex. Wave breaking is hardly seen. For the Jupiter-like simulations, zonal wind fields in the extratropics are shown in Fig. 5.5. When friction is reduced from $\tau_f = 5$ days to 5000 days, the outer jet seems to get stabilized while eddy activity is confined to latitudes above 45°.

b. Energy cycle

The energy cycle is key to understanding how the model equilibrates close to the limit of vanishing bottom friction. As a reference, the observed Lorenz energy cycle for Earth's atmosphere is shown in Fig. 5.6a (adapted from Peixto and Oort, 1984). In Lorentz's (1955) formalism, the energy is partitioned into available potential energy (APE) and kinetic energy (KE). Furthermore, APE and KE are partitioned into the zonal mean and eddy parts. Differential heating by solar radiation leads to a zonally symmetric temperature distribution with strong meridional temperature gradient at mid-latitudes, thus maintaining the APE of the zonal mean flow (ZAPE). The temperature field is stirred by the eddies which create temperature variance in the zonal direction and thus transferring ZAPE into eddy APE (EAPE, at a rate 1.27 W m^{-2}). Through baroclinic instability, EAPE is next converted into EKE (2.0 W m^{-2}). Some of the EKE is channeled into the zonal mean KE (ZKE) as the eddy momentum flux is up gradient of zonal mean angular velocity and thus accelerates the zonal jets (0.33 W m^{-2}). A majority of EKE is directly dissipated by bottom friction or molecular viscosity (1.7 W m^{-2}). Finally, some of the ZKE is dissipated by bottom friction or viscosity (0.2 W m^{-2}), while a comparable amount is converted into ZAPE (0.15 W m^{-2}). The latter conversion is achieved by the combined effect of the direct and indirect mean meridional circulations: the Hadley cell (direct circulation) generates ZKE, however, the Ferrel cell (indirect circulation) converts ZKE back into ZAPE at

a rate exceeding the production rate of the Hadley cell. Therefore, the net conversion is from ZKE into ZAPE[2].

Here we focus on the three energy reservoirs potential energy PE, EKE and ZKE, and we do not explicitly consider the budgets for ZAPE and EAPE since they may not be well defined if the isentropic slope becomes large, as is the case in our simulations with weak friction. In this perspective, the energy cycle for the Earth-like simulation with the largest bottom friction $\tau_f = 1$ day is shown in Fig. 5.6b and is comparable to the observed energy cycle described above. For our Earth-like simulations with different strength of friction, the energy budgets for EKE, ZKE and KE are shown in Fig. 5.7. The balance equations for EKE and ZKE are

$$\frac{\partial \mathrm{EKE}}{\partial t} = C(\mathrm{PE}, \mathrm{EKE}) - C(\mathrm{EKE}, \mathrm{ZKE}) - D(\mathrm{EKE}), \tag{5.9}$$

$$\frac{\partial \mathrm{ZKE}}{\partial t} = C(\mathrm{EKE}, \mathrm{ZKE}) - C(\mathrm{ZKE}, \mathrm{PE}) - D(\mathrm{ZKE}), \tag{5.10}$$

where EKE is dissipated by both bottom friction and hyperviscosity as

$$D(\mathrm{EKE}) = D_{fri}(\mathrm{EKE}) + D_{vis}(\mathrm{EKE}), \tag{5.11}$$

while the hyperviscosity for ZKE is negligible, and therefore

$$D(\mathrm{ZKE}) \simeq D_{fri}(\mathrm{ZKE}). \tag{5.12}$$

Adding together Eqs. (5.9) and (5.10) gives the energy budget for the total flow as

$$\frac{\partial \mathrm{KE}}{\partial t} = C(\mathrm{PE}, \mathrm{KE}) - D_{fri}(\mathrm{KE}) - D_{vis}(\mathrm{KE}). \tag{5.13}$$

[2]An updated Lorenz energy cycle calculation by Li et al. (2007) using reanalysis datasets shows that near surface processes in the Southern hemisphere play an important role in converting ZAPE into ZKE, and probably change the direction of net conversion rate between ZAPE and ZKE as shown by Peixto and Oort (1984). However, away from the surface, Li et. al. (2007) still supports Peixoto and Oort's (1984) results that the indirect Ferrel cell converts more ZKE into ZAPE than the ZKE produced by the direct Hadley cell, and the net conversion is thus from ZKE to ZAPE.

The detailed formulations for each term are included in Appendix A. In a statistical steady state, the left hand sides of Eqs. (5.9), (5.10) and (5.13) averaged over time are zero.

We first consider the EKE budget. For the control run ($\tau_f = 1$ day), the EKE generation rate $C(\mathrm{PE}, \mathrm{EKE})$ is similar to that observed in Earth's atmosphere. However, contrary to Earth's atmosphere, EKE conversion into ZKE $C(\mathrm{EKE}, \mathrm{ZKE})$ is slightly larger than dissipation rate $D(\mathrm{EKE})$. This may be due to the fact that our model only simulates large-scale quasi- two-dimensional motions and does not resolve convection and three dimensional turbulence which can dissipate energy by molecular viscosity. EKE is dissipated mainly by bottom friction, whose dissipation rate is roughly 1 order of magnitude larger than that of hyperviscosity. When bottom friction decreases from $\tau_f = 1$ to 10^3 days, the EKE generation rate $C(\mathrm{PE}, \mathrm{EKE})$ decreases monotonically by roughly 1 order of magnitude. This resembles the barotropic governor effect, that strong barotropic jets limit the growth of baroclinic instability. When bottom friction further decreases to $\tau_f = 10^4$ days, the barotropic governor effect appears to saturate, and the EKE generation rate increases slightly. The barotropic governor thus does not appear to be able to totally suppress baroclinic instability. For the whole range of decreasing bottom friction, EKE dissipation by bottom friction decreases monotonically by roughly 3 orders of magnitude. Dissipation by hyperviscosity decreases less than 1 order of magnitude, but is never a dominant term in the EKE budget. In the low friction end, the dominant balance for the EKE budget is between EKE generation $C(\mathrm{PE}, \mathrm{EKE})$ and EKE conversion into ZKE $C(\mathrm{EKE}, \mathrm{ZKE})$.

Next we will consider the ZKE budget. For the control run ($\tau_f = 1$ day), conversion from EKE into ZKE $C(\mathrm{EKE}, \mathrm{ZKE})$ is balanced by frictional dissipation $D_{fri}(\mathrm{ZKE})$ and conversion into PE $C(\mathrm{ZKE}, \mathrm{PE})$, which are of similar magnitudes. For τ_f between 10 and 10^2 days, all conversion terms decrease with decreasing friction. When bottom friction further decreases ($\tau_f = 10^3$ and 10^4 days), $C(\mathrm{ZKE}, \mathrm{PE})$

saturates, while $D_{fri}(\mathrm{ZKE})$ continues to decrease. In the low friction limit ($\tau_f = 10^4$ days), $D_{fri}(\mathrm{ZKE})$ is negligible compared with $C(\mathrm{ZKE}, \mathrm{PE})$, and the primary balance is between $C(\mathrm{EKE}, \mathrm{ZKE})$ and $C(\mathrm{ZKE}, \mathrm{PE})$. As the energy dissipation by bottom friction is negligible for our lowest friction run ($\tau_f = 10^4$ days), and the effect of hyperviscosity does not strongly influence the large scale motions, the simulation with $\tau_f = 10^4$ days may be regarded as effectively approaching the limit of vanishing bottom friction. In this limit, schematically the dominant energy cycle proceeds from PE and ends at PE:

$$\mathrm{PE} \rightarrow \mathrm{EKE} \rightarrow \mathrm{ZKE} \rightarrow \mathrm{PE}. \tag{5.14}$$

This energy cycle is illustrated in Fig. 5.6c. From the structure of PT flux shown in Fig. 5.2 and 5.3, we can see that baroclinicity is reduced within the easterly jets. As the net PE conversion into KE is negligible from the above energy cycle, a reduction of baroclinicity in the easterly jets must be balanced by an increase of baroclinicity in the westerly jets, which is achieved by the Ferrel cell. In other words, the effect of eddies and the zonal mean circulation is primarily to redistribute baroclinicity into a latitudinal structure different from that set by differential radiation: the baroclinicity is reduced in the easterly jets and enhanced in the westerly jets. The effect of eddies to enhance the baroclinicity of westerly jets has been seen in the wintertime Earth atmosphere and in numerical models, and is usually referred as self-maintenance of midlatitude jets (Robinson, 2006). The mechanism for the self-maintenance of midlatitude jets is shown to be a complicated feedback between waves and the mean flow, but in our low drag simulation, it is required by the structure of PT flux and, most fundamentally, by the energy cycle.

The mean meridional circulation that facilitates the conversion of ZKE into PE is shown in Fig. 5.8, for simulations with different strength of friction. Here the circulation is averaged over the last 10^4 days of the simulations, and the circulation's structure is quite robust even if a much shorter averaging period is used. When friction

reduces from τ_f =1 to 10^4 days, the meridional circulation develops a complex vertical structure. Still, we can identify a Hadley cell and a Ferrel cell in each hemisphere. The strength of the circulation decreases by roughly about 2 times, which is on the same order as the nearly 3 times decrease in the conversion of ZKE to PE.

For the total flow, the energy budget has a simpler picture as the recycling of kinetic energy at the largest scales are hidden away (Fig. 5.7 bottom). The the total conversion of PE to KE (which has to approximately equal the generation of PE by the restoring) is balanced by the sum of frictional and viscous dissipation. Dissipation by bottom friction dominates the total energy sink for moderate drag rates, while viscous dissipation starts to dominate the total energy sink in the limit of very small bottom friction. However, this does not mean that the viscous dissipation must have a stronger influence on the synoptic-scale flow as will be discussed in Subsection d. The generation and dissipation rates for total kinetic energy decrease monotonically as friction is reduced. Moreover, in the limit of small friction, the total energy generation and dissipation rates are much smaller than the conversion rates in the ZKE and EKE budgets – indicating the dominant role of energy "recycling".

A more detailed picture of the energy cycle is provided by the spectral kinetic energy budget. For a compressible fluid, the spectral budget is usually formulated in pressure coordinates in which the KE is a quadratic function of velocity $1/(2g)\int \mathbf{u}^2 dp$ so that KE can be exactly decomposed into each wave vector as $\mathrm{KE}(\mathbf{n}) = 1/(2g)\int \tilde{\mathbf{u}}(\mathbf{n})\cdot\tilde{\mathbf{u}}^*(\mathbf{n})dp$, where $\tilde{\mathbf{u}}(\mathbf{n})$ denotes the spectral coefficient of velocity at wave vector $\mathbf{n}$, and $*$ denotes the complex conjugate (Lambert, 1984; Koshyk and Hamilton, 2001). In general, the KE is a cubic quantity $1/2\int \rho\mathbf{u}^2 dV$ and thus in other vertical coordinates the KE spectrum is a complicated sum over triads of wave vectors. In this case, density is usually approximated as a constant in order to make KE a quadratic quantity (Waite and Snyder, 2009). For Earth's atmosphere, the pressure coordinate is convenient because a constant 1 bar pressure

level is approximately the planetary surface. However in our simulations with low bottom friction, there is large surface pressure variation in the meridional direction in order to support the very strong jets (see Fig. 5.2, the surface pressure at the poles is significantly lower than 1 bar). Therefore, the usual formalism for the spectral energy budget is not suitable for our purpose, and we derive a new formalism in σ coordinates that gives the approximate spectral KE budget (see Appendix B). For each wavenumber, we can write the spectral KE budget as

$$\partial_t \mathrm{KE}_n \approx G_{KE} + T_{NL} - D_{fri} - D_{vis}, \tag{5.15}$$

where KE_n denotes the vertically and surface area averaged global KE at total wavenumber n (with unit $\mathrm{m}^2\ \mathrm{s}^{-2}$); G_{KE} denotes the conversion from potential to kinetic energy; T_{NL} denotes nonlinear kinetic energy transfer from all other wavenumbers into wavenumber n; D_{fri} and D_{vis} denote dissipation by Rayleigh friction and by hyperviscosity respectively.

Similarly, for each wavenumber, the spectral EKE budget is

$$\partial_t \mathrm{EKE}_n \approx G_{EKE} + T_{EE} + T_{EM} - D_{fri} - D_{vis}. \tag{5.16}$$

Compared with the spectral KE budget, the main difference is that the nonlinear kinetic energy transfer term T_{NL} is further decomposed into T_{EE}, which denotes nonlinear eddy-eddy transfer, and T_{EM}, which denotes the eddy/mean-flow transfer. The difference between KE_n and EKE_n is that EKE_n does not include the spectral components with zonal wavenumber $m = 0$. In a statistically steady state, the left hand sides of Eqs. (5.15) and (5.16) averaged over time are zero, which means a balance between the various energy generation, transfer and dissipation terms.

The spectral EKE budget for Earth-like simulations with different bottom frictions are shown in the left panel of Fig. 5.9. The control run ($\tau_f = 1$ day) resembles

Earth's atmosphere: EKE generation peaks at about wavenumber 10; nonlinear eddy-eddy interactions transfer some energy upscale; most energy is transferred into the zonal mean flow or dissipated by bottom friction at scales slightly larger than the EKE generation scale. When friction is reduced to $\tau_f = 10^2$ days, the eddy-eddy interaction and dissipation by bottom friction become negligible, while eddy/mean-flow interactions directly transfer almost all the kinetic energy generated by baroclinic instability into the zonal mean flow at the scale where it is generated. This may be due to the sharpening of the jets, which shear the eddies apart and thus facilitate the energy transfer from eddies into zonal mean flow. When friction further reduces to $\tau_f = 10^4$ days, the spectral budget becomes more jagged. Nevertheless, the eddies are still generating EKE, which is subsequently transferred into the zonal mean flow.

The full spectral KE budget includes the contributions from the zonal mean flow (right panel of Fig. 5.7). For the control run ($\tau_f = 1$ day), bottom friction dissipates energy across broad scales (wavenumber 3 to 15). KE is generated at wavenumber larger than 4, while KE generation becomes negative at wavenumber 3, which means that KE is converted into PE. As the eddies are generating EKE across all scales as seen from the left panel, the conversion of KE into PE is achieved by the zonal mean flow. Wavenumber 3 corresponds to the zonal jet structure consisting of one easterly jet at the equator and one westerly jet in each hemisphere. Therefore, the conversion of KE back to PE at wavenumber 3 corresponds to the net effect of the Hadley and Ferrel cells as discussed before. When friction is reduced to $\tau_f = 10^2$ days, KE is dissipated by bottom friction almost exclusively in zonal jets with wavenumber 3, where the energy balance is nearly between the up-scale nonlinear transfer and frictional dissipation. Combined with the spectral EKE budget, it means that in physical space, the eddies are generating EKE and transferring EKE into the zonal jets, while bottom friction removes KE only from the zonal jets. When friction further reduces to $\tau_f = 10^4$ days, energy dissipation by bottom friction becomes negligible even

for the zonal jets. At wavenumber 3, the major balance is between upscale nonlinear energy transfer and conversion from KE into PE. Combined with the spectral EKE budget, we conclude that in the limit of negligible friction, the energy cycle starts from EKE generation by the eddies, followed by an EKE transfer into the largest zonal jets, and the energy cycle is closed by a conversion of ZKE back into PE by the zonal mean flow.

The spectral EKE budget of the Jupiter-like simulations shows some additional information. As the planetary size is much larger than the deformation radius, there is a clear scale separation between the EKE generating scale and the EKE dissipation scale (or eddy scale), and significant upscale energy transfer by eddy-eddy interactions between the two scales (Fig. 5.10 top). When friction reduces from $\tau_f = 5$ to 5000 days, the eddy-eddy energy cascade extends to larger scales. The eddy-mean energy transfer becomes positive at the largest scales, which may be a result of barotropic instability associated with the jets and we will return to this below in the discussion of momentum budget. Most importantly, the EKE generation becomes negative at the largest scales, meaning a conversion of EKE into PE. Therefore, the conversion from KE to PE does not have to occur within the zonal mean circulation, but can also occur within the largest eddies. For both Earth-like and Jupiter-like simulations, we do not see a significant change of downscale energy transfer when friction reduces towards zero.

In a shallow water model, the key for KE to convert back into PE is that the horizontal scale of the flow gets larger than the Rossby deformation radius $\sqrt{gH}/f$, where H is the mean layer depth (Scott and Dritschel, 2013; Polvani et al., 1994). We suspect that there is also a threshold in the primitive equation model, beyond which the flow can convert KE into PE. In the Earth-like simulations, the domain size is rather limited so that only the scale of the zonal mean flow may be large enough to convert ZKE into PE. Whereas in the Jupiter-like simulations, the much larger

domain size permits large enough eddies, which are able to directly convert EKE into PE. Alternatively, the wavy jets in Jupiter-like simulations may project onto the eddy component, without necessarily implying fundamentally different dynamics. This may explain why only in Jupiter-like simulations we observe the conversion of EKE into PE.

To summarize, close to the vanishing friction limit, at small scales eddies convert PE to EKE similar as in Earth's atmosphere. EKE inversely cascades to larger scales and eventually gets channeled into the zonal jets. At the largest scales, the zonal flow and possibly the eddies together convert KE back into PE, thus closing the energy cycle.

c. Momentum budget

In Earth's atmosphere, the Ferrel cell transfers the eddy momentum flux convergence from the upper atmosphere down to the surface where it is balanced by friction (Vallis, 2006). In the limit where the surface friction becomes negligible, there is still a Ferrel cell (Fig. 5.8), whose existence is important for closing the energy cycle. To examine how the momentum is balanced in the vanishing friction limit, we start by reviewing the momentum budget for Earth's atmosphere.

The zonally averaged zonal momentum equation is

$$\frac{\partial \bar{u}}{\partial t} = \bar{v}\left(f - \frac{\partial \bar{u}\cos\phi}{a\cos\phi\partial\phi}\right) - \bar{\omega}\frac{\partial \bar{u}}{\partial p} - \frac{1}{a\cos^2\phi}\frac{\partial \overline{u'v'}\cos^2\phi}{\partial\phi} - \frac{\partial \overline{u'\omega'}}{\partial p} - \bar{F}_x, \qquad (5.17)$$

where a is the planetary radius, $\omega = dp/dt$, ϕ is the latitude, and F_x describes the frictional processes. The overbar denotes a zonal average. In the extratropics, where the Rossby number is small, the time averaged momentum balance for a statistically

steady flow is approximately

$$f[\bar{v}] - \frac{1}{a\cos^2\phi}\frac{\partial[\overline{u'v'}]\cos^2\phi}{\partial\phi} - [\bar{F}_x] \approx 0, \tag{5.18}$$

where the brackets denote a time average (Vallis, 2006). In the upper atmosphere, friction is negligible while the eddy momentum flux attains its maximum. Therefore, the balance is between the Coriolis term and eddy momentum flux convergence as

$$f[\bar{v}] \approx \frac{1}{a\cos^2\phi}\frac{\partial[\overline{u'v'}]\cos^2\phi}{\partial\phi}. \tag{5.19}$$

By mass continuity, a return flow is necessary in the lower atmosphere, and for Earth's atmosphere it occurs within the planetary boundary layer, where friction becomes significant while the wind velocity is relatively small. The dominant momentum balance is thus between the Coriolis term of the return flow and friction as

$$f[\bar{v}] \approx [\bar{F}_x]. \tag{5.20}$$

Integrating Eq. (5.18) vertically from the top of the atmosphere to the bottom boundary, the Coriolis term vanishes due to mass continuity, and the vertically integrated eddy momentum flux convergence is balanced by the vertically integrated friction as

$$-\frac{1}{a\cos^2\phi}\frac{\partial}{\partial\phi}\int_0^{p_s}[\overline{u'v'}]\cos^2\phi dp \approx \int_0^{p_s}[\bar{F}_x]dp, \tag{5.21}$$

where p_s denotes surface pressure. It is clear from (5.21) that the role of the Ferrel cell is to transfer the momentum forcing between the upper and lower atmosphere while it does not change the vertically integrated zonal momentum budget.

In the limit of vanishing friction, Eq. (5.20) no longer holds while the Ferrel cell still exists. So how can the Coriolis term of the return flow be balanced? Within

the small Rossby number regime where Eq. (5.18) holds, the Coriolis term of the return flow in the lower atmosphere must be balanced by the eddy momentum flux convergence similar to the upper atmosphere but with the opposite sign. From Earth-like and Jupiter-like simulations shown in Fig. 5.11 and 5.12, we can see that this is indeed the case. In the upper atmosphere, eddies converge momentum into the westerly jets as in Earth's atmosphere. However, in the lower atmosphere, eddies diverge momentum out of the westerly jets when bottom friction is low enough. For the Earth-like simulation with the smallest bottom friction, the eddy momentum flux develops a somewhat more complicated vertical structure, with multiple sign reversals–consistent with the more complicated structure of the zonal-mean overturning circulation in Fig. 5.8. Nevertheless, the general picture of momentum flux into the westerly jet in the upper atmosphere and out of the jet near the surface remains.

It is natural to ask whether the unusual vertical structure of the momentum flux is a result of vertically coherent eddies or separate eddies in the upper and lower atmosphere. A useful tool to characterize the disturbances is the cospectra diagnostic developed by Hayashi (1973, 1982), Randel and Held (1991), and Wheeler and Kiladis (1999). We diagnosed eddy momentum flux cospectra as a function of latitude for the Earth-like simulations with $\tau_f = 1$ and $\tau_f = 10^3$ days. The upper-troposphere cospectrum for the Earth-like control run ($\tau_f = 1$ day) shows the familiar feature of Earth's atmosphere–that the eddy momentum flux is almost confined within the critical latitude $\bar{u} = c$ (Fig. 5.13 top). For the simulation with $\tau_f = 10^3$ days, the eddy momentum flux peaks at a phase speed of about -20 m/s, both for the upper and lower atmospheres (Fig. 5.13 middle and bottom). The similar phase speeds indicate that the waves are vertically coherent in the upper and lower atmosphere rather than two separate waves. A big difference compared to the control run ($\tau_f = 1$ day) is that the waves are propagating westwards instead of eastwards. As a result, the waves do not have a critical latitude in the upper atmosphere. Therefore, wave breaking is

strongly suppressed compared with the control run, which leads to a reduction of eddy diffusivity and thus a reduction of heat flux (Nakamura, 2004). As EKE generation rate is proportional to heat flux, a suppression of wave breaking may also explain why EKE generation is much smaller in the low friction runs. The reason for waves to propagate westwards is that the waves have a very long wavelength. The eddy momentum flux almost exclusively results from a zonal wavenumber 3 wave, which is evidently the dominant wavenumber seen from the snapshot of Ertel's potential vorticity (Fig. 5.4). In the lower atmosphere momentum fluxes peak at the critical level, and are directed from the westerly into the easterly jet (down-gradient). The momentum fluxes in the lower atmosphere thus resemble characteristics of barotropic instability–although the time- and zonal-mean flow does not show a reversal of the absolute vorticity gradient (not shown).

In the Jupiter-like simulations, the waves that contribute to opposite momentum fluxes in the upper and lower atmosphere seem to be somewhat less coherent in the vertical. Fig. 5.14 shows that waves in the lower atmosphere seem to move faster towards the west than those in the upper atmosphere for $\tau_f = 5000$ days simulation. Moreover the momentum fluxes are not as clearly dominated by a single wave with a well defined phase speed. Although the waves move westward, they still encounter a critical latitude in the upper troposphere. In the lower atmosphere, momentum fluxes again peak near the critical latitudes and are directed from the westerly into the easterly regions–resembling properties of barotropic instability. Down-gradient momentum fluxes are consistent with the spectral EKE budget in Fig. 5.10, which shows a conversion from ZKE to EKE at large scales. Primary mode analysis similar as above shows that vertically coherent waves also have opposite momentum fluxes in the upper and lower atmosphere, however, they only contribute to part of the momentum fluxes in the lower atmosphere.

The exact mechanism that leads to the reversed momentum fluxes in the lower atmosphere remains unclear, and may differ between the Earth-like and Jupiter-like simulations. However, two robust properties emerge: 1) lower-atmospheric poleward heat fluxes shift into the easterly jet regions (Figs. 5.2 and 5.3), and 2) lower-atmospheric momentum fluxes are down-gradient and peak near the critical latitudes (Figs. 5.13 and 5.14). Together, these observations suggest that wave generation in the lower atmosphere shifts into the easterly jet regions, and is possibly caused by a mixed baroclinic-barotropic instability. An analysis of Ertel's PV (not shown), reveals no clear reversals of the PV gradient along isentropes within the atmosphere, though the analysis is complicated by the large variations in surface pressure, and we note that flow characteristics may be impacted significantly by non-QG effects. In either case, the processes that govern momentum flux and mixing in the limit of very low bottom friction demand further investigation, which may profit from more idealized simulations.

d. Dynamical convergence with respect to hyperviscosity and bottom friction

In our low friction limit, although most of EKE generation is "recycled", a small remainder is balanced by the hyperviscosity. Hyperviscosity itself is often regarded as a numerical device to prevent energy or enstrophy from building up at grid scales and it does not directly represent any physical processes. However, all real fluids have a viscosity that removes energy or enstrophy, according to the situation, and it is common in numerical models to use hyperviscosity instead of a true viscosity because it achieves a greater scale-selectivity. In turbulent flows, the energy dissipation (or enstrophy dissipation in quasi-two-dimensional flow) becomes independent of the viscosity if the viscosity is small enough. Analogously, in our simulations we expect that the dynamics of the energy containing scales, and the dissipation itself,

should ideally become independent of the hyperviscosity if the latter is small enough. However, this does not mean that the hyperviscous dissipation itself need be small, and in the limit of small bottom friction it can be expected to dominate over the dissipation due to bottom friction.

To explore these expectations, Earth-like simulations with T127 resolution are carried out for all values of τ_f from 1 to 10^4 days, and at T213 resolution, with a lower hyperviscosity, for τ_f equal to 10^3 days. By varying τ_f we explore the convergence with respect to bottom friction, and by varying the resolution we explore convergence with respect to hyperviscosity (and resolution). In any given simulation we keep the damping time scale for the smallest waves the same as resolution varies, so that hyperviscosity decreases by a factor of about 3^8 in the T127 simulations relative to the T42 simulations, with a larger factor still in the T213 simulations. Generally speaking, T127 simulations have similar energy budgets (Fig. 5.15) and momentum budgets (Fig. 5.16) as the T42 simulations when friction is reduced towards zero, which confirms at least that the energy recycling and momentum reversal are robust mechanisms that enable the flow to equilibrate in the low friction limit.

Now consider convergence with respect to hyperviscosity. There are in fact some small differences at the lowest values of bottom drag, as is apparent by comparing Figs. 5.11 and 5.16. For $\tau_f = 1$ day, the jet strength and momentum fluxes are very similar between T42 and T127 runs, but for τ_f =10^3 days and 10^4 days , the jets and momentum fluxes are a little stronger in T127 runs. This is seen more clearly from the KE and EKE spectra of different resolution runs with $\tau_f = 1$ day (Fig. 5.17) and $\tau_f = 10^3$ days (Fig. 5.18). However, the basic picture of energy recycling remains largely the same (Figs. 5.7 and 5.15). At still higher resolution, T213, the simulation with τ_f =10^3 days also shows very similar KE and EKE spectra to the T127 run for wavenumbers smaller than 60 (Fig. 5.18), which suggests that the synoptic-scale flow essentially converges when the resolution is beyond T127.

As regards convergence with respect to bottom friction, lowering the bottom drag from $\tau_f = 10^3$ days to $\tau_f = 10^4$ days produces only a small change in the energy spectrum at T127 (Fig. 5.20). The total total energy budget in Fig. 5.15 shows an increasing energy dissipation rate by hyperviscosity at $\tau_f = 10^3$ days and $\tau_f = 10^4$ days. The spectral energy budget (Fig. 5.21) reveals that this increasing dissipation primarily balances increasing generation of EKE near the grid scale, which appears to be associated with grid-scale convection (compare also Schneider and Liu, 2009; Liu and Schneider, 2010, 2011, 2015). As EKE generated by grid-scale convection does not cascade to larger scales, the effect of this grid-scale convection on the synoptic-scale flow is likely to be small. Comparing the spectral kinetic energy budget for $\tau_f = 10^3$ and $\tau_f = 10^4$ (Fig. 5.21) also reveals some changes at larger scales, suggesting that true convergence has not been reached, but the main features remain robust. These results suggest that the two cases with smallest drag are indeed in a low bottom-friction regime and that further reducing the drag would likely only have a quantitative effect. Although we cannot claim to have achieved true convergence with respect to either bottom drag or hyperviscosity, the evidence of our simulations suggests that further reducing the drag, or the hyperviscosity, would affect the energy budget only in relatively minor ways.

5.4 Discussions and Conclusions

In this paper, we have explored the possibility of a baroclinic atmosphere to equilibrate close to the limit of vanishing bottom friction. By reducing bottom friction to extremely low values in a primitive equation model, we found that the baroclinic turbulence can adjust its energy and momentum budgets in order to equilibrate.

- *Energy budget.* Near the Rossby deformation radius, the eddies convert potential energy to eddy kinetic energy similar to Earth's atmosphere. Eddy kinetic

energy inversely cascades to larger scales or gets channeled into zonal jets. At the largest scales, kinetic energy is converted back into potential energy, thus closing the kinetic energy cycle without requiring significant dissipation. The total kinetic energy generation for the whole flow is strongly reduced, and thus can be balanced by hyperviscosity dissipation.

- *Momentum budget.* The vertically integrated eddy momentum flux convergence is close to zero as there is no bottom friction to balance it. In the upper atmosphere, eddies converge momentum into the westerly jets similar to Earth's atmosphere. However, in the lower atmosphere, the momentum flux reverses sign and diverges momentum *out* of the westerly jets. A Ferrel cell like circulation balances the zonal flow acceleration/deceleration by the momentum flux convergence/divergence, and thus at the same time converts kinetic energy into potential energy.

The entropy budget in Appendix C shows a consistent picture with the total kinetic energy budget, and it confirms that the energy "recycling" mechanism does not violate the third law of thermodynamics. Close to the vanishing friction limit, radiative forcing acts as the entropy sink, similar to but much smaller than in Earth's atmosphere, and the major entropy source is hyperviscosity. In addition, it confirms that hyperdiffusion on the temperature field is not important in dissipating entropy, and thus potential energy (Lapeyre and Held, 2003).

The above budgets are robust in a dry primitive equation model with different planetary parameters and different resolutions. The fact that eddy kinetic energy generated by baroclinic instability can be converted back into potential energy at the largest scales takes away the burden from the friction to dissipate kinetic energy, and thus a significant energy cycle with finite zonal wind can be maintained even when the friction is extremely small. Further reducing surface friction or hyperviscosity seems to only affect the energy budget in relatively minor ways. Therefore, we

believe that a baroclinic atmosphere described by the dry primitive equation model could equilibrate with finite velocity close to the limit of vanishing friction. Indeed, simulations without bottom friction do equilibrate, though we have not studied their dynamical convergence with resolution in detail. Also, these simulations inevitably depend on the initial conditions. For the Jupiter-like simulation we even saw a dependence on the initial conditions at finite, but very low, friction (τ_f=5000 days). The kinetic energy generation is very large when the model spins up and multiple jets form quickly. Once jets form, the kinetic energy generation rate becomes smaller and the flow becomes less turbulent. However, at model spin-up, the jets are less stable and can merge randomly. Due to the chaotic jet merging, the model can equilibrate in a non- hemispherically-symmetric state with a different number of jets in the Northern and Southern hemispheres. However, if we initialize the run from the end of the $\tau_f = 50$ days run, where the kinetic energy generation rate is already small and jets are already stable, the flow equilibrates in a hemispherically-symmetric state, which is used in this paper.

Returning to the hypotheses we proposed in the introduction, our results suggest a mixture of hypothesis 2 and 3 to be in effect. When friction reduces, we first get a strong reduction of EKE generation (in agreement with hypothesis 2) but then EKE generation plateaus and we get energy "recycling" (more consistent with hypothesis 3). Although small-scale disturbances become more energetic and more ageostrophic effects may come into play at smallest scales, dissipation by hyperviscosity is never dominant in the EKE budget, and we do not see a significant increase in downscale energy transfer. Therefore, hypothesis 1 is less favored.

The limit of vanishing bottom friction may be relevant for atmospheres where the frictional time scale is much much larger than the radiative forcing time scale, perhaps the Jovian atmosphere. Indirect evidence that may relate them is the kinetic energy spectrum, shown in Fig. 5.22. The zonal kinetic energy spectrum seems to

have a range with approximately -5 slope for either large ($\tau_f = 5$ days) or very small ($\tau_f = 5000$ days) friction, and the eddy kinetic energy spectrum has a slope slightly steeper than -5/3. At large friction, the zonal jets and eddies have similar scales and energy levels. However, when friction is very small, the zonal flow extends to larger scales than the eddies, and it contains much more energy than the eddies. Therefore, the total flow is dominated by the strong and slowly evolving zonal jets on the largest scale and the spectrum seems to follow a k^{-5} slope within wavenumbers 20 to 50, consistent with the zonostrophic turbulence regime (Sukoriansky et al., 2002; Galperin et al., 2006, 2014). At small scales, on the other hand, the spectrum is dominated by isotropic turbulence with a spectral slope near $k^{-5/3}$. These features resemble Jupiter's magnificent jets.

Appendix A: Lorenz Energy Cycle Formulation

The Lorenz energy cycle used in our calculations mostly follows the original formulation of Lorenz (1955) and Peixto and Oort (1984). The EKE and ZKE are defined as energy per unit surface area written as

$$\text{EKE} = \frac{1}{2}\int \mathbf{u}'^2 dm, \tag{5.22}$$

$$\text{ZKE} = \frac{1}{2}\int \overline{\mathbf{u}}^2 dm, \tag{5.23}$$

where $\mathbf{u}$ is the horizontal velocity vector. $\overline{A}$ and A' denote the zonal average of A and deviations from the zonal average, respectively. $\int dm$ denotes a mass-weighted global integral:

$$\int dm = \frac{1}{4\pi g}\int_0^{2\pi} d\lambda \int_0^{\pi} \cos\phi d\phi \int_0^{p_0} dp. \tag{5.24}$$

Therefore, the unit for EKE and ZKE is J m^{-2}. The energy conversion between potential and kinetic energy is evaluated as

$$C(\mathrm{PE}, \mathrm{EKE}) = -R \int p^{-1} \omega' T' dm, \tag{5.25}$$

and

$$C(\mathrm{PE}, \mathrm{ZKE}) = -R \int p^{-1} \overline{\omega}\,\overline{T} dm, \tag{5.26}$$

where R is the gas constant, $\omega = dp/dt$, and T is temperature. The energy transfer between eddy and zonal mean kinetic energy is evaluated as

$$C(\mathrm{EKE}, \mathrm{ZKE}) \approx \int \cos\phi \left(\overline{u'v'} \frac{\partial}{a\partial\phi} + \overline{u'\omega'} \frac{\partial}{\partial p} \right) \left(\frac{\overline{u}}{\cos\phi} \right) dm. \tag{5.27}$$

Note that we have neglected terms involving $\overline{v}$, which are inevitably small.

Appendix B: Spectral Kinetic Energy Budget in σ-coordinates

The kinetic energy per unit surface area (and eddy kinetic energy in a similar way) in $\sigma-$coordinates can be written as

$$\mathrm{KE} = \int ds \int_0^1 d\sigma \left(\frac{1}{2} p_s \mathbf{u}^2 \right), \tag{5.28}$$

where p_s is the surface pressure and the integral

$$\int ds = \frac{1}{4\pi g} \int_0^{2\pi} d\lambda \int_0^{\pi} \cos\phi d\phi. \tag{5.29}$$

To approximate (5.28) into a quadratic form, we must substitute p_s by its mean value $\bar{p}_s$ and obtain

$$\mathrm{KE} \approx \bar{p}_s \int ds \int_0^1 d\sigma \left(\frac{1}{2} \mathbf{u}^2 \right). \tag{5.30}$$

The horizontal velocity field on the sphere can be decomposed into vortical part and divergent part as $\mathbf{u} = \mathbf{u}_{vor} + \mathbf{u}_{div}$, where $\nabla \times \mathbf{u}_{vor} = \zeta$ and $\nabla^2 \psi = \zeta$ (ζ is relative vorticity and ψ is the stream function). The divergent part of the flow is much smaller than the vortical flow and it is safe to ignore it in the kinetic energy. Eq. (5.30) becomes

$$\begin{aligned}
\mathrm{KE} &\approx \bar{p}_s \int ds \int_0^1 d\sigma \left(\frac{1}{2} \mathbf{u}_{vor}^2 \right) && (5.31) \\
&= \bar{p}_s \int ds \int_0^1 d\sigma \left(-\frac{1}{2} \psi \nabla^2 \psi \right) = \bar{p}_s \int ds \int_0^1 d\sigma \left(-\frac{1}{2} \psi \zeta \right) && (5.32) \\
&= -\frac{1}{4} \bar{p}_s g^{-1} \int_0^1 d\sigma \sum_{n,m} \{\psi\}^*_{n,m} \{\zeta\}_{n,m}, && (5.33)
\end{aligned}$$

where $\{\}_{n,m}$ denotes the spectrum component of the fields with total wavenumber n and zonal wavenumber m. As stream function and relative vorticity are related in spectral space by

$$\{\zeta\}_{n,m} = -\frac{n(n+1)}{a^2} \{\psi\}_{n,m}, \tag{5.34}$$

where a is the planetary radius, (5.33) becomes

$$\mathrm{KE} \approx \frac{1}{4} \bar{p}_s g^{-1} \int_0^1 d\sigma \sum_n \sum_{m=-n}^{n} \frac{a^2}{n(n+1)} \{\zeta\}^*_{n,m} \{\zeta\}_{n,m}, \tag{5.35}$$

and kinetic energy within one wavenumber

$$\mathrm{KE}_n \approx \frac{1}{4} \bar{p}_s g^{-1} \int_0^1 d\sigma \sum_{m=-n}^{n} \frac{a^2}{n(n+1)} \{\zeta\}^*_{n,m} \{\zeta\}_{n,m}. \tag{5.36}$$

The kinetic energy budget can now be derived from the evolution equation for vorticity

$$\begin{aligned}\frac{\partial \zeta}{\partial t} =& -(f+\zeta)\nabla\cdot\mathbf{u} - \mathbf{u}\cdot\nabla f - \mathbf{u}\cdot\nabla\zeta - R\nabla T\times\nabla\ln p_s - \nabla\times\left(\dot{\sigma}\frac{\partial\mathbf{u}}{\partial\sigma}\right)\\ &- d_{fri} - d_{vis}\\ \approx& -(f+\zeta)\nabla\cdot\mathbf{u}_{div} - \mathbf{u}_{vor}\cdot\nabla f - \mathbf{u}_{vor}\cdot\nabla\zeta - R\nabla T\times\nabla\ln p_s - \nabla\times\left(\dot{\sigma}\frac{\partial\mathbf{u}}{\partial\sigma}\right)\\ &- d_{fri} - d_{vis},\end{aligned} \tag{5.37}$$

where d_{fri} and d_{vis} denote damping by friction and hyperviscosity respectively. Transforming (5.37) into spectral space and multiplying it by $\{\zeta\}^*_{n,m}$ leads to the spectral kinetic energy budget. Energy transfer from all other wavenumbers into wavenumber n by nonlinear interactions is computed as

$$T^n_{NL} = \frac{1}{2}\bar{p}_s g^{-1}\frac{a^2}{n(n+1)}\int_0^1 d\sigma \sum_{m=-n}^{n}\{\zeta\}^*_{n,m}\{-\mathbf{u}_{vor}\cdot\nabla\zeta\}_{n,m}, \tag{5.38}$$

which vanishes upon summation over all wavenumbers. Kinetic energy generation at wavenumber n is computed as

$$\begin{aligned}G^n_{KE} =& \frac{1}{2}\bar{p}_s g^{-1}\frac{a^2}{n(n+1)}\int_0^1 d\sigma\sum_{m=-n}^{n}\{\zeta\}^*_{n,m}\left\{-(f+\zeta)\nabla\cdot\mathbf{u}_{div} - \mathbf{u}_{vor}\cdot\nabla f\right.\\ &\left. - R\nabla T\times\nabla\ln p_s - \nabla\times\left(\dot{\sigma}\frac{\partial\mathbf{u}}{\partial\sigma}\right)\right\}_{n,m},\end{aligned} \tag{5.39}$$

where the largest contribution comes from the $f\nabla\cdot\mathbf{u}_{div}$ term, which can be shown to be related to the usual kinetic energy generation term, ωT, in pressure coordinates[3].

[3]Geostrophic balance is assumed so that $-f\frac{a^2}{n(n+1)}\{\zeta\}^*_{n,m}\sim\{\Psi\}^*_{n,m}$ where Ψ is the geopotential height. Assuming surface pressure is nearly constant so that $\nabla\cdot\mathbf{u}_{div}\sim-\frac{\partial\omega}{\partial p}$. Then the column integral $\int_0^{p_s}-\{\Psi\}^*_{n,m}\frac{\partial\{\omega\}_{n,m}}{\partial p}dp$ approximates $\int_0^{p_s}-\frac{R}{p}\{\omega\}_{n,m}\{T\}^*_{n,m}dp$ if ω vanishes in the upper and lower boundaries.

The second largest term is $-R\nabla T \times \nabla \ln p_s$, which is unique to the $\sigma-$coordinates. $-\mathbf{u}_{vor} \cdot \nabla f$ is actually a spectral flux by the Coriolis force, which does no net work and is not important in our simulations. The energy dissipation by friction and hyperviscosity are

$$D^n_{fri} = \frac{1}{2}\bar{p}_s g^{-1} \frac{a^2}{n(n+1)} \int_0^1 d\sigma \sum_{m=-n}^{n} \{\zeta\}^*_{n,m} \{-d_{fri}\}_{n,m}\,, \tag{5.40}$$

and

$$D^n_{vis} = \frac{1}{2}\bar{p}_s g^{-1} \frac{a^2}{n(n+1)} \int_0^1 d\sigma \sum_{m=-n}^{n} \{\zeta\}^*_{n,m} \{-d_{vis}\}_{n,m}\,, \tag{5.41}$$

respectively. When time averaged, The sum of the four terms should be close to zero, and a residual term is included to close the energy budget.

The eddy kinetic energy budget can be formulated by discarding zonal wavenumber 0 in (5.37) and further decompose (5.38) into eddy-eddy transfer

$$T^n_{EE} = \frac{1}{2}\bar{p}_s g^{-1} \frac{a^2}{n(n+1)} \int_0^1 d\sigma \sum_{m=-n,\ m\neq 0}^{n} \{\zeta\}^*_{n,m} \{-\mathbf{u}'_{vor} \cdot \nabla\zeta'\}_{n,m}\,, \tag{5.42}$$

and eddy/mean-flow transfer

$$T^n_{EM} = \frac{1}{2}\bar{p}_s g^{-1} \frac{a^2}{n(n+1)} \int_0^1 d\sigma \sum_{m=-n,\ m\neq 0}^{n} \{\zeta\}^*_{n,m} \left\{-\bar{\mathbf{u}}_{vor} \cdot \nabla\zeta' - \mathbf{u}'_{vor} \cdot \nabla\bar{\zeta}\right\}_{n,m}. \tag{5.43}$$

Appendix C: Entropy budget

Atmospheric motion is often compared to a heat engine to which the first and second laws of thermodynamics can be applied. The first law of thermodynamics states that energy conversion between different forms (e.g., internal, potential and kinetic energy) must conserve the total amount of energy. The second law of thermodynamics further

constrains the direction of energy conversion, such that the energy can only change from a more to a less usable form. Mathematically, it states that for an isolated system, there exists a state function S which satisfies

$$dS/dt \geq 0, \tag{5.44}$$

where S is the entropy. Eq. (5.44) means that entropy will increase monotonically until it reaches maximum at thermodynamic equilibrium. The second law of thermal dynamics constrains the maximum kinetic energy that can be generated from a reservoir of internal energy, and has been applied to various scales of terrestrial atmospheric motions ranging from moist convection (Rennó and Ingersoll, 1996; Emanuel and Bister, 1996), dust devils (Rennó et al., 1998), hurricane dynamics (Emanuel, 1986; Bister and Emanuel, 1998), to the general circulation (Barry et al., 2002).

Clearly on the global scale, Earth's atmosphere is not an isolated system, otherwise it would be in a thermodynamical equilibrium state with uniform temperature everywhere. Instead, Earth's atmosphere is an open system due to constant heating from the Sun. The second law can be extended to such an open system using that

$$\frac{dS}{dt} = \int \frac{\dot{Q}}{T} dm + \frac{dS_{irr}}{dt}, \tag{5.45}$$

where $\dot{Q}$ is the radiative heating rate per unit mass, T is temperature, $\int dm$ is mass-weighted global integral defined in (5.24), and dS_{irr} is the entropy production from irreversible processes (Pauluis and Held, 2002). The atmosphere is heated in the tropics where it is warm (T is large), and is cooled in high latitudes where it is cold (T is small), therefore the external heating acts as an entropy sink ($\int \frac{\dot{Q}}{T} dm < 0$). In our idealized dry GCM, the only physical irreversible process is the bottom friction. Additional irreversible processes arise from hyperviscosity on the velocity field and hyperdiffusion on the temperature field. The entropy production from irreversible

processes can be evaluated from the associated diabatic heating:

$$\begin{aligned}\frac{dS_{irr}}{dt} &= \int \frac{\dot{Q}_{irr}}{T} dm \\ &= \int \frac{\dot{Q}_f + \dot{Q}_{hyper,v} + \dot{Q}_{hyper,T}}{T} dm,\end{aligned}$$

where $\dot{Q}_f$,$\dot{Q}_{hyper,v}$ and $\dot{Q}_{hyper,T}$ represent diabatic heating resulting from friction, hyperviscosity on velocity and hyperdiffusion on temperature, respectively. For frictional heating, the associated entropy production is

$$\int \frac{\dot{Q}_f}{T} dm = \int \frac{\Gamma : \nabla \mathbf{v}}{T} dm, \tag{5.46}$$

where Γ is the stress tensor and $\mathbf{v}$ is the wind velocity. As we used Rayleigh damping to represent friction, (5.46) can be further reduced to

$$\int \frac{\dot{Q}_f}{T} dm = \int \frac{k(\sigma)\mathbf{v}^2}{T} dm, \tag{5.47}$$

where $k(\sigma)$ is defined in Eq.(5.2). Similarly, we can evaluate the entropy productions from hyperviscosity and hyperdiffusion.

In a statistically steady state, the entropy sink from external heating must be balanced by the sum of various entropy sources, written as

$$0 = \left[\int \frac{\dot{Q}}{T} dm\right] + \left[\int \frac{\dot{Q}_f}{T} dm\right] + \left[\int \frac{\dot{Q}_{hyper,v}}{T} dm\right] + \left[\int \frac{\dot{Q}_{hyper,T}}{T} dm\right], \tag{5.48}$$

where the square brackets denote time averaging. Fig. 5.23 shows each term in (5.48) from the Earth-like simulations with different values of bottom friction. For the control run ($\tau_f = 1$ day), the major entropy production to balance the entropy sink is the bottom friction, while the entropy production from hyperviscosity is negligible. When bottom friction first decreases, both the entropy sink and the frictional entropy

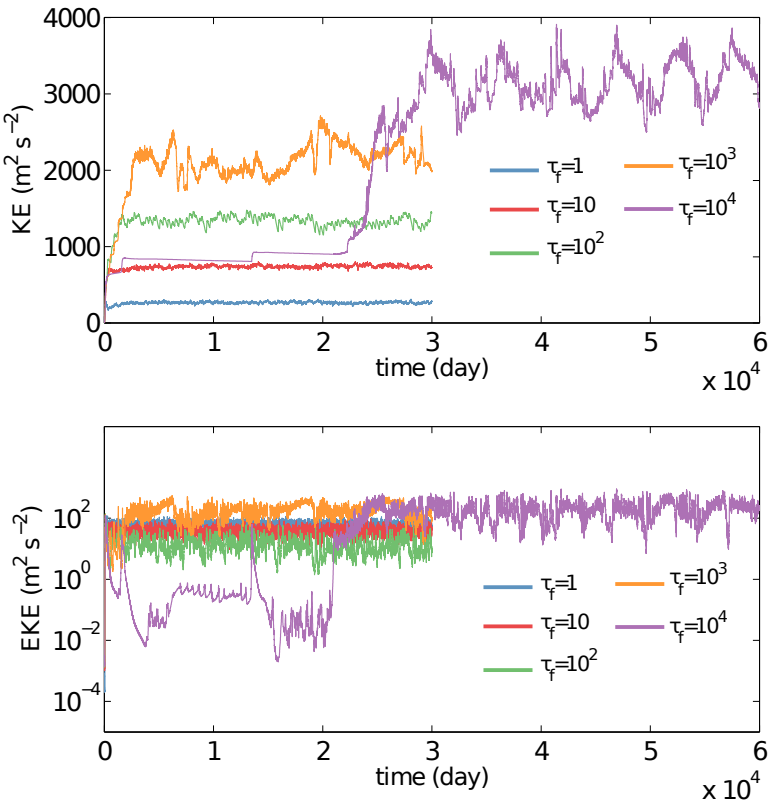


Figure 5.1: Evolution of (above) kinetic energy and (below) eddy kinetic energy in the Earth-like simulations with different strength of surface friction.

production decrease ($\tau_f = 10,\ 10^2$ day), and they nearly balance each other. When bottom friction further decreases, the entropy production by friction continues to decrease, while the entropy sink stays nearly constant and is mainly balanced by entropy production from hyperviscosity ($\tau_f = 10^3,\ 10^4$ day). The entropy production from hyperdiffusion negligible for all τ_f. The entropy budget is similar for the T127 runs. Close to the vanishing friction limit, the hyperviscosity becomes the the dominate entropy source, which in reality may correspond to three-dimensional turbulence at small scales.

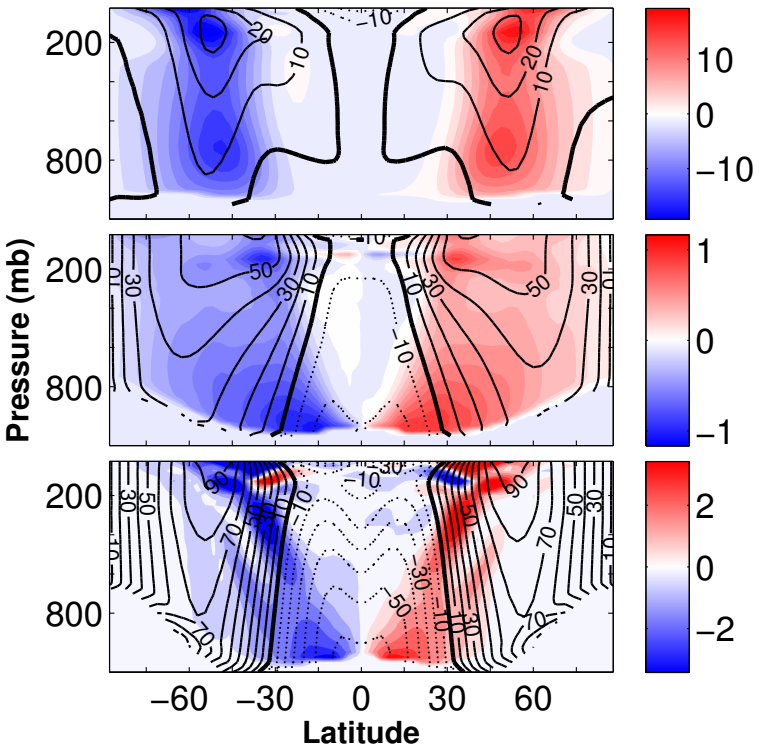


Figure 5.2: Zonal and temporal mean zonal wind (contour) and eddy potential temperature flux (color) for Earth-like simulations with different strength of surface friction: τ_f =(top) 1, (middle) 10^2, (bottom) 10^4 days. The contour interval for zonal wind is 10 m/s.

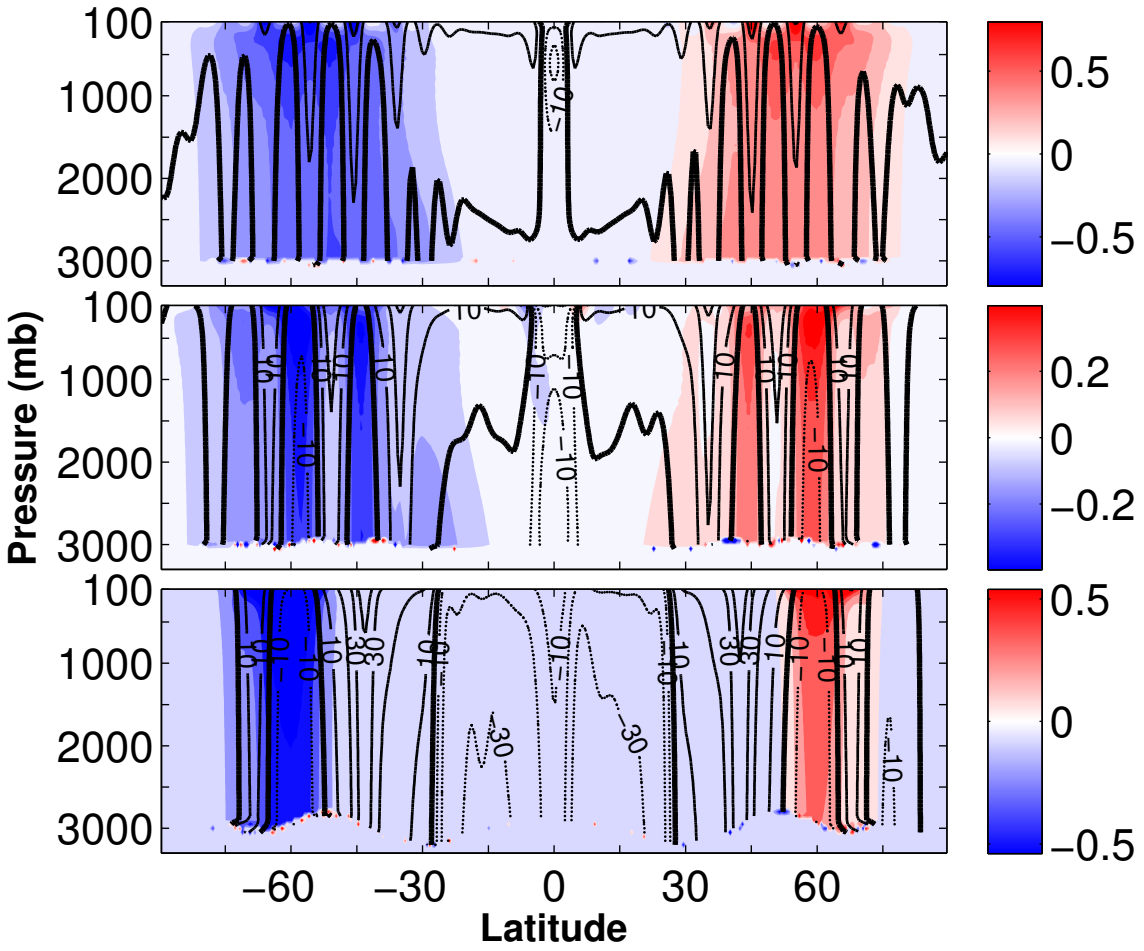


Figure 5.3: Zonal and temporal mean zonal wind (contour) and eddy potential temperature flux (color) for Jupiter-like simulations with different strength of surface friction: τ_f =(top) 5, (middle) 50, (bottom) 5000 days. The contour interval for zonal wind is 10 m/s.

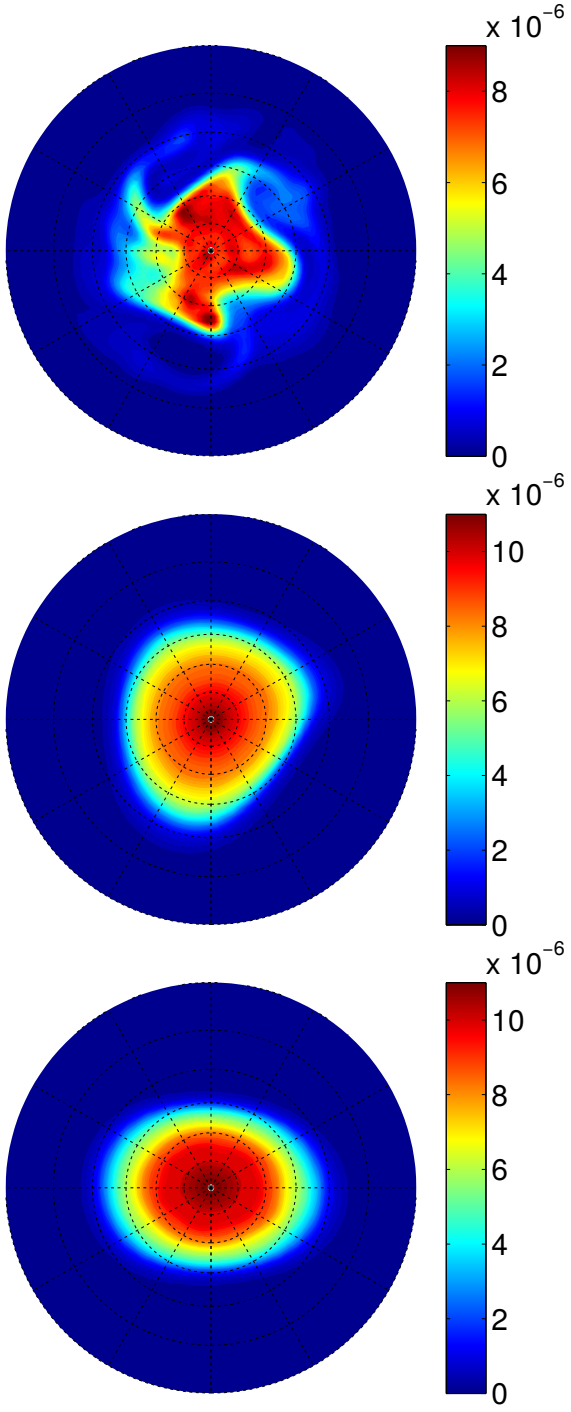


Figure 5.4: Instantaneous Ertel's potential vorticity fields on istentropic surface $\theta =$ 330 K for Earth-like simulations with different strength of surface friction: $\tau_f =$ (top) 1, (middle) 10^3 and (bottom) 10^4 days. The unit is $\mathrm{m^2\ K\ s^{-1}\ kg^{-1}}$. The whole Norther hemisphere (latitudinal range 0° to 90°) is shown.

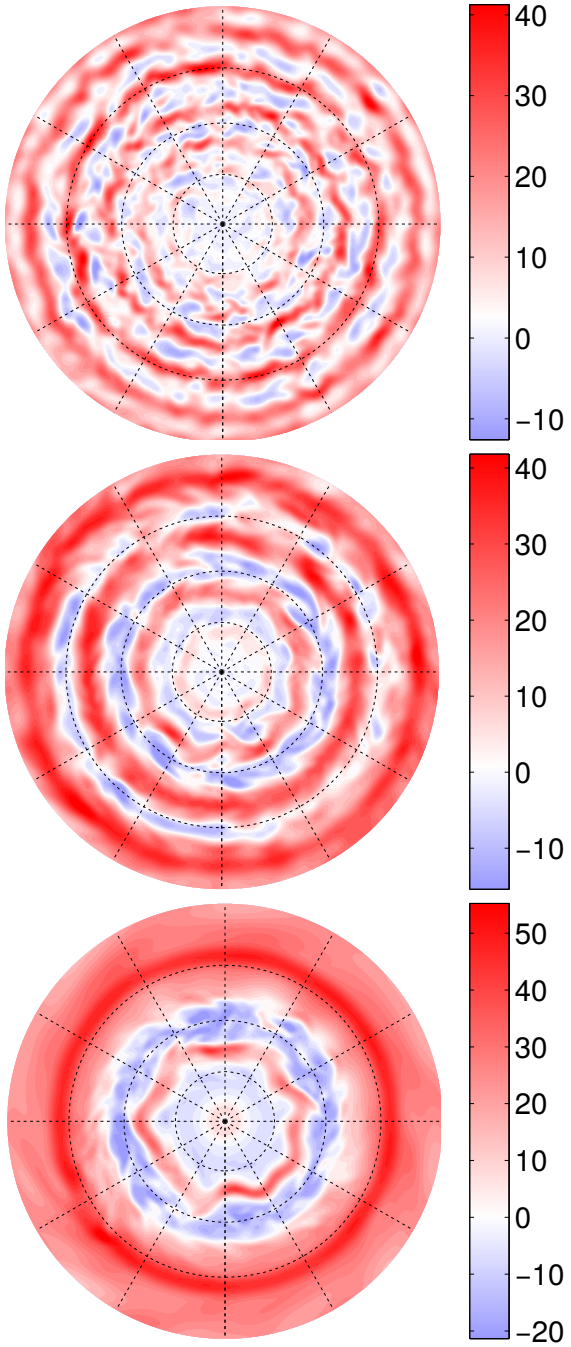


Figure 5.5: Instantaneous zonal wind fields in the upper atmopshere (σ =0.02) for Jupiter-like simulations with different strength of surface friction: τ_f = (top) 5, (middle) 50 and (bottom) 5000 days. The unit is m s^{-1}. Only the extratropical region (latitudinal range 30° to 90°) is shown.

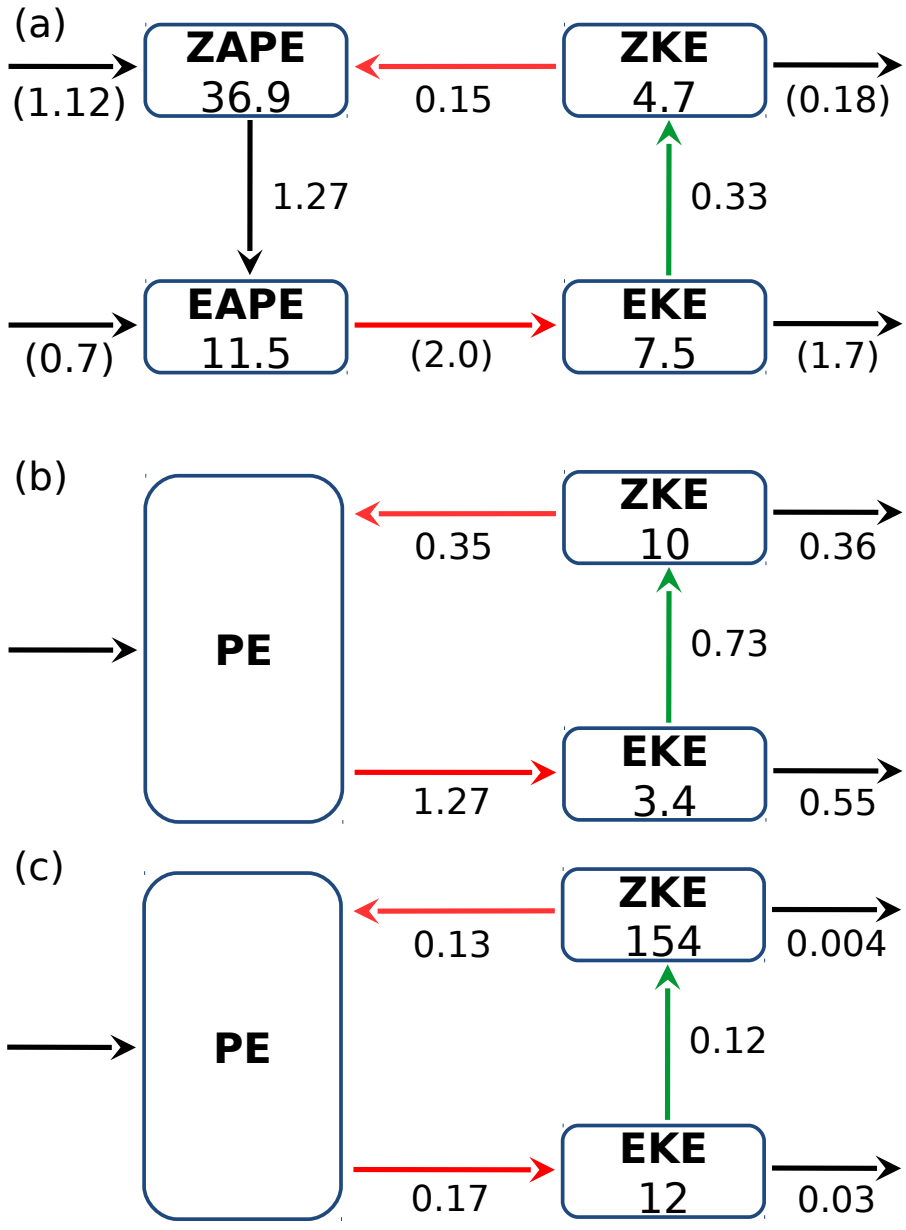


Figure 5.6: (a) The observed energy cycle for the global Earth's atmosphere. Energy amounts inside each box are given in 10^5 J m^{-2}, and rates of generation, conversion, and dissipation in W m^{-2}; not directly measured terms are shown in parentheses (adapted from Peixoto and Oort 1984). The energy cycle for Earth-like simulations with (b) the highest surface friction $\tau_f = 1$ day and (c) the lowest surface friction $\tau_f = 10^4$ days.

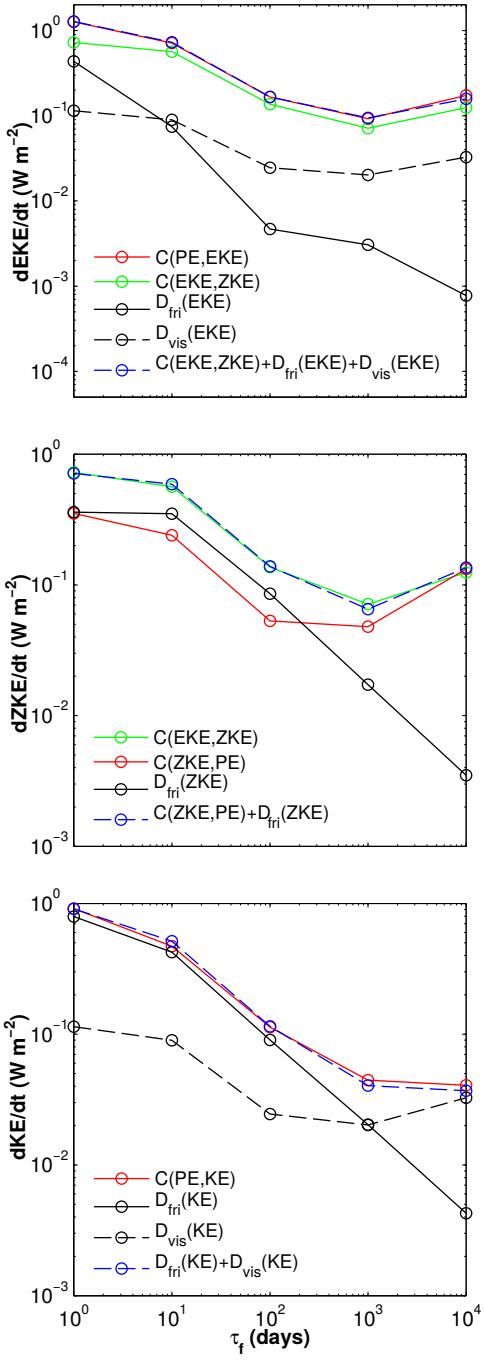


Figure 5.7: Rates of kinetic energy generation, conversion and dissipation in W m^{-2} for (top) eddy, (middle) zonal mean and (bottom) total flows for runs with different strength of surface friction.

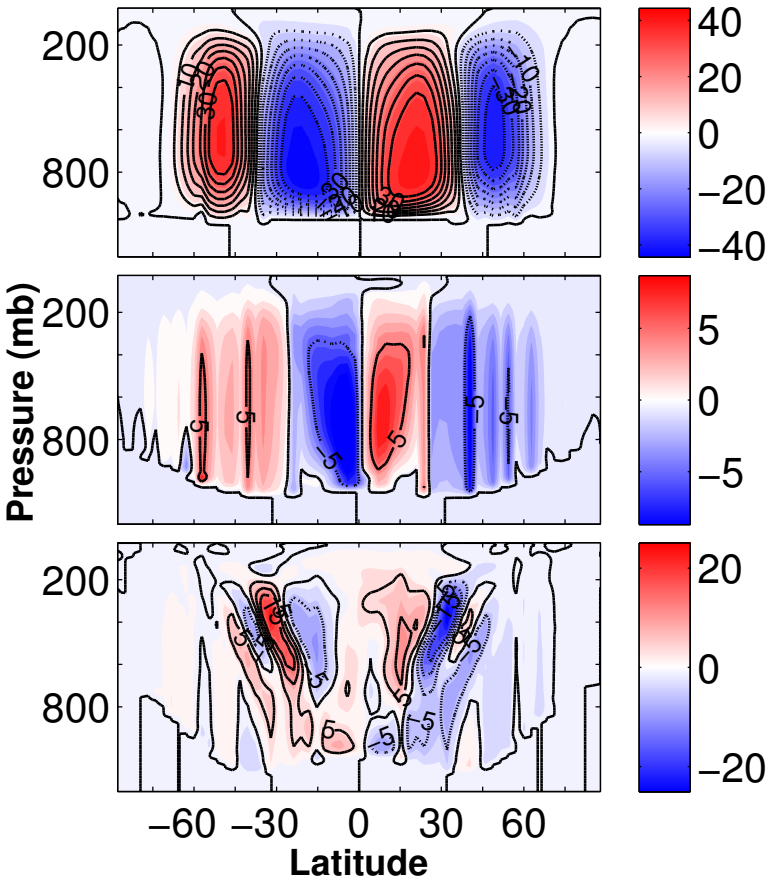


Figure 5.8: Time averaged zonal mean meridional circulation for Earth-like simulations with different strength of surface friction: τ_f =(top) 1, (middle) 10^2, and (bottom) 10^4 days. The unit is 10^9 kg s^{-1}, and the contour interval is 5×10^9 kg s^{-1}. Positive value denotes clockwise while negative value denotes counter-clockwise.

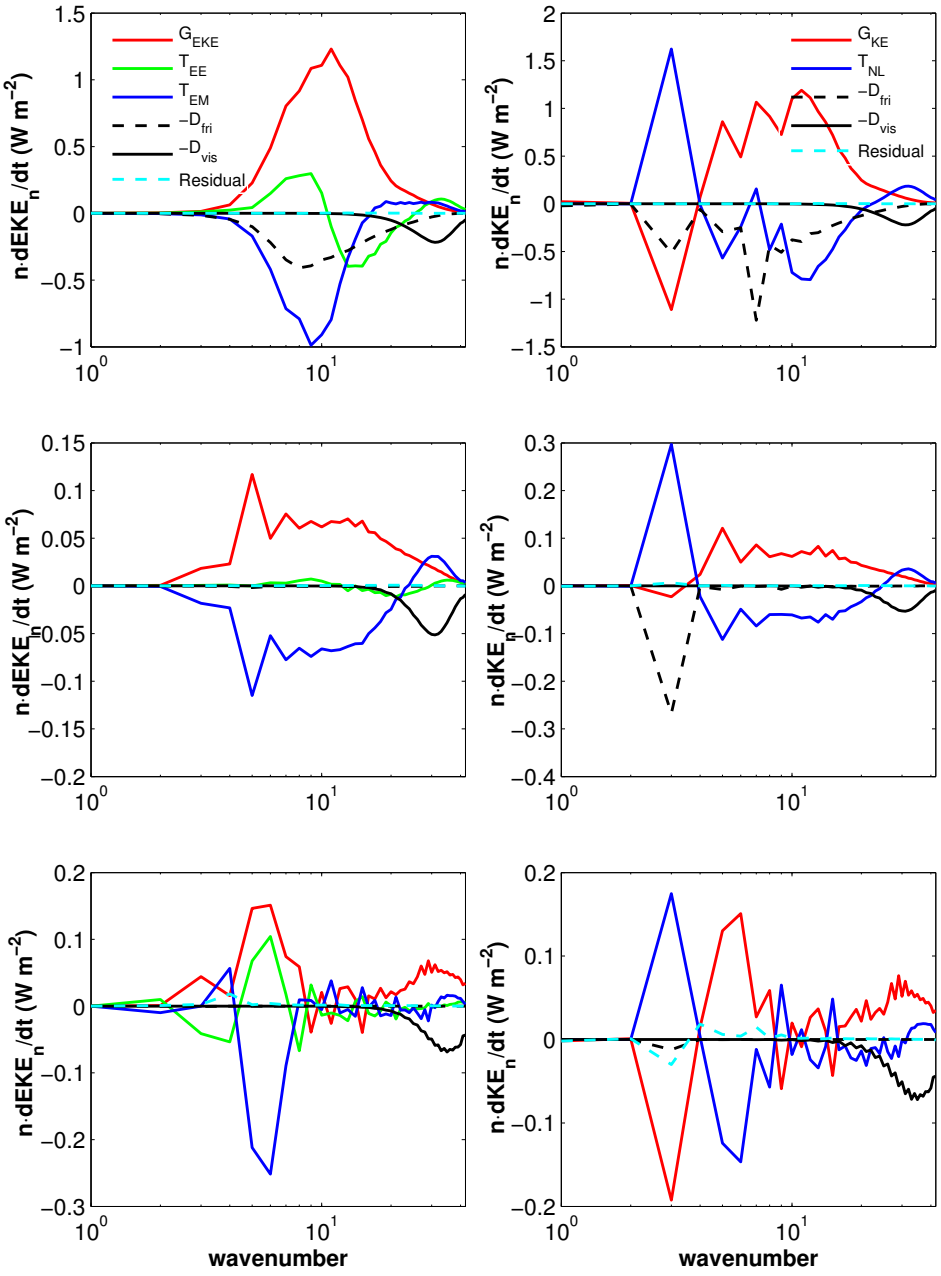


Figure 5.9: (Left panel) Spectral EKE budget and (right panel) spectral KE budget for Earth-like simulations with various bottom friction: τ_f =(top) 1, (middle) 10^2, and (bottom) 10^4 days.

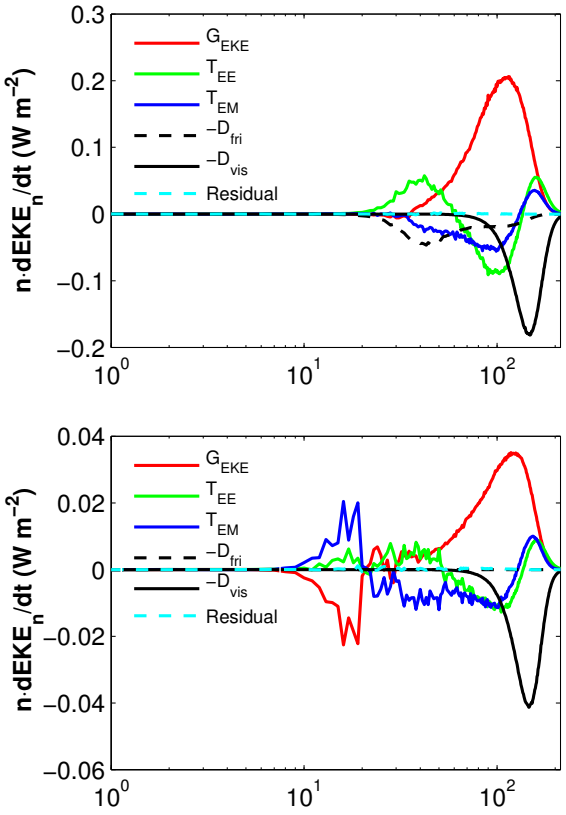


Figure 5.10: Spectral EKE budget for Jupiter-like simulations with various bottom friction: τ_f = (top) 5 and (bottom) 5000 days.

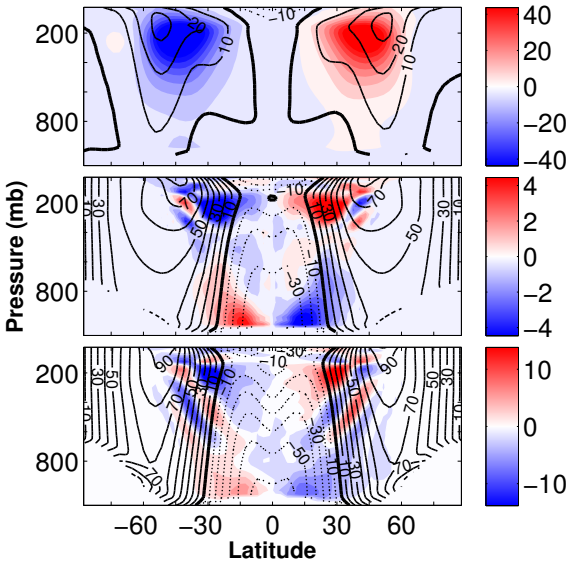


Figure 5.11: Eddy momentum flux together with zonal mean zonal wind for Earth-like simulations with various bottom friction: τ_f =(top) 1, (middle) 10^3, and (bottom) 10^4 days. The contour interval for zonal wind is 10 m/s.

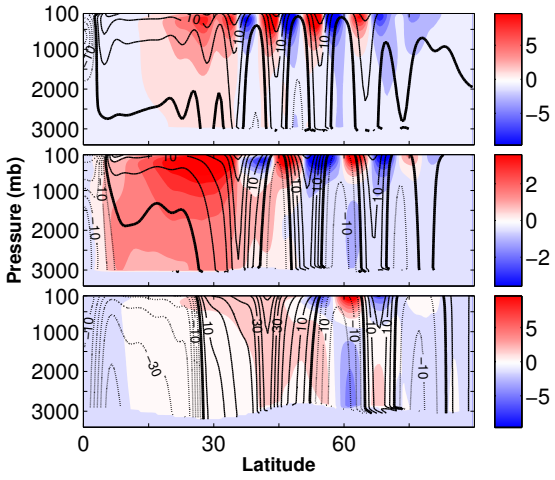


Figure 5.12: Eddy momentum flux together with zonal mean zonal wind for Jupiter-like simulations with various bottom friction: (top) τ_f =5, (middle) 50 and (bottom) 5000 days. Only Northern hemisphere is shown as Southern hemisphere is nearly symmetric. The contour interval for zonal wind is 5 m/s.

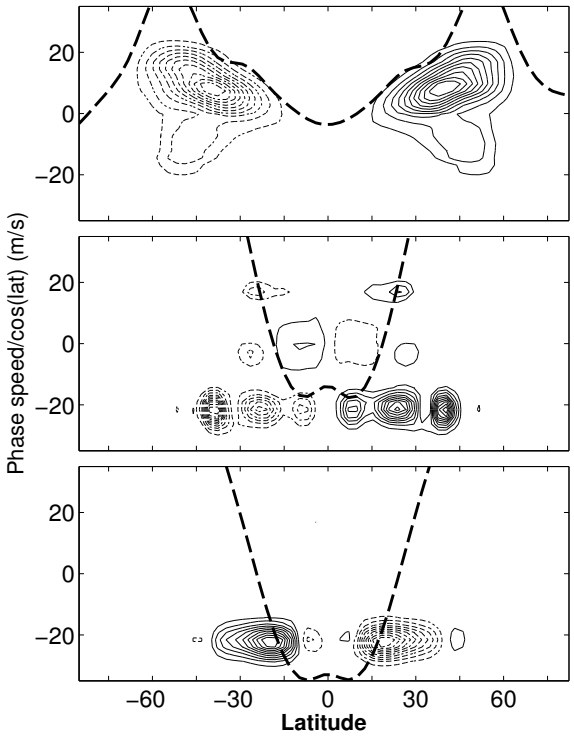


Figure 5.13: (Top) Eddy momentum flux phase speed cospectrum in the upper atmosphere ($\sigma = 0.316$) vs. latitude for Earth-like simulation with $\tau_f = 1$ day as a reference. The same spectra for Earth-like simulations with $\tau_f = 10^3$ days in the (middle) upper ($\sigma = 0.316$) and (bottom) lower ($\sigma = 0.816$) atmospheres. The thick black line shows temporal and zonal averaged zonal wind at the same level. The dashed contour denotes southward eddy momentum flux.

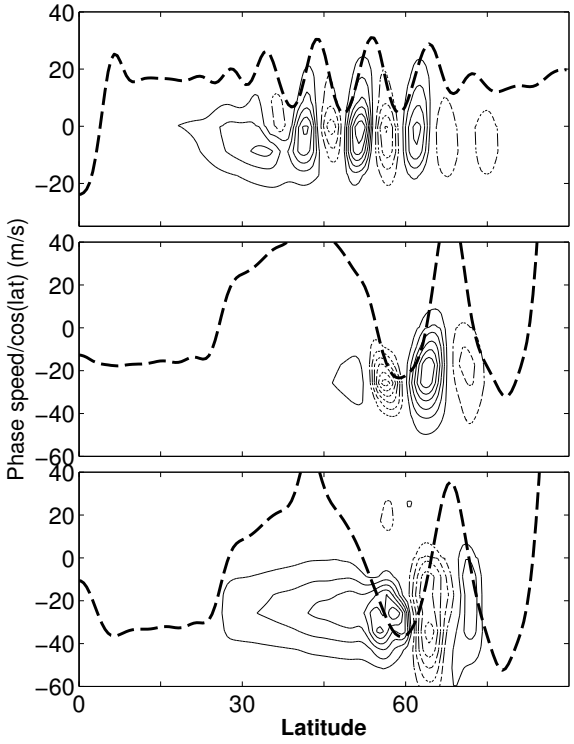


Figure 5.14: Similar to Fig. 5.13 but for Jupiter-like simulations. (Top) Eddy momentum flux phase speed cospectrum in the upper atmosphere ($\sigma = 0.02$) vs. latitude for Jupiter-like simulation with $\tau_f = 5$ day as a reference. The same spectra for Jupiter-like simulations with $\tau_f = 5000$ days in the (middle) upper ($\sigma = 0.02$) and (bottom) lower ($\sigma = 0.84$) atmospheres. The thick black line shows temporal and zonal averaged zonal wind at the same level. The dashed contour denotes southward eddy momentum flux.

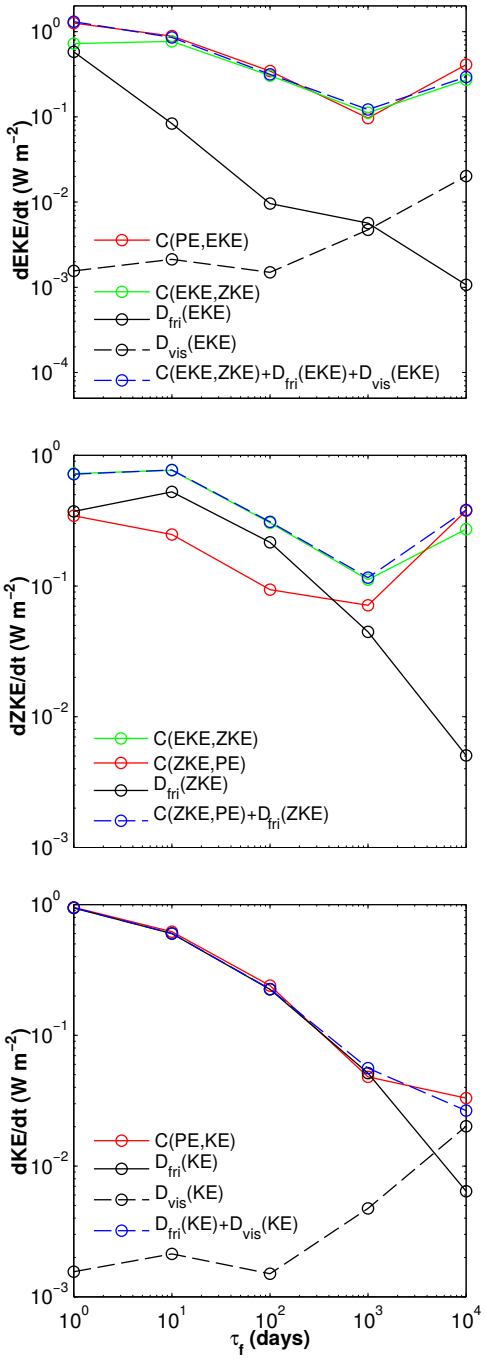


Figure 5.15: Similar to Fig. 5.7 but for T127 simulations. Rates of kinetic energy generation, conversion, and dissipation in W m^{-2} for (top) eddy, (middle) zonal mean and (bottom) total flows for runs with different strength of surface friction.

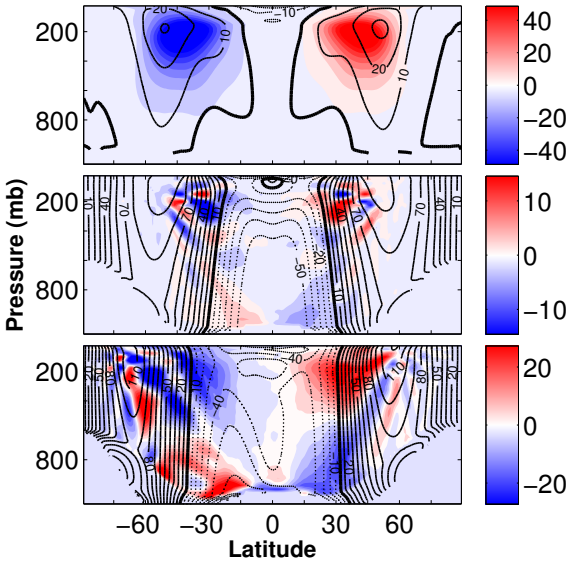


Figure 5.16: Similar to Fig. 5.11 but for T127 simulations. Eddy momentum flux together with zonal mean zonal wind for Earth-like simulations with various bottom friction: τ_f =(top) 1, (middle) 10^3, and (bottom) 10^4 days. The contour interval for zonal wind is 10 m/s.

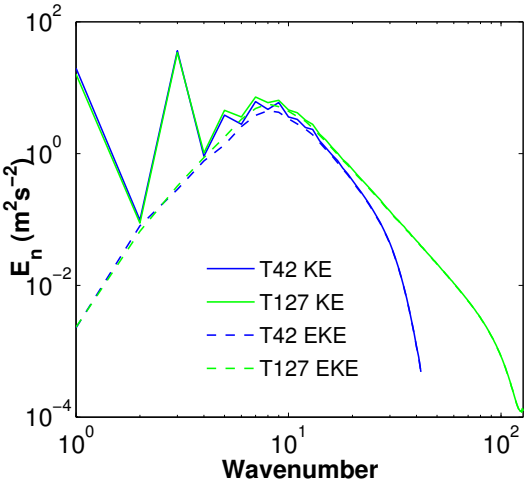


Figure 5.17: Total kinetic energy spectra (solid lines) and eddy kinetic energy spectra (dashed lines) from T42 (blue lines) and T127 (green lines) Earth-like simulations with frictional time scale τ_f=1 day.

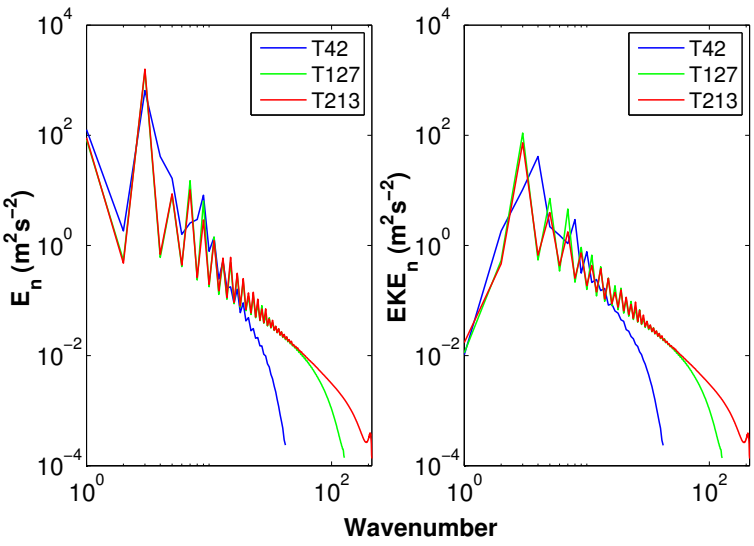


Figure 5.18: Total kinetic energy spectra (left) and eddy kinetic energy spectra (right) from T42 (blue lines), T127 (green lines) and T213 (red lines) Earth-like simulations with frictional time scale τ_f=10^3 day.

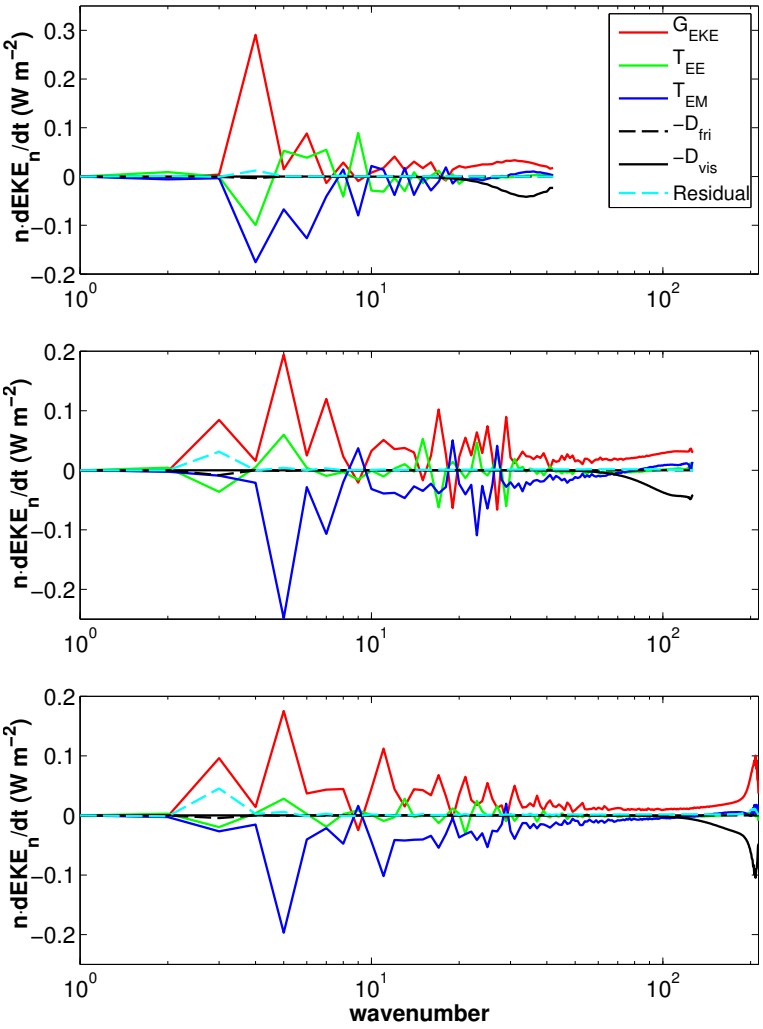


Figure 5.19: Spectral EKE budget for Earth-like simulations with bottom friction $\tau_f = 10^3$ days at various horizontal resolutions: (top) T42, (middle) T127 and (bottom) T213.

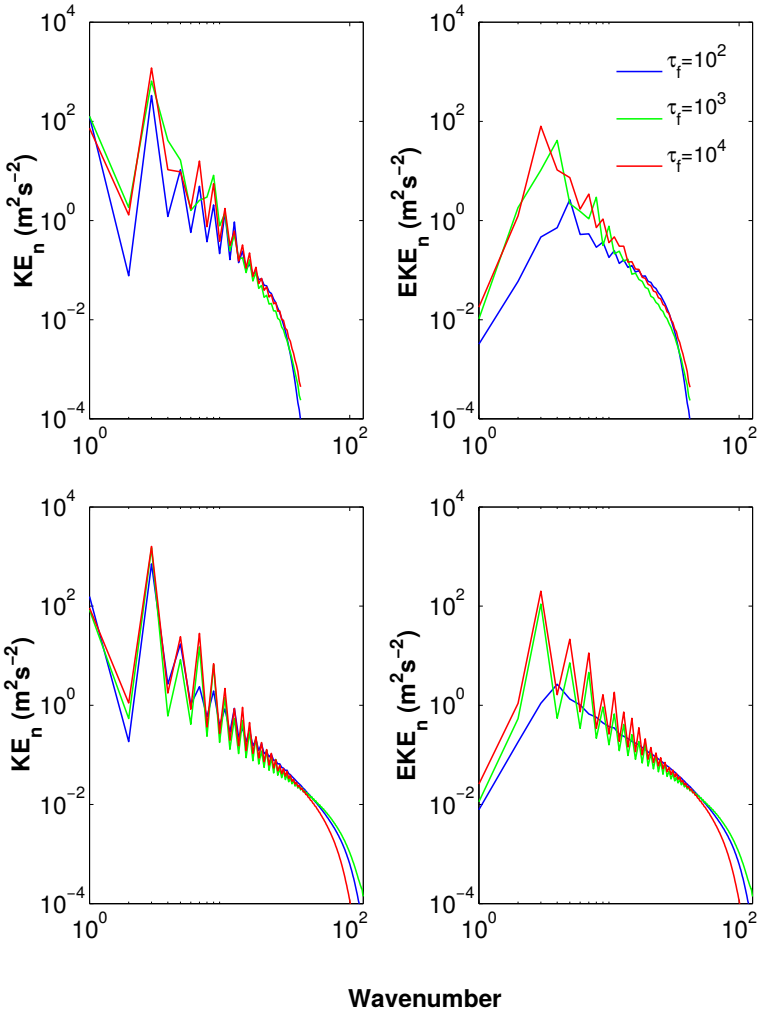


Figure 5.20: Total kinetic energy spectra (left) and eddy kinetic energy spectra (right) from T42 (top), T127 (bottom) Earth-like simulations with various frictional time scales: τ_f=10^2, 10^3 and 10^4 day.

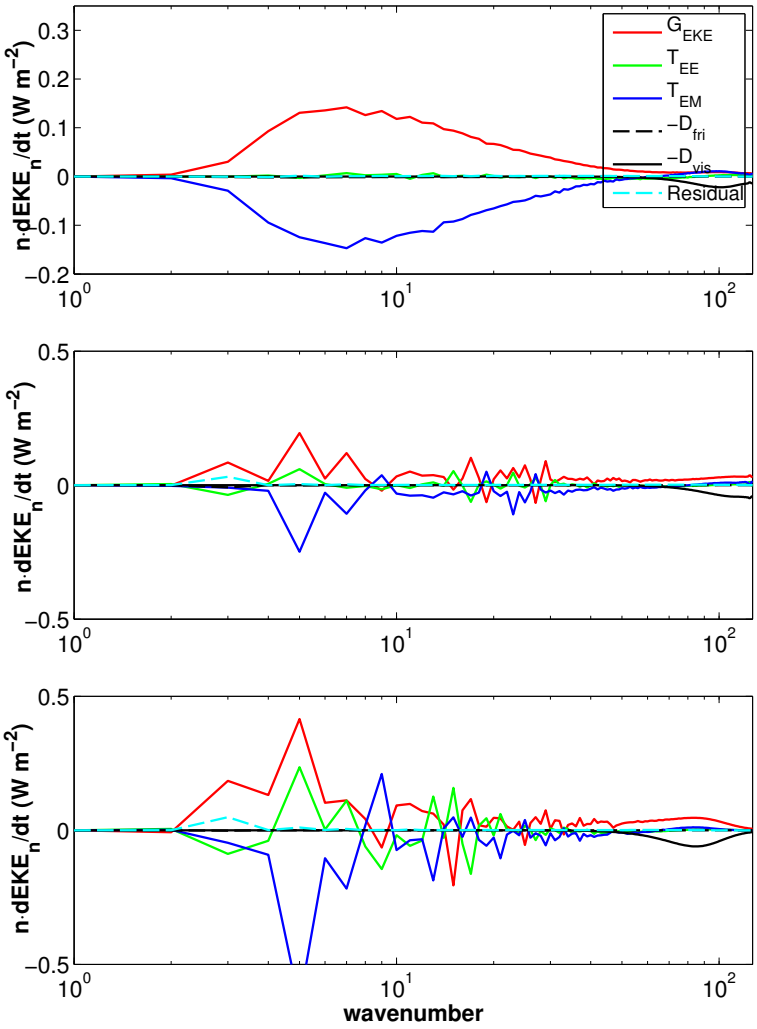


Figure 5.21: Spectral EKE budget for Earth-like simulations with horizonal resolution T127 and various bottom friction time scales: τ_f = (top) 10^2, (middle) 10^3 and (bottom) 10^4 days.

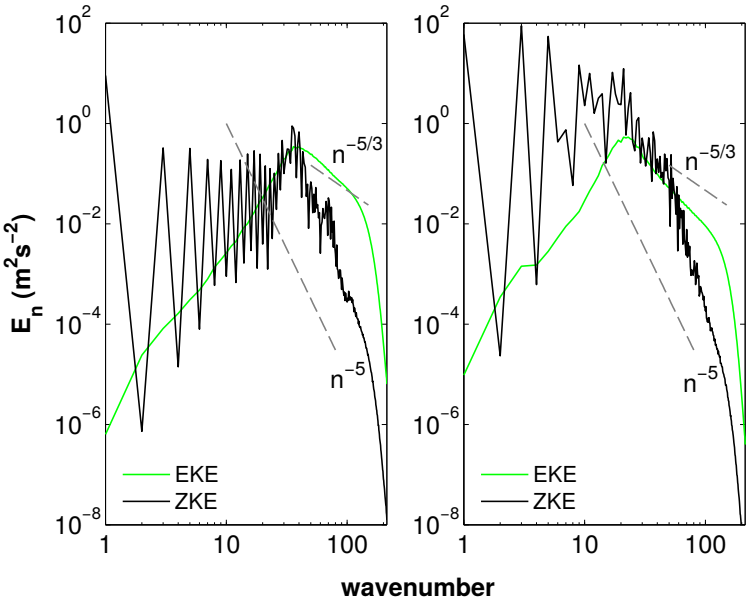


Figure 5.22: Eddy kinetic energy spectrum (solid green line) and zonal kinetic energy spectrum (solid black line) for Jupiter-like simulations with frictional time scale τ_f =(left) 5 days and (right) 5000 days. The dashed gray lines show spectrum slope of -5 and -5/3.

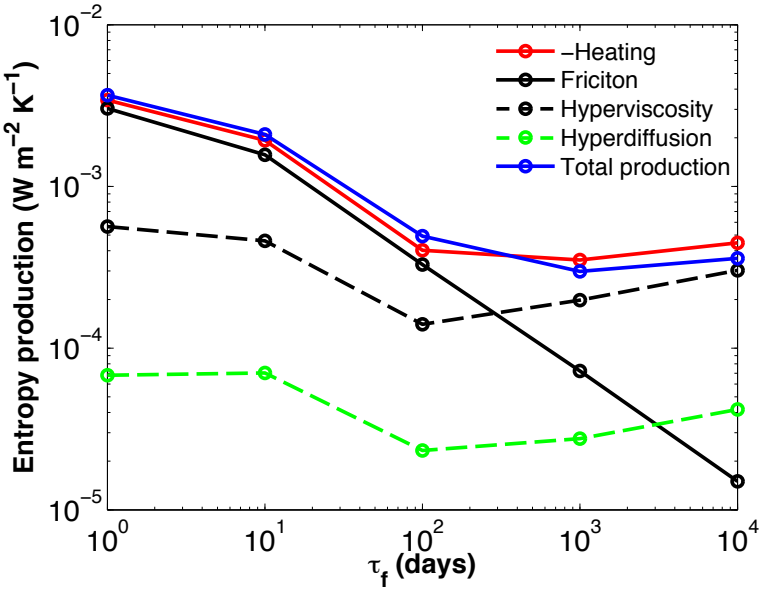


Figure 5.23: Entropy budget for the Earth-like simulations with various bottom friction. The entropy sink by radiative forcing is shown by its absolute value for plotting in logarithm coordinate.

Chapter 6

Horizontal and vertical scales of extratropical eddies in a dry GCM

This paper discusses the sensitivity of the horizontal and vertical scales of extratropical eddies when criticality is varied in a dry, primitive equation, general circulation model. Criticality is a measure of extratropical isentropic slope and when defined appropriately its value is often close to one for Earth's climate. The model is forced by a Newtonian relaxation of temperature to a prescribed temperature profile, and criticality is increased by increasing the thermal relaxation rate on the mean flow. When criticality varies near one, it is shown that there exists a weakly nonlinear regime in which the eddy scale increases with criticality without involving an inverse cascade, while at the same time the Rossby radius may in fact decrease. The quasi-geostrophic instability of Charney problem is revisited. It is demonstrated that both the horizontal and vertical scales of the most unstable wave depend on criticality, and simple estimates for the two scales are obtained. We reconcile the opposite trends of the eddy scale and Rossby radius and obtain an estimate for the eddy scale in terms of the Rossby radius and criticality that is broadly consistent with simulations.

6.1 Introduction

The theory of the scale of the energy-containing eddies in the extratropics for a given time-mean flow can be regarded as falling between two end-members which we call the linear regime and the turbulent regime. In the linear regime we take the eddy scale to be similar to that of the most unstable baroclinic wave. In Earth's atmosphere, the observed energy-containing eddy scale (spherical wavenumber ~ 8) is only slightly larger that of the most unstable waves, and the eddy turnover time ($\sim$3-5 days) is similar to their inverse growth rate (Simmons and Hoskins 1976; Valdes and Hoskins 1988). An estimation for the scale of the most unstable wave originates from Eady's (1949) classical work in baroclinic instability, in which the basic flow is simplified to be independent of latitude. The Eady model gives simple estimate for the most unstable wavelength λ_m, that it is only dependent on the Rossby deformation radius L_R according to $\lambda_m \approx 3.9 L_R$. For Earth's atmosphere, the Eady model gives a good estimate for the eddy scale and eddy turnover time. The Charney model of baroclinic instability does not give nearly as simple an estimate as the Eady problem (a problem we return to later on) but nevertheless the Rossby radius is often used as an estimate eddy scale and indeed it has been shown that for a wide range of mean flows, the Rossby radius multiplied by an empirical constant gives a decent estimate for the scale of the most unstable waves and eddy scale (Merlis and Schneider, 2009).

In the other end-member, the eddy scale is considered to be determined by geostrophic turbulence. Now, the baroclinic mode (proportional to temperature in the two-level quasi-geostrophic model) is maintained by differential heating of the atmosphere and stirred by the barotropic flow as if it were a passive tracer. Eddy available potential energy cascades to smaller scales until it arrives at the scale of baroclinic instability, where it is converted into barotropic eddy kinetic energy (Salmon, 1980). The kinetic energy is then cascaded to larger scales by nonlinear eddy-eddy interactions much as in two-dimensional turbulence. Unless halted by friction or limited

by domain size then, near the Rhines scale, energy becomes preferentially channeled into the zonal flow (Rhines, 1979; Vallis and Maltrud, 1993). Thus, in principle, the energy-containing eddy scale can be much larger than the Rossby radius. This conceptual picture generally agrees with the life cycles of nonlinear baroclinic waves (Simmons and Hoskins, 1978), and the inverse cascade is seen in many simulations of both the quasi-geostrophic and primitive equations (Vallis and Maltrud, 1993; Larichev and Held, 1995; Held and Larichev, 1996; Zurita-Gotor and Vallis, 2009; Jansen and Ferrari, 2012).

The regimes in which above two strands of theory are relevant can be separated by a non-dimensional number, the criticality ξ. Criticality is a measure of isentropic slope and it can be defined in layered and continuously stratified quasi-geostrophic (QG) and primitive equation (PE) models. Criticality has the cleanest expression in the two-layer QG model on the β plane (Phillips 1954). Here, the non-dimensional number $\xi = U/(\beta L_R^2)$ determines the linear instability, where L_R is the deformation radius and U is the mean thermal wind. The system is baroclinic unstable only if $\xi > 1$. However, this particular instability criteria is unique to the two layer model and in continuously stratified model there is generally no minimum requirement on criticality for the system to be unstable. Furthermore, for the full nonlinear model, baroclinic eddies can develop even if it is linearly stable (Farrell and Ioannou 1994; Lee and Held 1991). However, criticality can serve more generally as a measure of instability and as a measure of the extent of the inverse cascade. Generally when criticality $\xi \leq 1$, the inverse cascade is not important, and the energy-containing eddy scale, Rossby radius and Rhines scale are all very similar (Schneider and Walker 2006). When $\xi \gg 1$, there can be substantial inverse cascade. In this case, the eddy scale is much larger than Rossby radius, and an adequate estimate for eddy scale is sometimes found to be the Rhines scale (Jansen and Ferrari 2012). Although the Rhines scale may give a good estimate for the eddy scale in the high criticality

case, it is not an a priori or mean field estimate because it assumes knowledge of the root-mean square velocity at the eddy scale or, in the variant proposed by Vallis and Maltrud (1993), one needs to know the energy cascade rate. For baroclinic flow we need a second-order closure to calculate these quantities, such as that provided by Held and Larichev (1996). They took the eddy scale L_e and the Rhines scale L_β to be similar and derived a classical scaling to relate them to the mean field estimates Rossby radius L_R and criticality ξ, such that $L_e \sim L_\beta \sim \xi L_R$.

In between the linear regime and the turbulent one a theory for eddy scale is less clear. Intuitively, if we increase criticality from below 1 to much much larger than 1, we expect the eddy scale to increase from the deformation radius to the Rhines scale, but it is less clear just how the eddies adjust their scales to an increased criticality and when the inverse cascade becomes developed. However, there are very few studies on the relationship between eddy scale and criticality in a PE model mainly because, in a PE model, the criticality is difficult to change by perturbing model parameters. In a PE model, criticality can be intuitively thought of as the ratio of the potential temperature difference between subtropics and Poles $\Delta_h\theta$, to that between the surface and the tropopause $\Delta_v\theta$, written as $\xi = \Delta_h\theta/\Delta_v\theta$. In Earth's atmosphere, this quantity is well-known to stay at about unity throughout the seasons, even though the meridional temperature gradient changes significantly (Stone 1978). Earth's atmosphere thus appears to be in a low-criticality regime in which nonlinear interaction does not transfer much energy upscale beyond the Rossby radius (Boer and Shepherd 1983; Shepherd 1987; Straus and Ditlevsen 1999). It has been argued that such a marginal critical state for Earth's atmosphere does not appear by chance; it was first called "baroclinic adjustment" by Stone (1978) and later Schneider (2004) and Schneider and Walker (2006) argued that the constraint $\xi \approx 1$ arises using a turbulent closure for potential vorticity and potential temperature fluxes along with an assumption about the nature of the eddy diffusivity. Unlike a QG model in which

the vertical stratification is prescribed, in the PE model the macro-turbulence adjusts its extratropical thermal stratification to a state in which eddy-eddy interactions are weak. Schneider and Walker (2006) concluded that the supercritical state $\xi > 1$ is unobtainable in the PE model.

However, a number of studies have shows that the constraint $\xi \approx 1$ for a PE model can, in some circumstances, be violated, and the criticality can be continuously varied above 1. Zurita-Gotor (2008) first achieved this by changing diabatic heating rate in a PE dry GCM forced with Newtonian cooling. In order to vary the diabatic heating rate by several orders, Zurita-Gotor only changed the forcing time scale for the zonal mean flow and kept the diabatic damping time scale for the eddies to be the same. He showed that criticality increases when the diabatic heating rate increases and that there is nothing special about the state $\xi \approx 1$. In a later study, Zurita-Gotor and Vallis (2009) applied the same diabatic forcing technique in a two-level PE model on a β plane. By using a high diabatic heating rate, along with adjusting f and β, they obtained the classical $-5/3$ energy spectrum in the barotropic part of the flow, suggesting the existence of an inverse cascade. More recently, Jansen and Ferrari (2012) showed that criticality can be continuously varied by changing the thermal expansion coefficient in a Boussinesq model. When the thermal expansion coefficient decreases from atmosphere-like values to ocean-like values, the mean flow transits from marginally critical ($\xi \sim 1$) to highly supercritical states ($\xi \gg 1$). Jansen and Ferrari (2013a) further suggested that the constraint $\xi \approx 1$ can break down because the Schneider's (2004) formulation of averaging along isentropes in the surface layer is not consistent with the turbulence diffusive closure. Their subsequent scalings for criticality clearly suggested that criticality can vary with changes in the radiative forcing, and to a greater extent, with changes in the size and rotation rate of the planet (Jansen and Ferrari 2013b). The highly supercritical states are most likely to exist in real geophysical flows where the planetary radius is much larger than

the Rossby radius. This may account for the possible existence of inverse cascade in Jupiter's atmosphere (Choi and Showman 2011) and in Earth's ocean (Scott and Wang 2005).

These studies provide a basis for studying the relationship between eddy scale and criticality in a PE model. Interestingly, Zurita-Gotor (2008) showed that when criticality is increased by increasing the diabatic heating rate, the eddy scale *increases* while the Rossby radius *decreases*. This opposite trend of eddy scale and Rossby radius is surprising and suggests that the inverse cascade may increase its extent with criticality. However, Zurita-Gotor (2008) noticed that the measure of inverse cascade proposed by Schneider and Walker (2006), defined as the ratio between eddy available potential energy and baroclinic eddy kinetic energy, does not clearly support there being a significant inverse cascade in his simulations.

In this study, we aim to quantify the role of the criticality and the inverse cascade in setting the eddy scale in dry primitive equation model. (We do not involve ourselves in the discussion of whether and how states of high criticality can be reached in a natural way; rather, we treat criticality as an external parameter that can be varied using the thermodynamic forcing.) The regime we focus on involves criticality varying near unity, such that the flow transitions from a weakly nonlinear regime to a strongly nonlinear regime. This regime is further complicated by the fact that in linear QG instability theory, the most unstable wavelength has a dependency on criticality when criticality varies near 1. This may provide an additional mechanism for the eddy to adjust its length scale to an increased criticality without involving a well-developed inverse cascade. The classical Charney problem well illustrates this mechanism but fully solving that problem is analytically difficult and uninformative. Instead, by simple rescaling, we derive a simple approximate estimate for the most unstable wavelength's dependency on criticality in the Charney problem, and this work is presented in section 2. The numerical model we use to test the theory is described in

section 3 as are some numerical experiments. We use both a full model and a model that is modified to remove eddy-eddy interactions in order to quantify the role of the inverse cascade. Section 4 further analyzes the modeling results. Our overall goal is to understand the conditions under which, when criticality is varied, the inverse cascade is responsible for the increase in eddy scale, or whether we can understand eddy scale from linear or weakly nonlinear theory; a specific goal would be to estimate the eddy scale as a function of Rossby radius and criticality. Section 5 finishes with some concluding remarks.

6.2 Notation and linear instability theory

a. Definition of criticality

Following Jansen and Ferrari (2012, 2013), we define criticality as

$$\xi = \left| \frac{f \partial_y \overline{\theta}}{\beta \Delta_V \overline{\theta}} \right|, \tag{6.1}$$

where $\Delta_V \overline{\theta} = \overline{\theta}_t - \overline{\theta}_s$ is the potential temperature difference between the surface and tropopause, which is often called the bulk stability. The overbars denote temporal and zonal means. In pressure coordinates, we estimate the bulk stability as

$$\Delta_V \approx -\overline{\partial_p \theta}^s (\overline{p}_s - \overline{p}_t), \tag{6.2}$$

where the superscript s means that the evaluation is done near the surface; $\overline{p}_t$ and $\overline{p}_s$ denote the pressure at the tropopause and surface respectively[1].

[1] In Schneider and Walker's (2006) original paper on criticality, they defined $\Delta_V \approx -2\overline{\partial_p \theta}^s (\overline{p}_t - \overline{p}_s)$ and derived the constraint $\xi \sim 1$ under this definition. Jansen and Ferrari (2013a) suggested that Schneider and Walker's formulation of averaging along isentropes in the surface layer is not consistent with the diffusive closure and dropped the factor 2 noting there is nothing special about the observed $\xi \sim 1$ as criticality can be varied smoothly. In practice, the exact value of criticality depends on the latitude at which f and β are calculated, and also depends on the region one chooses to average over. Therefore, we also drop the factor of 2.

In spherical geometry, f and β cannot be adjusted independently, but the ratio f/β is on the order of the planetary radius. Therefore, $f\partial_y\overline{\theta}/\beta$ approximates the potential temperature difference between the subtropics and the pole, which we denote as Δ_h. The state $\xi \sim 1$ can be interpreted as an isentrope starting at the surface in the subtropics and ending at the tropopause near the pole. Intuitively, criticality can be thought as the isentropic slope if we plot isentropes in a coordinate such that the troposphere has the same meridional and vertical length scales.

b. Most unstable wave's dependency on criticality

The most unstable wavelength in the simplest Eady model only depends on Rossby radius. In more realistic models on a β plane, the most unstable wavelength usually has some dependency on criticality. For example in the two-layer Phillips model, the most unstable wavelength increases with criticality, though the dependency is weak. The dependency is much stronger in a continuous model, especially when criticality is much smaller than 1, and becomes weaker when criticality increases above 1. In the following, we show this using the Charney model and derive a simple approximate relationship between the most unstable wave's scale and criticality.

The Charney problem considers the QG instability of a non-Boussinesq continuously stratified fluid on the $\beta-$plane with a rigid bottom boundary condition (Charney 1947; Vallis 2006, Chapter 6; Pedlosky 1979, Chapter 7). The QG equation for the perturbation stream function Ψ, linearized about a zonally and meridionally homogeneous mean flow $U(z)$, is

$$\left(\frac{\partial}{\partial t} + U\frac{\partial}{\partial x}\right) q + \frac{\partial \Psi}{\partial x}\frac{\partial Q}{\partial y} = 0, \tag{6.3}$$

where q and Q are the potential vorticities of the perturbation and the mean flow respectively, and they are given by

$$q = \nabla^2\Psi + \frac{f^2}{\rho}\frac{\partial}{\partial z}\left(\frac{\rho}{N^2}\frac{\partial\Psi}{\partial z}\right), \quad \frac{\partial Q}{\partial y} = \beta - \frac{f^2}{\rho}\frac{\partial}{\partial z}\left(\frac{\rho}{N^2}\frac{\partial U}{\partial z}\right). \tag{6.4}$$

The rigid bottom boundary condition is

$$\left(\frac{\partial}{\partial t} + U\frac{\partial}{\partial x}\right)\frac{\partial\Psi}{\partial z} - \frac{\partial\Psi}{\partial x}\frac{\partial U}{\partial z} = 0, \quad \text{at } z = 0, \tag{6.5}$$

and the other boundary condition is that the perturbation vanishes at infinity:

$$\Psi(z = \infty) \to 0. \tag{6.6}$$

For the Charney problem, further simplifications for the mean flow and stratification are made. The zonal flow is assumed to have a constant vertical shear, such that $U(z) = (\partial_z U)z$, where $\partial_z U$ is constant. The vertical stratification specified by the Brunt-Väisälä frequency N is assumed to be constant. The density profile is characterized by a density scale height as $\rho = \rho_0 \exp(-z/H_\rho)$. Therefore, we can rewrite (6.4) as

$$q = \nabla^2\Psi + \frac{f^2}{N^2}\frac{\partial^2\Psi}{\partial z^2} - \boxed{\frac{f^2}{N^2 H_\rho}\frac{\partial\psi}{\partial z}}, \quad \frac{\partial Q}{\partial y} = \beta + \boxed{\frac{f^2\partial_z U}{N^2 H_\rho}} \tag{6.7}$$

where the boxed terms arise from density's derivative with respect to height. For a Boussinesq fluid that has no density variation, all the boxed terms above and in the following will disappear. As we will see later, the density variation introduces a significant difference between non-Boussinesq and Boussinesq flow.

As usual, we nondimensionalize the equation using

$$x,\ y = L_R(\hat{x},\ \hat{y}), \tag{6.8a}$$

$$z = H_\rho \hat{z}, \tag{6.8b}$$

$$t = L_R/(H_\rho \partial_z U)\hat{t}, \tag{6.8c}$$

where hats denote nondimensional quantities and the horizontal scale is the Rossby radius defined as:

$$L_R = \frac{NH_\rho}{f}. \tag{6.9}$$

A nondimensional parameter, which we define to be criticality for the Charney problem, naturally arises after the nondimensionalization:

$$\xi = \frac{f^2 \partial_z U}{\beta N^2 H_\rho}. \tag{6.10}$$

All information on the mean flow (shear, stratification, density profile, latitude, and etc.) is absorbed into this single parameter ξ after nondimensionalization, as Eq. (6.3) becomes

$$\left(\frac{\partial}{\partial \hat{t}} + \hat{z}\frac{\partial}{\partial \hat{x}}\right)\left(\hat{\nabla}^2 + \frac{\partial^2}{\partial \hat{z}^2} - \boxed{\frac{\partial}{\partial \hat{z}}}\right)\Psi + \left(\frac{1}{\xi} + \boxed{1}\right)\frac{\partial}{\partial \hat{x}}\Psi = 0, \tag{6.11}$$

and the boundary conditions (6.5) and (6.6) become

$$\frac{\partial^2 \Psi}{\partial \hat{t}\partial \hat{z}} - \frac{\partial \Psi}{\partial \hat{x}} = 0, \quad \text{at } \hat{z} = 0, \tag{6.12}$$

and

$$\Psi(\hat{z} = \infty) \to 0. \tag{6.13}$$

With the thermal wind relation, we can rewrite (6.10) as

$$\xi \approx \frac{f}{\beta H_\rho} |\frac{\partial_y \theta}{\partial_z \theta}|$$

and immediately see its relevance to the criticality definition in (6.1). Compared with the usual definitions for Rossby radius and criticality in a PE system, the density scale height replaces the tropopause height in (6.9) and (6.10). For Earth's atmosphere, the tropopause height and density scale height are of the same order in the extratropics. Also with $-\overline{\partial_p \theta}^s \sim g^{-1}\overline{\partial_z \theta}^s/\overline{\rho}^s \sim H_\rho \overline{\partial_z \theta}^s/\overline{p}_s$, we can rewrite the bulk stability in (6.2) as

$$\Delta_V \approx -\overline{\partial_p \theta}^s (\overline{p}_t - \overline{p}_s) \sim H_\rho \overline{\partial_z \theta}^s \frac{\overline{p}_s - \overline{p}_t}{\overline{p}_s}.$$

As long as the tropopause pressure is much smaller than surface pressure, $H_\rho \overline{\partial_z \theta}^s$ can serve as a lowest order estimate for bulk stability. Therefore, we use (6.9) and (6.10) as the definitions for Rossby radius and criticality respectively in the Charney problem.

Assuming plane-wave solutions of the form

$$\Psi = \psi(\hat{z}) \exp[ik(\hat{x} - c\hat{t})] \tag{6.14}$$

to the nondimensionalized equation (6.11) and its boundary conditions (6.12-6.13), the equation describing the vertical structure of the wave is

$$\frac{d^2\psi}{d\hat{z}^2} - \boxed{\frac{d\psi}{d\hat{z}}} - \left(k^2 - \frac{1/\xi + \boxed{1}}{\hat{z} - c} \right) \psi = 0, \tag{6.15}$$

with boundary conditions at rigid bottom and at infinity

$$c\frac{d\psi}{d\hat{z}}(0) + \psi(0) = 0, \quad \psi(\infty) \to 0. \tag{6.16}$$

For a given pair of criticality ξ and wavenumber k, the above equation (6.15) and its boundary conditions (6.16) form an eigenvalue problem. We can solve it to get an eigenfunction ψ and eigenvalue c. If the complex part of kc is positive, the wave is unstable. Its growth rate is given by kc_i, where c_i denotes the complex part of c. For a given ξ, there exists a unique k_m for which $k_m c_i$ reaches its maximum value $(kc_i)_{\max}$, where the subscript "max" denotes the maximum value of the bracket for k over $(0, \infty)$ and a definite ξ. The wave solution (6.14) with the wavenumber k_m is referred as the most unstable wave. It is often thought that the most unstable wave will dominate over other waves at finite amplitude, so the corresponding most unstable wavelength gives the energy containing eddy scale. Clearly, the most unstable wavenumber k_m is a function of criticality ξ.

To see how ξ controls most unstable wave, we rescale the variables as

$$\hat{z} = z^* / \left(\frac{1}{\xi} + \boxed{1} \right), \; c = c^* / \left(\frac{1}{\xi} + \boxed{1} \right), \; k = k^* \left(\frac{1}{\xi} + \boxed{1} \right). \tag{6.17}$$

Then the Eqs. (6.15) and (6.16) become

$$\frac{d^2\psi}{dz^{*2}} - \boxed{\frac{\xi}{\xi + 1} \frac{d\psi}{dz^*}} - \left(k^{*2} - \frac{1}{z^* - c^*} \right) \psi = 0, \tag{6.18}$$

$$c^* \frac{d\psi}{dz^*}(0) + \psi(0) = 0, \; \psi(\infty) = 0. \tag{6.19}$$

Under this rescaling the growth rate is unchanged as $kc = k^* c^*$, so the most unstable wave in the rescaled Eqs. (6.18) and (6.19) are also related to that in the Eqs. (6.15) and (6.16) through the rescaling relation (6.17). If the fluid is Boussinesq, the boxed terms are dropped. Therefore Eqs. (6.18) and (6.19) have no reference to the mean flow, and the most unstable wavenumber k_m^* for the rescaled equations is a constant for any ξ. Therefore for the Boussinesq fluid, rescaling relation (6.17) gives the familiar results that the most unstable wave has horizontal scale proportional

to $L_m \sim f\partial_z U/(\beta N)$ and vertical scale proportional to the Charney height $h = f^2\partial_z U/(\beta N^2)$.

For a compressible fluid, we cannot eliminate the dependency on the mean flow by this simple rescaling. But notice that the dependency on ξ in (6.18) is weak as $\xi/(1+\xi)$ only varies from 0 to 1 when ξ varies from 0 to ∞. Without the rescaling, the original Eq. (6.15) has a much higher dependency on ξ as $1/\xi$ can vary from 0 to ∞. So we may expect that for the rescaled equation (6.18) and its boundary condition (6.19), the most unstable wavenumber k_m^* is only weakly dependent on ξ. If so, we can drop the dependency of k_m^* on ξ, such that $k_m^*(\xi) \approx \overline{k_m^*}$, where $\overline{k_m^*}$ represents a characteristic value of k_m^*. Use rescaling (6.17) we get the dependency of k_m on criticality as $k_m(\xi) \approx (1 + 1/\xi)\overline{k_m^*}$. Finally, we can get the dimensional most unstable wavenumber for the original equation (6.3) by adding the length scale described by nondimensionalization relationship (6.8). Converting the wavenumber into wavelength, we get in dimensional variables that the most unstable wavelength is

$$L_m \approx C\frac{\xi}{\xi+1}L_R, \tag{6.20}$$

where $C = 2\pi/\overline{k_m^*}$ is the approximate constant. Its vertical scale is

$$h_m \approx D\frac{\xi}{\xi+1}H_\rho, \tag{6.21}$$

where D is another approximate constant on the order of 1. To test whether the above scalings offer a good estimate, we resort to numerical solutions. Before doing this, we note that the rescaling (6.17) was used by Lindzen and Farrell (1980a) to obtain an approximate simple formula for the maximum growth rate. Also, similar forms of the most unstable wavelength's estimate as (6.20) exist in the literature. Branscome (1983) derived the same estimate (6.20) through perturbation methods

in the short-wave limit ($k \gg 1$) and near the neutral curve separating Charney and Green modes (the right side boundary of the growth rate contour shown in Fig. 6.1), and he determined C to be 12. Wang et. al. (1985) obtained a more complicated estimate by using an integral representation of the solution and a Frobenious series expansion, and his estimate was later simplified into $L_m \sim 2\pi\xi/(0.48\xi + 1.48)L_R$ (Stone and Yao 1990; Barry, Craig and Thuburn 2002). Above all, the asymptotic limits for our scaling estimates are well-known (Held 1978; Vallis 2006). When $\xi \ll 1$ both horizontal and vertical scales of the most unstable wave are linearly proportional to ξ:

$$L_m \sim O(\xi L_R),\ h_m \sim O(\xi H_\rho),\ \text{when } \xi \ll 1.$$

In this limit, the vertical scale of the wave is much smaller than scale height, so we refer to such waves as *shallow wave*s. When $\xi \gg 1$ the sensitivity of L_m and h_m on ξ saturates. The horizontal scale is only given by deformation radius, while the vertical scale is limited by the density scale height, written as

$$L_m \sim O(L_R),\ h_m \sim O(H_\rho),\ \text{when } \xi \gg 1.$$

We refer to these waves as *deep waves* as their vertical scale is comparable to the scale height. Our scaling estimates (6.20) and (6.21) connect the two limits with a smooth transition.

c. Numerical validation

The non-dimensionalized Charney problem described by Eqs. (6.15) and (6.16) are solved numerically for various values of criticality ξ and wavenumber k. As we are interested in the regime $\xi \sim O(1)$, we vary ξ between 0.1 to 4. Fig. 6.1 is a contour of the growth rate against inverse wavenumber $1/k$ and ξ, together with two curves showing the numerically obtained inverse of the most unstable wavenumber $1/k_m$ and

our scaling estimate $1/k_m \approx 1.54\xi/(1+\xi)$, where the constant 1.54 is determined by a least square fit to give the best agreement between the our scaling estimate and numerical result. Only the Charney mode regime is plotted. The other modes have smaller maximum growth rates compared with the Charney mode (Pedlosky 1979). Clearly our scaling estimate gives a good approximation to the numerical results. The difference between the two is within 0.08. To convert wavenumber into wavelength, a factor of 2π needs to be multiplied. So in dimensional variables, our scaling estimate for most unstable wavelength is

$$L_m \approx 9.7\frac{\xi}{\xi+1}L_R.$$

Fig. 6.2a shows the vertical structure of the most unstable wave for $\xi = 1$. Three curves are shown, corresponding to amplitude of perturbation $|\psi|$, heat flux $\overline{v'\partial_z\psi}$, and PV flux. All of them are normalized by their maximum values. Generally for the most unstable wave, the heat flux decreases rapidly with height. To the lowest order, the vertical profile of heat flux can be approximated by an exponential decay:

$$\overline{v'\partial_z\psi} \sim \exp(-z/h_\theta). \tag{6.22}$$

Therefore we use (6.22) as the definition for the vertical scale of the wave, such that the vertical scale of the wave h_θ is the e-folding height of the heat flux. For the real atmosphere or a primitive equation model, we replace the heat flux in (6.22) by the potential temperature (PT) flux $\overline{v'\theta'}$. We can find h_θ by fitting the PT flux profile to an exponential function. To test our estimate for the vertical scale of the most unstable wave in (6.21), we calculate h_θ from the numerical solutions of the most unstable wave for different ξ and plot their relationship in Fig. 6.2b. The best estimate is $h_\theta \sim D\xi/(1+\xi)$, with the parameter D determined to be 1.09.[2] Again,

[2]Held (1978) gave a formally similar estimate for the vertical extent of eddy PV fluxes. His definition of vertical extent is based on the e-folding scale of $\rho\overline{v'q'}$. The density profile multiplied

our scaling estimate provides a reasonable approximation to the numerical results. Their difference is within 0.11. Because of the analytical difficulty in solving Charney problem, whose solution involves hypergeometric functions, deriving a more accurate estimate for the most unstable wavenumber will presumably make the formula more complicated. Therefore, our scaling estimate is useful in the sense that it provides a simple estimate for both practical use and theoretical understanding.

6.3 Idealized GCM and experiments

a. Model description

We investigate how eddy scale depends on criticality in an idealized GCM. The GCM is a primitive-equation model of a dry ideal gas atmosphere on a sphere of Earth's radius and rotation rate. The primitive equations are integrated with the spectrum transform method in the horizontal with resolution T42, and centered difference scheme in the vertical, with evenly spaced vertical σ levels. There is no bottom topography at the lower boundary. It is forced by idealized Held and Suarez (1994) physics where radiation is represented by a Newtonian relaxation of temperature to a prescribed "radiative equilibrium" profile and dissipation is represented by a Rayleigh damping of the velocities in the "boundary layer" ($\sigma \geq 0.7$). The model setup is very similar to that described in Zurita-Gotor (2008), except that we use a thermal relaxation rate of 1/40 day^{-1} in the free troposphere, which is the original value used by Held and Suarez (1994), and we use 30 vertical levels.

Criticality is varied by varying thermal forcing. To vary the thermal forcing by several orders without damping out the eddies, Zurita-Gotor (2008) suggests seperating the forcing into zonal mean flow and eddy terms, and only vary the forcing time

to PV flux limits this vertical extent with an upper bound of density scale height, whereas in our definition the vertical scale h_θ can be larger than density scale height. That h_θ saturates when ξ becomes large is not because of being limited by density's decay with height.

scale on the mean flow. The thermodynamic equation is then

$$\frac{\partial T}{\partial t} = \ldots - k_T T' - \gamma k_T (\overline{T} - T_{eq}).$$

Overbars denote zonal mean fields and primes denote the deviations from zonal means. The forcing on the zonal mean flow is increased by γ times. Presumably, we can have a very high forcing rate on the mean flow so that the time-mean temperature field is close to the prescribed profile, while the eddies are still nearly adiabatic.

b. Reduced GCM

In order to isolate the effects of the inverse energy cascade on the eddy scale, we use the GCM without nonlinear eddy-eddy interactions introduced by O'Gorman and Schneider (2007), which we will refer as the *reduced* GCM. As a comparison, the original GCM described above is referred as the *full* GCM. The reduced GCM is constructed from the full GCM by eliminating the nonlinear eddy-eddy interactions but retaining the eddy/mean-flow interactions. Therefore in the reduced GCM, there is no inverse cascade, which is a scale-by-scale energy transfer, but there is still direct energy transfer between eddy and mean flow (Tobias and Marston 2013). We run the reduced GCM in parallel with the full GCM. The reduced GCM has shown to reproduce many atmospheric flow features, including the eddy length scale, the -3 slope in energy spectrum and the jet formation. This is interpreted as the Earth-like regime being weakly nonlinear (O'Gorman and Schneider 2007).

c. Series of simulations

To vary criticality, we vary the rate of thermal forcing on the mean flow by changing γ. The baroclinicity is varied by varying δ_y. For each setting of δ_y =30, 60, 90, and 120 K, we consider 9 different values of γ=(0.1, 0.2, 0.5, 1, 2, 5, 10, 20, 40). For

$\gamma = 1$ run, the forcing rates on zonal mean flow and eddies are the same, and we refer it as the control run. We run each combination of δ_y and γ in both the full and reduced GCMs. Each simulation is integrated for 1500 days. The first 1000 days are discarded as spin-up and the last 500 days are used to calculate the flow statistics.

6.4 Results

A comparison of the basic climatology of the control run with $\gamma = 1$ and $\delta_y = 60$ K from the full and reduced GCMs is shown in Fig. 6.3. The full GCM simulation resembles Earth's climatology. It has similar magnitude of zonal wind and eddy kinetic energy (EKE= $(\overline{u'^2} + \overline{v'^2})/2$) as Earth. We determine the tropopause height using Schneider's (2004) definition, that the tropopause is the boundary layer below which the bulk of the entropy the atmosphere receives by the heating at the surface is redistributed. Schneider's (2004) definition is based on isentropic diagnostics, and we use Czaja and Marshal's (2006) method to convert fields from pressure coordinates to isentropic coordinates. This tropopause is lower than the WMO tropopause. We use Schneider's tropopause for evaluations of criticality and Rossby radius. Repeating the calculations using the WMO tropopause does not change the results much. The reduced GCM can reproduce the upper-level westerly jets, which are driven by the eddy/mean-flow interactions. But the jets are narrower in the reduced GCM, and there is an extra jet in each hemisphere. The EKE in the reduced GCM is about 2 times larger than that in the full GCM. These results are in accordance with O'Gorman and Schneider (2007). In the following, all simulations are from full GCM if not specified. We will only use reduced GCM in subsection (a).

In our study, the tropopause height varies little because the mean extratropical surface temperature changes little by our model construction (Eq. [17] in Zurita-Gotor 2008; also see Schneider 2007). Therefore the variation of bulk stability Δ_v

is mostly due to variation of $|\overline{\partial_p \theta}|$, which is a measure of vertical stability. $|\overline{\partial_p \theta}|$ is set by two competing processes. The first process is the Newtonian relaxation of the temperature field to the prescribed radiative equilibrium profile. As the prescribed profile in extratropics has very small thermal stratification, this process tends to reduce the vertical stability. The second process is the baroclinic eddy activity, which modifies the thermal stratification (Schneider and Walker 2006, 2008), and in our cases it increases the stratification above that of the prescribed profile.

Fig. 6.4 shows that for the runs with $\gamma = 1$ and varying δ_y, the bulk stability $\Delta_v = |\overline{\partial_p \theta}^s(\overline{p}_t - \overline{p}_s)|$ increases proportionally with the scaled meridional temperature gradient $\Delta_h = |(f/\beta)\partial_y \overline{\theta}^s|$. This is because when δ_y increases and other parameters are kept the same, the meridional temperature gradient and baroclinicity increase, and as a result the eddy activity becomes stronger. The stronger eddies transport more heat upward, which increases the vertical stability. The temperature gradients $\partial_y \overline{\theta}^s$ and $\overline{\partial_p \theta}^s$ are evaluated at 850 mb and averaged over the baroclinic zone, defined as the region where the PT flux at 850 mb $\overline{v'\theta'}^s \cos(\phi)$ is within 30% of its maximum. We use superscript s in this section to denote that the evaluation is done at 850 mb. The Coriolis parameters f and β are evaluated at the reference latitude that is defined as the centroid of the PT flux at 850 mb in each hemisphere:

$$\phi_{\text{ref}} = \frac{\int_0^{\pi/2} \phi \overline{v'\theta'}^s \cos(\phi) d\phi}{\int_0^{\pi/2} \overline{v'\theta'}^s \cos(\phi) d\phi}.$$

Under these conventions, the criticality $\xi = \Delta_h/\Delta_v$ for the control simulations ($\gamma = 1$) is close to one. These results are in accordance with Schneider and Walker's (2006) that criticality is not sensitive to changes in radiative equilibrium baroclinicity.

Following Zurita-Gotor (2008), we vary the criticality by varying γ, which controls the thermal forcing rate on the mean flow. When γ increases, the vertical stratification transitions from the regime that it is set by eddy activity to the regime that is set

by the thermal forcing. For the series of runs with fixed δ_y but increasing γ, Δ_v initially increases nearly proportional to Δ_h when $\gamma \leq 0.5$ (Fig. 6.4). This is the regime in which eddy activity dominates over thermal relaxation in setting the thermal stratification. In this regime, the criticality stays close to 1. When γ further increases above 1, Δ_v starts to decrease while Δ_h saturates. This is because thermal relaxation becomes so strong that it forces the Δ_v and Δ_h to approach the values of prescribed profile. For $\delta_y = 90$ K and 120 K, Δ_h decreases slightly when γ is very large because the PT flux moves slightly towards the equator, so the reference latitude and f/β decrease slightly.

Our major motivation is to investigate the eddy scale's relationship to criticality. As criticality is varied by varying γ, we show the eddy scale L_e vs. γ for runs with $\delta_y = 60$ K in Fig. 6.5a, along with the Rossby radius L_R. The eddy scale and Rossby radius are normalized by their control values ($\gamma = 1$). The eddy scale is calculated from the "inverse centroid" of the barotropic EKE spectrum (see Appendix A). The Rossby radius is calculated as

$$L_R = \frac{N_p(\bar{p}_s - \bar{p}_t)}{f}, \tag{6.23}$$

where $N_p^2 = -(\overline{\rho}^s\overline{\theta}^s)^{-1}\overline{\partial_p\theta}^s$ is a vertical stability measure, evaluated at 850 m; $\bar{p}_s$ and $\bar{p}_t$ are the surface pressure and tropopause pressure respectively. N_p, $\bar{p}_s$ and $\bar{p}_t$ are averaged over the baroclinic zone. This Rossby radius multiplied by an empirical constant is shown to be a good estimate for eddy scale for a wide range of climates whose criticality is close to 1 (Merlis and Schneider 2009). However, when γ varies the Rossby radius can no longer offer a good estimate for eddy scale. As shown in Fig. 6.5a, when γ increases the eddy scale increases monotonically[3]; while the Rossby

[3]In Zurita-Gotor's (2008), the eddy scale saturates at largest γ, while in our simulations eddy scale does not saturate. This is mainly because we calculated eddy scale using the inverse centroid rather than the centroid of the EKE spectrum, which gives more weight to larger scales. Also, the largest thermal forcing rate we used is still 5 times smaller than that used by Zurita-Gotor. This

radius initially increases with a similar trend when $\gamma \leq 0.5$, and then decreases steady when γ increases above 1. The decrease in Rossby radius is mainly dominated by the decrease in vertical stability N_p as shown in Fig. 6.5b. Again, N_p decreases because the thermal forcing dominates over eddy activity in setting vertical stratification when γ is large, so that N_p is relaxed towards the prescribed equilibrium profile. The tropopause height $H_p = \bar{p}_s - \bar{p}_t$ increases slightly when γ is small and then saturates for large γ. If WMO tropopause definition is used, the decreasing trend for Rossby radius is even stronger as the WMO tropopause height slightly decreases for large γ. If the density scale height is used to evaluate Rossby radius as that in the Charney problem, the results here and in the following would not change much either. This is because changes in vertical stability dominate changes in Rossby radius in our simulations. For all series of simulations with different δ_y as shown in Fig. 6.6, the criticality and eddy scale increases steady with γ, while Rossby radius decreases when γ becomes large enough. For the range of δ_y and γ in this study, criticality is approximately a function of γ.

Why can the eddy scale and Rossby radius have opposite trends when criticality varies? One possible explanation comes from the Rhines scale argument. When thermal forcing is accelerated, eddies become more energetic. So it is obvious that the Rhines scale would increase, which gives the correct trend for the eddy scale. Quantitatively, the Rhines scale gives a good estimate for the eddy scale for all the runs as shown in Fig. 6.7b. On the other hand, Rossby radius can predict the eddy scale only when criticality is nearly constant, as can been seen if we connect the points in Fig. 6.7a that have the same γ and different δ_y. However, the Rossby radius loses its predictive power when criticality varies. The Rhines scale is calculated as

$$L_\beta = \sqrt{\frac{1/2\overline{\mathbf{u}'^2_{\mathrm{bt}}}}{\beta}}$$

difference does not change our results much as in both cases, the ratio of eddy scale and Rossby radius does not saturate.

in accordance with Schneider and Walker (2006). The barotropic velocity $\mathbf{u}_{\mathrm{bt}}$ is calculated by averaging the horizontal velocity (including both zonal and meridional velocities) vertically from the lowest layer to 150 mb. The barotropic EKE $1/2\overline{\mathbf{u}_{\mathrm{bt}}'^2}$ is averaged over the baroclinic zone.

It may seem that the increase in eddy scale can be interpreted as an increase in the extent of the inverse cascade when criticality increases. However, one needs to be cautious to make this conclusion, as we show in section 2 that the most unstable wavelength increases with criticality, which allows the eddy scale to adjust without involving an inverse cascade. In order to quantify the role of the inverse cascade in determining eddy scale, we compare the results from the full GCM with that from the reduced GCM in the following subsection. The reduced GCM does not have eddy-eddy interaction, so it does not support an inverse cascade. In addition, we calculate the spectral EKE budget for the full GCM runs. Therefore we can clearly see how the inverse cascade contributes to the eddy scale.

a. Role of inverse cascade

The reduced GCM can reproduce many first and second order flow statistics from the full GCM. Eddy statistics are examined using the barotropic EKE spectrum. The spectrum is defined using spherical wavenumbers (see Appendix A). Fig. 6.8 compares the barotropic EKE spectra for runs with $\delta_y = 60$ K and varying thermal forcing $\gamma = 0.1$, 1 and 10 from both the full and reduced GCMs. The shape of the energy spectrum in the reduced GCM shares many similarities with that of full GCM. In wavenumber regime 10$\sim$40, all the full GCM runs exhibits the n^{-3} power-law range. On the other hand, in the reduced GCM, for $\gamma = 0.1$ and 1, the spectrum exhibits the -3 slope. For $\gamma = 10$ the slope is shallower than -3 for wavenumber 20$\sim$40. This shallower spectrum in the reduced GCM is explained by O'Gorman and Schneider (2007) as the lack of eddy-eddy interactions preventing the build-up of

energy at small scales. On the larger scales where wavenumber is smaller than 10, the energy spectra in the reduced GCM are generally lower than that in the full GCM, which suggests that the nonlinear eddy-eddy interaction does transfer some energy upscale.

It is striking that the eddy scales are comparable in the full and reduced GCMs. For $\gamma = 1$, the most energetic wavenumbers are both 8 in full and reduced GCMs, so the eddy scales are very similar in both GCMs. More interestingly, in the reduced GCM eddy scale increases with γ similarly to that of the full GCM. Fig. 6.9a compares the eddy scale for all runs from the full and reduced GCMs. The eddy scales in the full and reduced GCMs roughly changes proportionally to each other with a slope close to 1 for $\gamma \leq 10$. This suggests that in the full GCM the eddy scale can increase with criticality without involving an inverse cascade before it enters the strongly nonlinear regime. In the high criticality end where $\gamma \geq 10$, the eddy scale in the reduced GCM saturates or even decreases while eddy scale in the full GCM continues to increase. This implies that eddy-eddy interactions become important in inversely cascading EKE to larger scales.

Another confirmation is from spectral EKE budget analysis (see Appendix B for the methods). We calculate the average scale at which available potential energy is converted into eddy kinetic energy, which we refer as the EKE generation scale. Fig. 6.9b compares the EKE generation scale with the eddy scale, both from the full GCM. The energy generation scale generally increases proportional to the eddy scale until γ increases above 10, beyond which the energy generation scale saturates. Therefore, we conclude that when criticality varies around 1, there exists a weakly nonlinear regime in which the eddy scale can increase with criticality *without* involving the inverse cascade, but the EKE generation moves to larger scales as well. When criticality increases above the weakly nonlinear regime, the nonlinear eddy-eddy interactions become important, and the inverse cascade plays a role in continuing to increase the

eddy scale. In the weakly nonlinear regime, we need an explanation for why the eddy scale and Rossby radius can have different trends.

b. Linear instability perspective

Discussions in section 2 suggest that the most unstable wavelength depends on criticality. When criticality varies, the Rossby radius is not enough to estimate the most unstable wavelength. This may solve the apparent conundrum that the eddy scale and Rossby radius can have opposite trends when criticality is varied. In the following, we only use results from the full GCM.

The Charney problem predicts that when the most unstable wave transitions from being a shallow wave to a deep wave, it also increases its wavelength. However, if the vertical scale of the wave is already so large that it is comparable to density scale height, the most unstable wavelength is no longer sensitive to criticality. Fig. 6.10 shows the eddy flux of potential temperature $\overline{v'\theta'}\cos(\phi)$ for γ=0.1, 1, 10 from simulations with δ_y=60 K. The potential temperature flux reaches its maximum near the surface. For very small γ=0.1, the maximum occurs above the surface near 850 mb. This is probably because of the Rayleigh damping in the "surface layer" that reduces eddy amplitude. For larger γ, the maximum moves towards the surface. Clearly, the vertical extent of the eddy PT flux gradually increases when γ increases. The change in tropopause height also captures the increase of eddies' vertical extent to some degree.

To obtain a quantitative estimate for the change in the wave's vertical scale, we calculate the vertical scale of the wave h_θ defined in Eq. (6.22), where h_θ is the e-folding scale of the eddy PT flux. Fig. 6.11a shows the vertical eddy PT flux profile, which is $\overline{v'\theta'}\cos(\phi)$ horizontally averaged over the baroclinic zone. Clearly when γ increases, PT flux decreases with height slower, which means that the vertical scale of the eddies is larger. Because for very small γ the PT flux's maximum is above the

surface, and also the PT flux has a second maxima in the upper atmosphere near the tropopause, we only use the PT flux profile between 580 mb and 820 mb to extract the vertical scale of the eddies. This pressure range is marked by dashed lines in Fig. 6.11a. In practice, the ratio of the eddies' vertical scale h_θ to the density scale height H_ρ is naturally obtained by a linear regression between $\ln \overline{v'\theta'} \cos(\phi)$ and $\ln p$, if we assume that $p \approx p_0 \exp(-z/H_\rho)$. As shown in Fig. 6.11b, the vertical scale of the eddies h_θ generally increases monotonically with γ. For $\gamma \leq 10$, the vertical scale of the eddies generally increases from below the scale height towards the scale height. This suggests that the eddies can also increase their horizontal scales linearly as the most unstable wave. When γ increases above 10, the vertical scale of the eddies either saturates (for δ_y=90 and 120 K runs) or increases above the scale height (for δ_y=30 and 60 K runs), which suggests that the eddies enters the deep wave regime and the most unstable wavelength loses its sensitivity on criticality. In the deep wave regime, an inverse cascade is needed to continue increasing the eddy scale.

In the Charney model, the wave's vertical and horizontal scales increase nearly proportionally to each other. However, for all series of experiments here, the vertical scale of the wave generally increases by about a factor of 3 while eddy scale increases by about a factor of 1.7 when γ increases from 0.1 to 40. This discrepancy may result from the vertical inhomogeneity. In the model, the tropopause provides a dynamically relevant boundary layer, which may be viewed as a rigid lid as a first approximation. If we add a rigid lid in the Charney problem, in the limit $\xi \gg 1$, the most unstable wave will approach that in the Eady problem. In this limit, the vertical scale of the most unstable wave in our definition approaches infinity, as the Eady solution is vertically symmetric. Therefore, the vertical inhomogeneity may allow the vertical scale to increase faster than its horizontal scale when criticality increases.

The estimate for the most unstable wavelength, including its dependency on criticality, is given in Eq. (6.20) as $L_m \sim C L_R \xi/(1+\xi)$. Although L_R decreases when

γ increases, the increase in ξ can still give an increase in L_m. Therefore, the most unstable wavelength can increase despite the Rossby radius decreasing, giving the correct trend for eddy scale. As the exact value of criticality depends on the conventions we used, and there is a difference between the mean flows in the Charney model and our simulations, we expect to add a degree of freedom to criticality before we use Eq. (6.20). In the sense that eddy scale scales with the most unstable wavelength, our eddy scale estimate is

$$L_e \sim L_m \sim C L_R \frac{A\xi}{A\xi + 1},$$

where A and C are two empirical constants. The criticality in Eq. (6.20) is replaced by an "effective" criticality $A\xi$. Fig. 6.12b shows this estimate vs. the eddy scale from the simulations. The empirical constants are determined by a least square fit as C=8.7 and A=0.36. We see that our estimate is in good agreement with the simulations. That the "effective" criticality is smaller than criticality may partly result from the vorticity gradient of the jet $-\bar{u}_{yy}$ that adds to β (Zurita-Gotor 2007). Compared with Held and Larichev's (1996) scaling for eddy scale $C\xi L_R$, which is also the estimate for the most unstable wavelength in the shallow wave limit, our estimate has one more empirical constant A. However, this is necessary because the dependency of the eddy scale on criticality is not simply linear. This is seen in Fig. 6.12a, where we show the best fit using $C\xi L_R$, with C determined to be 1.8. This estimate increases too fast with criticality when criticality is large.

6.5 Conclusion and discussion

In this paper we have studied the relationship between criticality and eddy scale using a dry, three-dimensional, primitive equation model. By varying the Newtonian thermal forcing on the mean flow the criticality can be varied smoothly. The main

question we have tried to answer is: what is the role of the inverse cascade on eddy scale when criticality varies? We showed that when criticality varies near a value of one, there exists a weakly nonlinear regime in which the eddy scale increases with criticality without involving an inverse cascade. When criticality increases beyond this weakly nonlinear regime, the inverse cascade becomes important in continuing to increase the eddy scale. The Rossby radius is no longer a useful estimate for eddy scale as criticality increases and the Rossby radius and eddy scale can, in fact, have opposite trends.

To understand these results, we began with linear quasi-geostrophic instability theory, as the classical Charney model shows a dependency of the most unstable wavelength on criticality. By using a simple rescaling, we showed that both the horizontal and vertical scales of the most unstable wave increase with criticality and we derived approximate estimates for these scales. In the weakly nonlinear regime, the increase of eddy scale with criticality is found to be associated with the transition of the most unstable wave from a shallow wave into deep wave and the corresponding increase of the most unstable wavelength. The formula for the most unstable wavelength derived in Charney problem is modified to give a semi-empirical estimate for the eddy scale that is consistent with our simulations.

The way in which an eddy can adjust its horizontal and vertical scales when criticality varies has some precedents in the quasi-geostrophic literature although it has not been systematically studied. Thus, Held and O'Brien (1992) showed that in a three-layer QG model the vertical scale of eddies increases with increasing criticality, and that linear instability theory can make an adequate prediction for this vertical scale. Whitaker and Barcilon (1995) showed that in a two-layer QG model the most energetic wave increases its horizontal scale with increasing criticality without involving nonlinear upscale energy transfer. These studies were limited by their low vertical resolutions and QG studies with higher vertical resolutions would be useful.

Although the most unstable wave in the Charney problem shows quantitative similarities with the eddy scale in our simulations, there are still substantial difficulties in bridging linear instability theory with modeling results. The vertical and horizontal inhomogeneities of the time-mean flows in modeling prohibit extracting a simple relationship between the most unstable wave and criticality. Therefore, we need to resort to even simpler models such as the Charney problem, but still hope to capture the essential physics. A drawback of the Charney problem is that it does not take into account the tropopause. One step forward would be to consider the Green problem, which adds a rigid lid to the Charney problem to represent the tropopause (Green 1960). In the Boussinesq limit, the Green problem can be formulated with a single non-dimensional parameter, criticality (assuming constant vertical shear and Brunt-Väisälä frequency, and using tropopause height as the vertical scale). In this limit, the most unstable wavelength has a similar dependency on criticality as the Charney problem (see Fig. 3 in Green 1960). This may suggest that for more general time-mean flows, the most unstable wavelength can increase with criticality when it varies near 1, and saturates when criticality is much larger than 1. Nevertheless, the tropopause has a significant impact on the vertical structure of the unstable waves. For example, a more realistic representation of tropopause leads to larger upper-level amplitudes for the unstable waves (Simmons and Hoskins 1976, 1977).

There are of course alternate theories that may explain the behavior of the horizontal and vertical scales of eddies in modeling. One alternative is that the horizontal scale is proportional to the wavelength of the (first) neutral mode in the Charney problem, which also increases with criticality (see Fig. 6.1). Exact analytical expressions exist for the wavelength of neutral modes. For example, the wavelength of the first neutral mode is $4\pi L_R \xi / \sqrt{2\xi + 1}$ (Burger 1962). Another alternative is that the vertical scale of eddies is determined by the baroclinic adjustment hypothesis (Lindzen and Farrell 1980b; Held 1982), that the vertical scale is the minimum height above the

ground up to which eddies need modify the flow in order to neutralize it. Applying this hypothesis to the Charney problem leads to a vertical scale $H_\rho \ln(1+\xi)$. If we replace the criticality in these formulas with an "effective" criticality $A\xi$, it is difficult to check which formula works better.

It is interesting that, although the inverse cascade is not important in most of our simulations, the Rhines scale still serves as a good estimate for the eddy scale in most simulations (Fig. 6.7), despite that the Rhines scale is usually thought of as a cross-over between homogeneous turbulence and Rossby wave regimes. The result here suggests that the Rhines scale may not crucially depend on the presence of an classical inverse cascade and may have a somewhat more general applicability. The effects of friction are also likely to be important in any real simulation (Sukoriansky et. al. 2007).

In our study, criticality varies between about 1 and 3. Consider Jansen and Ferrari's (2013b) scaling for criticality $\xi \sim (f\tau_r)^{-1/5}(a/L_R)^{3/5}$, where τ_r is the time scale of thermal forcing and is inversely proportional to γ in our experiments, and $a = f/\beta$ is on the order of the planetary radius. The scaling explains why we have to vary γ by several orders in order to vary criticality, as criticality is only dependent on γ to one-fifth power. Note that we cannot get very high criticality by increasing the thermal forcing rate only. Rather, to get very high criticality, it may be better to increase a/L_R. Indeed, we obtained very high criticality and a substantial inverse cascade in a simulation with planetary radius 10 times Earth's. Combined with results from this study, it follows that Earth's atmosphere is within the weakly nonlinear regime because the Rossby radius is on the same order as the planetary radius, and also that the most unstable wave can adjust its horizontal and vertical scale so as to stay weakly nonlinear.

Appendix A: Barotropic EKE spectrum and eddy scale

The barotropic EKE spectrum E_n is computed using spherical harmonics as basis functions and the details are described by Boer and Shepherd (1983). Briefly, it is defined as

$$E_n = \frac{1}{4} \sum_{l=-n}^{n} \left\langle (|\{u'_{bt}\}_{n,l}|^2 + |\{v'_{bt}\}_{n,l}|^2) \right\rangle , \tag{6.24}$$

where u'_{bt} and v'_{bt} denote the zonal and meridional components of barotropic eddy velocity, which is velocity's derivation from zonal mean and vertically averaged from 150 mb to 1 bar. The angle brackets denote a time mean. The subscripts n, l denote the spectrum component of the fields with total wavenumber n and zonal wavenumber l. The wavenumbers are nondimensional. For the T42 resolution, n ranges from 1 to 42. E_n has unit of $\mathrm{m}^2\ \mathrm{s}^{-2}$ and the sum of E_n for all wavenumbers equals the surface area averaged barotropic EKE.

The energy-containing eddy scale, which we usually refer as eddy scale for short, is calculated from the "inverse centroid" introduced by Schneider and Walker (2006, 2008). Compared with the normal centroid, this definition gives a scale closer to the peak in E_n. To get the eddy scale, the energy containing wavenumber n_e is first calculated as as

$$n_e(n_e + 1) = \frac{\sum_n E_n}{\sum_n [n(n+1)]^{-1} E_n}, \tag{6.25}$$

and then the eddy scale L_e is given by

$$L_e = \frac{\pi a}{\sqrt{n_e(n_e + 1)}}, \tag{6.26}$$

where a is the planetary radius. Using the vertical averaged EKE spectrum defined below in (6.28) instead of barotropic EKE spectrum in (6.28) gives a slightly smaller eddy scale, which does not change our result much.

Appendix B: Spectral EKE budget

The spectral EKE budget can then be written as

$$\partial_t \mathrm{EKE}_n = G + T_{EE} + T_{EM} - D + \mathrm{Resi}, \quad \text{where} \tag{6.27}$$

$$\mathrm{EKE}_n = \frac{1}{4}\sum_{l=-n}^{n}\left\langle \int_{p_1}^{p_2} (|u'_{n,l}|^2 + |v'_{n,l}|^2) dp \right\rangle / \Delta p, \tag{6.28}$$

where EKE_n denotes the vertically averaged EKE at total wavenumber n, the range between p_1 and p_2 is from 150 mb to 1 bar[4], and the angle brackets denote a time mean. By dividing the vertical integral by the pressure range $\Delta p = p_2 - p_1$, the units for EKE_n are $\mathrm{m}^2\ \mathrm{s}^{-2}$. In the right hand side terms above,

$$G = -\frac{1}{2}\sum_{l=-n}^{n}\left\langle \int_{p_1}^{p_2} \frac{R}{p}\mathrm{Re}(T'_{n,l}\omega'^{*}_{n,l}) dp \right\rangle / \Delta p,$$

denotes the energy conversion from eddy available potential energy to eddy kinetic energy, and we refer it as EKE generation for short,

$$T_{EE} = \frac{1}{2}\sum_{l=-n}^{n}\left\langle \int_{p_1}^{p_2} \mathrm{Re}[-u'^{*}_{n,l}(\mathbf{u}'\cdot\nabla u')_{n,l} - v'^{*}_{n,l}(\mathbf{u}'\cdot\nabla v')_{n,l}] dp \right\rangle / \Delta p$$

denotes nonlinear eddy-eddy kinetic energy transfer,

[4]In actual calculations, we use the model's sigma coordinate to approximate the pressure coordinate. This avoids the complications related to the lower boundary condition in pressure coordinate (the planetary surface pierces the near-surface pressure levels). This is a decent approximation as long as the surface pressure variation is small enough.

$$T_{EM} = \frac{1}{2}\sum_{l=-n}^{n}\left\langle \int_{p_1}^{p_2} \mathrm{Re}[-u'^{*}_{n,l}(\mathbf{u}'\cdot\nabla\overline{u})_{n,l} - v'^{*}_{n,l}(\mathbf{u}'\cdot\nabla\overline{v})_{n,l} - u'^{*}_{n,l}(\overline{\mathbf{u}}\cdot\nabla u')_{n,l} - v'^{*}_{n,l}(\overline{\mathbf{u}}\cdot\nabla v')_{n,l}]dp \right\rangle /\Delta p$$

denotes the eddy/mean-flow kinetic energy transfer, and

$$D = \frac{1}{2}\sum_{l=-n}^{n}\left\langle \int_{p_1}^{p_2} k_v(p)(u'^{*}_{n,l}u'_{n,l} + v'^{*}_{n,l}v'_{n,l})dp \right\rangle /\Delta p$$

denotes the dissipation by Rayleigh damping of low level winds, where $k_v(p)$ is the linear damping coefficient as a function of pressure. The contributions from the Coriolis terms, dissipation by hyper-diffusivity, and gravitational potential energy flux through the boundaries are absorbed in the residual term Resi. In a statistical steady state, the sum of the right hand side terms should be zero. Detailed derivations and notations can be found in Lambert (1984) or Koshyk and Hamilton (2001). The corresponding formulation using Fourier series as basis functions in a Cartesian geometry is given in Jansen and Ferrari (2012).

Fig. 6.13a shows the terms in the spectral EKE budget for the control ($\gamma = 1$) simulation with $\delta_y = 60$ K. The EKE generation is predominately transferred into the zonal-mean flow or dissipated by friction at similar scales. The eddy-eddy interactions do transfer some energy upscale, but this does not increase the eddy scale substantially from EKE generation scale. To quantify the role of eddy-eddy interaction, we define EKE generation scale in a similar way as the eddy scale defined in Appendix A. The EKE generation wavenumber is calculated as an inverse centroid of G_n similar to Eq. (6.25), and the EKE generation wavenumber is converted into the EKE generation scale by Eq. (6.26). As can be seen in Fig. 6.13b, the energy generation wavenumber

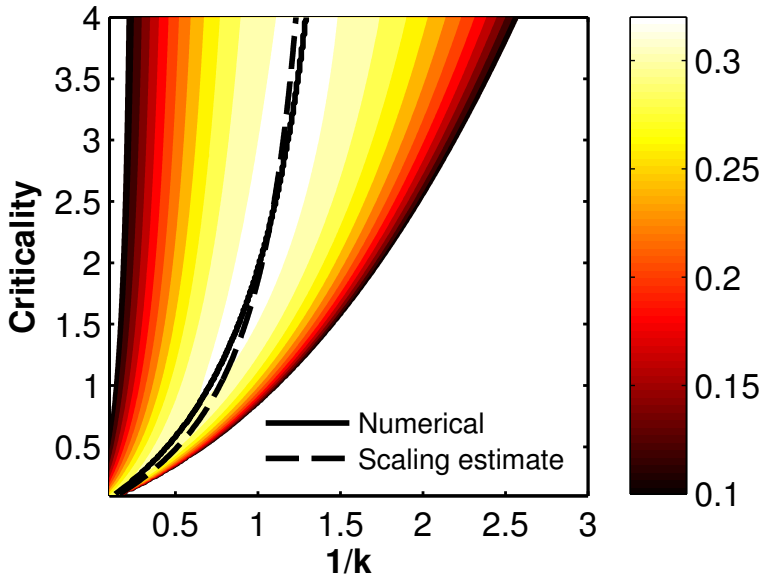


Figure 6.1: A contour plot showing the growth rate against the inverse wavenumber $1/k$ and criticality ξ for the Charney model. The solid line marks the most unstable wavenumber determined numerically, and the dashed line shows our scaling estimate $1.54\xi/(1+\xi)$. The horizontal and vertical length scales are nondimensionalized by Rossby radius L_R and density scale height H_ρ respectively. The contour interval is 0.02, and it is nondimensionalized by $H_\rho \partial_z U / L_R$.

follows closely the peak of G_n, which moves towards larger scales when γ increases from 0.1 to 10.

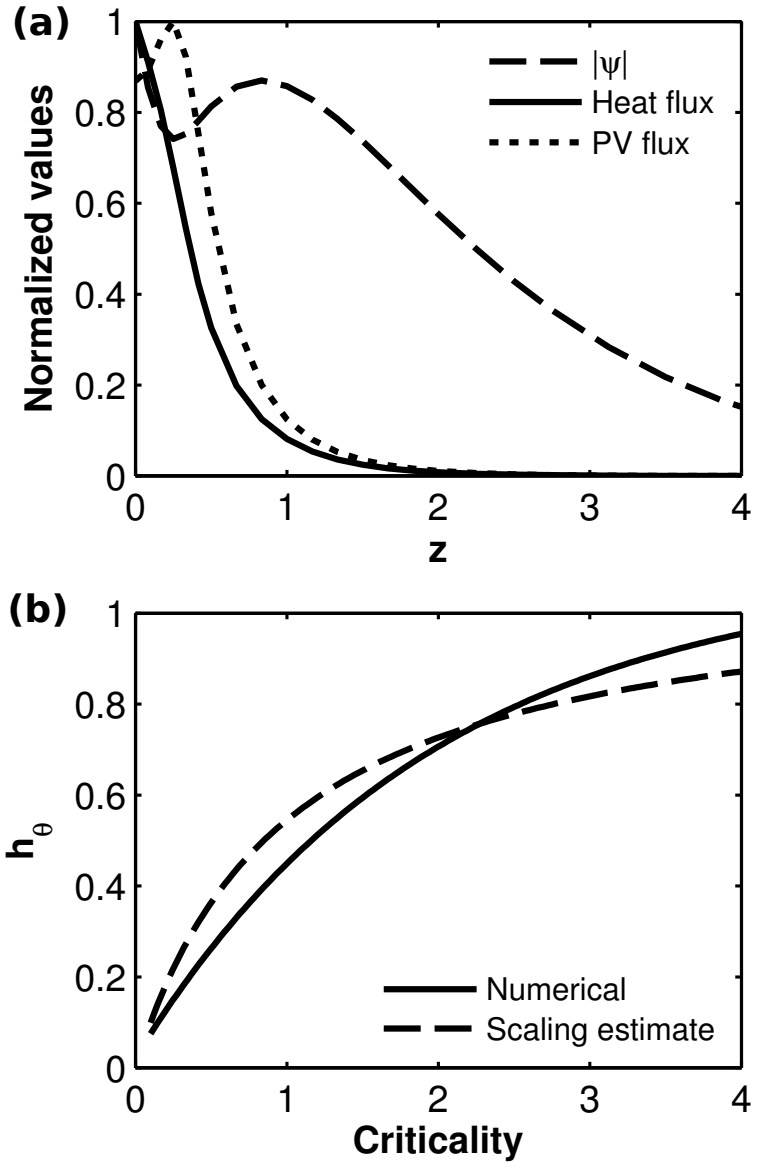


Figure 6.2: (a) Vertical structure of the most unstable Charney wave when $\xi = 1$. Dashed line is the amplitude of the perturbation stream function $|\psi|$, solid line is heat flux $\overline{v'\partial_z\psi}$, and dotted line is PV flux. All three curves are normalized by their maximum values. (b) Vertical scale of the most unstable wave h_θ defined in Eq. (6.22) vs. criticality: solid line is from numerical results and dashed line is our scaling estimate $1.09\xi/(1+\xi)$.

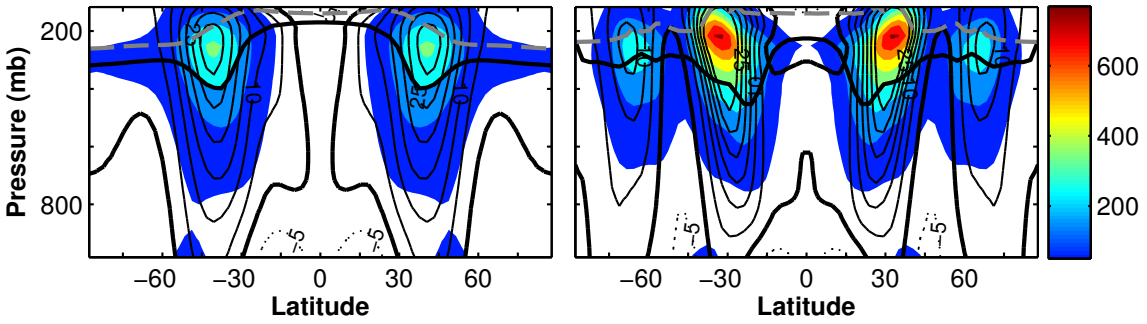


Figure 6.3: Mean zonal wind (contours) and EKE (colors) for the control run ($\gamma = 1$) with $\delta_y = 60$ K from full GCM (left) and reduced GCM (right). The contour interval for zonal wind is 5 m/s and for EKE is 100 $\mathrm{m}^2/\mathrm{s}^2$. The zero zonal wind contour is thick, and negative contours are dashed. The tropopause calculated from isentropic diagnostics is marked by the thick black line, and the WMO tropopause is marked by the thick gray line.

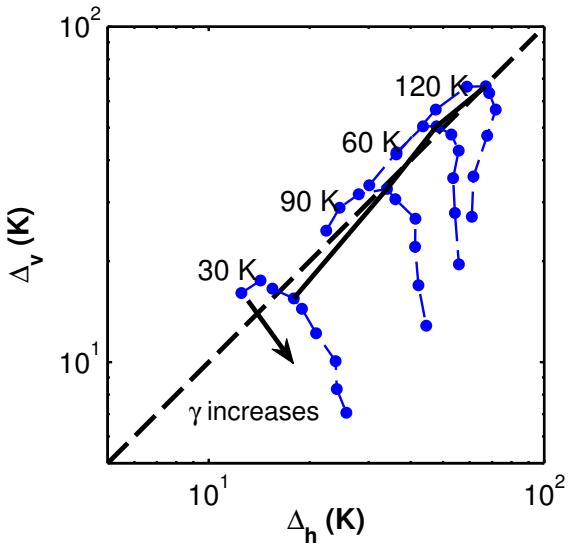


Figure 6.4: Extratropical bulk stability $\Delta_v = \overline{\partial_p \theta}^s (\overline{p}_t - \overline{p}_s)$ vs. scaled meridional temperature gradient $\Delta_h = |(f/\beta)\partial_y \overline{\theta}^s|$ evaluated at 850 mb for different combinations of γ and δ_y. The control runs with $\gamma = 1$ but different δ_y are connected with a black line. Each series of runs with varying γ and with the same δ_y are connected with a blue line, and the corresponding value δ_y is indicated by the label besides.

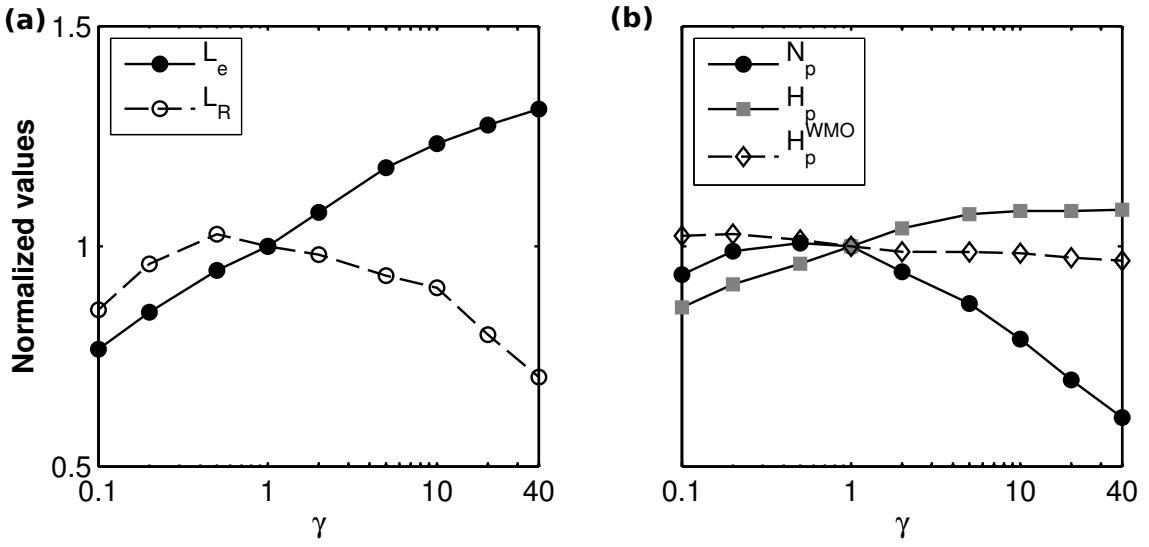


Figure 6.5: Results from simulations with $\delta_y = 60$ K and varying γ. (a) Eddy scale L_e and Rossby radius L_R, all normalized by their control run values ($\gamma = 1$). (b) Tropopause height H_p based on isentropic diagnostics, WMO tropopause height H_p^{WMO} and vertical stability measure N_p, all normalized by their control run values.

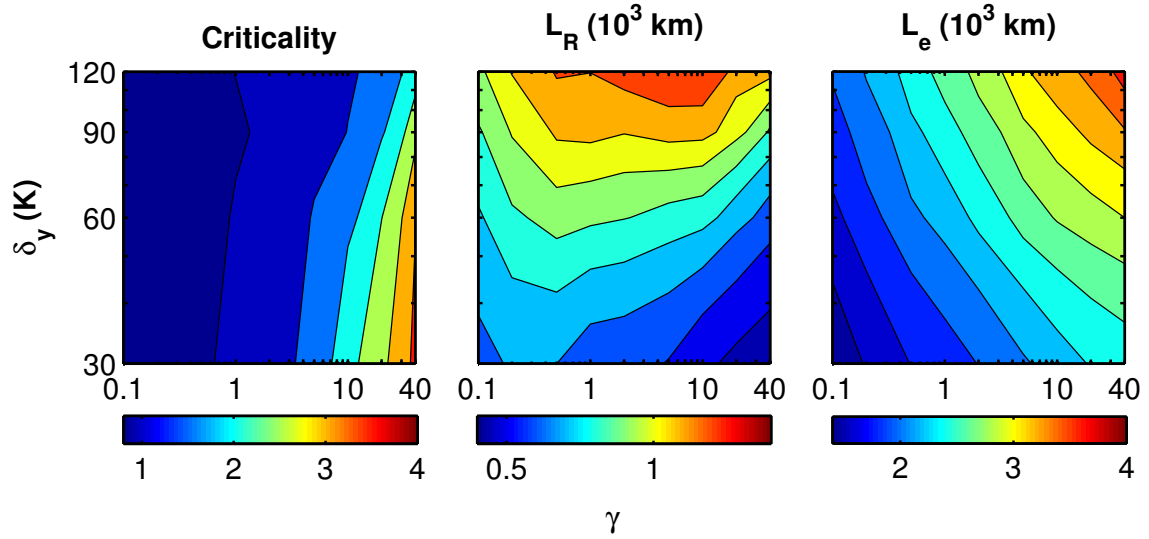


Figure 6.6: Criticality ξ, Rossby radius L_R, and eddy scale L_e as a function of γ and δ_y.

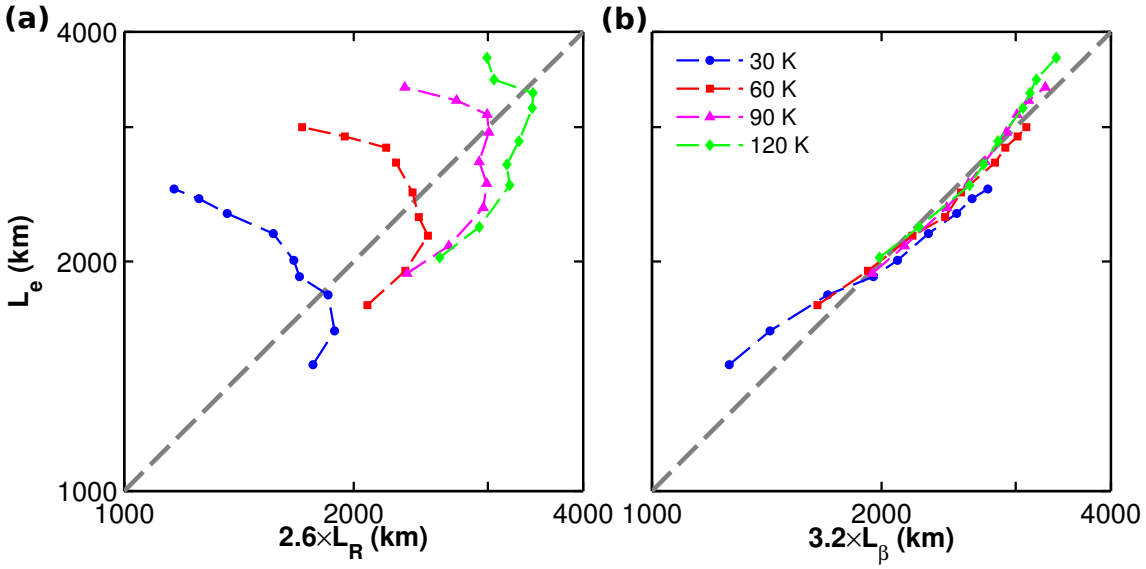


Figure 6.7: (a) Best Rossby radius estimate $C_R L_R$ and (b) Rhines scale estimate $C_\beta L_\beta$ for eddy scale. The empirical constants C_R and C_β are determined to be 2.6 and 3.2 respectively by a least square fit to the modeling results. The legends denote the series of experiments with a certain δ_y and varying γ.

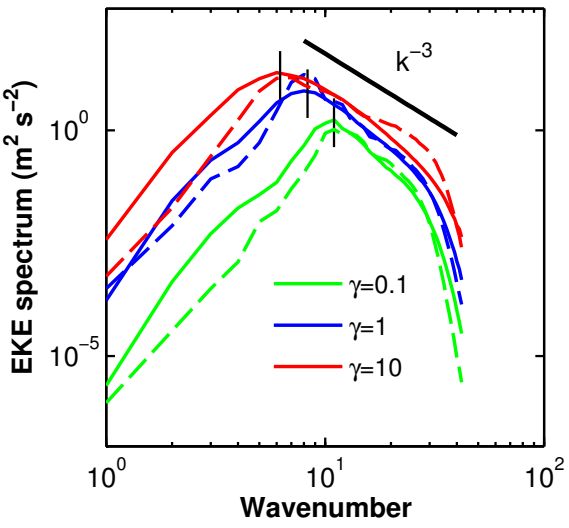


Figure 6.8: For the Earth-like settings with $\delta_y = 60$ K, $\Omega = \Omega_0$ and $r = a_0$, and varying thermal forcing γ =0.1, 1, 10, comparison of EKE spectrum between the full and reduced GCMs. The solid lines denote the full GCM, and the dashed lines denote the reduced GCM. The vertical black lines indicate energy containing wavenumber for the full GCM runs.

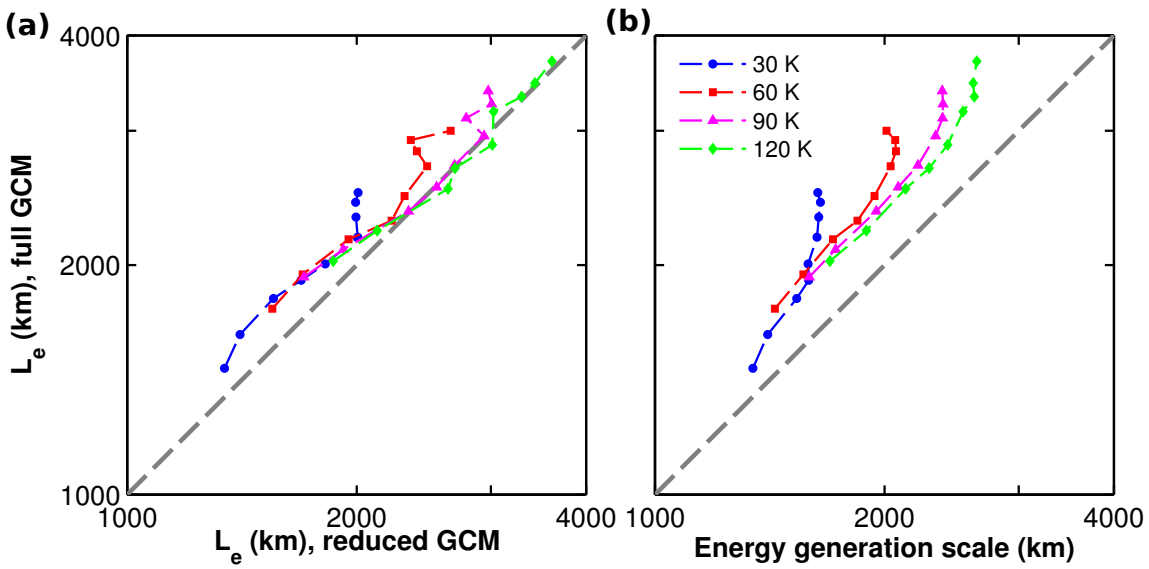


Figure 6.9: (a) Comparison of eddy scale L_e in the full and reduced GCMs. (b) Comparison of eddy scale and eddy kinetic energy generation scale (see Appendix A and B for definitions) in the full GCM. The legends denote the series of experiments with a certain δ_y and varying γ.

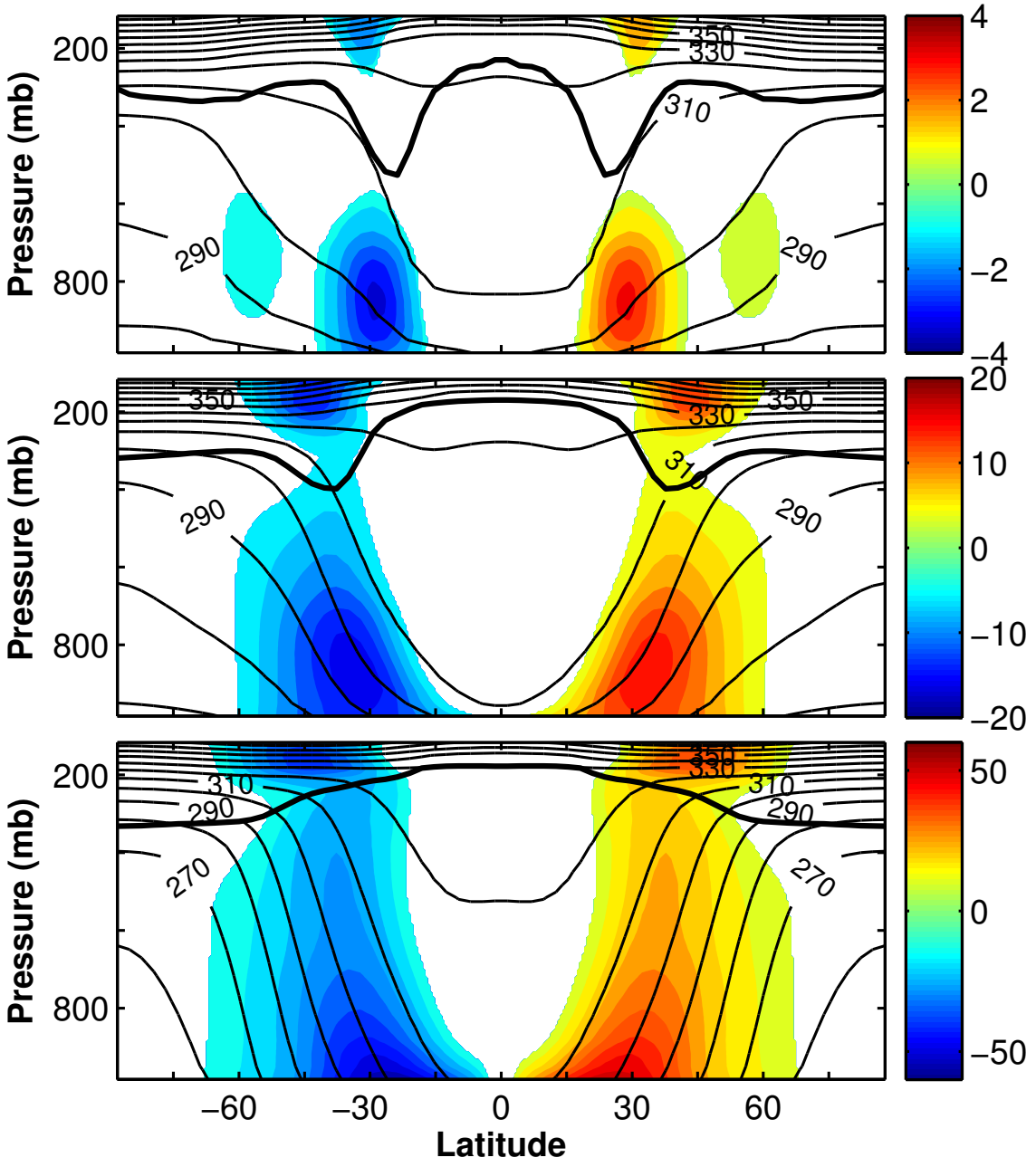


Figure 6.10: Eddy potential temperature flux $\overline{v'\theta'}\cos(\phi)$ (colors) and mean potential temperature (contours) from simulations with δ_y=60 K, and γ=0.1 (top), 1 (middle), and 10 (bottom). The thick black lines denote the tropopause determined from isentropic diagnostics.

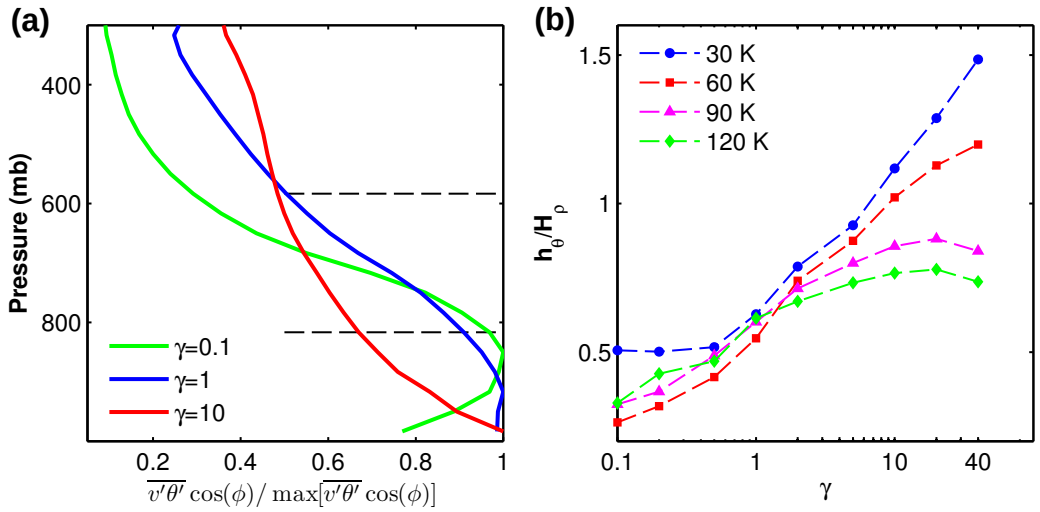


Figure 6.11: (a) The vertical structure of eddy potential temperature flux $\overline{v'\theta'}\cos(\phi)$ averaged over the baroclinic zone and normalized by its maximum value from simulations with δ_y=60 K, and γ=0.1, 1, 10. (b) The vertical scale of the wave h_θ defined in Eq. (6.22) for all series of simulations with different δ_y and varying γ, normalized by the scale height H_ρ. The horizontal dashed lines in (a) denote the pressure range over which we fit potential temperature flux profile to an exponential decay with height to get the vertical scale of the wave h_θ.

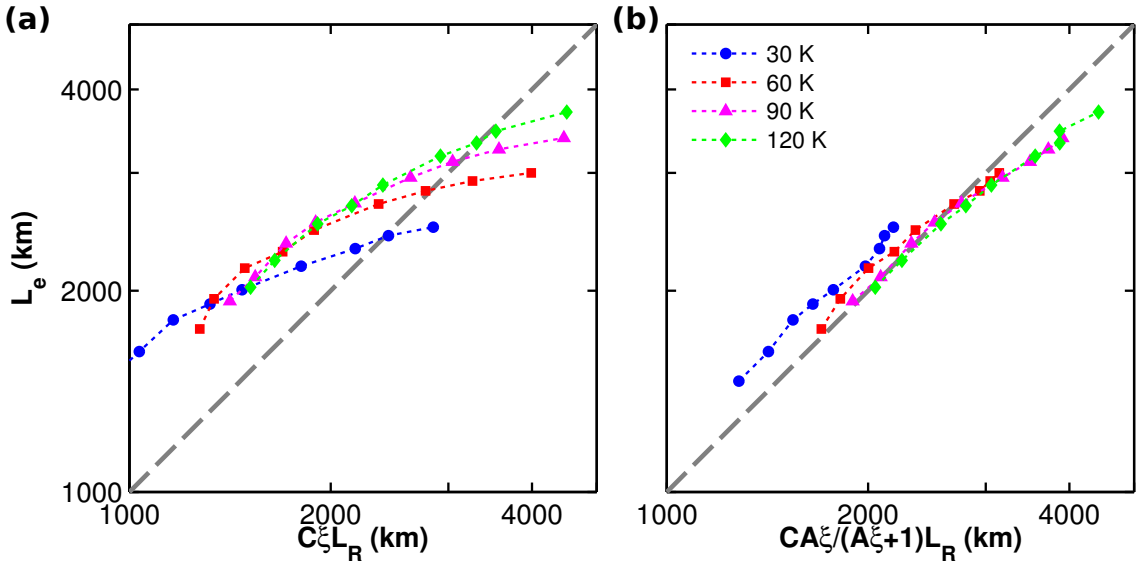


Figure 6.12: (a) Best estimate using $C\xi L_R$ vs observed eddy scale in all runs, with C=1.8. (b) Best estimate using the form $CL_R(A\xi)/(1+A\xi)$ vs observed eddy scale in all runs, with C=8.7 and A=0.36. The legends denote the series of experiments with a certain δ_y and varying γ.

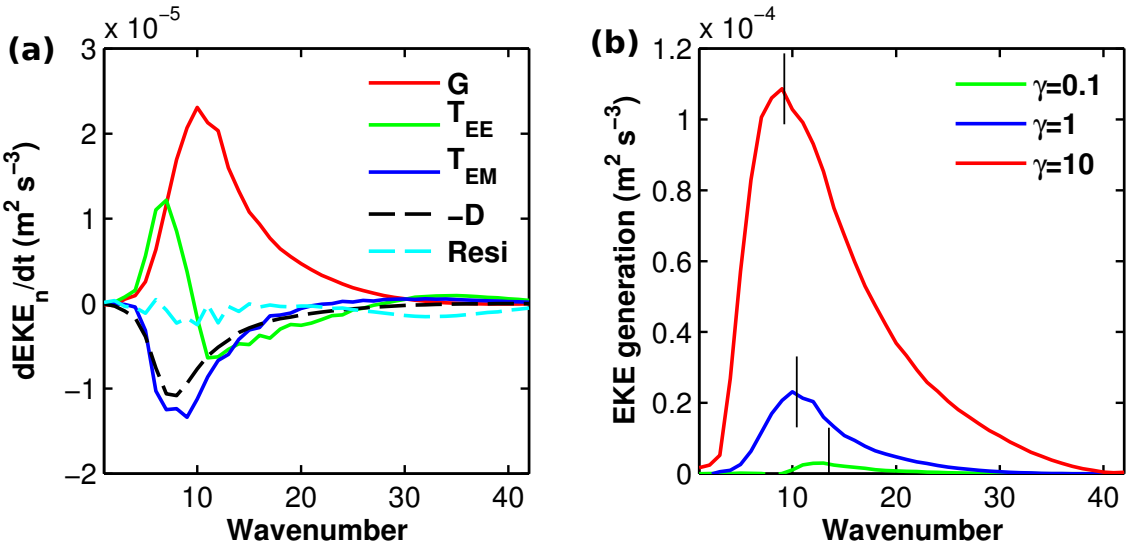


Figure 6.13: (a) Spectral EKE budget for the simulation with $\gamma = 1$ and δ_y=60 K: conversion from eddy APE to EKE (G, solid red), EKE transfer by eddy-eddy interactions (T_{EE}, solid green), energy transfer between zonal-mean flow and eddy (T_{EM}, solid blue), explicit dissipation by Rayleigh damping of winds ($-D$, dashed black), and the residual term (Resi, dashed cyan). The residual term is not significant compared to other leading order terms at wavenumbers away from the grid scale. (b) Conversion from eddy available potential energy to EKE for three simulations with γ=0.1, 1, 10 and δ_y=60 K. The vertical black lines indicate the corresponding EKE generation wavenumber.

Chapter 7

Conclusion

In this thesis, we study geostrophic turbulence in a hierarchy of models with different levels of complexity and we particularly focus on formulation some theoretical understandings. Our results are relevant for mid-latitude atmosphere and oceans, where the large-scale fluid motion is strongly influenced by the planetary rotation. Our discussions are primarily based on a quasi-geostrophic perspective of the large-scale motion. Various theoretical and diagnostic tools are used to gain some theoretical understanding. The biggest challenge in formulating a theory for a phenomenon is to isolate the essential physical process out of all the potential mechanisms. The idealized models eliminate many physical processes such as radiation, precipitation and et. al., though they still contain enough complicated turbulent processes to be challenging.

We start with arguably the simplest model for geostrophic turbulence–a forced-dissipated two-dimensional fluid on β-plane–in chapters 2 and 3. Two important aspects are studied: jet formation and eddy diffusion. The β-plane turbulence is characterized in the (Z, Π) space, where Z is the zonostrophic index and Π is an additional nondimensional parameter we proposed to highlight the role of forcing scale as $\Pi = k_f/k_\varepsilon$, with k_f to be the forcing wavenumber and k_ε to be the turbulence-

wave crossover wavenumber. A new turbulence regime is found at $\Pi \lesssim 1$ and $Z \gtrsim 2.5$ which we name as "quasi-linear" turbulence for the fact that eddy-eddy interactions are negligible while eddy/mean-flow interactions dominate the nonlinear energy and enstrophy transfers. A new form of turbulence-wave crossover scale is proposed for the quasi-linear turbulence regime as $k_\varepsilon \Pi^{-2/3}$. Eddy diffusion is studied with a new approach based Ferrari and Nikurashin's (2010) suppressed diffusivity formula that captures the essence of how diffusivity of waves is suppressed due to their relative propagation to the mean flow. In the regime $\Pi \ll 1$, we discover a new scaling of eddy diffusivity as $D_\eta \sim \beta^{-2}\eta$, where η is the enstrophy flux rate. The classical scaling $D_\varepsilon \sim \varepsilon^{3/5}\beta^{-4/5}$ is recovered in the other limit $\Pi \gg 1$. We further demonstrate that the suppression of diffusivity due to the relative wave/mean-flow propagation to be more fundamental than the assumption that waves do not contribute to mixing. The role of forcing scale has so far not been well recognized in many studies. To the best of our knowledge, this is the first comprehensive study on the role of forcing scale. We admit that other aspects such as the details of the forcing may also influence the flow. However, our impression is that they may play a minor role than the forcing scale.

The understandings from the two-dimensional β-plane turbulence are then applied to the two-layer quasi-geostrophic (QG) model, which serves as the bridge between 1-layer fluid to more complicated baroclinic turbulence. The two-layer QG model is crucially determined by two nondimensional parameters criticality and dimensionless friction, which are also the crucial parameters in more complicated baroclinic models. The closure theory for the 2-layer QG model centers on the heat flux. The dependency of heat flux on criticality can be easily derived based on the diffusivity scaling from the 1-layer model. On the other hand, the dependency on friction is more difficult to understand. Though the role of friction has long been known from the "barotropic governor" effect (James, 1987), quantitative understandings are lacking. In chapter

4, we attempt to understand the role of friction on heat flux more quantitatively using Ferrari and Nikurashin's (2010) suppressed diffusivity formula, which we have already used in chapter 3.

In Chapter 4, we move to more realistic models. Our tool now is a dry primitive equation general circulation model (GCM). Motivated by Jovian atmosphere, we discuss whether and how a baroclinic atmosphere can equilibrate with very small bottom friction in the dry GCM. When friction is decreased by four orders of magnitude, kinetic energy dissipation by friction gradually becomes negligible, while "energy recycling" becomes dominant. In this limit kinetic energy is converted back into potential energy at the largest scales, thus closing the energy cycle without significant frictional dissipation. The momentum fluxes are of opposite sign in the upper and lower atmosphere: in the upper atmosphere, eddies converge momentum into the westerly jets, however, in the lower atmosphere, the eddies diverge momentum out of the westerly jets. The secondary circulation driven by the meridional eddy momentum fluxes thus acts to increase the baroclinicity of the westerly jet. This energy recycling mechanism is likely to also exist in the 2-layer QG model if the baroclinic mode is damped by a thermal relaxation.

In Chapter 5, we look at the other nondimensional number – criticality – in the dry GCM. We look at the sensitivity of the horizontal and vertical scales of extratropical eddies when criticality is varied close to 1. When criticality varies near one, we show that there exists a weakly nonlinear regime in which the eddy scale increases with criticality without involving an inverse cascade, while at the same time the Rossby radius may in fact decrease. The dependency of eddy scales on criticality is explained in terms of linear instability theory, and analytical predictions are derived from the Charney model. When criticality increases well above 1, the flow will eventually become highly nonlinear. This result is related to Fig. 4.2 from the 2-layer QG

model. We see that Π is smaller than 1 when criticality is small, which suggests the flow to be in the quasi-linear regime when criticality is close to 1.

Interestingly, the way we carried out our study does not begin with the 1-layer model and then moving to more complicated models as the way the thesis is organized. For the first 4 chapters, we actually first found the dependency of heat flux on friction in the 2-layer model and tried very hard to explain it. Our first quantitative explanation came from Nakamura's effective diffusivity framework, though our theory requires too strong assumptions to be convincing. Nevertheless, in Nakamura's framework we found a new diffusivity scaling that depends on the forcing scale in the 1-layer model as included in the appendix of chapter 3, which seemed to require fewer assumptions and therefore may be robust. To test this new diffusivity scaling, we carried out and analayzed a series of simulations. It was only until months later that we discovered the new form of crossover scale and the quasi-linear turbulence regime. The new diffusivity scaling was derived again using the new form of crossover scale as in Section 3.2, however, we were still puzzled by its physical picture. It was only after another few weeks later until Malte suggested the use of Ferrari and Nikurashin's (2010) formula that we fully understood the no-wave-mixing assumption. Less surprisingly, the whole thesis is in the reverse chronological order as when the actual work was done, which illustrates the tortuous process of formulating some theoretical understanding.

Bibliography

Balk, A., 1991: A new invariant for Rossby wave systems. *Phys. Lett. A*, **155 (1)**, 20–24, doi:10.1016/0375-9601(91)90501-X.

Balk, A. M., 2005: Angular distribution of Rossby wave energy. *Phys. Lett. A*, **345**, 154–160, doi:10.1016/j.physleta.2005.07.033.

Barry, L., G. C. Craig, and J. Thuburn, 2002: Poleward heat transport by the atmospheric heat engine. *Nature*, **415 (6873)**, 774–7, doi:10.1038/415774a.

Batchelor, G. K., 1959: Small-scale variation of convected quantities like temperature in turbulent fluid Part 1. General discussion and the case of small conductivity. *J. Fluid Mech.*, **5 (01)**, 113, doi:10.1017/S002211205900009X.

Bister, M., and K. A. Emanuel, 1998: Dissipative heating and hurricane intensity. *Meteor. Atmos. Phys.*, **65 (3-4)**, 233–240, doi:10.1007/BF01030791.

Boer, G. J., and T. G. Shepherd, 1983: Large-Scale Two-Dimensional Turbulence in the Atmosphere. *J. Atmos. Sci.*, **40 (1)**, 164–184, doi:10.1175/1520-0469(1983)040⟨0164:LSTDTI⟩2.0.CO;2.

Boffetta, G., and R. E. Ecke, 2012: Two-Dimensional Turbulence. *Annu. Rev. Fluid Mech.*, **44 (1)**, 427–451, doi:10.1146/annurev-fluid-120710-101240.

Borue, V., 1993: Spectral exponents of enstrophy cascade in stationary two-dimensional homogeneous turbulence. *Phys. Rev. Lett.*, **71 (24)**, 3967–3970, doi:10.1103/PhysRevLett.71.3967.

Bouchet, F., and J. Sommeria, 2002: Emergence of intense jets and Jupiter's Great Red Spot as maximum-entropy structures. *J. Fluid Mech.*, **464**, 165–207, doi:Doi10.1017/S0022112002008789, 0003079.

Bouchet, F., and A. Venaille, 2012: Statistical mechanics of two-dimensional and geophysical flows. *Phys. Rep.*, **515 (5)**, 227–295, doi:10.1016/j.physrep.2012.02.001.

Branscome, L. E., 1983: The Charney Baroclinic Stability Problem: Approximate Solutions and Modal Structures. *J. Atmos. Sci.*, **40 (6)**, 1393–1409, doi:10.1175/1520-0469(1983)040⟨1393:TCBSPA⟩2.0.CO;2.

Burger, A. P., 1962: On the non-existence of critical wavelengths in a continuous baroclinic stability problem. *J. Atmos. Sci.*, **19 (1)**, 31–38, doi:10.1175/1520-0469(1962)019⟨0031:OTNEOC⟩2.0.CO;2.

Chai, J., M. Jansen, and I. M. Held, 2016a: The role of forcing scale on the beta-plane turbulence. Part I: jet formation.

Chai, J., M. Jansen, and I. M. Held, 2016b: The role of forcing scale on the beta-plane turbulence. Part II: eddy diffusion.

Chai, J., M. Jansen, and G. K. Vallis, 2015: Zonostrophic Turbulence in Two-layer Quasi-geotrophic Model. *AGU Fall Meeting*.

Chai, J., M. Jansen, and G. K. Vallis, 2016c: Equilibration of a baroclinic planetary atmosphere toward the limit of vanishing bottom friction. *J. Atmos. Sci.*, JAS–D–15–0329.1, doi:10.1175/JAS-D-15-0329.1.

Chai, J., and G. K. Vallis, 2014: The Role of Criticality on the Horizontal and Vertical Scales of Extratropical Eddies in a Dry GCM. *J. Atmos. Sci.*, **71 (7)**, 2300–2318, doi:10.1175/JAS-D-13-0351.1.

Charney, J. G., 1947: The Dynamics of Long Waves in a Baroclinic Westerly Current. *J. Meteor.*, **4 (5)**, 136–162, doi:10.1175/1520-0469(1947)004⟨0136:TDOLWI⟩2.0.CO;2.

Charney, J. G., 1971: Geostrophic Turbulence. *J. Atmos. Sci.*, **28 (6)**, 1087–1095, doi:10.1175/1520-0469(1971)028⟨1087:GT⟩2.0.CO;2.

Chekhlov, A., S. a. Orszag, S. Sukoriansky, B. Galperin, and I. Staroselsky, 1996: The effect of small-scale forcing on large-scale structures in two-dimensional flows. *Physica D*, **98 (2-4)**, 321–334, doi:10.1016/0167-2789(96)00102-9, 9601012.

Chemke, R., and Y. Kaspi, 2015: The Latitudinal Dependence of Atmospheric Jet Scales and Macroturbulent Energy Cascades. *J. Atmos. Sci.*, **72 (10)**, 3891–3907, doi:10.1175/JAS-D-15-0007.1.

Chen, G., and A. Plumb, 2014: Effective Isentropic Diffusivity of Tropospheric Transport. *J. Atmos. Sci.*, **71 (9)**, 3499–3520, doi:10.1175/JAS-D-13-0333.1.

Chen, S., R. E. Ecke, G. L. Eyink, M. Rivera, M. Wan, and Z. Xiao, 2006: Physical mechanism of the two-dimensional inverse energy cascade. *Phys. Rev. Lett.*, **96 (8)**, 3–6, doi:10.1103/PhysRevLett.96.084502.

Chertkov, M., C. Connaughton, I. Kolokolov, and V. Lebedev, 2007: Dynamics of Energy Condensation in Two-Dimensional Turbulence. *Phys. Rev. Lett.*, **99 (8)**, 084 501, doi:10.1103/PhysRevLett.99.084501.

Choi, D. S., and A. P. Showman, 2011: Power spectral analysis of Jupiter's clouds and kinetic energy from Cassini. *Icarus*, **216 (2)**, 597–609, doi:10.1016/j.icarus.2011.10.001.

Czaja, A., and J. Marshall, 2006: The Partitioning of Poleward Heat Transport between the Atmosphere and Ocean. *J. Atmos. Sci.*, **63 (5)**, 1498–1511, doi:10.1175/JAS3695.1.

Danilov, S., and V. M. Gryanik, 2004: Barotropic Beta-Plane Turbulence in a Regime with Strong Zonal Jets Revisited. *J. Atmos. Sci.*, **61 (18)**, 2283–2295, doi:10.1175/1520-0469(2004)061⟨2283:BBTIAR⟩2.0.CO;2.

Dowling, T. E., 1995: Dynamics of Jovian Atmospheres. *Annu. Rev. Fluid Mech.*, **27 (1)**, 293–334, doi:10.1146/annurev.fl.27.010195.001453.

Dritschel, D. G., and M. E. McIntyre, 2008: Multiple Jets as PV Staircases: The Phillips Effect and the Resilience of Eddy-Transport Barriers. *J. Atmos. Sci.*, **65 (3)**, 855–874, doi:10.1175/2007JAS2227.1.

Dunkerton, T. J., and R. K. Scott, 2008: A Barotropic Model of the Angular Momentum-Conserving Potential Vorticity Staircase in Spherical Geometry. *J. Atmos. Sci.*, **65 (4)**, 1105–1136, doi:10.1175/2007JAS2223.1.

Eady, E. T., 1949: Long Waves and Cyclone Waves. *Tellus*, **1 (3)**, 33–52, doi:10.1111/j.2153-3490.1949.tb01265.x.

Edmon, H. J., B. J. Hoskins, and M. E. McIntyre, 1980: Eliassen-Palm Cross Sections for the Troposphere. *J. Atmos. Sci.*, **37 (12)**, 2600–2616, doi:10.1175/1520-0469(1980)037⟨2600:EPCSFT⟩2.0.CO;2.

Emanuel, K., and M. Bister, 1996: Moist convective velocity and buoyancy scales. *J. Atmos. Sci.*, **53 (22)**, 3276–3285, doi:10.1175/1520-0469(1996)053⟨3276:MCVABS⟩2.0.CO;2.

Emanuel, K. a., 1986: An Air-Sea Interaction Theory for Tropical Cyclones. Part I: Steady-State Maintenance. *J. Atmos. Sci.*, **43 (6)**, 585–605, doi:10.1175/1520-0469(1986)043⟨0585:AASITF⟩2.0.CO;2.

Falkovich, G., and V. Lebedev, 1994: Nonlocal vorticity cascade in two dimensions. *Phys. Rev. E*, **49 (3)**, R1800–R1803, doi:10.1103/PhysRevE.49.R1800.

Farrell, B. F., and P. J. Ioannou, 1994: A Theory for the Statistical Equilibrium Energy Spectrum and Heat Flux Produced by Transient Baroclinic Waves. *J. Atmos. Sci.*, **51 (19)**, 2685–2698, doi:10.1175/1520-0469(1994)051⟨2685:ATFTSE⟩2.0.CO;2.

Ferrari, R., and M. Nikurashin, 2010: Suppression of Eddy Diffusivity across Jets in the Southern Ocean. *J. Phys. Oceanogr.*, **40 (7)**, 1501–1519, doi:10.1175/2010JPO4278.1.

Flierl, G. R., 1978: Models of vertical structure and the calibration of two-layer models. *Dynam. Atmos. Oceans*, **2 (4)**, 341–381, doi:10.1016/0377-0265(78)90002-7.

Frierson, D. M. W., I. M. Held, and P. Zurita-Gotor, 2006: A Gray-Radiation Aquaplanet Moist GCM. Part I: Static Stability and Eddy Scale. *J. Atmos. Sci.*, **63 (10)**, 2548–2566, doi:10.1175/JAS3753.1.

Frierson, D. M. W., I. M. Held, and P. Zurita-Gotor, 2007: A Gray-Radiation Aquaplanet Moist GCM. Part II: Energy Transports in Altered Climates. *J. Atmos. Sci.*, **64 (5)**, 1680–1693, doi:10.1175/JAS3913.1.

Frisch, U., 1995: *Turbulence : the legacy of A.N. Kolmogorov*, Vol. 1. 296 pp., doi:10.1017/S0022112096210791.

Galperin, B., H. Nakano, H. P. Huang, and S. Sukoriansky, 2004: The ubiquitous zonal jets in the atmospheres of giant planets and Earth's oceans. *Geophys. Res. Lett.*, **31 (13)**, 1–5, doi:10.1029/2004GL019691.

Galperin, B., S. Sukoriansky, and N. Dikovskaya, 2010: Geophysical flows with anisotropic turbulence and dispersive waves: flows with a β-effect. *Ocean Dynam.*, **60 (2)**, 427–441, doi:10.1007/s10236-010-0278-2.

Galperin, B., S. Sukoriansky, N. Dikovskaya, P. L. Read, Y. H. Yamazaki, and R. Wordsworth, 2006: Anisotropic turbulence and zonal jets in rotating flows with a beta-effect. *Nonlinear Proc. Geophys.*, **13 (1)**, 83–98, doi:10.5194/npg-13-83-2006.

Galperin, B., R. M. Young, S. Sukoriansky, N. Dikovskaya, P. L. Read, A. J. Lancaster, and D. Armstrong, 2014: Cassini observations reveal a regime of zonostrophic macroturbulence on Jupiter. *Icarus*, **229**, 295–320, doi:10.1016/j.icarus.2013.08.030.

Gotoh, T., 1998: Energy spectrum in the inertial and dissipation ranges of two-dimensional steady turbulence. *Phys. Rev. E*, **57 (3)**, 2984–2991, doi:10.1103/PhysRevE.57.2984.

Green, J. S. A., 1960: A problem in baroclinic stability. *Quart. J. Roy. Meteor. Soc.*, **86 (368)**, 237–251, doi:10.1002/qj.49708636813.

Green, J. S. A., 1971: Transfer properties of the large-scale eddies and the general circulation of the atmosphere. *Q. J. R. Meteorol. Soc.*, **97 (414)**, 579–580, doi:10.1002/qj.49709741422.

Guillot, T., 2005: The Interiors of Giant Planets: Models and Outstanding Questions. *Annu. Rev. Earth Planet. Sci.*, **33 (1)**, 493–530, doi:10.1146/annurev.earth.32.101802.120325.

Gürcan, Ö. D., 2012: Effect of Sheared Flow on the Growth Rate and Turbulence Decorrelation. *Phys. Rev. Lett.*, **109 (15)**, 155 006, doi:10.1103/PhysRevLett.109.155006.

Hayashi, Y., 1973: A Method of Analyzing Transient Waves by Space-Time Cross Spectra. *J. Appl. Meteor.*, **12 (2)**, 404–408, doi:10.1175/1520-0450(1973)012⟨0404:AMOATW⟩2.0.CO;2.

Hayashi, Y., 1982: Space-time spectral analysis and its applications to atmospheric waves. *J. Meteorol. Soc. Jpn.*, **60 (1)**, 156–171.

Haynes, P. H., and M. E. McIntyre, 1987: On the Evolution of Vorticity and Potential Vorticity in the Presence of Diabatic Heating and Frictional or Other Forces. *J. Atmos. Sci.*, **44 (5)**, 828–841, doi:10.1175/1520-0469(1987)044⟨0828:OTEOVA⟩2.0.CO;2.

Haynes, P. H., D. A. Poet, and E. F. Shuckburgh, 2007: Transport and Mixing in Kinematic and Dynamically Consistent Flows. *J. Atmos. Sci.*, **64 (10)**, 3640–3651, doi:10.1175/JAS4030.1.

Held, I. M., 1975: Momentum Transport by Quasi-Geostrophic Eddies. *J. Atmos. Sci.*, **32 (7)**, 1494–1497, doi:10.1175/1520-0469(1975)032⟨1494:MTBQGE⟩2.0.CO;2.

Held, I. M., 1978: The Vertical Scale of an Unstable Baroclinic Wave and Its Importance for Eddy Heat Flux Parameterizations. *J. Atmos. Sci.*, **35 (4)**, 572–576, doi:10.1175/1520-0469(1978)035⟨0572:TVSOAU⟩2.0.CO;2.

Held, I. M., 1982: On the Height of the Tropopause and the Static Stability of the Troposphere. *J. Atmos. Sci.*, **39 (2)**, 412–417, doi:10.1175/1520-0469(1982)039⟨0412:OTHOTT⟩2.0.CO;2.

Held, I. M., 1983: Stationary and quasi-stationary eddies in the extratropical troposphere: theory. *Large-scale Dynamical Processes in the Atmosphere*, **(1949)**, 127–168.

Held, I. M., 1999: The macroturbulence of the troposphere. *Tellus A*, **51 (1)**, 59–70, doi:10.1034/j.1600-0870.1999.t01-1-00006.x.

Held, I. M., 2005: The Gap between Simulation and Understanding in Climate Modeling. *Bull. Am. Meteorol. Soc.*, **86 (11)**, 1609–1614, doi:10.1175/BAMS-86-11-1609.

Held, I. M., 2007: Progress and problems in large-scale atmospheric dynamics. *The Global Circulation of the Atmosphere*, T. Schneider, and A. Sobel, Eds., Princeton University Press, Princeton, NJ, chap. 1, 1–21.

Held, I. M., and V. D. Larichev, 1996: A Scaling Theory for Horizontally Homogeneous, Baroclinically Unstable Flow on a Beta Plane. *J. Atmos. Sci.*, **53 (7)**, 946–952, doi:10.1175/1520-0469(1996)053⟨0946:ASTFHH⟩2.0.CO;2.

Held, I. M., and E. O'Brien, 1992: Quasigeostrophic Turbulence in a Three-Layer Model: Effects of Vertical Structure in the Mean Shear. *J. Atmos. Sci.*, **49 (19)**, 1861–1870, doi:10.1175/1520-0469(1992)049⟨1861:QTIATL⟩2.0.CO;2.

Held, I. M., D. T. Pierrehumbert, S. Garner, and K. L. Swanson, 1995: Surface quasi-geostrophic dynamics. *J. Fluid Mech*, **282**, 1–20, doi:10.1017/S0022112095000012.

Held, I. M., and M. J. Suarez, 1994: A Proposal for the Intercomparison of the Dynamical Cores of Atmospheric General Circulation Models. *Bull. Am. Meteorol. Soc.*, **75 (10)**, 1825–1830, doi:10.1175/1520-0477(1994)075⟨1825:APFTIO⟩2.0.CO;2.

Huang, H. P., B. Galperin, and S. Sukoriansky, 2001: Anisotropic spectra in two-dimensional turbulence on the surface of a rotating sphere. *Phys. Fluids*, **13 (1)**, 225–240, doi:10.1063/1.1327594.

Ingersoll, A. P., 1990: Atmospheric dynamics of the outer planets. *Science*, **248 (4953)**, 308–15, doi:10.1126/science.248.4953.308.

Isern-Fontanet, J., G. Lapeyre, P. Klein, B. Chapron, and M. W. Hecht, 2008: Three-dimensional reconstruction of oceanic mesoscale currents from surface information. *J. Geophys. Res.*, **113 (C9)**, C09 005, doi:10.1029/2007JC004692.

James, I. N., 1987: Suppression of Baroclinic Instability in Horizontally Sheared Flows. *J. Atmos. Sci.*, **44 (24)**, 3710–3720, doi:10.1175/1520-0469(1987)044⟨3710:SOBIIH⟩2.0.CO;2.

James, I. N., and L. J. Gray, 1986: Concerning the effect of surface drag on the circulation of a baroclinic planetary atmosphere. *Q. J. R. Meteorol. Soc.*, **112 (474)**, 1231–1250, doi:10.1002/qj.49711247417.

Jansen, M., and R. Ferrari, 2012: Macroturbulent Equilibration in a Thermally Forced Primitive Equation System. *J. Atmos. Sci.*, **69 (2)**, 695–713, doi:10.1175/JAS-D-11-041.1.

Jansen, M., and R. Ferrari, 2013a: Equilibration of an Atmosphere by Adiabatic Eddy Fluxes. *J. Atmos. Sci.*, **70 (9)**, 2948–2962, doi:10.1175/JAS-D-13-013.1.

Jansen, M., and R. Ferrari, 2013b: The Vertical Structure of the Eddy Diffusivity and the Equilibration of the Extratropical Atmosphere. *J. Atmos. Sci.*, **70 (5)**, 1456–1469, doi:10.1175/JAS-D-12-086.1.

Kaspi, Y., and G. R. Flierl, 2007: Formation of Jets by Baroclinic Instability on Gas Planet Atmospheres. *J. Atmos. Sci.*, **64 (9)**, 3177–3194, doi:10.1175/JAS4009.1.

Killworth, P. D., 1997: On the parameterization of eddy transfer Part I. Theory. *J. Mar. Res.*, **55 (6)**, 27, doi:10.1357/0022240973224102.

Klocker, A., and R. P. Abernathey, 2014: Global Patterns of Mesoscale Eddy Properties and Diffusivities. *J. Phys. Oceanogr.*, **44 (3)**, 1030–1046, doi:10.1175/JPO-D-13-0159.1.

Klocker, A., R. Ferrari, and J. H. LaCasce, 2012: Estimating Suppression of Eddy Mixing by Mean Flows. *J. Phys. Oceanogr.*, **42 (9)**, 1566–1576, doi: 10.1175/JPO-D-11-0205.1.

Koshyk, J. N., and K. Hamilton, 2001: The Horizontal Kinetic Energy Spectrum and Spectral Budget Simulated by a High-Resolution Troposphere-Stratosphere-Mesosphere GCM. *J. Atmos. Sci.*, **58 (4)**, 329–348, doi:10.1175/1520-0469(2001)058⟨0329:THKESA⟩2.0.CO;2.

Kraichnan, R. H., 1967: Inertial Ranges in Two-Dimensional Turbulence. *Phys. Fluids*, **10 (7)**, 1417, doi:10.1063/1.1762301.

Kraichnan, R. H., 1971: Inertial-range transfer in two- and three-dimensional turbulence. *J. Fluid Mech.*, **47 (03)**, 525, doi:10.1017/S0022112071001216.

Kraichnan, R. H., 1976: Eddy Viscosity in Two and Three Dimensions. *J. Atmos. Sci.*, **33 (8)**, 1521–1536, doi:10.1175/1520-0469(1976)033⟨1521:EVITAT⟩2.0.CO;2.

Ladyzhenskaya, O. A., 1969: *The mathematical theory of viscous incompressible flows.* 2nd ed., New York : Gordon and Breach.

Lambert, S. J., 1984: A global available potential energy-kinetic energy budget in terms of the two-dimensional wavenumber for the FGGE year. *Atmos.-Ocean*, **22 (3)**, 265–282, doi:10.1080/07055900.1984.9649199.

Lapeyre, G., and I. M. Held, 2003: Diffusivity, Kinetic Energy Dissipation, and Closure Theories for the Poleward Eddy Heat Flux. *J. Atmos. Sci.*, **60 (23)**, 2907–2916, doi:10.1175/1520-0469(2003)060⟨2907:DKEDAC⟩2.0.CO;2.

Lapeyre, G., and P. Klein, 2006: Dynamics of the Upper Oceanic Layers in Terms of Surface Quasigeostrophy Theory. *J. Phys. Oceanogr.*, **36 (2)**, 165–176, doi: 10.1175/JPO2840.1.

Larichev, V. D., and I. M. Held, 1995: Eddy Amplitudes and Fluxes in a Homogeneous Model of Fully Developed Baroclinic Instability. *J. Phys. Oceanogr.*, **25 (10)**, 2285–2297, doi:10.1175/1520-0485(1995)025⟨2285:EAAFIA⟩2.0.CO;2.

Lee, S., and I. M. Held, 1991: Subcritical Instability and Hysteresis in a Two-Layer Model. *J. Atmos. Sci.*, **48 (8)**, 1071–1077, doi:10.1175/1520-0469(1991)048⟨1071:SIAHIA⟩2.0.CO;2.

Lee, S., and I. M. Held, 1993: Baroclinic Wave Packets in Models and Observations. *J. Atmos. Sci.*, **50 (10)**, 1413–1428, doi:10.1175/1520-0469(1993)050⟨1413:BWPIMA⟩2.0.CO;2.

Leith, C. E., 1971: Atmospheric Predictability and Two-Dimensional Turbulence. 145–161 pp., doi:10.1175/1520-0469(1971)028⟨0145:APATDT⟩2.0.CO;2.

Leith, C. E., and R. H. Kraichnan, 1972: Predictability of Turbulent Flows. 1041–1058 pp., doi:10.1175/1520-0469(1972)029⟨1041:POTF⟩2.0.CO;2.

Li, L., A. P. Ingersoll, X. Jiang, D. Feldman, and Y. L. Yung, 2007: Lorenz energy cycle of the global atmosphere based on reanalysis datasets. *Geophys. Res. Lett.*, **34**, 1–5, doi:10.1029/2007GL029985.

Lian, Y., and A. P. Showman, 2008: Deep jets on gas-giant planets. *Icarus*, **194 (2)**, 597–615, doi:10.1016/j.icarus.2007.10.014.

Lindzen, R. S., and B. Farrell, 1980a: A simple approximate result for the maximum growth rate of baroclinic instabilities. *J. Atmos. Sci.*, **37**, 1648–1654.

Lindzen, R. S., and B. Farrell, 1980b: The Role of Polar Regions in Global Climate, and a New Parameterization of Global Heat Transport. *Mon. Wea. Rev.*, **108 (12)**, 2064–2079, doi:10.1175/1520-0493(1980)108⟨2064:TROPRI⟩2.0.CO;2.

Liu, J., and T. Schneider, 2010: Mechanisms of Jet Formation on the Giant Planets. *J. Atmos. Sci.*, **67 (11)**, 3652–3672, doi:10.1175/2010JAS3492.1.

Liu, J., and T. Schneider, 2011: Convective Generation of Equatorial Superrotation in Planetary Atmospheres. *J. Atmos. Sci.*, **68 (11)**, 2742–2756, doi:10.1175/JAS-D-10-05013.1.

Liu, J., and T. Schneider, 2015: Scaling of Off-Equatorial Jets in Giant Planet Atmospheres. *J. Atmos. Sci.*, **72 (1)**, 389–408, doi:10.1175/JAS-D-13-0391.1.

Lorenz, D. J., 2015: Understanding Midlatitude Jet Variability and Change Using Rossby Wave Chromatography: Methodology. *J. Atmos. Sci.*, **72 (1)**, 369–388, doi:10.1175/JAS-D-13-0199.1.

Lorenz, E. N., 1955: Available Potential Energy and the Maintenance of the General Circulation. *Tellus A*, **7**, 157–167, doi:10.3402/tellusa.v7i2.8796.

Mahlman, J. D., 1997: Dynamics of Transport Processes in the Upper Troposphere. *Science*, **276 (5315)**, 1079–1083, doi:10.1126/science.276.5315.1079.

Maltrud, M. E., and G. K. Vallis, 1991: Energy spectra and coherent structures in forced two-dimensional and beta-plane turbulence. *J. Fluid Mech.*, **228**, 321, doi:10.1017/S0022112091002720.

Manz, P., M. Ramisch, and U. Stroth, 2009: Physical mechanism behind zonal-flow generation in drift-wave turbulence. *Phys. Rev. Lett.*, **103 (16)**, 1–4, doi:10.1103/PhysRevLett.103.165004.

Marcus, P. S., 1993: Jupiter's Great Red Spot and Other Vortices. *Annu. Rev. Astron. Astrophys.*, **31 (1)**, 523–569, doi:10.1146/annurev.aa.31.090193.002515.

Marcus, P. S., and C. Lee, 1998: A model for eastward and westward jets in laboratory experiments and planetary atmospheres. *Phys. Fluids*, **10 (6)**, 1474, doi:10.1063/1.869668.

Merlis, T. M., and T. Schneider, 2009: Scales of Linear Baroclinic Instability and Macroturbulence in Dry Atmospheres. *J. Atmos. Sci.*, **66 (6)**, 1821–1833, doi:10.1175/2008JAS2884.1.

Miller, J., 1990: Statistical mechanics of Euler equations in two dimensions. *Phys. Rev. Lett.*, **65 (17)**, 2137–2140, doi:10.1103/PhysRevLett.65.2137.

Nakamura, N., 2004: Quantifying Asymmetric Wave Breaking and Two-Way Transport. *J. Atmos. Sci.*, **61 (22)**, 2735–2748, doi:10.1175/JAS3296.1.

Nazarenko, S., and B. Quinn, 2009: Triple Cascade Behavior in Quasigeostrophic and Drift Turbulence and Generation of Zonal Jets. *Phys. Rev. Lett.*, **103 (11)**, 118 501, doi:10.1103/PhysRevLett.103.118501.

Nikurashin, M., and G. Vallis, 2011: A Theory of Deep Stratification and Overturning Circulation in the Ocean. *J. Phys. Oceanogr.*, **41 (3)**, 485–502, doi:10.1175/2010JPO4529.1.

Nikurashin, M., and G. Vallis, 2012: A Theory of the Interhemispheric Meridional Overturning Circulation and Associated Stratification. *J. Phys. Oceanogr.*, **42 (10)**, 1652–1667, doi:10.1175/JPO-D-11-0189.1.

O'Gorman, P. a., and T. Schneider, 2007: Recovery of atmospheric flow statistics in a general circulation model without nonlinear eddy-eddy interactions. *Geophys. Res. Lett.*, **34 (22)**, L22 801, doi:10.1029/2007GL031779.

Paret, J., and P. Tabeling, 1997: Experimental Observation of the Two-Dimensional Inverse Energy Cascade. *Phys. Rev. Lett.*, **79 (21)**, 4162–4165, doi:10.1103/PhysRevLett.79.4162.

Patterson, G. S., and A. S. Orszag, 1971: Spectral Calculations of Isotropic Turbulence: Efficient Removal of Aliasing Interactions. *Phys. Fluids*, **14 (11)**, 2538, doi:10.1063/1.1693365.

Pauluis, O., and I. M. Held, 2002: Entropy Budget of an Atmosphere in Radiative-Convective Equilibrium. Part I: Maximum Work and Frictional Dissipation. *J. Atmos. Sci.*, **59 (2)**, 125–139, doi:10.1175/1520-0469(2002)059⟨0125:EBOAAI⟩2.0.CO;2.

Pedlosky, J., 1979: *Geophysical Fluid Dynamics*. Springer-Verlag, 624 pp.

Peixto, J. P., and A. H. Oort, 1984: Physics of climate. *Rev. Mod. Phys.*, **56 (3)**, 365–429, doi:10.1103/RevModPhys.56.365.

Phillips, N. A., 1954: Energy Transformations and Meridional Circulations associated with simple Baroclinic Waves in a two-level, Quasi-geostrophic Model. *Tellus*, **6 (3)**, 273–286, doi:10.1111/j.2153-3490.1954.tb01123.x.

Polvani, L. M., J. C. McWilliams, M. A. Spall, and R. Ford, 1994: The coherent structures of shallow-water turbulence: Deformation-radius effects, cyclone/anticyclone asymmetry and gravity-wave generation. *Chaos*, **4 (2)**, 177, doi:10.1063/1.166002, arXiv:1011.1669v3.

Randel, W. J., and I. M. Held, 1991: Phase speed spectra of transient eddy fluxes and critical layer absorption. *J. Atmos. Sci.*, **48**, 688–697, doi:10.1175/1520-0469(1991)048⟨0688:PSSOTE⟩2.0.CO;2.

Rennó, N. O., M. L. Burkett, and M. P. Larkin, 1998: A Simple Thermodynamical Theory for Dust Devils. *J. Atmos. Sci.*, **55 (21)**, 3244–3252, doi:10.1175/1520-0469(1998)055⟨3244:ASTTFD⟩2.0.CO;2.

Rennó, N. O., and A. P. Ingersoll, 1996: Natural Convection as a Heat Engine: A Theory for CAPE. *J. Atmos. Sci.*, **53 (4)**, 572–585, doi:10.1175/1520-0469(1996)053⟨0572:NCAAHE⟩2.0.CO;2.

Rhines, P. B., 1975: Waves and turbulence on a beta-plane. *J . Fluid Mech*, **69 (3)**, 417–443, doi:10.1017/S0022112075001504.

Rhines, P. B., 1979: Geostrophic Turbulence. *Annu. Rev. Fluid Mech.*, **11 (1)**, 401–441, doi:10.1146/annurev.fl.11.010179.002153.

Robert, R., and J. Sommeria, 1991: Statistical equilibrium states for two-dimensional flows. *J. Fluid Mech.*, **229 (-1)**, 291, doi:10.1017/S0022112091003038.

Robinson, W. a., 2006: On the Self-Maintenance of Midlatitude Jets. *J. Atmos. Sci.*, **63 (8)**, 2109–2122, doi:10.1175/JAS3732.1.

Saffman, P. G., 1971: On the Spectrum and Decay of Random Two-Dimensional Vorticity Distributions at Large Reynolds Number. *Stud. Appl. Math.*, **50 (4)**, 377–383, doi:10.1002/sapm1971504377.

Salmon, R., 1978: Two-layer quasi-geostrophic turbulence in a simple special case. *Geophys. Atro. Fluid*, **10 (1)**, 25–52, doi:10.1080/03091927808242628.

Salmon, R., 1980: Baroclinic instability and geostrophic turbulence. *Geophys. Atro. Fluid*, **15**, 167–211, doi:10.1080/03091928008241178.

Schneider, T., 2004: The Tropopause and the Thermal Stratification in the Extratropics of a Dry Atmosphere. *J. Atmos. Sci.*, **61 (12)**, 1317–1340, doi:10.1175/1520-0469(2004)061⟨1317:TTATTS⟩2.0.CO;2.

Schneider, T., 2007: The Thermal Stratification of the Extratropical Troposphere. *The Global Circulation of the Atmosphere*, T. Schneider, and A. H. Sobel, Eds., Princeton University Press, 47–77.

Schneider, T., and J. Liu, 2009: Formation of Jets and Equatorial Superrotation on Jupiter. *J. Atmos. Sci.*, **66 (3)**, 579–601, doi:10.1175/2008JAS2798.1.

Schneider, T., and C. C. Walker, 2006: Self-Organization of Atmospheric Macroturbulence into Critical States of Weak Nonlinear Eddy-Eddy Interactions. *J. Atmos. Sci.*, **63 (6)**, 1569–1586, doi:10.1175/JAS3699.1.

Schneider, T., and C. C. Walker, 2008: Scaling Laws and Regime Transitions of Macroturbulence in Dry Atmospheres. *J. Atmos. Sci.*, **65 (7)**, 2153–2173, doi:10.1175/2007JAS2616.1.

Scott, R. B., and F. Wang, 2005: Direct Evidence of an Oceanic Inverse Kinetic Energy Cascade from Satellite Altimetry. *J. Phys. Oceanogr.*, **35 (9)**, 1650–1666, doi:10.1175/JPO2771.1.

Scott, R. K., and D. G. Dritschel, 2012: The structure of zonal jets in geostrophic turbulence. *J. Fluid Mech.*, **711 (September)**, 576–598, doi:10.1017/jfm.2012.410.

Scott, R. K., and D. G. Dritschel, 2013: Halting scale and energy equilibration in two-dimensional quasigeostrophic turbulence. *J. Fluid Mech.*, **721**, R4, doi:10.1017/jfm.2013.120.

Scott, R. K., and D. G. Dritschel, 2014: Numerical Simulation of a Self-Similar Cascade of Filament Instabilities in the Surface Quasigeostrophic System. *Phys. Rev. Lett.*, **112 (14)**, 144 505, doi:10.1103/PhysRevLett.112.144505.

Scott, R. K., and A.-S. Tissier, 2012: The generation of zonal jets by large-scale mixing. *Phys. Fluids*, **24 (12)**, 126 601, doi:10.1063/1.4771991.

Shepherd, T. G., 1987: A Spectral View of Nonlinear Fluxes and Stationary-Transient Interaction in the Atmosphere. *J. Atmos. Sci.*, **44 (8)**, 1166–1179, doi:10.1175/1520-0469(1987)044⟨1166:ASVONF⟩2.0.CO;2.

Showman, A. P., 2007: Numerical Simulations of Forced Shallow-Water Turbulence: Effects of Moist Convection on the Large-Scale Circulation of Jupiter and Saturn. *J. Atmos. Sci.*, **64 (9)**, 3132–3157, doi:10.1175/JAS4007.1.

Showman, A. P., P. J. Gierasch, and Y. Lian, 2006: Deep zonal winds can result from shallow driving in a giant-planet atmosphere. *Icarus*, **182 (2)**, 513–526, doi:10.1016/j.icarus.2006.01.019.

Showman, A. P., and A. P. Ingersoll, 1998: Interpretation of Galileo probe data and implications for Jupiter's dry downdrafts. *Icarus*, **132 (2)**, 205–220, doi:10.1006/icar.1998.5898.

Shuckburgh, E., and P. Haynes, 2003: Diagnosing transport and mixing using a tracer-based coordinate system. *Phys. Fluids*, **15 (11)**, 3342, doi:10.1063/1.1610471.

Simmons, A. J., and B. J. Hoskins, 1976: Baroclinic Instability on the Sphere: Normal Modes of the Primitive and Quasi-Geostrophic Equations. *J. Atmos. Sci.*, **33 (8)**, 1454–1477, doi:10.1175/1520-0469(1976)033⟨1454:BIOTSN⟩2.0.CO;2.

Simmons, A. J., and B. J. Hoskins, 1977: Baroclinic Instability on the Sphere: Solutions with a More Realistic Tropopause. *J. Atmos. Sci.*, **34 (4)**, 581–588, doi:10.1175/1520-0469(1977)034⟨0581:BIOTSS⟩2.0.CO;2.

Simmons, A. J., and B. J. Hoskins, 1978: The Life Cycles of Some Nonlinear Baroclinic Waves. *J. Atmos. Sci.*, **35 (3)**, 414–432, doi:10.1175/1520-0469(1978)035⟨0414:TLCOSN⟩2.0.CO;2.

Simon-Miller, A. A., B. J. Conrath, P. J. Gierasch, G. S. Orton, R. K. Achterberg, F. M. Flasar, and B. M. Fisher, 2006: Jupiter's atmospheric temperatures: From Voyager IRIS to Cassini CIRS. *Icarus*, **180 (1)**, 98–112, doi:10.1016/j.icarus.2005.07.019.

Smith, K. S., 2004: A Local Model for Planetary Atmospheres Forced by Small-Scale Convection. *J. Atmos. Sci.*, **61 (12)**, 1420–1433, doi:10.1175/1520-0469(2004)061⟨1420:ALMFPA⟩2.0.CO;2.

Smith, K. S., 2005: Tracer transport along and across coherent jets in two-dimensional turbulent flow. *J. Fluid Mech.*, **544 (-1)**, 133, doi:10.1017/S0022112005006750.

Smith, K. S., and G. K. Vallis, 2002: The Scales and Equilibration of Midocean Eddies: Forced-Dissipative Flow. *J. Phys. Oceanogr.*, **32 (6)**, 1699–1720, doi:10.1175/1520-0485(2002)032⟨1699:TSAEOM⟩2.0.CO;2.

Smith, L., and V. Yakhot, 1993: Bose condensation and small-scale structure generation in a random force driven 2D turbulence. *Phys. Rev. Lett.*, **71 (3)**, 352–355, doi:10.1103/PhysRevLett.71.352.

Srinivasan, K., and W. R. Young, 2014: Reynolds stress and eddy diffusivity of β -plane shear flows. *J. Atmos. Sci.*, **(2)**, 140203145704009, doi:10.1175/JAS-D-13-0246.1.

Starr, V. P., 1968: *Physics of Negative Viscosity Phenomena*. McGraw Hill, 224 pp.

Stone, P. H., 1978: Baroclinic Adjustment. *J. Atmos. Sci.*, **35 (4)**, 561–571, doi:10.1175/1520-0469(1978)035⟨0561:BA⟩2.0.CO;2.

Stone, P. H., and M.-S. Yao, 1990: Development of a Two-Dimensional Zonally Averaged Statistical-Dynamical Model. Part III: The Parameterization of the Eddy Fluxes of Heat and Moisture. *J. Climate*, **3 (7)**, 726–740, doi:10.1175/1520-0442(1990)003⟨0726:DOATDZ⟩2.0.CO;2.

Straus, D. M., and P. Ditlevsen, 1999: Two-dimensional turbulence properties of the ECMWF reanalyses. *Tellus A*, **51**, 749–772, doi:10.3402/tellusa.v51i5.14473.

Sukoriansky, S., N. Dikovskaya, and B. Galperin, 2007: On the Arrest of Inverse Energy Cascade and the Rhines Scale. *J. Atmos. Sci.*, **64 (9)**, 3312–3327, doi: 10.1175/JAS4013.1.

Sukoriansky, S., N. Dikovskaya, and B. Galperin, 2009: Transport of momentum and scalar in turbulent flows with anisotropic dispersive waves. *Geophys. Res. Lett.*, **36 (14)**, L14 609, doi:10.1029/2009GL038632.

Sukoriansky, S., B. Galperin, and N. Dikovskaya, 2002: Universal Spectrum of Two-Dimensional Turbulence on a Rotating Sphere and Some Basic Features of Atmospheric Circulation on Giant Planets. *Phys. Rev. Lett.*, **89 (12)**, 124 501, doi: 10.1103/PhysRevLett.89.124501.

Tao, T., 2015: Finite time blowup for an averaged three-dimensional Navier-Stokes equation. *J. Amer. Math. Soc.*, **29 (3)**, 601–674, doi:10.1090/jams/838, 1402.0290.

Thompson, A. F., and W. R. Young, 2007: Two-Layer Baroclinic Eddy Heat Fluxes: Zonal Flows and Energy Balance. *J. Atmos. Sci.*, **64 (9)**, 3214–3231.

Tobias, S. M., and J. B. Marston, 2013: Direct Statistical Simulation of Out-of-Equilibrium Jets. *Phys. Rev. Lett.*, **110 (10)**, 104 502, doi:10.1103/PhysRevLett. 110.104502.

Tulloch, R., J. Marshall, C. Hill, and K. S. Smith, 2011: Scales, Growth Rates, and Spectral Fluxes of Baroclinic Instability in the Ocean. *J. Phys. Oceanogr.*, **41 (6)**, 1057–1076, doi:10.1175/2011JPO4404.1.

Valdes, P. J., and B. J. Hoskins, 1988: Baroclinic Instability of the Zonally Averaged Flow with Boundary Layer Damping. *J. Atmos. Sci.*, **45 (10)**, 1584–1593, doi: 10.1175/1520-0469(1988)045⟨1584:BIOTZA⟩2.0.CO;2.

Vallis, G. K., 2006: *Atmospheric and Oceanic Fluid Dynamics*. Cambridge University Press, Cambridge, U.K., 745 pp.

Vallis, G. K., and M. E. Maltrud, 1993: Generation of Mean Flows and Jets on a Beta Plane and over Topography. *J. Phys. Oceanogr.*, **23 (7)**, 1346–1362, doi: 10.1175/1520-0485(1993)023⟨1346:GOMFAJ⟩2.0.CO;2.

Vasavada, A. R., and A. P. Showman, 2005: Jovian atmospheric dynamics: an update after Galileo and Cassini. *Rep. Prog. Phys.*, **68 (8)**, 1935–1996, doi: 10.1088/0034-4885/68/8/R06.

Waite, M. L., and C. Snyder, 2009: The Mesoscale Kinetic Energy Spectrum of a Baroclinic Life Cycle. *J. Atmos. Sci.*, **66**, 883–901, doi:10.1175/2008JAS2829.1.

Wang, B., A. Barcilon, and L. N. Howard, 1985: Linear Dynamics of Transient Planetary Waves in the Presence of Damping. *J. Atmos. Sci.*, **42 (18)**, 1893–1910, doi:10.1175/1520-0469(1985)042⟨1893:LDOTPW⟩2.0.CO;2.

Wheeler, M., and G. N. Kiladis, 1999: Convectively Coupled Equatorial Waves: Analysis of Clouds and Temperature in the Wavenumber-Frequency Domain. *J. Atmos. Sci.*, **56 (3)**, 374–399, doi:10.1175/1520-0469(1999)056⟨0374:CCEWAO⟩2.0.CO;2.

Whitaker, J. S., and A. Barcilon, 1995: Low-Frequency Variability and Wavenumber Selection in Models with Zonally symmetric Forcing. *J. Atmos. Sci.*, **52 (4)**, 491–503, doi:10.1175/1520-0469(1995)052⟨0491:LFVAWS⟩2.0.CO;2.

Williams, G. P., 1978: Planetary Circulations: 1. Barotropic Representation of Jovian and Terrestrial Turbulence. *J. Atmos. Sci.*, **35 (8)**, 1399–1426, doi:10.1175/1520-0469(1978)035⟨1399:PCBROJ⟩2.0.CO;2.

Williams, G. P., and J. L. Halloway, 1982: The range and unity of planetary circulations. *Nature*, **297 (5864)**, 295–299, doi:10.1038/297295a0.

Williams, P., 1985: *Issues in Atmospheric and Oceanic Modeling - Part A Climate Dynamics*, Advances in Geophysics, Vol. 28. Elsevier.

Yuan, L., and K. Hamilton, 1994: Equilibrium dynamics in a forced-dissipative f -plane shallow-water system. *J. Fluid Mech.*, **280 (-1)**, 369, doi:10.1017/S0022112094002971.

Zurita-Gotor, P., 2007: The Relation between Baroclinic Adjustment and Turbulent Diffusion in the Two-Layer Model. *J. Atmos. Sci.*, **64 (4)**, 1284–1300, doi:10.1175/JAS3886.1.

Zurita-Gotor, P., 2008: The Sensitivity of the Isentropic Slope in a Primitive Equation Dry Model. *J. Atmos. Sci.*, **65 (1)**, 43–65, doi:10.1175/2007JAS2284.1.

Zurita-Gotor, P., and G. K. Vallis, 2009: Equilibration of Baroclinic Turbulence in Primitive Equations and Quasigeostrophic Models. *J. Atmos. Sci.*, **66 (4)**, 837–863, doi:10.1175/2008JAS2848.1.